

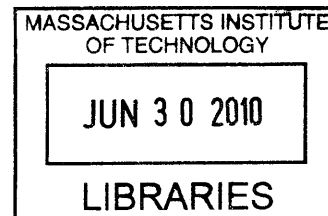
# Predicting Combustion Properties of Hydrocarbon Fuel Mixtures

by

Claude Franklin Goldsmith III

B.S., North Carolina State University (2003)

B.A., University of North Carolina (1998)



**ARCHIVES**

Submitted to the Department of Chemical Engineering  
in partial fulfillment of the requirements for the degree of

Doctor of Philosophy

at the

MASSACHUSETTS INSTITUTE OF TECHNOLOGY

June 2010

© Massachusetts Institute of Technology 2010. All rights reserved.

Author .....  
Department of Chemical Engineering  
May 3, 2010

Certified by .....  
William H. Green  
Professor  
Thesis Supervisor

Accepted by.....  
William M. Deen  
Chairman, Department Committee on Graduate Theses



# Predicting Combustion Properties of Hydrocarbon Fuel Mixtures

by

Claude Franklin Goldsmith III

Submitted to the Department of Chemical Engineering  
on May 3, 2010, in partial fulfillment of the  
requirements for the degree of  
Doctor of Philosophy

## Abstract

In this thesis, I applied computational quantum chemistry to improve the accuracy of kinetic mechanisms that are used to model combustion chemistry. I performed transition state theory calculations for several reactions that are critical in combustion, including a detailed analysis of the pressure dependence of these rate coefficients. I developed a new method for rapidly estimating the vibrational modes and hindered rotor parameters for molecules. This new method has been implemented in an automatic reaction mechanism generation software, RMG, and has improved the accuracy of the density of states computed in RMG, which in turn has improved RMG's ability to predict the pressure-dependence of rate coefficients for complex reaction networks. I used statistical mechanics to compute the thermochemistry for over 170 of the most important species in combustion. These calculations form a new library of thermodynamic parameters, and this library will improve the accuracy of kinetic models, particularly for fuel lean conditions. I measured reaction rate coefficients using both laser flash-photolysis absorption spectroscopy in a slow-flow reactor and time-of-flight mass spectrometry and laser Schlieren densitometry in a shock tube. Based upon these experimental projects, I helped design a one-of-a-kind instrument for measuring rate coefficients for combustion-relevant reactions. The new reactor combines photoionization time-of-flight mass spectrometry with multi-pass absorption spectroscopy in a laser-flash photolysis cell. The cumulative effect of these efforts should advance our understanding of combustion chemistry and allow us to make more accurate predictions of how hydrocarbons burn.

Thesis Supervisor: William H. Green  
Title: Professor

# **Dedication**

For Tania.



## Acknowledgments

I would like to thank my supervisor, Prof. William H. Green. I had a wonderful five years in his group, enjoying each year more than the last, this is due to his insight, patience, dedication to good science, and above all his infectious enthusiasm for the subject. I am grateful for the freedom he gave me to choose hard problems and his understanding when things didn't work out as hoped. His guidance as an academic advisor will serve as a model for me.

I would like to thank my thesis committee members: Prof. Paul Barton, Prof. Herb Sawin, and Prof. Troy Van Voorhis. Their distinct backgrounds led to exciting committee meetings, and their comments were always thoughtful and constructive.

I would especially like to acknowledge the past and present members of the Green Group. I have had the best colleagues in the department, and my work has benefitted immeasurably from their presence. I would like to thank Dr. Sandeep Sharma for all his help over the years; Sandeep tackled all my questions, no matter how random, and made the whole process seem fun. Dr. Rob Ashcraft, whom I first befriended at NCSU, continued to be an amazing colleague, whose clarity of mind and analytical skill was invaluable. Dr. Huzeifa Ismail got me started in the lab, as he patiently explained – often many times – why we do what we do. Our collaboration on vinyl chemistry is beautiful merging of experiment and theory. Dr. Richard West has been the post-doc extraordinaire. His policy of twice-daily tea breaks increased both the productivity and conviviality of our group. Joshua Middaugh has been a great colleague in designing the new reactor; it was exciting to see how quickly his knowledge of the spectroscopy lab eclipsed my own. Joshua Allen did more for pressure dependence in RMG in two years than four previous colleagues did in ten. Michael Harper was a model of graciousness, no matter how many times I interrupted his work; my work on oxidation thermo would not have been possible without the software developed by Sandeep and Mike.

I would like to thank Dr. Robert Tranter at Argonne National Laboratory for allowing me to join his lab for six months in 2008. Our discussions on equipment design, shock tubes, and combustion kinetics had a profound impact on my understanding of experimen-

tal research. Dr. Stephen Klippenstein at Argonne has been an enormous influence on my work. Long before we met, he patiently answered my emails regarding the subtleties of VariFlex. We have since collaborated on two exciting projects on ignition chemistry. Our work on the kinetics of allyl and hydroperoxyl radicals is a great example of using cutting-edge computational techniques to address experimentally challenging problems in combustion chemistry. I would also like to thank Dr. Craig Taatjes at Sandia National Lab for his helpful comments and suggestions over the years on many issues of combustion chemistry.

And finally, I would like to give the biggest thanks to my parents, Dianne Tuttle and Frank Goldsmith. Without their love, support, and encouragement, none of this would have been possible. Each in their own way, they instilled in both their children a love of science, a strong work ethic, and a desire to do good.

# Contents

<b>1 Vinyl Radical with Alkenes</b>	<b>21</b>
1.1 Experimental Summary . . . . .	22
1.2 Theory . . . . .	25
1.3 Results . . . . .	27
1.3.1 Vinyl Plus Ethene . . . . .	27
1.3.2 Vinyl Plus Propene . . . . .	29
1.3.3 Vinyl Plus 1-butene . . . . .	40
1.3.4 Vinyl Plus 2-butene . . . . .	46
1.3.5 Vinyl Plus iso-butene . . . . .	51
1.4 Discussion . . . . .	56
1.4.1 Rate Rules for Vinyl + Alkenes: Arrhenius Parametrization . . . . .	64
1.4.2 Conclusion . . . . .	71
1.5 Supplemental C <sub>5</sub> H <sub>9</sub> Potential Energy Surfaces . . . . .	73
<b>2 Allyl + HO<sub>2</sub></b>	<b>77</b>
2.1 Introduction . . . . .	77
2.2 Theory . . . . .	81
2.2.1 Potential Energy Surfaces . . . . .	81
2.2.2 Variable Reaction Coordinate TST Calculations . . . . .	84
2.2.3 Master Equation Calculations . . . . .	86
2.3 Results and Discussion . . . . .	87
2.3.1 Allyl + HO <sub>2</sub> Reaction . . . . .	87
2.3.2 Allylhydroperoxide Dissociation . . . . .	90

2.3.3	Allyloxy Kinetics . . . . .	91
2.4	Kinetic Model . . . . .	92
2.5	Conclusion . . . . .	95
<b>3</b>	<b>Frequency Estimation in RMG</b>	<b>97</b>
3.1	Introduction . . . . .	97
3.2	Background . . . . .	97
3.2.1	Formulation of the Master Equation . . . . .	98
3.3	Method for Estimating Density of States . . . . .	109
3.3.1	The Three-Frequency Model . . . . .	112
3.3.2	The Functional-Group Frequency Model . . . . .	113
3.4	Case Study: The Acetyl + Oxygen System . . . . .	116
3.4.1	Density of States Comparison . . . . .	122
3.5	Recommendations for Future Work . . . . .	123
3.6	Conclusion . . . . .	124
3.7	Appendix: Tables . . . . .	124
<b>4</b>	<b>Primary Thermo Library for Oxidation Chemistry of Light Alkanes</b>	<b>131</b>
4.1	Introduction . . . . .	131
4.2	Improvements to CanTherm . . . . .	134
4.2.1	Hindered Rotor Potentials . . . . .	134
4.2.2	Free Rotors . . . . .	135
4.2.3	Barrier Heights . . . . .	136
4.2.4	Heat Capacity Routines . . . . .	137
4.3	Computational Methods . . . . .	138
4.3.1	Benchmark Study of Computational Methods . . . . .	140
4.4	Recommendation for Future Work . . . . .	140
<b>5</b>	<b>Design of Time-of-Flight Mass Spectrometer Gas Sampling System</b>	<b>157</b>
5.1	Introduction . . . . .	158

5.1.1	Motivation: Vinyl + O <sub>2</sub> , and the need for a new way to measure radical kinetics . . . . .	158
5.1.2	Argonne National Laboratory . . . . .	161
5.2	Design of the TOF-MS Reactor . . . . .	163
5.2.1	Comparison with other TOF-MS Reactors . . . . .	163
5.2.2	Gas Sampling System Overview . . . . .	164
5.2.3	Interference with Laser Absorption Spectroscopy . . . . .	165
5.2.4	Volume of Sample Gas . . . . .	167
5.2.5	Pressure Increase Around the Nozzle . . . . .	170
5.2.6	Formation of the Supersonic Expansion . . . . .	172
5.2.7	Collimation of the Molecular Beam . . . . .	177
5.2.8	Estimation of Sensitivity . . . . .	180
5.3	Conclusion . . . . .	181
<b>6</b>	<b>Recommendations for Future Work</b>	<b>183</b>
6.1	Vinyl Plus Alkenes . . . . .	183
6.2	Allyl + HO <sub>2</sub> . . . . .	184
6.3	Frequency Estimation . . . . .	185
6.4	Thermo Library . . . . .	186
6.5	RMG in General . . . . .	187



# List of Figures

1-1	Vinyl + ethene potential energy surface . . . . .	27
1-2	Vinyl + ethene results . . . . .	28
1-3	Vinyl + propene potential energy surface . . . . .	32
1-4	Vinyl + propene results . . . . .	38
1-5	Vinyl + 1-butene potential energy surface . . . . .	42
1-6	Vinyl + 1-butene results . . . . .	44
1-7	Vinyl + 2-butene potential energy surface . . . . .	48
1-8	Vinyl + 2-butene Results . . . . .	49
1-9	Vinyl + iso-butene potential energy surface . . . . .	53
1-10	Vinyl + iso-butene Results . . . . .	54
1-11	Evans-Polanyi plot for vinyl + alkenes . . . . .	62
1-12	Electrophilic polar correction for vinyl addition to alkenes . . . . .	66
1-13	Rate rule activation energies . . . . .	67
1-14	Test of rate rules . . . . .	69
1-15	Group additivity rate rule versus experimental data . . . . .	72
1-16	Potential energy surface for 4-penten-2-yl. . . . .	73
1-17	Potential energy surface for 2-methyl-3-buten-1-yl. . . . .	73
1-18	Potential energy surface for 1-ethyl-allyl. . . . .	74
1-19	Potential energy surface for 1-penten-1-yl. . . . .	74
1-20	Potential energy surface for 1-penten-2-yl. . . . .	74
1-21	Potential energy surface for 2-methyl-cyclopropylmethyl. . . . .	75
1-22	Potential energy surface for 3-methyl-cyclobutyl. . . . .	75
1-23	Potential energy surface for 4-penten-1-yl. . . . .	75

2-1	Allyl + HO <sub>2</sub> potential energy surface . . . . .	82
2-2	C <sub>3</sub> H <sub>6</sub> O <sub>2</sub> potential energy surface . . . . .	83
2-3	Allyl + HO <sub>2</sub> addition/dissociation rate coefficients . . . . .	87
2-4	Allyl + HO <sub>2</sub> abstraction . . . . .	88
2-5	Allyloxy decomposition . . . . .	92
2-6	Allyl + HO <sub>2</sub> kinetic model results . . . . .	94
3-1	Acetyl plus oxygen potential energy surface . . . . .	116
3-2	Comparison of density of states, partition functions, and heat capacities . . .	121
4-1	Allylic hindered rotors . . . . .	137
5-1	Location of the sampling nozzle in the Herriott cell . . . . .	165
5-2	Sampling plate . . . . .	166
5-3	Cross section of the new reactor . . . . .	166
5-4	Limiting cases for spherical cone . . . . .	168
5-5	Sample gas volume . . . . .	169
5-6	Pressure drop at 3000 sccm . . . . .	171
5-7	Continuum free jet expansion . . . . .	172
5-8	Mach disk location and centerline properties . . . . .	175
5-9	Number of collision in free jet expansion . . . . .	176
5-10	Number of collisions along flight path length . . . . .	177
5-11	Optimum skimmer placement . . . . .	179
5-12	Flight time . . . . .	180



# List of Tables

1.1	Species for vinyl + ethene potential energy surface . . . . .	28
1.2	Transition states for vinyl + ethene potential energy surface . . . . .	29
1.3	Species for vinyl + propene potential energy surface . . . . .	32
1.4	Transition states for vinyl + propene potential energy surface . . . . .	33
1.5	Species for vinyl + 1-butene potential energy surface . . . . .	45
1.6	Transition states for vinyl + 1-butene potential energy surface . . . . .	46
1.7	Species for vinyl + 2-butene potential energy surface . . . . .	50
1.8	Transition states for vinyl + 2-butene potential energy surface . . . . .	51
1.9	Species for vinyl + iso-butene potential energy surface . . . . .	55
1.10	Transition states for vinyl + iso-butene potential energy surface . . . . .	56
1.11	Modified-Arrhenius parameters for experimental data and theoretical addition rates . . . . .	57
1.12	Reaction path degeneracy and rotational effects . . . . .	58
1.13	Barrier heights and reaction enthalpies for vinyl + alkenes . . . . .	59
1.14	Molecular orbitals and polar effects for reactants . . . . .	59
1.15	Barrier heights and reaction enthalpies for methyl + alkenes (from literature)	61
1.16	Modified-Arrhenius parameters for H-abstraction rate coefficients . . . . .	70
2.1	Literature rate constants for allyl + HO <sub>2</sub> . . . . .	80
2.2	Species for allyl + HO <sub>2</sub> potential energy surface . . . . .	83
2.3	Transition states for allyl + HO <sub>2</sub> potential energy surface . . . . .	84
2.4	Species for C <sub>3</sub> H <sub>5</sub> O potential energy surface . . . . .	84
2.5	Transition states for C <sub>3</sub> H <sub>5</sub> O potential energy surface . . . . .	85

2.6	Calculated rate coefficients for allyl + HO <sub>2</sub> . . . . .	89
2.7	Rate coefficients for allyl-hydroperoxide . . . . .	90
2.8	Rate coefficients for allyloxy decomposition . . . . .	93
3.1	Calculated rate coefficients for acetyl + O <sub>2</sub> . . . . .	119
3.2	Comparison of methods for harmonic oscillator degrees of freedom . . . . .	120
3.3	Comparison of methods for hindered rotor degrees of freedom . . . . .	120
3.4	List of group types and the corresponding frequency range . . . . .	124
3.5	Cases used within RMG to solve for unknown parameters . . . . .	128
4.1	Benchmark study of computation method . . . . .	141
4.2	C1 species in new thermo library . . . . .	143
4.3	C2 species in new thermo library . . . . .	145
4.4	C3 species in new thermo library . . . . .	149
4.5	C4 species in new thermo library . . . . .	154

# Introduction

The combustion of hydrocarbons is the most prevalent energy conversion technology. As a result of its dominance, the focus on the future and sustainability of combustion continues to rise. The long-term availability of fossil fuels and the political stability of principal exporting nations are a serious geo-political concerns. The environmental costs associated with combustion are both local and global, from the risks to human health caused by conventional pollutants to global climate change caused by anthropogenic production of carbon dioxide.

These geo-political and environmental concerns have created a renewed interest in improving the performance of combustion devices. Combustion technology, although quite mature, has significant room for improvement. However, incremental improvements often come at great cost. To use internal combustion engines as an example: Essential engineering tasks – such as blending novel fuels for enhanced engine performance, or optimizing the engine design for a fixed range of fuels – are complicated, time consuming, and above all incredibly expensive. The high cost is a consequence of the complex chemistry of combustion. A detailed description of internal combustion engines is inherently multi-scale, with time scales ranging from the nanosecond to the second, and length scales ranging from the Angstrom to the meter. Because of this complexity, the old approach to combustion was to treat the chemistry like a black box: fuel went in, burnt fuel and heat came out. Attempts to predict engine performance based upon fuel variables had limited success. Because the chemistry is so complex, it could not be handled explicitly, so it was reduced into lumped-parameter models. These oversimplifications yielded models that could not be extrapolated outside a narrow range; consequently, they had a limited predictive power. This chemistry-blind approach to fuel and engine design has worked well in the past, but it

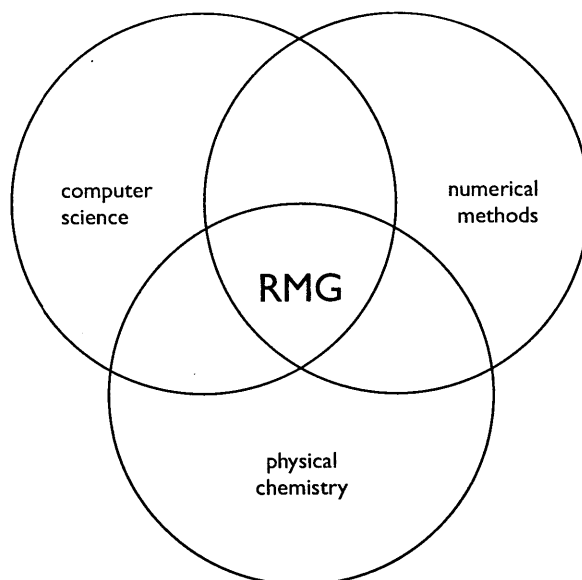
has reached a point of diminishing returns.

Fortunately, we are poised for a renaissance in combustion technologies. This renaissance has been possible because of a deeper understanding of the fundamental physico-chemical phenomena. We no longer need to treat the chemistry as a black box. Instead, we can begin to understand combustion at the atomistic level, which allows us to make quantitative predictions about how fuels burn. We can more easily and more confidently extrapolate from one set of conditions to another. Because much of this work could be done on a computer, it would be both faster and cheaper to design new combustion devices.

One of the grand challenges with an atomic scale approach is complexity of the chemistry, even for simple fuels. Keeping track of all the intermediate species and the corresponding elementary reactions requires hundreds of species and thousands of rate coefficients. For larger fuels such as diesel fuels, and for real-world fuel blends with additives, the number of species and reactions will increase by an order of magnitude. Creating a chemical kinetic mechanism of this size is difficult at best, even for experts in the field. The sheer number of physical parameters required is daunting.

One approach to this problem is to automate the process on a computer. Our research group has developed a software package, Reaction Mechanism Generator (RMG), that automatically generates a detailed chemical kinetic mechanism. These mechanisms are composed entirely of elementary reactions and are valid for a wide range of conditions. The process is systematic and thorough: it finds many reactions that even an expert might miss, and it does not get bored in the process.

Broadly speaking, RMG is a blend of computer science (making sure the code works), numerical methods (making sure the problem can be solved), and physical chemistry (making sure the numbers are realistic). Over the course of my thesis, I contributed something to each of these disciplines. Although the contributions were distinct, the overall objective of my thesis was to improve the accuracy of the physical parameters used by RMG. These contributions can be divided into (i) improvements made to the kinetics data in RMG, and (ii) improvements made to the thermochemistry in RMG. The kinetics work involved detailed calculations of rate coefficients using transition state theory and computational quantum mechanics. These projects are detailed in Chapters 1 and 2. The thermodynamic work



involved improving RMG's ability to compute the density of states for a molecule, detailed in Chapter 3, and developing a new database of enthalpy, entropy, and heat capacities for more nearly 200 of the most important species in combustion, detailed in Chapter 4. Chapter 5 shifts gears from computational work to experiments. It describes the design of a new reactor for measuring reaction rates. This new reactor, once completed, should provide unparalleled amounts of data for complex reaction networks. The final chapter suggests future research in all of these topics. The first five chapters are summarized below.

## Chapter 1: Kinetics of Vinyl + Alkenes

This chapter describes the kinetics of the various reactions involving the vinyl radical,  $C_2H_3$ , with the first five alkenes: ethene, propene, 1-butene, 2-butene, and iso-butene. These reactions are important in low-temperature fuel-rich flames, and a proper description of them is essential for modeling early soot chemistry. This work was done in collaboration with Dr. Huzeifa Ismail. Dr. Ismail performed laser flash-photolysis absorption spectroscopy experiments to measure the overall rate constant for vinyl consumption, and I computed the theoretical rate coefficients for all the various channels using transition state theory and computational quantum chemistry. According to the calculations, the dominant product for each system will be the collisionally stabilized initial adducts, which

are a mixture of unsaturated hydrocarbon radicals. At higher temperatures, the addition-isomerization-dissociation channels will yield a mixture of dienes, H atoms, and alkyl radicals, and the direct H-abstraction channels will yield ethene plus allylic radicals. The experimental activation energies for the addition reactions do not vary monotonically with  $\Delta H_{rxn}$ ; instead they scale with electrophilicity and steric effects consistent with the present and prior quantum chemical calculations. A new group-additivity based rate rule has been provided for both the addition reactions and H-abstraction reactions for the vinyl radical with generic alkenes. This rate rule is in excellent agreement with both the available experimental data and quantum chemical calculations. Between Dr. Ismail's experiments and the computational methods presented here, this work is the most detailed analysis yet of this important class of reactions.

## Chapter 2: Kinetics of Allyl + HO<sub>2</sub>

Chapter 2 presents a theoretical investigation of the kinetics of the allyl + HO<sub>2</sub> bimolecular reaction and the subsequent kinetics of allyloxy decomposition. This reaction is important in oxidation chemistry, particularly in understanding the negative temperature coefficient in ignition delays. This study presents for the first time a set of comprehensive pressure-dependent rate coefficients for a wide range of temperatures and pressures relevant for combustion modeling. Rate coefficients were calculated using *ab initio* theory, variable reaction coordinate transition state theory, variational transition state theory, and master equation simulations. The present calculations are in good agreement with available experimental data for the addition reaction, but differ substantially from the literature rate for the H-abstraction reaction. Based upon an error analysis, we concluded that the experimentally inferred rate constant is in error. At combustion-relevant temperatures, most of the allyl + HO<sub>2</sub> goes directly to allyloxy + OH via chemical activation. Allyloxy will decompose to H + acrolein, HCO + ethene, and vinyl + CH<sub>2</sub>O. The prompt formation of OH via chemical activation, and the slower rate of formation of propene + O<sub>2</sub>, suggest that this reaction can promote chain branching significantly more than previous models suggest.

## **Chapter 3: Functional-Group Frequency Estimation**

One of the biggest challenges in combustion chemistry is the pressure dependence of rate coefficients. Predicting pressure dependence requires solving the so-called Master Equation, which in turn requires microcanonical rate theory. Microcanonical rate theory presumes that the vibrational modes of the reactants are accurately known. Predicting these vibrational modes is a challenge for RMG, since it does not have three-dimensional representations of molecules. In this chapter I present a new framework for estimating vibrational frequencies and hindered internal rotor parameters. The new method – inspired by IR spectroscopy – separates a molecule into its functional groups and assigns frequencies accordingly. The remaining frequencies are fit from heat capacity data. The new method is physically more realistic and more accurate than the pre-existing three-frequency model. This new approach improves the accuracy of pressure-dependent rate coefficients calculated within RMG.

## **Chapter 4: A New Primary Thermo Library for Oxidation Chemistry of Light Alkanes**

This chapter presents detailed computational quantum chemistry calculations for over 170 molecules that are critically important in combustion chemistry. Statistical mechanics was used to compute the enthalpy, entropy, and heat capacity from 300 to 6000 K. The results have been fit to the fourteen-coefficient NASA polynomial, which is the industry standard in reactive flow simulation software. In addition to the basic thermodynamic quantities, key spectroscopic data have been calculated as well. The rotational constants, vibrational frequencies, reduced moments of inertia, and rotational potentials for internal rotation for each species are available. This work should improve the accuracy of combustion models, particularly for light alkanes and oxygenated species.

## Chapter 5: Design of a Time-of-Flight Mass Spectrometer Flow Reactor

We have designed a new laser flash photolysis reactor that will allow us to combine the current multi-pass laser absorption spectroscopy (LAS) system with a time-of-flight mass spectrometer (TOF-MS) to measure chemical kinetics. This simultaneous LAS/TOF-MS system would be a one-of-a-kind reactor for measuring reactions under combustion relevant conditions: The LAS will continue to provide high-accuracy measurements of the reaction rates, and the TOF will provide concentration profiles of all the product channels. The combination of these two pieces of information would provide unprecedented data for complex reactions. This chapter describes the essential gas dynamics problems in the new design, i.e. getting the reactive gas from the photolysis region to the detector as quickly as possible with as few collisions as possible. The reactor cell has a novel sampling nozzle built into the side. This cell is surrounded by a low-vacuum region, which creates a supersonic free jet expansion. The low-vacuum region is connected to a high-vacuum region via a nickel skimmer, which collimates the free jet expansion into a molecular beam. This molecular beam is ionized in the high-vacuum region – either via electron impact or photoionization – before continuing to the detector. Based upon the calculations presented in this chapter, the differential pumping system should allow us to (i) sample gas from the photolysis beam without disturbing the probe laser, (ii) rapidly quench the gas so that the chemical composition is frozen, and (iii) transport it to the ionization region and thence the detector with a minimum number of collisions. The photoionization detection limit should be on the order of 0.1 ppm, which should provide us with excellent signal for kinetics experiments.



# Chapter 1

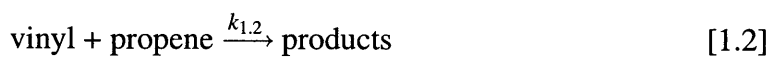
## Vinyl Radical with Alkenes

Reactions involving vinylic radicals are important in combustion processes [98]. The simplest radical of this class is vinyl ( $C_2H_3$ ), which has a pivotal role in the competition between oxidation and molecular weight growth chemistry leading to soot formation. At high temperatures, vinyl rapidly decomposes to acetylene [50]. In  $O_2$ -starved environments at lower temperatures, vinyl will either add to unsaturated hydrocarbons or abstract an H-atom; these two competing reactions will create a mixture of dienes, cyclic species, and resonantly stabilized free radicals, each of which can lead to the formation of polycyclic aromatic hydrocarbons (PAHs) and other early precursors of soot [86]. In contrast, if  $O_2$  is present, then vinyl reacts rapidly to form vinylperoxy, which after several fast chemically activated isomerization reactions decomposes to  $HCO + CH_2O$  and then to  $CO$  or  $CO_2$  [67]. Therefore, the relative rates of these addition, abstraction, and oxidation reactions of vinyl are central in the determination of when various fuels will form soot and when they form complete combustion products.

Despite its importance, relatively little experimental work has been performed on vinyl chemistry. With respect to vinyl addition to unsaturated hydrocarbons, the only experimental rate coefficients are for vinyl + ethene. Fahr and Stein [13] employed the very low pressure pyrolysis (VLPP) technique to study the kinetics and products of the  $C_2H_3 + C_2H_4$  reaction over a temperature range of 1023-1273 K and at low pressure between 1.3 and 13  $\mu$ bar. Temperature-dependent rate parameters for the  $C_2H_3 + C_2H_4$  reaction were derived relative to the vinyl self-reaction,  $C_2H_3 + C_2H_3$ . Shestov et al. [92] reported kinetic studies

of the  $C_2H_3 + C_2H_4$  reaction from 625 to 950 K and at pressures between 7 and 15 mbar, using the laser photolysis/photoionization mass spectroscopy (LP/PIMS) technique. Tsang has published five rate coefficients for vinyl + propene, but each of these rate coefficients is based upon other reaction systems [99]. Neither experimental nor thermochemically-derived estimates rate coefficients were published for vinyl plus butene isomers.

As a component of his doctoral thesis, Dr. Huzeifa Ismail measured the rate coefficients for the reaction of the vinyl radical with the first five alkenes: ethene, propene, 1-butene, 2-butene, and iso-butene [35].

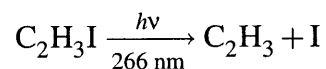


In collaboration with Dr. Ismail, I performed the accompanying theoretical calculations. This collaboration culminated in three papers [37, 24, 23]. This chapter presents the theoretical second-order rate coefficients for the five vinyl plus alkene reactions. In addition to the calculated rates for those five reactions, a generic rate rule for vinyl addition to various alkenes is recommended; a similar rate rule for the abstraction of H atoms by vinyl from alkenes is also provided. Lastly, an explanation is provided for the anomalous Evans-Polanyi plots exhibited by the vinyl addition reactions.

## 1.1 Experimental Summary

This section summarizes the experimental conditions. A complete description of the experiments, including the raw data from the experiments, is available in Dr. Ismail's thesis [35]. Since my contribution was in the theoretical calculations, only brief description of the experimental setup is provide here. These experiments were performed in the Combustion

Dynamics Laboratory at the Massachusetts Institute of Technology. Vinyl radicals ( $C_2H_3$ ) were generated via laser photolysis of vinyl iodide at 266 nm



Photolysis pulses were generated by frequency-doubling the 532 nm output of a short pulse (2 ns) Nd/YAG laser. Vinyl radicals were detected by multiple pass laser absorption at one of two absorption lines, 423.2 or 475.0 nm [34, 78, 89]. The detection wavelength was generated using a mode-locked Ti/sapphire laser (1.2 ps at 80 MHz) pumped by a 532 nm diode-pumped solid state continuous-wave (CW) laser. The output of the Ti/sapphire laser was frequency-doubled using a BBO crystal. The laser pulses every 12 ns, providing an effective continuous probe of the vinyl radical decay, which occurs on a much longer time scale. The spectral range of the laser, when used with a harmonic generator, covers most of the visible wavelengths, allowing for the detection of a wide array of organic radical species. The line width of the laser is  $13 \text{ cm}^{-1}$  in the 400 nm detection region. The excellent stability of this laser system allows accurate measurement of rate constants from the microsecond-to-millisecond time scale. A complete transient is measured following each photolysis pulse, making the measurement relatively insensitive to fluctuations in the photolysis laser output. A Herriott-type multipass resonator is used to increase the path length by 40 m. An Ocean Optics spectrometer (0.1 nm fwhm) was used to determine the output wavelength. The spectrum of vinyl radical is ideal for such a probe laser because its absorption features are broader than the laser fwhm yet still narrow enough to allow tuning off-resonance. The off-resonance background signal contains contributions arising from thermal lensing; the vinyl concentration is taken to be proportional to the difference in absorption between traces taken on- and off-resonance.

The experiments were carried out in a 160 cm long temperature-controlled stainless steel flow reactor. To improve the signal-to-noise ratio, a balanced detection scheme was used where a reference beam ( $I_0$ ) that does not pass through the reactor is subtracted from the probe beam ( $I$ ) via a low-noise differential amplifier. To maintain a constant flow of the reactant and buffer gases, calibrated mass flow controllers were used. The internal pressure

of the reactor is measured by a capacitance manometer and controlled via an automated butterfly valve. The flow reactor was housed in a cylindrical oven. Additional resistive heating was supplied to the reactor entrance and exit region. The entrance, center, and exit temperatures were monitored using K-type thermocouples that were fed into three independent PID controllers to maintain a uniform, constant temperature ( $\pm 5$  K). All experiments were performed between 300 to 700 K and at a pressure of 100 Torr. Additionally, the experiments for vinyl plus ethene and vinyl plus propene were repeated at 10 Torr.

To maintain pseudo-first-order conditions, alkene concentrations were in large excess over vinyl concentration, which ensured that the pseudo-first-order decays were at least five times faster than the decay without added alkenes. For most of the experiments, vinyl iodide concentrations were maintained at  $[C_2H_3I] = 1 \times 10^{15}$  molecules  $cm^{-3}$ . We performed some experiments at several concentrations of vinyl by varying photolysis laser intensity and  $C_2H_3I$  concentration. It was found that the rate constants did not depend on  $[C_2H_3I]$  or on photolysis energy, confirming the validity of a pseudo-first-order approximation and suggesting a negligible role for photolytic interferences. Typically, the photolysis laser pulsed once per second. Only 0.2% of vinyl iodide dissociates on each pulse. In most experiments, flow rates were sufficient to completely refresh the cell every 3-5 s. To confirm that the products from previous shots were not interfering with the reaction, the flow rate was increased for several experiments so that the cell was refreshed every second. The results were indistinguishable from experiments in which the cell was refreshed every 3-5 s. Thus, we felt confident that the products from secondary chemistry from previous laser pulses were not interfering with the measurements. The rate of decay of the vinyl radical was measured at several alkene concentrations.

The raw data were fit to a single exponential decay, yielding a pseudo-first-order rate constant,  $k'$ . Rate constants were taken from the slope of a plot of  $k'$  versus [alkene], which yielded a linear slope. The effective rate constant,  $k_0$ , represented by the zero-alkene intercept of this plot, is attributable to all other loss processes for vinyl radical, including self-reaction, reaction with I atoms, reaction with vinyl iodide, and diffusion out of the probe beam. The measured values for  $k_0$  reported in Dr. Ismail's thesis are comparable to what would be expected from the vinyl self-reaction [36]. The uncertainty limits of  $k$

represent the statistical uncertainty resulting from the fit of the  $C_2H_3$  decay data to a single exponential. Alkene concentrations used were large enough that the error in simply including the second-order contribution from self-reaction in the intercept was small. Extracting  $k$  from the first-order component of a fit to the functional form for a combined first- and second-order decay resulted in identical values of  $k$  to within experimental uncertainty.

Vinyl iodide was purchased from Oakwood Products ( $C_2H_3I$  90.0%) and was purified by repeated freeze-pump-thaw cycles. Additional gas-phase chemicals were purchased from the following suppliers and were used without further purification:  $C_2H_4$  99.0% (2.0 grade from Airgas),  $C_3H_6$  99.0% (2.0 grade from Advanced Gas Technologies Inc.), 1-butene 99.0% (2.0 grade from Advanced Gas Technologies), 2-butene 99.0 (2.0 grade from Advanced Gas Technologies), isobutene 99.0 (2.0 grade from Advanced Gas Technologies), and He 99.999 (5.0 grade, Airgas). The 2-butene is a mix of the cis and trans isomers,  $50\% \pm 15\%$  trans.

## 1.2 Theory

The optimized geometries and zero-point corrected energies for the stationary points, transition states, and product channels on the  $C_4H_7$ ,  $C_5H_9$ , and  $C_6H_{11}$  potential energy surface (PES) were calculated using the G3 compound method [11]. The G3 method was chosen for two reasons: first, it is an efficient compounds method with accuracy less than  $\pm 2$  kcal/mol, and second, the  $C_4H_7$  potential energy surface had been recently published by Miller [74]. The HF/6-31G(d) vibrational frequencies from the G3 calculations were replaced with subsequent B3PW91/6-311++G(3df,pd) calculations to improve the accuracy of the vibrational partition function and density of state calculations. Conformers for each isomer were treated as hindered internal rotors. The potential barrier for each hindered rotor, here assumed to be any single carbon-carbon bond not included in a ring, was calculated at the B3PW91/6-31+G(d,p) level. A relaxed scan along the dihedral angle in  $10^\circ$  increments was performed, and the resulting potential barrier was fit to a Fourier series. The partition function and density of state for each rotor was treated as a 1D hindered rotor with a semiclassical Pitzer-Gwinn-like [80] approximation

$$Q = \frac{Q_{\text{quantum harmonic oscillator}}}{Q_{\text{classical harmonic oscillator}}} Q_{\text{classical hindered rotor}} \quad (1.1)$$

The effective moment of inertia used for each rotor was  $I^{(2,3)}$  evaluated at the equilibrium geometry. Tunneling was included for all transition states by use of an Eckart approximation [41]. For energy transfer in the master equation, a single-exponential down model was used with an average  $\langle \Delta E_{\text{down}} \rangle$  for He given by  $100 \text{ cm}^{-1} (T/298)^{0.8}$  [73, 72]. The collision frequency was estimated using a Lennard-Jones model. The LJ parameters for the  $\text{C}_4\text{H}_7$  intermediates were  $\sigma = 5.28 \text{ \AA}$  and  $\epsilon = 209.9 \text{ cm}^{-1}$ ; these parameter values were estimated from literature values for 1- $\text{C}_4\text{H}_8$  [3]. The LJ parameters for the  $\text{C}_5\text{H}_9$  intermediates were  $\sigma = 5.57 \text{ \AA}$  and  $\epsilon = 218.4 \text{ cm}^{-1}$ ; these parameter values were estimated from literature values for 1- $\text{C}_4\text{H}_8$ , and n- $\text{C}_5\text{H}_{12}$  [3]. The LJ parameters for the  $\text{C}_6\text{H}_{11}$  intermediates were  $\sigma = 6.25 \text{ \AA}$  and  $\epsilon = 238.4 \text{ cm}^{-1}$ ; these parameter values were estimated from literature values for n- $\text{C}_6\text{H}_{12}$  [3]. In order to test the sensitivity of the overall rate coefficients to the LJ parameters, the LH parameters for the  $\text{C}_6\text{H}_{11}$  intermediates were replaced by values for 1- $\text{C}_4\text{H}_8$ . The change in rate coefficients was typically less than 40%. The same source was used for the He bath gas LJ parameters:  $\sigma = 2.55 \text{ \AA}$  and  $\epsilon = 6.95 \text{ cm}^{-1}$ . For all  $\text{C}_4\text{H}_7$ -He,  $\text{C}_5\text{H}_9$ -He, and  $\text{C}_6\text{H}_{11}$ -He complexes,  $\sigma$  was calculated by the arithmetic mean of the values for the two species, and  $\epsilon$  was calculated by the geometric mean [3]. The same calculations were repeated at higher pressures (0.1 to 100 atm in  $\text{N}_2$ , with  $\Delta E_{\text{down}}$  for  $\text{N}_2$  given by  $400 \text{ cm}^{-1} (T/298)^{0.8}$ ,  $\sigma = 3.74 \text{ \AA}$ , and  $\epsilon = 56.99 \text{ cm}^{-1}$ ). All G3 and DFT calculations were performed using the Gaussian 03 software package [17]. Additional coupled cluster calculations were done using MOLPRO [101]. Doublet species wave functions were unrestricted for both the energy and frequency calculations. An RRKM/ME program package, VariFlex [47] was used to calculate the density of states, microcanonical rate constants, and the pressure- and temperature-dependent rate constants for Reaction [1.1] through Reaction [1.5] on the basis of the PESs shown in Figures 1-1, 1-3, 1-5, 1-7, and 1-9.

## 1.3 Results

### 1.3.1 Vinyl Plus Ethene

The details of the vinyl plus ethene results are described in detail in Dr. Ismail's thesis [35] and will only be summarized here. As mentioned in the theory section, the  $C_4H_7$  potential energy surface was computed by Miller using the G3 and G3B3 compound methods [74]. For simplicity, and to facilitate comparison with the other vinyl + alkene reactions, we settled on the G3 method for computing electronic energies. The potential energy surface is shown in Figure 1-1; the energies of the species and transition states are listed in Tables 1.1 and 1.2, respectively. The RRKM/ME results for the experimental conditions of 100 Torr of He are shown in Figure 1-2.

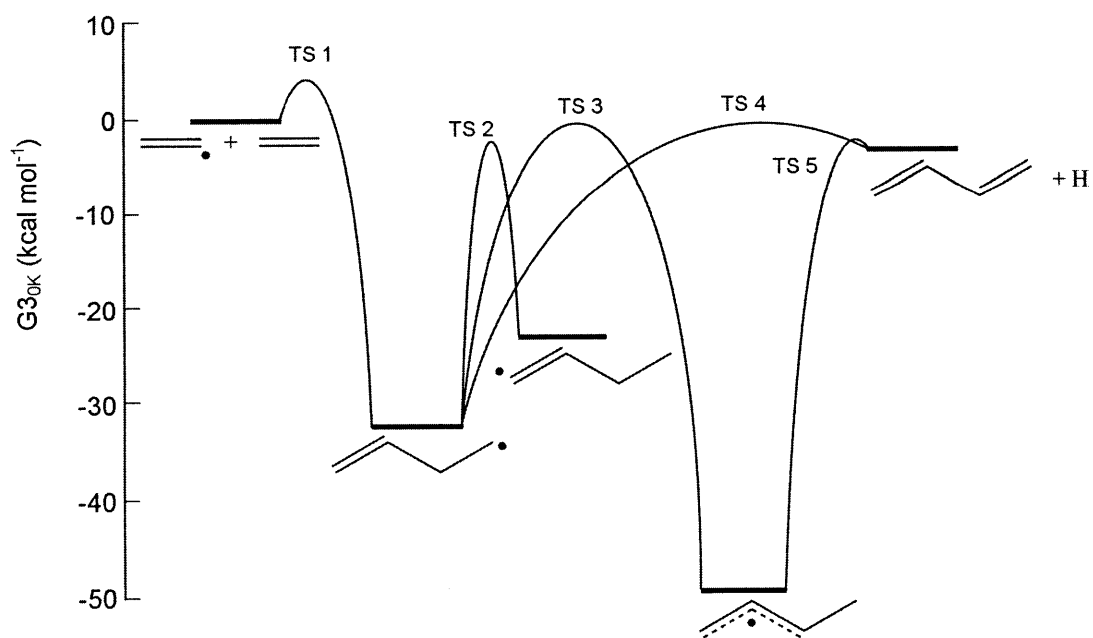
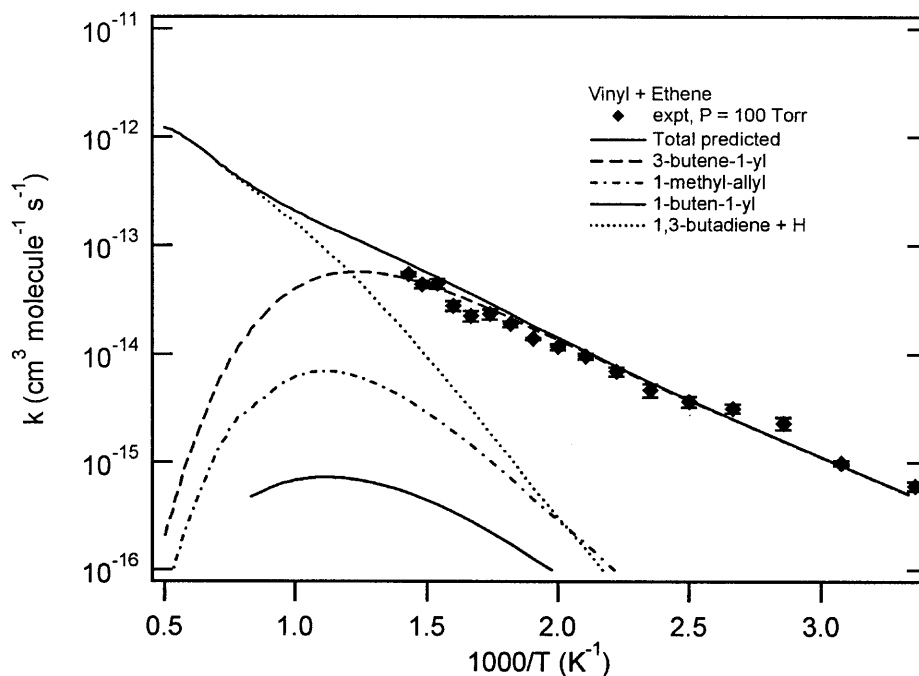


Figure 1-1 – Vinyl + ethene potential energy surface.



**Figure 1-2** – Temperature dependence of the total rate coefficient and RRKM/ME predictions for the reaction of vinyl + ethene. The symbols are the experimental data from Dr. Ismail’s thesis [35]; the solid line is the total predicted rate coefficient; the broken lines are the RRKM/Master Equation predictions for the various product channels.

**Table 1.1** – Species for vinyl + ethene potential energy surface.

Identifier	Name	Structure	Relative Energy (kcal/mol)
R1	vinyl + ethene	<chem>C=C.C=C</chem>	0
W1	3-buten-1-yl	<chem>C=CC</chem>	-32.5
W2	1-buten-1-yl	<chem>C=C.C</chem>	-23.0
W3	1-methyl-allyl	<chem>C=CC</chem>	-49.1
P1	1,3-butadiene + H	<chem>C=CC=C.H</chem>	-4.1



**Table 1.2** – Transition states for vinyl + ethene potential energy surface.

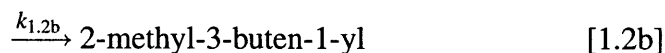
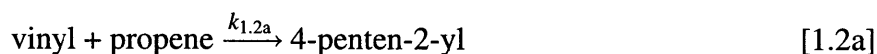
Identifier	Reaction	Relative Energy (kcal/mol)
TS 1	R1 to W1	3.7
TS 2	W1 to W2	-3.6
TS 3	W1 to W3	-1.2
TS 4	W1 to P1	0.3
TS 5	W2 to P1	-4.0

### 1.3.2 Vinyl Plus Propene

The chemistry of vinyl plus propene is richer and more complex than vinyl plus ethene and presents a better test case for vinyl plus larger alkenes. Unlike the previous case, vinyl plus propene has two possible addition channels; it also has several H-abstraction channels, the dominant channel forming allyl + ethene. The addition of vinyl to propene can lead to the formation of several dienes (predominantly 1,3-butadiene and 1,3-pentadiene), as well as resonantly-stabilized free radicals, and three, four, and five-member ring structures. As mentioned in the introduction, Dr. Ismail was the first to measure this rate constant. Prior to his thesis, the only available rate information were estimates by Tsang [99]. In Tsang's work, the rate coefficient for vinyl + propene  $\rightarrow$  allyl + ethene via direct H-abstraction,  $1.16 \times 10^{-13} \times (T/1000)^{3.5} \times \exp[-2365 / T]$  cm<sup>3</sup> molecule<sup>-1</sup> s<sup>-1</sup>, was based upon the thermochemically-derived estimate for methyl + propene [43]. Similarly, the estimated rate coefficients for vinyl + propene  $\rightarrow$  1,3-butadiene + methyl,  $1.2 \times 10^{-12} \times \exp[-2520 / T]$  cm<sup>3</sup> molecule<sup>-1</sup> s<sup>-1</sup>, and 1,3-pentadiene + H,  $1.2 \times 10^{-12} \times \exp[-3240 / T]$  cm<sup>3</sup> molecule<sup>-1</sup> s<sup>-1</sup> were based upon vinyl addition to ethene and acetylene [13]. In order to calculate the high-pressure limit rate coefficients as well as the pressure-dependent RRKM/ME rate coefficients, I computed a more comprehensive potential energy surface, taking into consideration 15 possible C<sub>5</sub>H<sub>11</sub> isomers.

## Vinyl Plus Propene: Potential Energy Surface

The system consists of five straight-chain, two branched, three three-member ring, four four-member ring, and one five-member ring species. The potential energy surfaces for these isomers are presented at the end of this chapter in the Section 1.5 in Figures 1-16 through 1-23. The structure of the isomers and product channels, and their energies relative to the reactants are listed in Table 1.3. The transition states, the wells and/or products they connect, and their energies relative to the reactants are listed in Table 1.4. For most of the transition states considered in the kinetic model, the tunneling contribution was minor. For TS 8, TS 12, and TS 19, however, the imaginary frequencies corresponding to the reaction were between 1000 and 1600  $\text{cm}^{-1}$ ; consequently, the model predicted significant tunneling for these reactions, especially at lower temperatures. In the high-pressure limit, the vinyl radical and propene can react via three distinct low-barrier transition states:

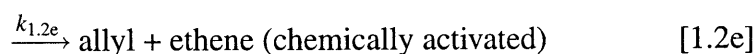
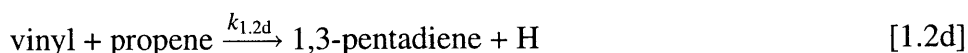


The lowest energy path for Reaction [1.2] is Reaction [1.2a], in which the vinyl radical forms a single bond with carbon 1 (i.e. the head) in propene, yielding 4-penten-2-yl, via TS 6. From 4-penten-2-yl, four H-migration and two ring-closing isomerization reactions have been identified, as well as two  $\beta$ -scission reactions. The immediate isomerization and dissociation channels available to 4-penten-2-yl are shown in Figure 1-16. The second possible reaction, [1.2b], is when the vinyl radical forms a single bond with carbon 2 (i.e. the tail) in propene, yielding 2-methyl-3-buten-1-yl, via TS 7. Because this transition state is 1.5 kcal/mol higher than TS 6, this channel is comparatively minor. Consequently, fewer isomerization reactions for 2-methyl-3-buten-1-yl were considered: one H-migration, two ring closing, and two  $\beta$ -scission reactions. The immediate isomerization and dissociation channels available to 2-methyl-3-buten-1-yl are shown in Figure 1-17. The slowest of the three elementary reactions is available to vinyl + propene is Reaction [1.2c], in which the

vinyl radical abstracts an H directly from the methyl group in propene, yielding ethene and allyl radical, via TS 8. The barrier to H-abstraction is 2.9 kcal/mol higher than the addition reaction to form 4-penten-2-yl, so it is expected to be negligible over the temperature range probed in the present experiments. However, this channel is expected to be important at high temperature. Other direct H-abstractions are possible but were not considered because the barriers were comparatively too high; the barriers for H-abstraction from carbons 1 or 2 are 6 and 4 kcal/mol higher, respectively, than abstraction from the methyl group, TS 8.

The electronic energy for the transition state between 1,1-dimethyl-allyl and 2-methyl-1,3-butadiene + H, TS 48, was 0.4 kcal/mol lower than the electronic energy for the product channel. However, because little 1,1-dimethyl-allyl is formed, TS 48 was not included in the final model. In contrast, all the transition states included in the final model were tight, so conventional transition state theory was used for all the transition states.

Based upon the results in Tables 1.3 and 1.4, a simplified potential energy surface was determined, shown in Figure 1-3. This PES contains six wells: 4-penten-2-yl, 1-penten-1-yl, 4-penten-1-yl, cyclopentyl, 2-methyl-cyclopropylmethyl, and 2-methyl-3-buten-1-yl. For Reaction [1.2], both of the addition reactions ([1.2a] and [1.2b]) and the direct H-abstraction channel [1.2c] are included. In addition, rate constants are calculated for four chemically activated channels:



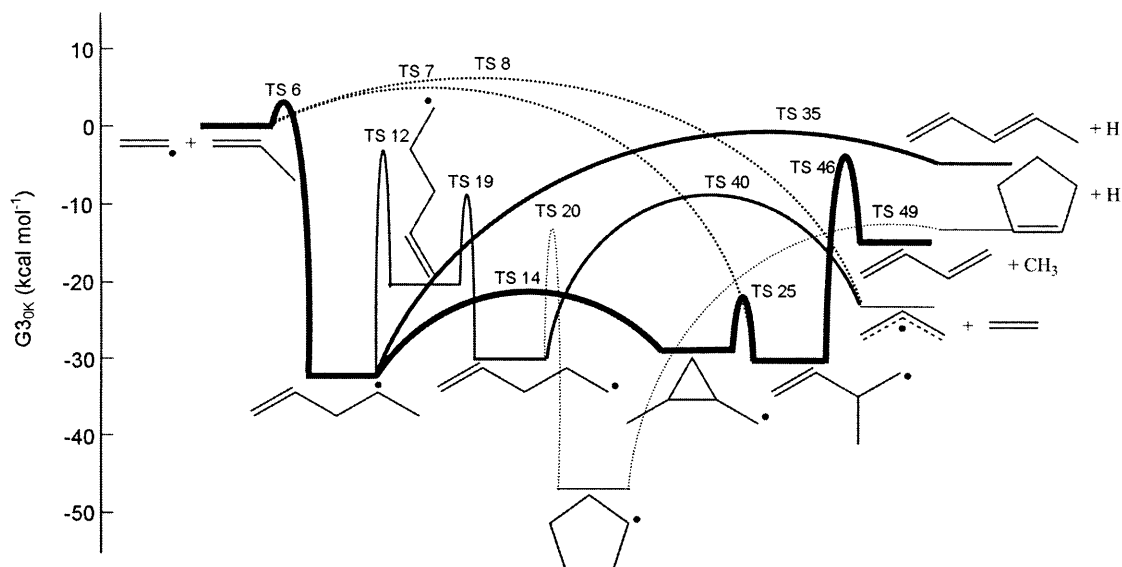


Figure 1-3 – Vinyl + propene potential energy surface.

Table 1.3 – Species for vinyl + propene potential energy surface.

Identifier	Name	Structure	Relative Energy (kcal/mol)
R2	vinyl + propene	<chem>C=C.C=C</chem>	0
W4	4-penten-2-yl	<chem>CCC=C[CH2]</chem>	-32.3
W5	1-ethyl-allyl	<chem>CC=C[CH2]</chem>	-47.1
W6	4-penten-1-yl	<chem>CCC=C[CH2]</chem>	-30.3
W7	1-penten-2-yl	<chem>CCC=C[CH2]</chem>	-23.8
W8	1-penten-1-yl	<chem>CCC=C[CH2]</chem>	-20.7
W9	2-methyl-3-buten-1-yl	<chem>CC(C)C=C[CH2]</chem>	-30.4
W10	1,1-dimethyl-allyl	<chem>CC(C)C=C[CH2]</chem>	-50.6
W11	cyclopentyl	<chem>C1CCCC1[CH2]</chem>	-47.1
W12	3-methyl-cyclobutyl	<chem>CC1CCC1[CH2]</chem>	-26.5
W13	cyclobutylmethyl	<chem>C1CCC1[CH2]</chem>	-26.8
W14	2-methyl-cyclobutyl	<chem>CC1CCC1[CH2]</chem>	-26

Table 1.3 – Continued


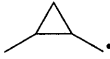

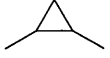
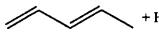
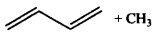
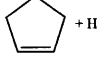
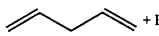
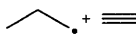
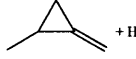
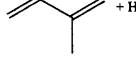
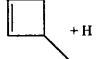
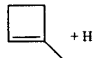
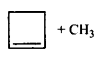
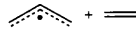
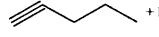
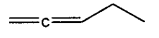
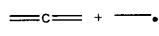
Identifier	Name	Structure	Relative Energy (kcal/mol)
W15	1-methyl-cyclobutyl		-28.4
W16	2-methyl-cyclopropylmethyl		-28.9
W17	1,2-dimethyl-cyclopropyl		-20.5
W18	2,3-dimethyl-cyclopropyl		-17.6
P2	1,3-pentadiene + H		-4.8
P3	1,3-butadiene + methyl		-15.1
P4	cyclopentene + H		-13.5
P5	1,4-pentadiene + H		2
P6	1-propyl + acetylene		3.4
P7	2-methyl-1-methylene cyclopropane + H		16.1
P8	2-methyl-1,3-butadiene + H		-5
P9	4-methyl-cyclobutene + H		9.3
P10	1-methyl-cyclobutene + H		6.2
P11	cyclobutene + methyl		-1.7
P12	allyl + ethene		-23.2
P13	1-pentyne + H		11.2
P14	1,2-pentadiene + H		10.1
P15	allene + ethyl		-1.9

Table 1.4 – Transition states for vinyl + propene potential energy surface.

Identifier	Reaction	Relative Energy (kcal/mol)	Identifier	Reaction	Relative Energy (kcal/mol)
TS 6	R2 to W4	3.1	TS 30	W13 to W15	13.7
TS 7	R2 to W9	4.6	TS 31	W14 to W15	14.5
TS 8	R2 to P12	6	TS 32	W16 to W17	20.9
TS 9	W4 to W5	0.65	TS 33	W16 to W18	19.9
TS 10	W4 to W6	8.4	TS 34	W17 to W18	24.6
TS 11	W4 to W7	18	TS 35	W4 to P2	-0.8
TS 12	W4 to W8	-3.2	TS 36	W4 to P5	3.3
TS 13	W4 to W12	1.3	TS 37	W5 to P2	-2.3
TS 14	W4 to W16	-21.3	TS 38	W5 to P3	-9
TS 15	W5 to W6	4.8	TS 39	W6 to P5	4.7
TS 16	W5 to W7	15.8	TS 40	W6 to P12	-9.4
TS 17	W5 to W8	18.1	TS 41	W7 to P13	12.5
TS 18	W6 to W7	-2.3	TS 42	W7 to P14	12.5
TS 19	W6 to W8	-8.5	TS 43	W7 to P15	6.5
TS 20	W6 to W11	-12.9	TS 44	W8 to P6	11.2
TS 21	W6 to W13	-13.4	TS 45	W8 to P13	14
TS 22	W7 to W8	23.9	TS 46	W9 to P3	-4.2
TS 23	W9 to W10	-1.6	TS 47	W9 to P8	0.3
TS 24	W9 to W14	1.6	TS 48	W10 to P8	-5.5
TS 25	W9 to W16	-22.3	TS 49	W11 to P4	-12.5
TS 26	W12 to W13	6	TS 50	W12 to P9	10.8
TS 27	W12 to W14	15.7	TS 51	W14 to P10	8.9
TS 28	W12 to W15	25.4	TS 52	W14 to P11	6.5
TS 29	W13 to W14	16.1	TS 53	W16 to P7	20

## Vinyl Plus Propene: RRKM/ME Calculations

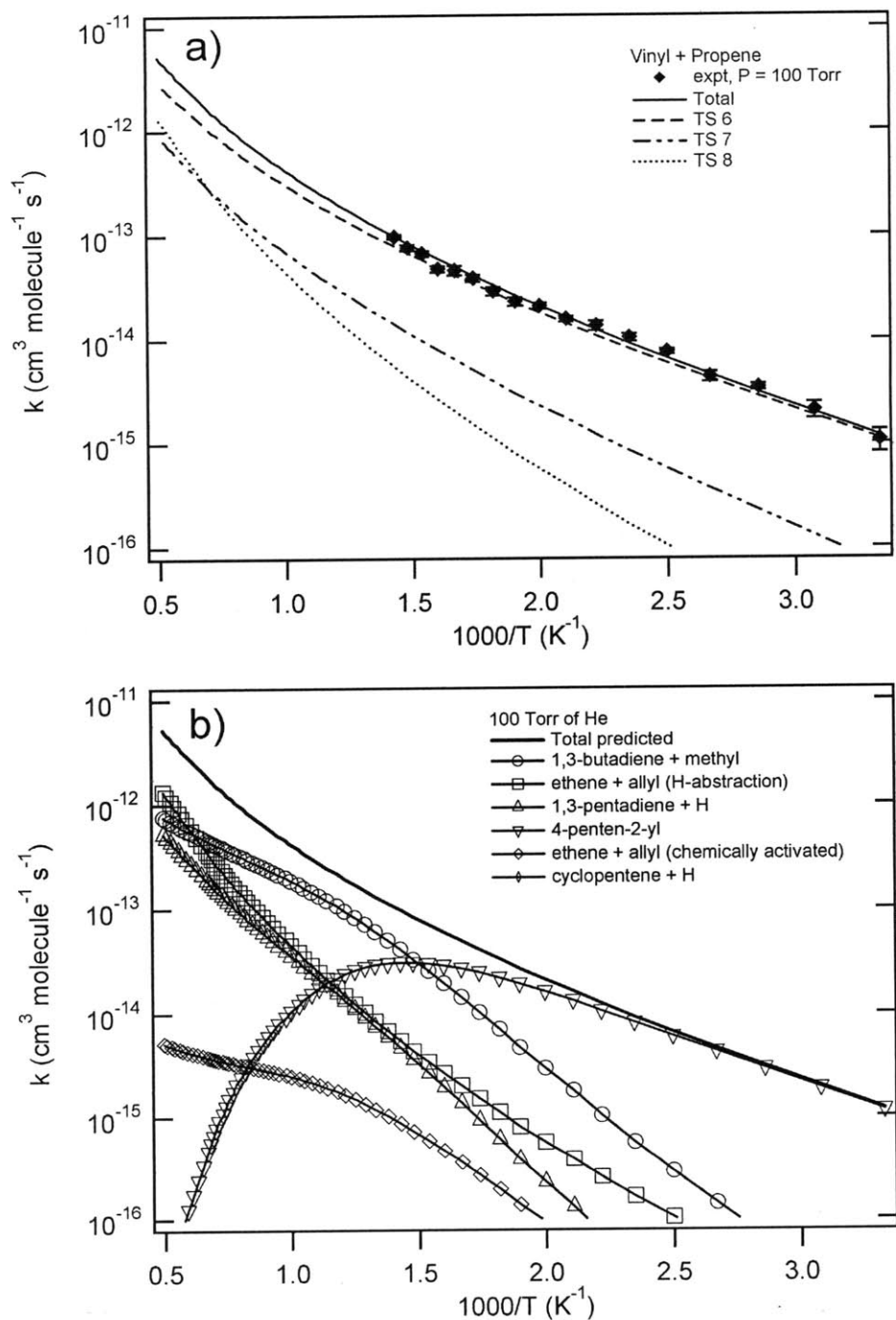
VariFlex simulations were performed at four pressures between 1 and 1000 Torr and 59 temperatures between 300 to 2000 K. At 300 and 325 K, the calculated rate is roughly 50% faster than experiment; between 350 and 700 K, however, the agreement with the experimental data is within 20%. The discrepancy at low temperature is attributed to the following effects: first, the tunneling correction and hindered-rotor approximation are less accurate at lower temperatures; second, the experimental numbers are less reliable at 300 K, because competing loss processes are relatively more important at lower temperatures. The temperature dependence of the three entrance channels at the high-pressure limit are shown in Figure 1-4a. The temperature dependence of the rate coefficients in 100 Torr of He for the primary entrance channel and the four product channels are shown in Figure 1-4b. At high pressures and low temperatures, the dominant product is the collisionally stabilized 4-penten-2-yl. Based upon an analysis of the eigenvalues, 4-penten-2-yl, 2-methyl-3-buten-1-yl, and 2-methyl-cyclopropylmethyl are equilibrated by 350 K, so the latter two species are also produced at significant rates. At 1 Torr, chemically activated product formation becomes significant at temperatures greater than 450 K. As the pressure increases, the switching temperature (defined here as the lowest temperature at which the rate of chemically-activated product formation exceeds the rate of collisional stabilization of the entrance channel) increases to 550 K at 15 Torr, 700 K at 100 Torr, and 1000 K at 1000 Torr. At all four pressures, the dominant product channel in temperatures in excess of the switching temperature is 1,3-butadiene + methyl, followed by ethene + allyl, and 1,3-pentadiene + H. Although not considered in the model, it is expected that 1,4-pentadiene + H, via TS 36, and 2-methyl-1,3-butadiene + H, via TS 47, also might be significant product channels at higher temperatures. The rate for allyl + ethene via direct H-abstraction is  $k_{1.2c} = 3.0 \times 10^{-13} \times (T/1000)^{3.5} \times \exp[-1920/T] \text{ cm}^3 \text{ molecule}^{-1} \text{ s}^{-1}$ . At 100 Torr and  $T < 650 \text{ K}$ , the rate of stabilization for 4-penten-2-yl is  $k_{1.2a} = 6.1 \times 10^{-13} \times \exp[-1860/T] \text{ cm}^3 \text{ molecule}^{-1} \text{ s}^{-1}$ . At 100 Torr and  $T > 650 \text{ K}$ , the rates of chemically activated product formation are:  $k_{1.2d} = 5.2 \times 10^{-12} \times \exp[-4960/T] \text{ cm}^3 \text{ molecule}^{-1} \text{ s}^{-1}$ ;  $k_{1.2e} = 1.4 \times 10^{-14} \times \exp[-1850/T] \text{ cm}^3 \text{ molecule}^{-1} \text{ s}^{-1}$ ;  $k_{1.2g} = 3.8 \times 10^{-12} \times \exp[-3100/T]$

$\text{cm}^3 \text{ molecule}^{-1} \text{ s}^{-1}$ ; the rate for cyclopentene + H is roughly constant above the switching temperature,  $k_{1,2f} = 2 \times 10^{-17} \text{ cm}^3 \text{ molecule}^{-1} \text{ s}^{-1}$ . As the pressure is increased, the rates of product formation decrease, since more of the initial channel is stabilized by collision. Because the barrier to direct H-abstraction is 2.9 kcal/mol higher than addition, most of the reactive flux is through the addition channels. However, because the A-factor for direct H-abstraction has a stronger temperature dependence, it will dominate the addition channels at higher temperatures. By 1600 K,  $k_{1,2c}$  becomes the dominant product channel; by 1900 K,  $k_{1,2c}$  exceeds the sum of all addition channels. The rates published by Tsang do not agree well with the rates predicted by VariFlex, largely because the rates in Tsang are not pressure dependent. Tsang's estimates for the butadiene and pentadiene channels are reasonably close to the VariFlex results at 1 Torr; at higher pressures the Tsang coefficients are orders of magnitude too large, particularly below the switching temperature. The rate for allyl formation predicted by Tsang is for the direct H-abstraction, which is considerably slower than the rate for direct H-abstraction calculated here. Additionally, as shown below, a significant amount of allyl is formed via addition-isomerization-decomposition at intermediate temperatures; consequently the Tsang rate coefficient significantly underestimates the total rate of production of allyl + ethene.

Given the potential energy surface in Figure 1-3, the trends in product formation are somewhat unexpected. That 1,3-butadiene + methyl is the dominant product is clear, since the lowest energy path is: 4-penten-2-yl  $\rightarrow$  TS 14  $\rightarrow$  2-methyl-cyclopropylmethyl  $\rightarrow$  TS 25  $\rightarrow$  2-methyl-3-buten-1-yl  $\rightarrow$  TS 46  $\rightarrow$  1,3-butadiene + methyl. However, the second lowest path is: 4-penten-2-yl  $\rightarrow$  TS 12  $\rightarrow$  1-penten-1-yl  $\rightarrow$  TS 19  $\rightarrow$  4-penten-1-yl  $\rightarrow$  TS 20  $\rightarrow$  cyclopentyl  $\rightarrow$  TS 49  $\rightarrow$  cyclopentene + H, and the highest pathway to dissociation is: 4-penten-2-yl  $\rightarrow$  TS 35  $\rightarrow$  1,3-pentadiene + H. Therefore, from the PES, one would expect the following trend:  $k_{1,2g} > k_{1,2f} > k_{1,2e} > k_{1,2d}$ . Instead the model suggests:  $k_{1,2g} > k_{1,2d} > k_{1,2e} > k_{1,2f}$ . This discrepancy is explained by entropic constraints on a few key transition states. Consider two transition states available to the primary entrance well, TS 12 and TS 35. The barrier for TS 12 is 4 kcal/mol lower than the barrier for TS 35, so at lower energies TS 12 will dominate TS 35. However, TS 12 requires the formation of a five-member ring, whereas TS 35 involves breaking a C-H bond. As a consequence,



TS 12 will have a much smaller A-factor. Thus at higher energies, which is precisely when these competing channels become significantly faster than collisional stabilization, TS 35 dominates TS 12. An analogous argument can be made for TS 20 and TS 40, which explains why 4-penten-1-yl is more likely to dissociate to allyl + ethene than to isomerize to cyclopentyl, despite the difference of 3.5 kcal/mol in barrier height.



**Figure 1-4** – (a) Temperature dependence of the total rate constant of the reaction between the vinyl radical and propene. The symbols are the experimental data from Dr. Ismail’s thesis [35]; the total high-pressure limit rate coefficient is shown as the solid line; the dashed lines show the rate coefficients through each entrance channel. (b) RRKM/Master Equation predictions for the product channels of the reaction between the vinyl radical and propene in 100 Torr of He. The symbol  $\nabla$  indicate initial adduct; all other symbols indicate chemically activated product channels.

### **Vinyl Plus Propene: Sensitivity of product formation**

As seen in Figure 1-3, transition states TS 12 and TS 46 are the highest barriers for paths  $k_{1.2f}$  (as well as  $k_{1.2e}$ ) and  $k_{1.2g}$ , respectively, and these transition states differ by less than 1 kcal/mol. To test the sensitivity of the predicted branching fractions to these two transition states, the barrier height for TS 12 was decreased by 1.0 kcal/mol, and the barrier height for TS 46 was increased by 1.0 kcal/mol. Under this modified PES, the lowest pathway is  $k_{1.2f}$ , followed by  $k_{1.2e}$ , then  $k_{1.2g}$  and  $k_{1.2d}$ . At 1 Torr, both  $k_{1.2e}$  and  $k_{1.2f}$  increased by roughly a factor of 2, and  $k_{1.2g}$  decreased by roughly a factor of 1.5. Similarly, the rate of stabilization for the wells 4-penten-2-yl, 2-methyl-3-buten-1-yl, and 2-methyl-cyclopropylmethyl all increased by roughly a factor of 1.5. By increasing the barrier for TS 46, the fraction of 2-methyl-3-buten-1-yl that can escape is reduced; consequently, the fraction of these three wells that will be stabilized by collision or will dissociate to form other products is increased. As the pressure is increased, a greater percentage of each well is stabilized by collision, so changes to these two transition states becomes less significant, and the relative change in rates diminishes. At all pressures, the general product trends remain unchanged. Thus we conclude that the overall product formation is not very sensitive to uncertainties in these transition states energies.

### **Vinyl Plus Propene: Cyclic species and resonantly-stabilized radicals**

As noted in the introduction, both cyclic species and resonantly-stabilized radicals are of particular interest, due to their significance in soot formation. Several ring-containing  $C_5H_9$  isomers and product channels are considered in the potential energy surface. Of these species, only 2-methyl-cyclopropylmethyl is formed at a significant rate. As noted previously, 2-methyl-cyclopropylmethyl rapidly equilibrates with 4-penten-2-yl. At 298 K, the change in free energy and enthalpy for this isomerization reaction are 4.3 kcal/mol and 3.09 kcal/mol, respectively, so the rate of formation for 2-methyl-cyclopropylmethyl is expected to be between two and three orders of magnitude slower than the rate of formation for 4-penten-2-yl. The rate for the other cyclic radical, cyclopentyl, could not be calculated accurately, due to numerical issues at lower temperatures; based upon the

rates near the switching temperature, however, it is expected to be less than  $3 \times 10^{-18} \text{ cm}^3 \text{ molecule}^{-1} \text{ s}^{-1}$ . All other cyclic radicals listed in Table 1.4 were not included in the master equation model because the corresponding isomerization barriers to their formation were prohibitively high.

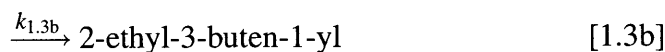
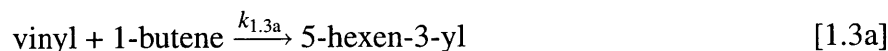
Both of the entrance channels can isomerize to form resonantly-stabilized free radicals: 4-penten-2-yl to 1-ethyl-allyl, and 2-methyl-3-buten-1-yl to 1,1-dimethyl-allyl. The lowest barrier to form 1-ethyl-allyl is TS 9, which is 1.4 kcal/mol higher than the dissociation reaction to form 1,3-pentadiene + H, TS 35. Similarly, the barrier to form 1-dimethyl-allyl, TS 23, is 2.6 kcal/mol higher than the dissociation reaction to form 1,3-butadiene + methyl, TS 46. Consequently, it is not expected that any significant quantities of five-carbon resonantly-stabilized free radicals will be formed, since at energies high enough to isomerize to resonantly stabilized radicals the competing channel for decomposition is both entropically and energetically more favorable. The only resonantly stabilized radical that is formed at an appreciable rate is the allyl radical. As noted above, there are two pathways that lead to allyl formation: (i) direct H-abstraction,  $k_{1,2c}$ , and (ii) addition-isomerization-dissociation,  $k_{1,2e}$ . For all temperatures and pressure, the H-abstraction channel dominates over the indirect path; however,  $k_{1,2e}$  is within an order of magnitude of  $k_{1,2c}$  for temperatures below 900 K. At higher pressures, collisional stabilization is more effective, and the addition-isomerization-dissociation channel becomes less significant. It should be possible to test this prediction experimentally by isotopically labeling carbon in the propene and observing how much of the ethene formed is labeled.

### 1.3.3 Vinyl Plus 1-butene

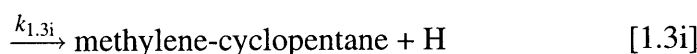
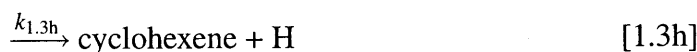
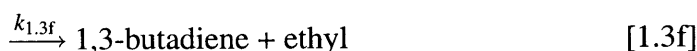
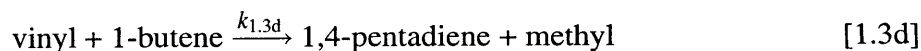
The potential surface calculated for vinyl + 1-butene is shown in Figure 1-5 and summarized in Table 1.5 and 1.6. A detailed PES for vinyl + 1-butene is provided because this reaction is the most likely to form an endo-cyclic six-member ring, cyclohexyl radical, as well as the exo-cyclic five-member ring, cyclopentylmethyl radical, both of which could be particularly important in PAH chemistry. Although it is possible for four- and other five-member rings to be formed, they were not included in the master equation calculation,

because they are not expected to be formed at significant rates.

The vinyl radical and 1-butene can react via three distinct low-barrier transition states:

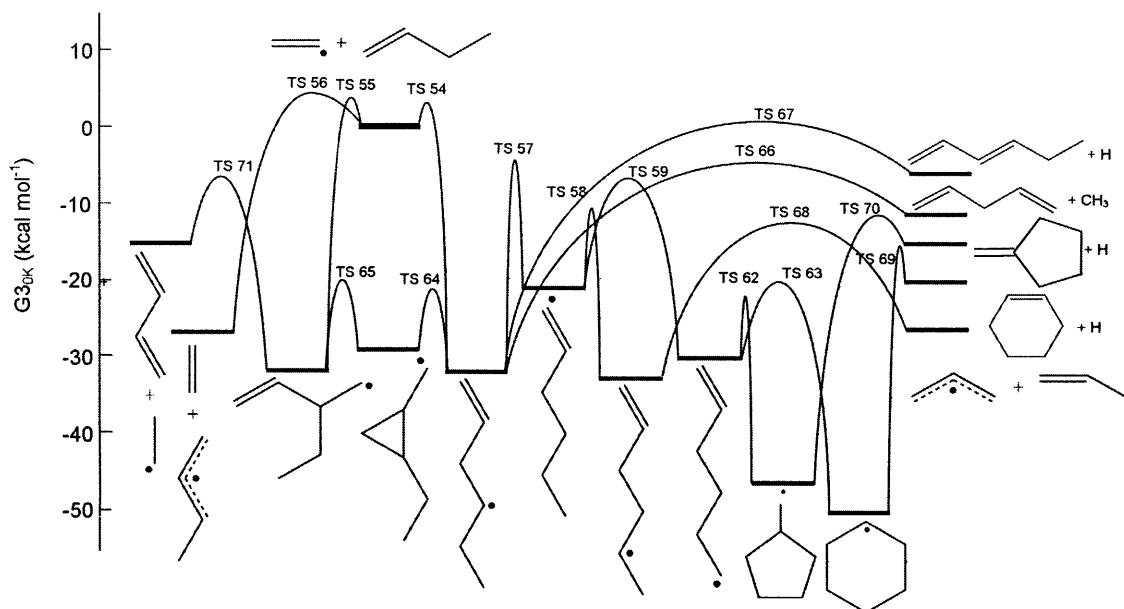


The lowest energy path for Reaction [1.3] is Reaction [1.3a], in which the vinyl radical forms a single bond with carbon 1 (i.e. the head) in 1-butene, via TS 54 (see Table 1.6 for a complete list of transition states for vinyl + 1-butene). The second possible reaction, [1.3b], is when the vinyl radical forms a single bond with carbon 2 (i.e. the tail) in 1-butene via TS 55. Reaction [1.3c] is when the vinyl radical abstracts an H directly from the Carbon 3 in 1-butene, yielding ethene and 1-methyl-allyl radical, via TS 56. Other direct H-abstractions are possible but were not considered because the barriers were comparatively too high: e.g. the barrier for H-abstraction from the methyl group in 1-butene is 5 kcal/mol higher than the barrier for TS 56. In addition to the three reactions listed above, rate coefficients are calculated for six chemically activated channels:



Channels 1.3d and 1.3e are formed from  $\beta$ -scission from 5-hexen-3-yl, and 1.3f is the result of  $\beta$ -scission from the other entrance adduct, 2-ethyl-3-buten-1-yl; Channel 1.3g is

the result of rapid isomerization between 5-hexen-3-yl  $\leftrightarrow$  1-hexen-1-yl  $\leftrightarrow$  5-hexen-2-yl followed by  $\beta$ -scission; and Channels 1.3h and 1.3i are the result of rapid isomerization between 5-hexen-3-yl  $\leftrightarrow$  1-hexen-1-yl  $\leftrightarrow$  5-hexen-1-yl  $\leftrightarrow$  cyclohexyl/cyclopentylmethyl followed by  $\beta$ -scission.



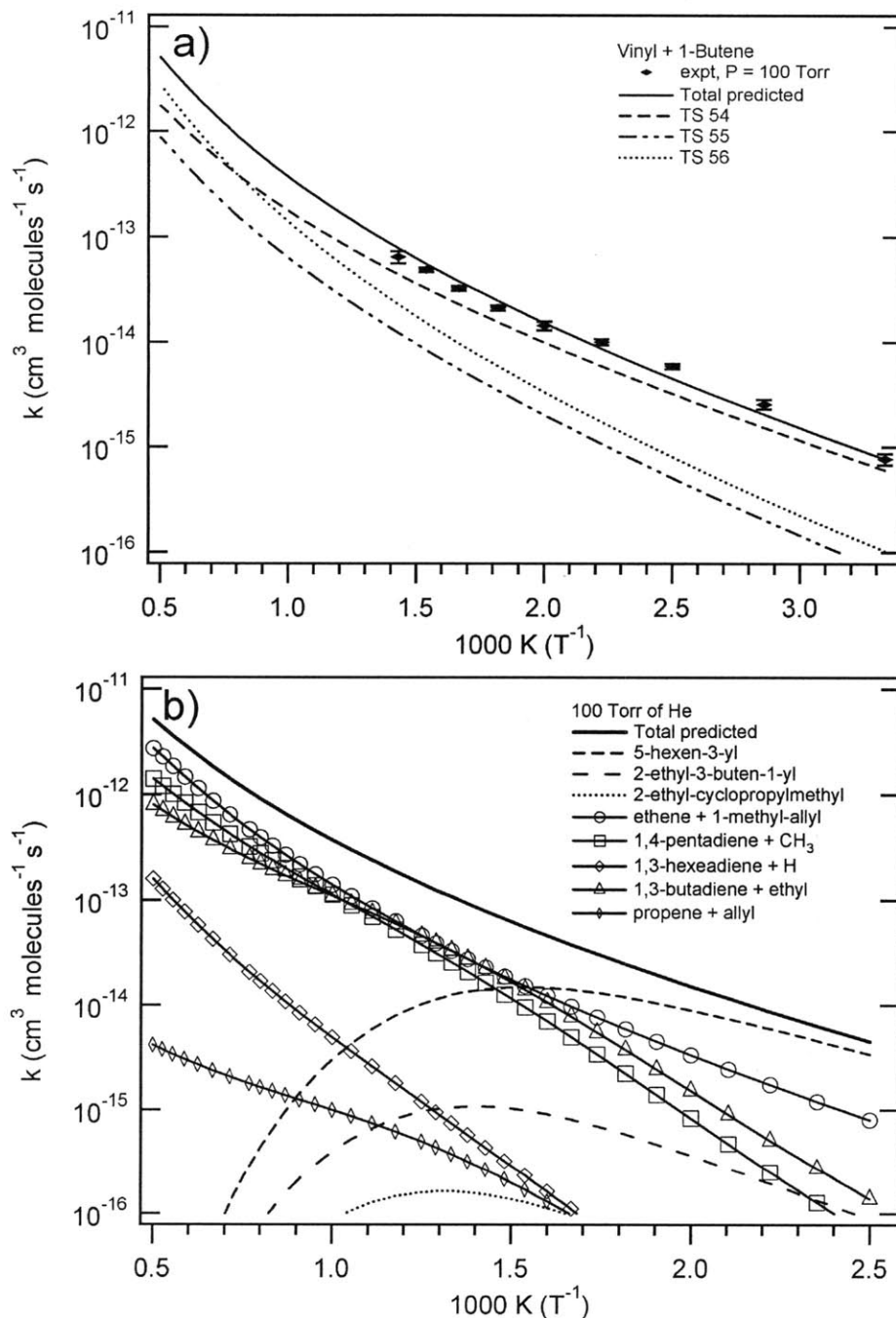
**Figure 1-5** – Vinyl + 1-butene potential energy surface.

A list of the species and their energies relative to the reactants are listed in Table 1.5; a corresponding list of the transition states and their energies are listed in Table 1.6. Because of the high barriers to isomerization, neither 1-propyl-allyl nor 1-methyl-1-ethyl-allyl was included in the master equation calculation. Similarly, the product channel 2-ethyl-1,3-butadiene + H was not included, since the barrier is higher than the reactant energy and is several kcal/mol higher than competing dissociation channels. The RRKM/ME results are shown in Figure 1-6. For temperatures below 400 K, the eigenvalue decomposition resulted in at least one positive eigenvalue. This result, not uncommon for low temperature systems [71, 72], is unphysical, so RRKM/ME results at these temperatures are not reported. By 400 K, only negative eigenvalues were computed. The isomer 2-hexen-2-yl has isomerization barriers below reactants in energy; however, including this species in the PES made no difference to the final rate coefficients. Consequently, this isomer was omitted from the master equation calculations to improve numerical accuracy. Based upon an analysis of

the eigenvalues, the two initial adducts, 5-hexen-3-yl and 2-ethyl-3-buten-1-yl, are rapidly equilibrated via 2-ethyl-cyclopropylmethyl above 350 K.

At low temperatures, the major products will be the collisionally stabilized initial adducts: 5-hexen-3-yl, 2-ethyl-3-buten-1-yl, and 2-ethyl-cyclopropylmethyl. The rate of formation for 5-hexen-2-yl, although of similar stability, is three orders of magnitude slower than 5-hexen-3-yl. The proportionally low yield of this isomer can be explained by the low barrier for  $\beta$ -scission from 5-hexen-2yl to form allyl + propene, TS 68. This barrier is almost 2 kcal/mol below the barrier for isomerization from 1-hexen-1yl, so 5-hexen-2-yl is initially populated at energy levels in excess of the dissociation barrier. At 100 Torr of He, the collision rate is insufficient to quench 5-hexen-2-yl, and thus the rate of formation for allyl + propene is greater than the rate of stabilization of 5-hexen-2-yl at all temperatures. Neither of the other two straight-chain isomers is formed at a significant rate. It is both energetically and entropically favorable for 1-hexen-1-yl to isomerize to 5-hexen-2-yl rather than 5-hexen-1-yl; the 5-hexen-2-yl intermediate will then undergo  $\beta$ -scission to form propene + allyl, whereas the less favored 5-hexen-1-yl can either undergo 6-endo or 5-exo cyclization. The barrier to form cyclopentylmethyl from 5-hexen-1-yl is roughly 1 kcal/mol lower than the corresponding barrier to form cyclohexyl, and the RRKM calculations confirm that cyclopentylmethyl is formed at a slightly faster rate. In contrast, the subsequent barrier for H-atom  $\beta$ -scission to form a cycloalkene is roughly 4 kcal/mol higher for cyclopentylmethyl than for cyclohexyl, and the RRKM calculations confirm that cyclohexene + H is formed more rapidly than methylene-cyclopentane + H. However, none of the cyclic isomers or the respective bi-molecular products is formed at a significant rate; the rate coefficients for the cyclic species were between four and five orders of magnitude slower than the fastest rate coefficient.

At 100 Torr of He, chemically-activated product formation exceeds collisional stabilization of the adducts above 600 K. At temperatures greater than 700 K, the adduct stabilization rates drop off precipitously, and the dominant product channels are 1,4-pentadiene + methyl, 1,3-butadiene + ethyl, and ethene + 1-methyl-allyl. The other allylic channel, propene + allyl, is roughly two orders of magnitude slower.



**Figure 1-6** – (a) Temperature dependence of the total rate constant of the reaction between the vinyl radical and 1-butene. The symbols are the experimental data from Dr. Ismail’s thesis [35]; the total high-pressure limit rate coefficient is shown as the solid line; the dashed lines show the rate coefficients through each entrance channel. (b) RRKM/Master Equation predictions for the product channels of the reaction between the vinyl radical and 1-butene in 100 Torr of He. The broken lines are the rate coefficients for collisional stabilization of the initial adducts; the lines with symbols are chemically activated bimolecular products; the solid line is the total rate coefficient.



[H]

Table 1.5 – Species for vinyl + 1-butene potential energy surface.

Identifier	Name	Structure	Relative Energy (kcal/mol)
R2	vinyl + 1-butene		0
W19	5-hexen-3-yl		-32.4
W20	1-hexen-1-yl		-21.1
W21	5-hexen-2-yl		-32.9
W22	1-hexen-2-yl		-24.5
W23	5-hexen-1-yl		-30.8
W24	cyclohexyl		-50.5
W25	2-ethyl-cyclopropylmethyl		-29.7
W26	2-ethyl-3-buten-1-yl		-31
W27	1-propyl-allyl		-47.7
W28	1-methyl-1-ethyl-allyl		-50.6
W29	cyclopentylmethyl		-44.5
P16	1,4-pentadiene + methyl		-11.8
P17	propene + allyl		-26
P18	cyclohexene + H		-18.3
P19	1,3-butadiene + ethyl		-15.3
P20	ethene + 1-methyl-allyl		-26.2
P21	1,3-hexadiene + H		-4.7
P22	2-ethyl-1,3-butadiene + H		-4.5
P23	methylene-cyclopentane + H		-14.9

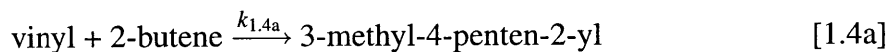
**Table 1.6** – Transition states for Vinyl + 1-butene potential energy surface.

Identifier	Reaction	Relative Energy (kcal/mol)	Identifier	Reaction	Relative Energy (kcal/mol)
TS 54	R3 to W19	2.9	TS 67	W19 to P21	-0.9
TS 55	R3 to W26	3.9	TS 68	W21 to P17	-12.6
TS 56	R3 to P20	4.1	TS 69	W24 to P18	-15.4
TS 57	W19 to W20	-3.4	TS 70	W129 to P23	-11.1
TS 58	W20 to W21	-10.9	TS 71	W26 to P19	-6.4
TS 59	W20 to W23	-5.6	TS 72	W19 to W27	0.2
TS 60	W21 to W22	-4.7	TS 73	W26 to W28	-2.2
TS 61	W22 to W23	-10.3	TS 74	W19 to W21	6.5
TS 62	W23 to W24	-20.4	TS 75	W19 to W22	16.9
TS 63	W23 to W29	-21.4	TS 76	W19 to W23	8.5
TS 64	W19 to W25	-22.1	TS 77	W20 to W22	23.5
TS 65	W25 to W26	-21.5	TS 78	W21 to W24	7.8
TS 66	W19 to P16	-4.5	TS 79	W26 to P25	1.1

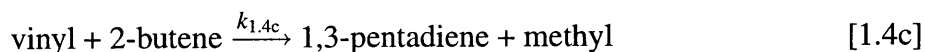
### 1.3.4 Vinyl Plus 2-butene

A detailed understanding of the potential energy surfaces for vinyl + 2-butene can be obtained by analogy from the vinyl + propene PES. Those results suggest that the initial adduct must undergo several high-barrier isomerization reactions before it can form either six-member rings or five-member rings. Additionally, the 1,2 H-transfer isomerization to form 1-methyl-1-ethyl-allyl, TS 84, has a barrier height that is above the reactant energies and is more than 6 kcal/mol higher than the competing  $\beta$ -scission reaction. Consequently, although vinyl + 2-butene can form several cyclic and six-member allylic species, none of them is formed at an appreciable rate, and thus only a simple PES is provided here, shown in Figure 1-7. Because of the symmetry of 2-butene, there is only one primary adduct;

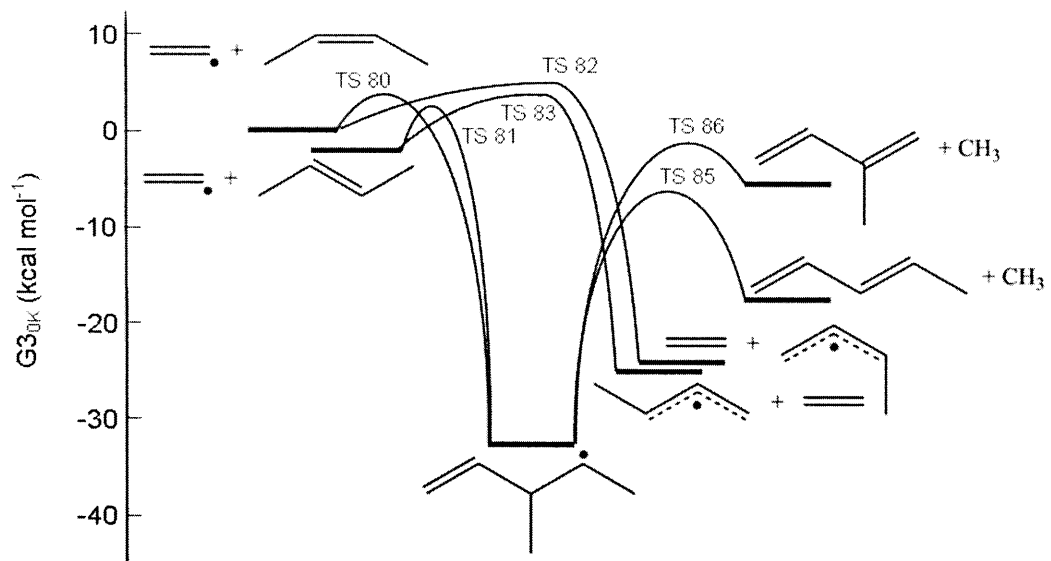
hence there is no need to calculate the isomerization via 2,3-dimethyl-cyclopropylmethyl (which would scramble isotopic labels). The vinyl radical and 2-butene can react via two distinct low-barrier transition states:



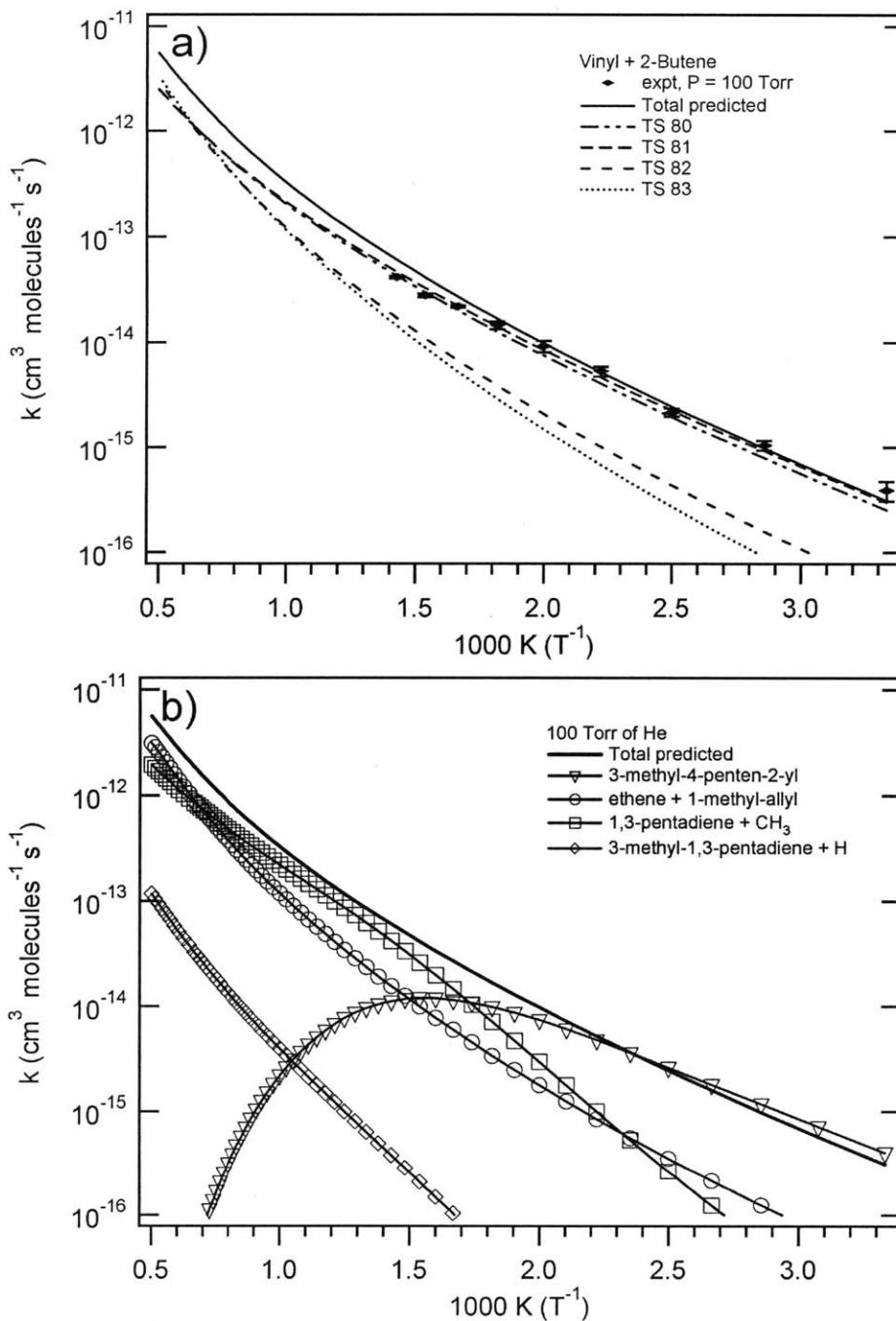
The lowest energy path for Reaction [1.4] is Reaction [1.4a], in which the vinyl radical forms a single bond with carbon 2 via TS 80 and TS 81. The next lowest energy elementary reaction is Reaction [1.4b], in which the vinyl radical abstracts an H directly from either of the CH<sub>3</sub> groups in 2-butene via TS 82 and TS 83. In addition to the two reactions listed above, rate constants are calculated for two chemically activated channels:



Both of these channels result from  $\beta$ -scission of the initial adduct. A list of the species and their energies relative to the reactants are listed in Table 1.7; a corresponding list of the transition states and their energies are listed in Table 1.8. At 100 Torr of He, chemically-activated product formation becomes significant by 600 K. From 600 K – 1500 K, the dominant product channel is 1,3-pentadiene + methyl, followed closely by ethene + 1-methyl-allyl. The other product channel, 3-methyl-1,3-pentadiene + H, is roughly two orders of magnitude slower. Although the PES in Figure 1-7 shows two distinct channels for direct H-abstraction, starting from cis- or trans-2-butene, for simplicity the channels for cis-1-methyl-allyl and trans-1-methyl-allyl are lumped together as a single channel in Figure 1-8. These isomers are expected to rapidly equilibrate in a flame environment.



**Figure 1-7 – Vinyl + 2-butene potential energy surface.**



**Figure 1-8** – (a) Temperature dependence of the total rate constant of the reaction between the vinyl radical and 2-butene. The symbols are the experimental data from Dr. Ismail’s thesis [35]; the total high-pressure limit rate coefficient is shown as the solid line; the dashed lines show the rate coefficients through each entrance channel. (b) RRKM/Master Equation predictions for the product channels of the reaction between the vinyl radical and 2-butene in 100 Torr of He. The broken lines are the rate coefficients for collisional stabilization of the initial adducts; the lines with symbols are chemically activated bimolecular products; the solid line is the total rate coefficient.

**Table 1.7** – Species for vinyl + 2-butene potential energy surface.

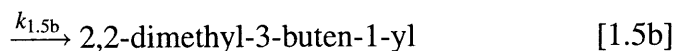
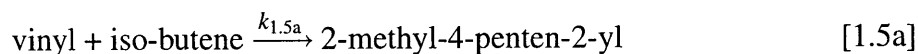
Identifier	Name	Structure	Relative Energy (kcal/mol)
R4a	vinyl + cis-2-butene		0
R4b	vinyl + trans-2-butene		-1.3
W30	3-methyl-4-penten-2-yl		-33.4
W31	1-methyl-1-ethyl-allyl		-49.2
P24	1,3-pentadiene + methyl		-17.1
P25	3-methyl-1,3-pentadiene + H		-5.3
P26a	ethene + cis-1-methyl-allyl		-24.2
P26b	ethene + trans-1-methyl-allyl		-24.8
P27	3-methyl-1,4-pentadiene + H		1.8

**Table 1.8** – Transition states for vinyl + 2-butene potential energy surface.

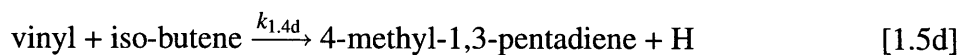
Identifier	Reaction	Relative Energy (kcal/mol)
TS 80	R4a to W30	3.9
TS 81	R4b to W30	2.4
TS 82	R4a to P26a	5.2
TS 83	R4b to P26b	4.4
TS 84	W30 to W31	0.2
TS 85	W30 to P24	-6.3
TS 86	W30 to P25	-0.9
TS 87	W30 to P27	3.2

### 1.3.5 Vinyl Plus iso-butene

A detailed understanding of the potential energy surfaces for vinyl + iso-butene can be obtained by analogy from the vinyl + propene PES. Those results suggest that the initial adduct must undergo several high-barrier isomerization reactions before it can form either six-member rings or five-member rings. Additionally, the 1,2 H-transfer isomerization to form isopropyl-allyl, TS 93, has a barrier height that is above both the reactant energies and the competing  $\beta$ -scission reaction. Consequently, although vinyl + iso-butene can form several cyclic and six-member allylic species, none of them is formed at an appreciable rate, and thus only a simple PES is provided here, shown in Figure 1-9. The vinyl radical and iso-butene can react via three distinct low-barrier transition states:

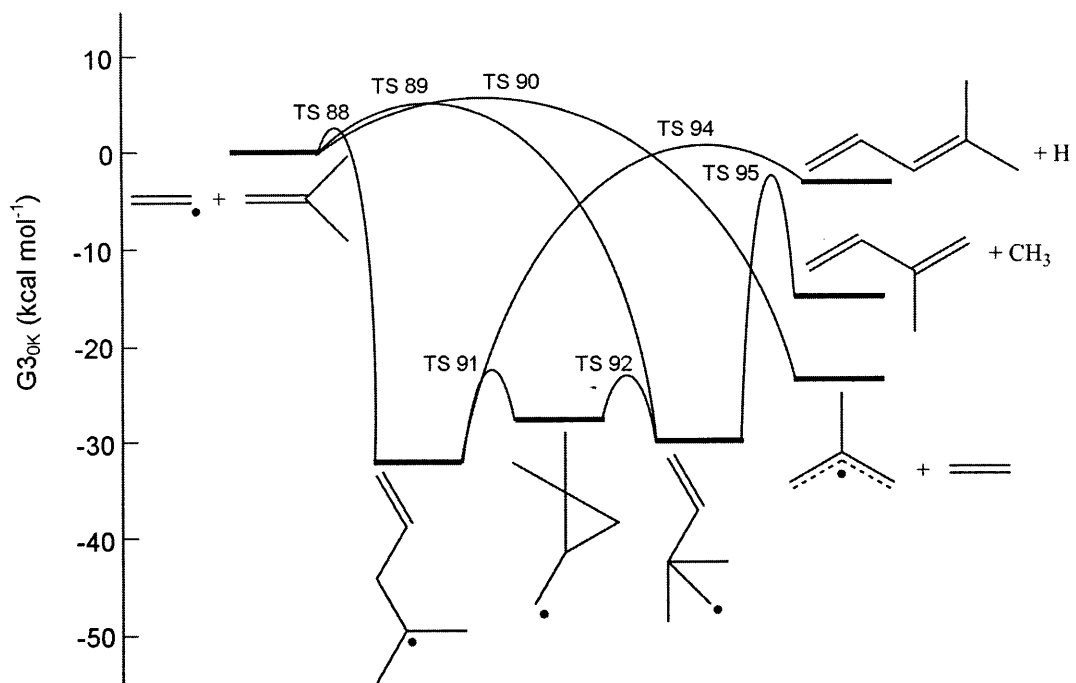


The lowest energy path for Reaction [1.5] is Reaction [1.5a], in which the vinyl radical forms a single bond with carbon 1 (i.e. the head) in iso-butene via TS 88. The second lowest energy path is when the vinyl radical forms a single bond with carbon 2 (i.e. the tail) in iso-butene via TS 89. Reaction [1.5c] is when the vinyl radical abstracts an H directly from either of the methyl groups in iso-butene via TS 90. Although the barrier to this reaction is 0.5 kcal/mol higher than Reaction [1.5b], it is roughly an order of magnitude faster, as seen in Figure 1-10. In addition to the three reactions listed above, rate constants are calculated for two chemically activated channels:

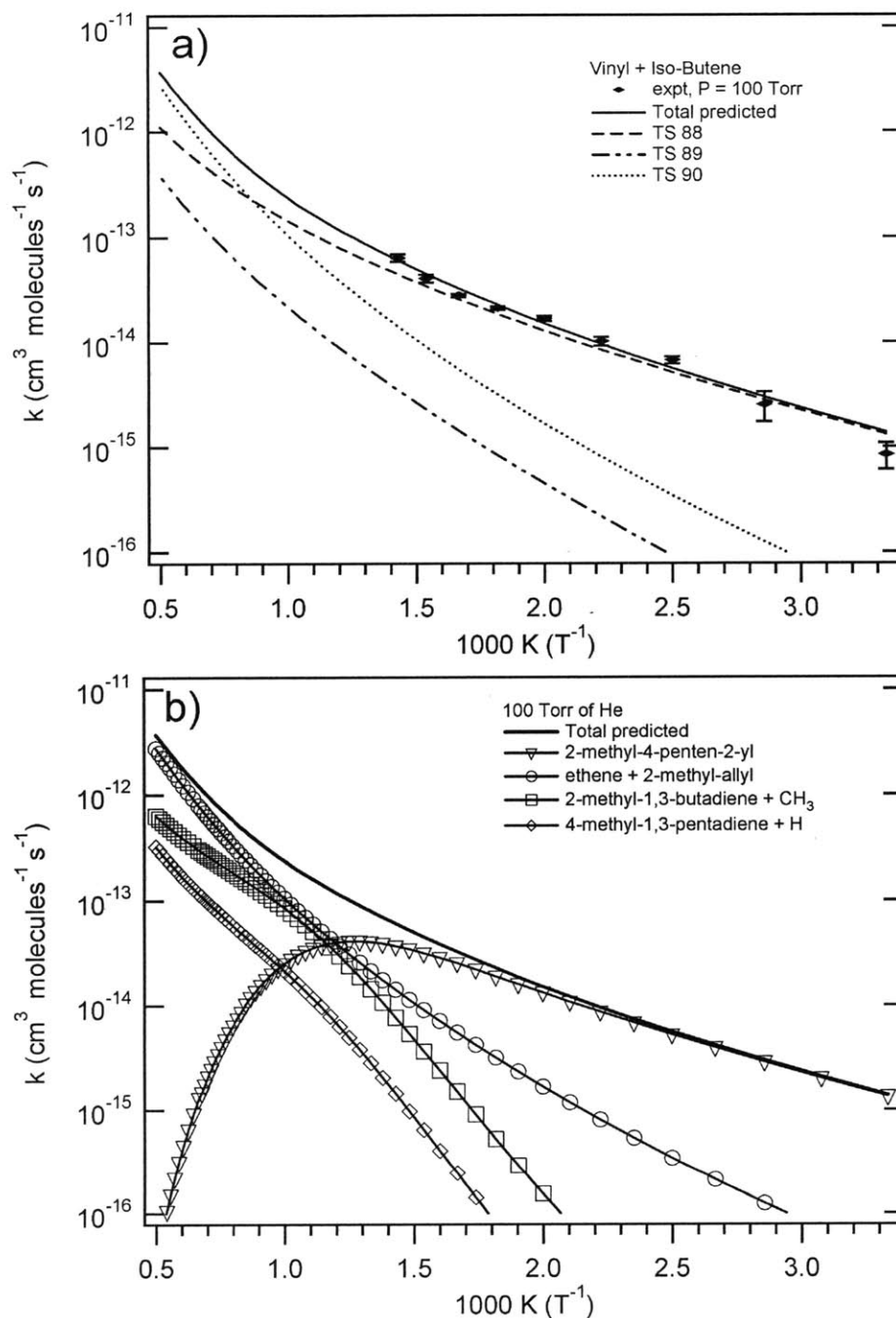


Channel 1.5d is the result of  $\beta$ -scission of the initial adduct, 2-methyl-4-penten-2-yl; channel 1.5e results from rapid isomerization between the initial adducts 2-methyl-4-penten-2-yl  $\leftrightarrow$  2,2-dimethyl-cyclopropylmethyl  $\leftrightarrow$  2,2-dimethyl-3-buten-1-yl, followed by  $\beta$ -scission. A list of the species and their energies relative to the reactants are listed in Table 1.9; a corresponding list of the transition states and their energies are listed in Table 1.10. Of the five vinyl + alkenes reactions studied so far, Reaction [1.5] is the only reaction in which the initial adduct is a tertiary radical. The increased stability of the initial adduct, and the lack of any low-energy C-C bond  $\beta$ -scission routes, implies that it is more difficult for chemically activated product formation to occur; at 100 Torr in He, chemical activation does not dominate over collisional stabilization until temperatures in excess of 850 K. Additionally, unlike vinyl + propene, 1-butene, and 2-butene, for temperatures above 700 K the dominant product channel for vinyl + iso-butene is predicted to be the direct H-abstraction, yielding ethene + 2-methyl-allyl. Between 300 and 700 K, the H-abstraction channel is computed to increase from 5% to 25% of the total rate of disappearance of vinyl.





**Figure 1-9** – Vinyl + iso-butene potential energy surface.



**Figure 1-10** – (a) Temperature dependence of the total rate constant of the reaction between the vinyl radical and iso-butene. The symbols are the experimental data from Dr. Ismail's thesis [35]; the total high-pressure limit rate coefficient is shown as the solid line; the dashed lines show the rate coefficients through each entrance channel. (b) RRKM/Master Equation predictions for the product channels of the reaction between the vinyl radical and iso-butene in 100 Torr of He. The broken lines are the rate coefficients for collisional stabilization of the initial adducts; the lines with symbols are chemically activated bimolecular products; the solid line is the total rate coefficient.

**Table 1.9** – Species for vinyl + iso-butene potential energy surface.

Identifier	Name	Structure	Relative Energy (kcal/mol)
R5	vinyl + iso-butene		0
W32	2-methyl-4-penten-2-yl		-32
W33	2,2-dimethyl-cyclopropylmethyl		-28.2
W34	2,2-dimethyl-3-buten-1-yl		-29.9
W35	isopropyl-allyl		-45.2
P28	4-methyl-1,3-pentadiene + H		-3.5
P29	2-methyl-1,3-butadiene + methyl		-14.8
P30	ethene + 2-methyl-allyl		-21.9

**Table 1.10** – Transition states for vinyl + iso-butene potential energy surface.

Identifier	Reaction	Relative Energy (kcal/mol)
TS 88	R5 to W32	2.4
TS 89	R5 to W34	4.9
TS 90	R5 to P30	5.4
TS 91	W32 to W33	-22
TS 92	W33 to W34	-22.4
TS 93	W32 to W35	1.1
TS 94	W32 to P28	0.3
TS 95	W34 to P29	-2.3

## 1.4 Discussion

To facilitate comparison, the Arrhenius parameters for all five vinyl + alkene systems are summarized in Table 1.11.

Between 300 and 700 K at 100 Torr of He, the fastest rate is vinyl + propene, followed by iso-butene, 1-butene, ethene, and 2-butene. Although the experimental rates are quite similar, with less than a factor of five separating the slowest from the fastest, the ordering of the rates cannot be explained solely by molecular weight or reaction enthalpy. Three competing effects determine the relative ranking of the rates: reaction path degeneracy, rotational effects, and variations in the barrier height due to sterics and charge donation.

Reaction path degeneracy: Statistical factors, such as the external symmetry of the molecule and the number of energetically equivalent transition states, will impact the relative ranking. The external symmetry numbers for the reactants are: vinyl, 1; ethene, 4; propene and 1-butene, 1; 2-butene and iso-butene, 2. The external symmetry number for all the transition states is 1; however, the reactions for propene, 1-butene, and 2-butene each have two energetically equivalent chiral transition states. Thus, the reaction path degen-

**Table 1.11** – Modified-Arrhenius parameters for experimental data and theoretical Addition rates<sup>a</sup>.

	$E_0$	$A \left( \frac{T}{1000[\text{K}]} \right)^n = \frac{k_B T}{h} \frac{Q_{TS}}{Q_{AB}}$		experiment, $n = 1.7$		TST, $n = 1.7$	
		A	n	A	$E_a$	A	$E_a$
ethene	3.7	$1.2 \times 10^{-12}$	1.2	$8.5 \times 10^{-13}$	3.1	$1.1 \times 10^{-12}$	3.3
propene	3.1	$1.3 \times 10^{-12}$	1.7	$1.3 \times 10^{-12}$	2.9	$1.4 \times 10^{-12}$	3.1
1-butene	2.9	$6.9 \times 10^{-13}$	1.9	$8.6 \times 10^{-13}$	2.8	$7.9 \times 10^{-13}$	3.2
cis-2-butene	3.9	$1.3 \times 10^{-12}$	1.8			$1.4 \times 10^{-12}$	4.1
trans-2-butene	3.7	$1.3 \times 10^{-12}$	1.9			$1.4 \times 10^{-12}$	3.9
2-butene, 50/50				$9.2 \times 10^{-13}$	3.5		
iso-butene	2.4	$4.2 \times 10^{-13}$	1.6	$7.8 \times 10^{-13}$	2.8	$5.5 \times 10^{-13}$	2.6
propene, minor	4.3	$5.3 \times 10^{-13}$	1.6			$5.7 \times 10^{-13}$	4.3
1-butene, minor	3.9	$3.9 \times 10^{-13}$	1.9			$4.9 \times 10^{-13}$	4.3
iso-butene, minor	4.8	$2.2 \times 10^{-13}$	1.8			$2.7 \times 10^{-13}$	5.2
2-methyl-1-butene	2.1	$4.0 \times 10^{-13}$	1.6			$4.1 \times 10^{-13}$	2.1

<sup>a</sup>  $E_0$  is the G3 barrier height at 0 K in units of kilocalories per mole,  $n$  is the fitted temperature dependence of the A factor of the major addition channel, A has units of cubic centimeters per molecule per second, and  $E_a$  has units of kilocalories per mole. 2-Butene 50/50 corresponds to a 50% by volume blend of cis-2-butene and trans-2-butene, corresponding to the experimental gases. Minor refers to the addition to the substituted carbon. TST corresponds to the calculated rate constants using transition-state theory.

eracies for the reactions are: ethene and 2-butene, 4; propene, 1-butene, and iso-butene, 2. Consequently, other things being equal, one would expect the reaction of vinyl with ethene or 2-butene to be twice as fast as the other alkenes. The importance of reaction path degeneracy is shown in Table 1.12.

Rotational effects: The moments of inertia for ethene and propene are significantly smaller than those of the butenes, as shown in Table Table 1.12. Consequently, due to rotational partition functions only, one would expect the reaction of vinyl + ethene to be the fastest, followed by propene, with the butenes roughly equivalent.

Barrier height: The initial adduct for vinyl + ethene is a primary radical; for propene, 1-butene, and 2-butene, the initial adduct of the major channel is a secondary radical; for iso-butene, it is a tertiary radical. Since the reaction barrier should be lower for more stable adducts, from this argument one would expect vinyl + iso-butene to be the fastest and vinyl + ethene to be the slowest. Since the addition of vinyl to an unsubstituted CH<sub>2</sub> end group is less hindered than addition to a substituted carbon, one would expect propene and 1-butene

to be faster than 2-butene. Additionally, one would expect 1-butene to react slightly faster than propene due to increased hyperconjugation.

**Table 1.12** – Reaction path degeneracy and rotational effects<sup>a</sup>.

Species	$\frac{m^\dagger}{m} \frac{\sigma}{\sigma^\dagger}$	$\left[ \frac{\Theta_A \Theta_B \Theta_C}{\Theta_A^\dagger \Theta_B^\dagger \Theta_C^\dagger} \right]^{1/2}$
Ethene	4	22.3
Propene	2	8.4
1-butene	2	3.5
Cis-2-butene, trans-2-butene	4	4.6, 5.5
iso-butene	2	4.4

<sup>a</sup>  $m$  is the number of energetically equivalent chiral states,  $\sigma$  is the external rotational symmetry number,  $\Theta_A$  is the largest rotational constant of the alkene, and the superscript  $\dagger$  denotes the transition state.

In order to quantify the importance of these competing effects, quantum calculations were performed to calculate the reaction enthalpies and transition-state theory rate coefficients for all addition and abstraction rates. The reaction enthalpies and barrier heights are provided in Table 1.13. For each addition reaction, the geometry of the transition state indicates an early transition state, which is consistent with the low-barrier and high-exothermicity of these reactions. The geometry of the alkene is virtually unchanged: the  $\pi$ -bond is well preserved, with the C=C bond length in the transition state increasing by less than 0.02 Angstroms. The frontier molecular orbitals for the reactants are presented in Table 1.14. These calculations were performed at the RHF/aug-cc-pvtz level using MOLPRO. The vinyl radical has a low-energy singly occupied molecular orbital (SOMO). This orbital is much closer in energy to the highest occupied molecular orbital (HOMO) of the alkene than to the lowest unoccupied molecular orbital (LUMO). Consequently, the SOMO-HOMO interaction is favored, and the vinyl radical acts as a strong electrophile.

**Table 1.13** – Barrier heights and reaction enthalpies for vinyl + alkenes (present work)<sup>a</sup>

	vinyl addition to			vinyl addition to		
	unsubstituted $\alpha$ -carbon			substituted center		
	$E_0$	$\Delta H_0$	$\Delta H_{298}$	$E_0$	$\Delta H_0$	$\Delta H_{298}$
Ethene	3.7	-32.5	-33.4			
Propene	3.1	-32.3	-33	4.4	-30.4	-31.2
1-butene	2.9	-32.1	-33.3	3.9	-31	-31.7
c-2-butene				3.9	-32.5	-33.3
t-2-butene				3.7	-31.2	-32
iso-butene	2.4	-31.9	-33.2	4.9	-29.9	-30.7
2-methyl-1-butene	2.1	-32.8	-33.4			

<sup>a</sup>  $E_0$  is the difference between the zero-point corrected electronic energies of the transition state and reactants,  $\Delta H_0$  is the difference between the zero-point corrected electronic energies of the reactants and products, and  $\Delta H_{298K}$  is the reaction enthalpy at 298 K. All units are in kilocalories per mole.

**Table 1.14** – Molecular orbitals and polar effects for reactants<sup>a</sup>

Species	HOMO	SOMO	LUMO	Ionization potential	Electron affinity
Vinyl	-0.5824	-0.425	0.0317	8.67	0.64
Ethene	-0.3794		0.0924	13.96	-0.72
Propene	-0.361		0.0315	9.77	-0.65
1-butene	-0.3604		0.0316	9.66	-0.64
c-2-butene	-0.3441		0.0311	9.17	-0.87
t-2-butene	-0.3443		0.032	9.17	-0.82
iso-butene	-0.3484		0.0304	9.28	-0.58
2-methyl-1-butene	-0.3478		0.0306	9.17	-0.8

<sup>a</sup> Molecular orbital energies (in hartree/particle) were taken from RHF/aug-cc-pvtz//RHF/aug-cc-pvdz calculations. The ionization potentials and electron affinities, both in electronvolts, were calculated at the CCSD(T)aug-cc-pvtz//RHF/aug-cc-pvdz level theory.

In order to put these reactions in a broader framework, it is useful to compare these

results with other results for the addition of a carbon-centered radical to unsaturated hydrocarbons. In 2001 Fischer and Radom published an experimental and computational review of addition reactions involving carbon-centered radicals and alkenes [15]. This work compared the rate constants for the addition of methyl and ten other radicals to monosubstituted and 1,1,-disubstituted alkenes. Radom and coworkers have updated the calculations for methyl addition to alkenes and compared the results with calculations for methyl addition to carbonyl and thiocarbonyl species [29]. Most recently, Sabbe et al. have published a computational study of carbon-centered radical addition to alkenes and the reverse  $\beta$ -scission reactions [87]. Sabbe et al. focused primarily on methyl addition to various alkenes, but also included the addition of seventeen other radicals to ethene for comparative purposes. (Note that Tables 1-3 in Sabbe incorrectly label the units for the Arrhenius A-factor as m<sup>3</sup>/mol-s; the correct units are m<sup>3</sup>/kmol-s [61]). Sabbe et al. predicts the rate constant for vinyl + ethene to be  $k_{1,1} = 4.8 \times 10^{-13} \times \exp[-1620/T] \text{ cm}^3 \text{ molecule}^{-1} \text{ s}^{-1}$ . The experimentally measured rate constant by Dr. Ismail in his doctoral thesis is  $k_{1,1} = (1.2 \pm 0.2) \times 10^{-12} \times \exp[-(2310 \pm 70)/T] \text{ cm}^3 \text{ molecule}^{-1} \text{ s}^{-1}$ . The rate constant in Sabbe et al. is roughly a factor of three higher than the experimental data at room temperature but agrees well with the 700 K data. The difference in activation energies is presumably due in part to the fact that Sabbe's rate coefficient was determined by fitting transition state theory rate constants between 198 and 398 K; since the pre-exponential A-factor has a pronounced temperature dependence, the activation energy for a two-parameter Arrhenius expression will depend strongly on the temperature region over which it was fit. To facilitate comparison between methyl and vinyl addition to the first five alkenes, the barrier heights and reaction enthalpies for methyl addition to the alkenes from Henry[29] and Sabbe[87] are reproduced in Table 1.15. In the following discussion, the  $\alpha$ -carbon refers to the bonding carbon, and the  $\beta$ -carbon is the adjacent carbon that shares the double bond in the reactant alkene. Comparing the results in Table 1.13 and Table 1.15, it is clear that for radical addition to an unsubstituted  $\alpha$ -carbon, the barrier height decreases with each substitution to the  $\beta$ -carbon. This result is expected, since each substitution to the  $\beta$ -carbon provides more charge donation to the double bond, which facilitates the electrophilic addition reaction. Additionally, each substitution on the  $\beta$ -carbon increases the stability of the product radi-



cal (from a primary to a secondary to a tertiary radical), since the radical site is localized on that  $\beta$ -carbon.

**Table 1.15** – Barrier heights and reaction enthalpies for methyl + alkenes (from literature).

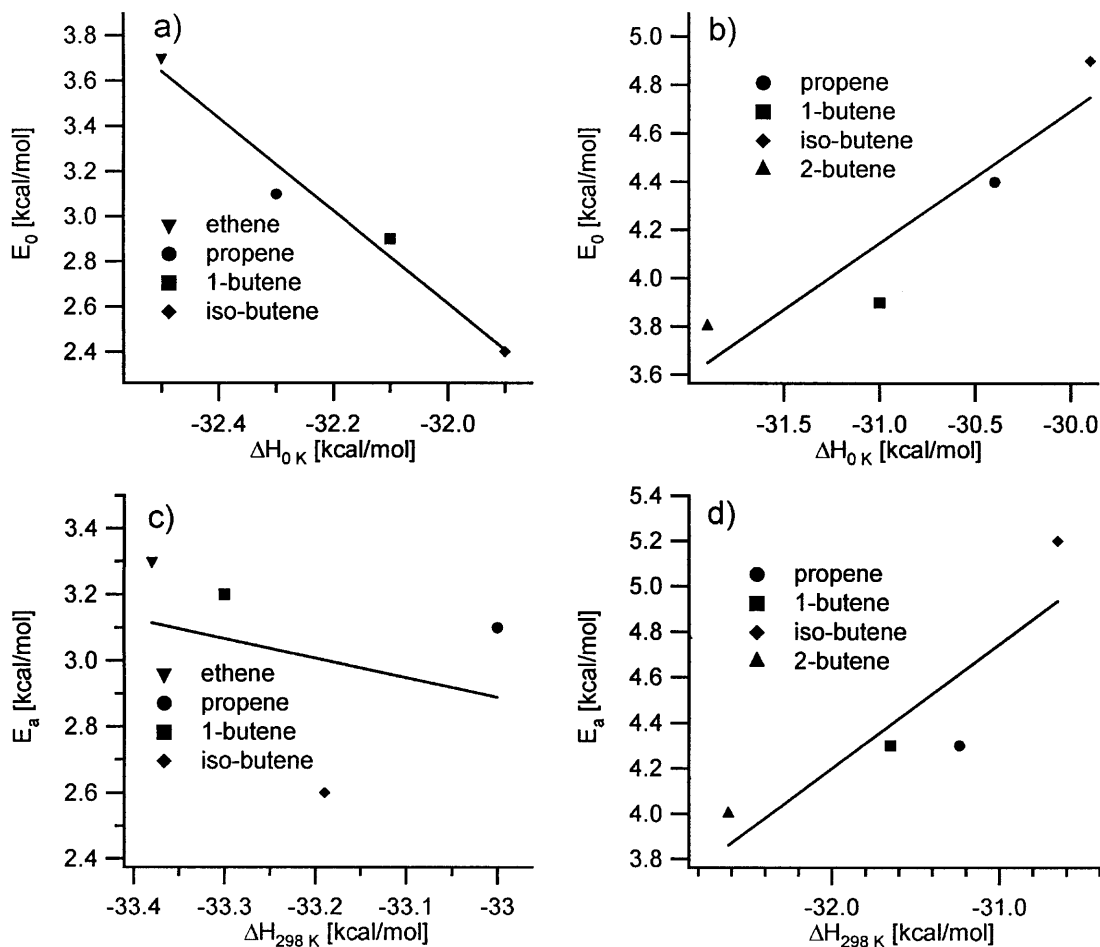
	methyl addition to unsubstituted carbon <sup>a</sup>		methyl addition to substituted carbon		methyl addition to unsubstituted carbon <sup>b</sup>		methyl addition to substituted carbon	
	$E_0$	$\Delta H_0$	$E_0$	$\Delta H_0$	$E_a$	$\Delta H_{298}$	$E_a$	$\Delta H_{298}$
Ethene	9.2	-21			7.3	-23.2		
Propene	8.8	-21.1	10.1	-20.1	7.0	-23.4	8.5	-22.2
1-butene					7.0	-23.0	8.1	-22.1
iso-butene	8.2	-20.5	11.2	-19	6.6	22.9	9.6	-21

<sup>a</sup> QCISD/6-31G(d)//G3X-RAD calculated 0 K barriers ( $E_0$ ) and reaction enthalpies ( $\Delta H_0$ ) in kilocalories per mole from Henry.<sup>24</sup>

<sup>b</sup> Fitted activation energies ( $E_a$ ) and calculated reaction enthalpies ( $\Delta H_{298K}$ ) from CBS-QB3 calculations from Sabbe25 in kilocalories per mole.

Further analysis of the reaction enthalpies in Table 1.13 and Table 1.15 shows an unexpected trend: as the reaction becomes more exothermic, the barrier increases. Figures 1-11a plots the calculated barrier height versus the reaction enthalpy at 0 K, and 1-11c plots the calculated activation energy versus the reaction enthalpy at 298 K for vinyl addition to an unsubstituted  $\alpha$ -carbon. In contrast to the data, one would expect a positive slope for these Evans-Polanyi plots, typically on the order of 0.25 to 0.5. The experimental activation energies also exhibit a negative Evans-Polanyi slope, suggesting that this behavior is not limited to computational results.

The decrease in exothermicity with substitution at the  $\beta$ -carbon is explained as follows: Each substitution to the  $\beta$ -carbon in the reactant alkene stabilizes the transition state the most, the reactant the second most, and the product the least. The difference in stabilization can be explained by considering the molecular orbitals. The CH<sub>3</sub> (or CH<sub>2</sub>) orbitals of the substituent mix with the  $\pi$ -orbitals of the double bond in the alkene, thereby stabilizing the reactant. However, in the addition reaction, the  $\pi$ -bond in the reactant is converted to a  $\sigma$ -bond in the product, so the stabilizing effect due to mixing with the orbitals on substituent group is greatly reduced. The stabilizing effect due to mixing with the  $\pi$ -bonding orbital is greater than the stabilizing effect caused by the increased charge donation when going



**Figure 1-11** – Evans-Polanyi plot for vinyl + alkenes. (a) Data are the calculated barrier heights for addition to the unsubstituted end of the alkene, and the solid line is the least-squares straight-line fit, given by  $E_0 = -62.99 - 2.05\Delta H_{0K}$ . (b) Data are the calculated barrier heights for addition to the substituted end of the alkene, and the solid line is the least-squares straight-line fit, given by  $E_0 = 21.56 + 0.56\Delta H_{0K}$ . (c) Data are the calculated activation energies for addition to the unsubstituted end of the alkene, and the solid line is the least-squares straight-line fit, given by  $E_a = -16.71 - 0.59\Delta H_{298K}$ . (d) Data are the calculated activation energies for addition to the substituted end of the alkene, and the solid line is the least-squares straight-line fit, given by  $E_a = 21.67 + 0.54\Delta H_{298K}$ .

from a primary to a secondary to a tertiary alkyl radical. Thus, although the adduct radical is indeed stabilized by the transformation from a primary to secondary to tertiary radical, the reactant is stabilized even more, and thus the overall reaction exothermicity decreases. This effect can be seen more clearly by contrasting the reaction enthalpies for vinyl addition to an unsubstituted carbon with addition to a substituted carbon in Table 1.13. The most exothermic reaction is vinyl + ethene; the least exothermic reaction is vinyl addition to the substituted end of iso-butene. Substitution at the  $\alpha$ -carbon stabilizes the alkene, but it does not significantly change the product radical stability. The results suggest that the stabilization associated with  $\pi$ -orbital mixing with each substituent on either carbon is roughly 1.3 kcal/mol, whereas the product radical is stabilized by nearest-neighbor substituents by roughly 1.0 kcal/mol. Indeed, this trend is largely predicted by basic Benson group additive thermochemistry: group additivity predicts that the exothermicity should decrease with substitution, and that addition to an unsubstituted carbon is more exothermic than addition to a substituted carbon. Because the transition state is early, the the alkene moiety preserves the  $\pi$ -orbital mixing that stabilizes the reactants. Additionally, each substitution increases the available charge donation, as in the product. Thus the transition state is stabilized by both effects and is therefore most stabilized.

In contrast to addition to unsubstituted carbons, addition to substituted carbons does not exhibit a negative Evans-Polanyi slope, as shown in Figures 1-11b and 1-11d. Here the dominant effect is steric hindrance in the transition state. As mentioned at the beginning of the discussion, the addition of vinyl radicals to alkenes are characterized by an early transition state. For addition to an unsubstituted carbon, the angle of attack for the radical center relative to the double bond is close to the value in the product:  $108.5^\circ$  in the transition state vs.  $113.2^\circ$  in the product. For addition to a substituted carbon, in contrast, the angle of attack is decreased by five degrees:  $103.3^\circ$  for propene and 1-butene and  $98.6^\circ$  for iso-butene. The addition of each carbon atom to the bonding site creates a steric hindrance that constrains the angle of attack, thereby increasing the barrier by roughly 0.5 kcal/mol for each substitution. Thus, increased substitution to the  $\alpha$ -carbon stabilizes the reactant alkene, destabilizes the transition state due to sterics, and has little effect on the product stability, so substitution increases the activation energy and the reaction enthalpy – hence,

a positive slope.

### 1.4.1 Rate Rules for Vinyl + Alkenes: Arrhenius Parametrization

A modified-Arrhenius fit for both the experimental values and the transition state calculations are shown in Table 1.11. For addition to the unsubstituted carbon in iso-butene, the transition-state rate constant is slightly higher than the measured rate constant for temperatures below 350 K. This discrepancy could be due to a small under-prediction in the calculated barrier height, or it could be due to the hindered rotor and tunneling corrections, both of which are more sensitive to low temperature behavior. To correct for this discrepancy, the computed value for the activation energy was increased by 0.2 kcal/mol, and the A-factor adjusted accordingly. With this minor correction, the addition to the  $\alpha$ -carbon of iso-butene correctly matches the experimental values. At those low temperatures, the two competing channels will be negligible.

To determine the temperature exponent for the rate expression, the exponential pre-factor for the transition-state theory rate constant was fit to an equation of the form:

$$A \left( \frac{T}{1000 \text{ [K]}} \right)^n = \kappa(T) \frac{k_B T}{h} \frac{Q_{TS}}{Q_{AB}} \quad (1.2)$$

The resulting values for the pre-exponential factor, A, and the temperature exponent, n, are shown in columns 3 and 4, respectively, of Table 1.11. Between 300 and 700 K, the dominant rate for each vinyl + alkene system is the major addition channel, and the average value of n for these channels is 1.7; thus, to simplify comparison, an average value of n = 1.7 was used for the Arrhenius fits in Table 1.11.

### Rate Rules for Vinyl + Alkenes: Addition

Two approaches for generating rate rules are commonly employed for carbon-centered radical addition to unsaturated hydrocarbons. One approach is to the curve-crossing model or state correlation diagram, which is the method used by Fischer and Radom[15] and by Henry et al.[29]. The other approach is group additivity, which is used by Sabbe et al.[87].

Each method will be applied to the reaction of vinyl radical with alkenes below.

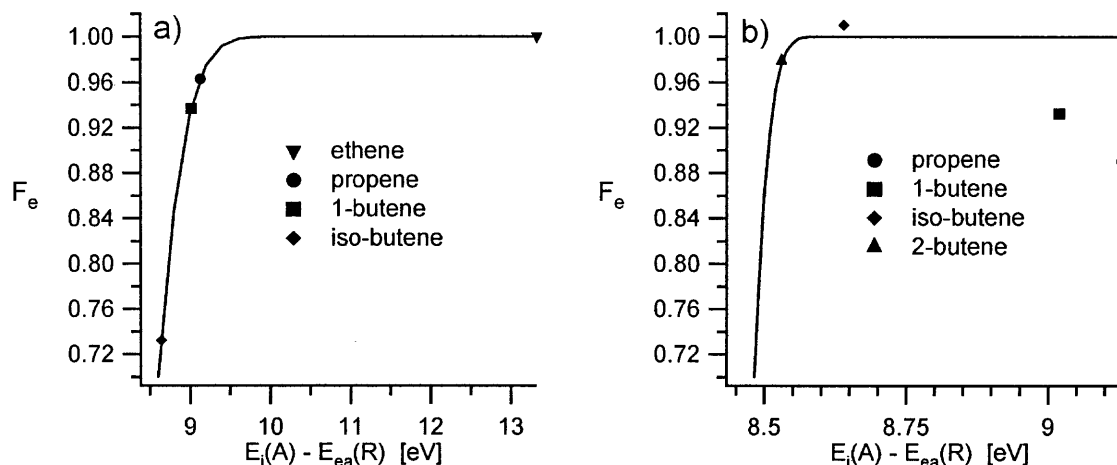
In the curve-crossing model, it is assumed that the activation energy can be fit to an Evans-Polanyi expression, multiplied by a polar correction factor

$$E_a = (E_a^0 + \alpha \Delta H_{298 \text{ K}}) F_n F_e \quad (1.3)$$

where the terms  $F_n$  and  $F_e$  are nucleophilic and electrophilic correction factors, respectively. The expression for the electrophilic correction factor is given by

$$F_e = 1 - \exp \left[ - \left( [E_{ip}(A) - E_{ea}(R) - C_e] / \gamma_e \right)^2 \right] \quad (1.4)$$

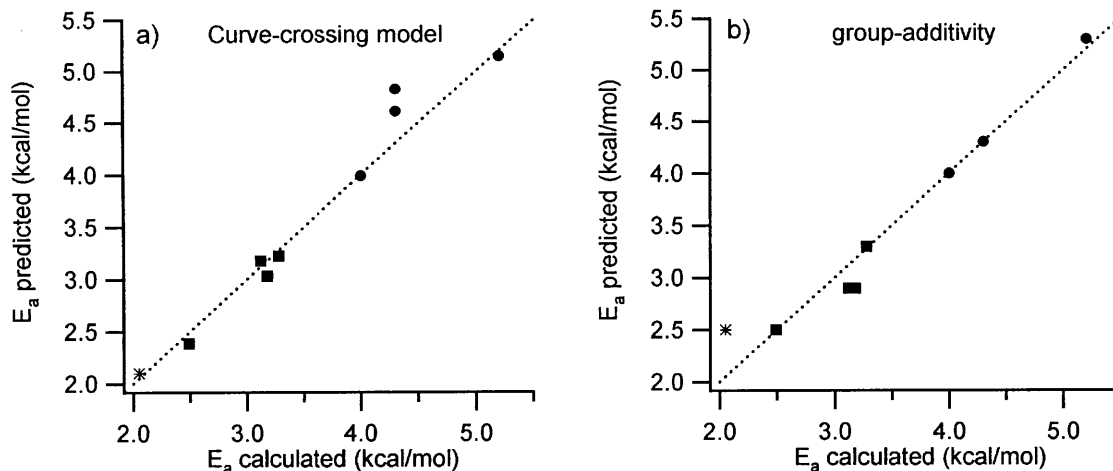
where  $E_{ip}$  is the ionization energy,  $E_{ea}$  is the electron affinity,  $R$  is the radical,  $A$  is the alkene,  $C_e$  is the Coulomb attraction, and  $\gamma_e$  is the strength of the interaction. Details of the ionization energy and electron affinity calculations are described below. The parameters  $E_a^0$ ,  $\alpha$ ,  $C_e$ , and  $\gamma_e$  are usually adjusted to fit the data. For reactions that exhibit strong electrophilic polar effects, the nucleophilic correction factor is assumed to be unity[15]. According to this model, strong electrophilic polar effects are sufficient to cause a negative slope in an Evans-Polanyi plot. To utilize this method properly, one must calculate the electronic energies for the ionic species. The final step of the G3 method in Gaussian03 failed to converge for some of the ionic species, so these results could not be compared to the G3 energies for the neutral species. Instead, coupled cluster calculations were used to determine the necessary ionization energies and electron potentials. The neutral species, the cation, and the anion geometries were calculated at the RCCSD(T)/aug-cc-pvtz//RHF/aug-cc-pvdz level theory. These calculations were performed in MOLPRO, and the results, summarized in Table 1.14, are in excellent agreement with experimental values[56]. The curve-crossing method is typically used for larger data sets which generally exhibit an Evans-Polanyi relation with a positive slope, which as noted above does not describe the current set of reactions. To use this approach, we fixed a slope of  $\alpha = 0.2$ , which is a comparatively small value, typical for early transition states with low barriers (for comparison,



**Figure 1-12** – Electrophilic polar correction for vinyl addition to alkenes. (a) Addition to the unsubstituted carbon. Data are the activation energies from Table 1.11 divided by the Evans-Polanyi relation:  $E_a = 9.9 + 0.2\Delta H_{298\text{ K}}$ . The solid line is the fit from Equation (1.4) with  $C_e = 7.8$  eV and  $\gamma_e = 0.73$  eV. (b) Addition to the substituted carbon. Data are the activation energies from Table 1.11 divided by the Evans-Polanyi relation:  $E_a = 21.7 + 0.5\Delta H_{298\text{ K}}$ . The solid line is the fit from Equation (1.4) with  $C_e = 8.4$  eV and  $\gamma_e = 0.06$  eV.

$\alpha = 0.244$  for methyl addition to alkenes, which has a higher activation energy[15]).

Figure 1-12a is a plot of the electrophilic correction factor,  $F_e$ , versus the electrophilic polar effect,  $E_{ip}(A) - E_{ea}(R)$ . The symbols are the result of dividing the  $E_a$ s in Table 1.11 by  $(E_a^0 + 0.2 * \Delta H_{298\text{ K}})$ , where  $E_a^0$  as adjusted to provide a good fit, and the solid line is the result of fitting  $C_e$  and  $\gamma_e$  in Equation (1.4) to the data. As seen in the figure, the fit is remarkably good, even noting the model is adjusting three parameters ( $E_a^0$ ,  $C_e$ , and  $\gamma_e$ ) to fit four data. The fitted values of  $E_a^0$ ,  $C_e$ , and  $\gamma_e$  are 9.9 kcal/mol, 7.8 eV, and 0.73 eV, respectively. As a result of the excellent fit, the activation energies estimated by using Equation (1.4) agree with the calculated activation energies in Table 1.11 to within 0.01 kcal/mol. Despite the strong agreement, there are three disadvantages to this approach. First, the selection of  $\alpha = 0.2$ , although reasonable, is somewhat arbitrary. Second, we may be overfitting the data, so there is no guarantee that Equation (1.4) would work equally well for vinyl addition to unsubstituted carbons in larger alkenes. Third, this method does not work well for addition to substituted carbons. Since the polar correction factor does not account for steric hindrances, a separate Evans-Polanyi relation is required for addition to the substituted end. These results are shown in Figure 1-12b, which uses the Evans-



**Figure 1-13** – Rate rule activation energies. (a) Activation energies predicted by the curve-crossing method. (b) Activation energies predicted by the group additivity method. In both plots, the  $x$  axis is the activation energy from Table 1.11. The squares are the addition to the unsubstituted carbon, the circles are the addition to the substituted carbon, and the star is the value for vinyl + 2-methyl-1-butene. The curve-crossing method predicts the activation energy for the test reaction, vinyl + 2-methyl-1-butene, with greater accuracy (agreement within 0.1 kcal/mol)

Polanyi parameters from Figure 1-11b. The fitted values for  $C_e$ , and  $\gamma_e$  are 8.4 eV, and 0.06 eV, respectively. Unlike addition to an unsubstituted carbon, the electrophilic correction factor for addition to a substituted carbon is not monotonically increasing with  $E_{ip}(A) - E_{ea}(R)$ , which suggests that there is little to be gained by using this method for addition to substituted alkenes. The curve-crossing model predictions for the activation energies are shown in Figure 1-13a. It should be noted that the curve-crossing method does not predict A-factors. Consequently, a general A-factor (equivalent to that for vinyl + isobutene) is suggested:  $A = 5.5 \times 10^{-13} \times (T/1000)^{1.7} \text{ cm}^3 \text{ molecule}^{-1} \text{ s}^{-1}$ . The A-factors derived below from the group-additivity approach should not be used in conjunction with the activation energies derived from the curve-crossing method, as these A-factors were optimized with the group-additivity  $E_a$ s, and resulting rate constant would be too high.

The group additivity approach is more flexible. In this method, one begins with a rate equation for a reference reaction – here assumed to be vinyl + ethene – and suggests changes to the A-factor and activation energy based upon substitutions to the reference reactants. For each substitution, the A-factor will decrease due to rotational effects, and

substitutions that cause steric effects will decrease the A-factor further. Substitutions to the  $\beta$ -carbon will decrease the activation energy due to increased charge donation, and substitutions made to the  $\alpha$ -carbon will increase the barrier due to steric repulsion.

For the addition of the vinyl radical to a double-bonded carbon in a generic alkene:

1. Start with  $A = 1.2 \times 10^{-12} \times (T/1000)^{1.7} \text{ cm}^3 \text{ molecule}^{-1} \text{ s}^{-1}$  and  $E_a = 3.3 \text{ [kcal/mol]}$ .
2. For each substituted group on the  $\beta$ -carbon, decrease A by  $0.5 \times 10^{-12} \times (T/1000)^{1.7} \text{ cm}^3 \text{ molecule}^{-1} \text{ s}^{-1}$  and increase  $E_a$  by 1.0 kcal/mol.
3. For each substituted group added to the  $\alpha$ -carbon, decrease A by  $0.3 \times 10^{-12} \times (T/1000)^{1.7} \text{ cm}^3 \text{ molecule}^{-1} \text{ s}^{-1}$  and decrease  $E_a$  by 0.4 kcal/mol.

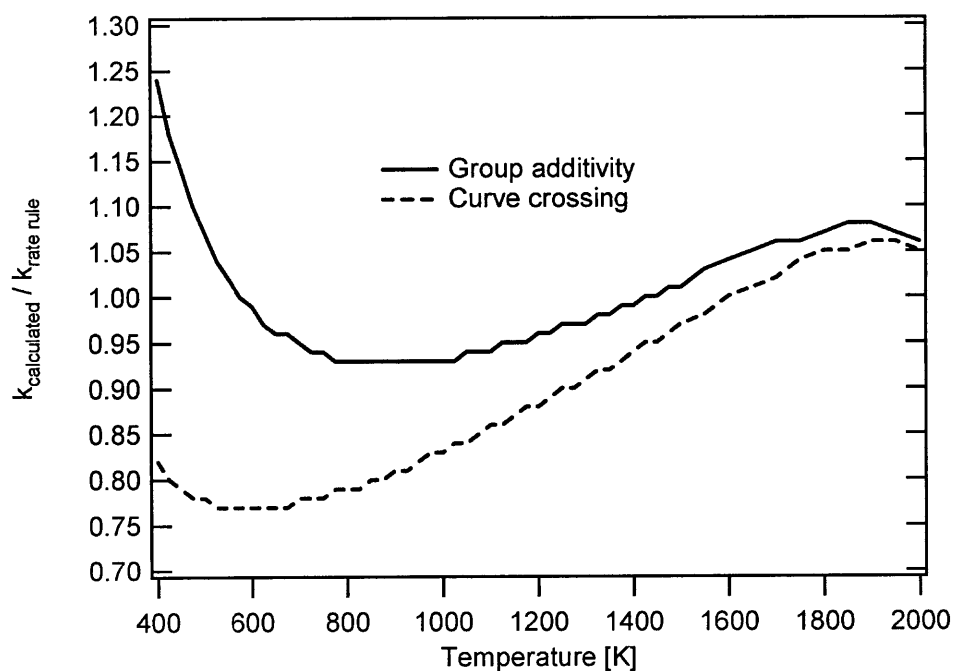
This rate estimation method is compared to the experimental results in Figure 11-15, with details at the end of the next section. The group-additivity predictions for the activation energies are shown in Figure 1-13b.

To compare the curve-crossing method and the group-additivity approach, the rate constant for vinyl + 2-methyl-1-butene was calculated using the same methods described in the Theory section. The modified-Arrhenius parameters are provided in Table 1.11. As seen in Figures 1-13a and 1-13b, the curve-crossing model does a slightly better job of predicting the activation energy, which suggests that it has a firmer theoretical foundation for addition reactions of highly electrophilic radicals. However, the group-additivity approach is still remarkably accurate. Furthermore, the group-additivity approach is considerably simpler, since it requires neither Evans-Polanyi parameters nor ionization potential and electron affinity calculations. The ratio of the calculated rate constant to the predicted rate constant for each method is shown in Figure 1-14. This figure illustrates that the calculated rate constant and the group-additivity predicted rate constant agree to within 25% over the entire range of 400 to 2000 K, which suggests there is no need for the more detailed calculations required by the curve-crossing method.

### Rate Rules for Vinyl + Alkenes: H Abstraction

As mentioned previously, the vinyl radical can abstract an H-atom from the alkene. For ethene, the result is a symmetric reaction, so it is not considered here. For the other four





**Figure 1-14** – Rate rules versus calculated rate coefficient for vinyl + 2-methyl-1-butene. For both methods, the calculated rate coefficient is divided by the rate coefficient predicted by the rate rule. The solid line is the rate coefficient predicted by the group additivity method, and the dashed line is the rate coefficient predicted by the curve-crossing method. The curve-crossing method used the A-factor of  $A = 5.5 \times 10^{-13} \times (T/1000)^{1.7}$  [cm<sup>3</sup> molecule<sup>-1</sup> s<sup>-1</sup>], which is equivalent to the A-factor of vinyl addition to the unsubstituted end of iso-butene.

alkenes studied, the lowest barrier to abstraction is when the alkene becomes a resonantly stabilized (allylic) radical: propene to allyl, 1-butene and 2-butene to 1-methyl-allyl, and iso-butene to 2-methyl-allyl. Although it is possible for vinyl to abstract other H-atoms, the barriers are significantly higher: for vinyl + propene, the barriers to abstract an H-atom from C1 or C2 are roughly 6 and 4 kcal/mol higher, respectively, and for vinyl + 1-butene, the barrier to abstract an H-atom from the methyl group is 5 kcal/mol higher. The Arrhenius parameters for these calculations are shown in Table 1.16. Comparing the rates for addition and H-abstraction, it is clear that the addition rates have lower barriers, and that the abstraction rate A-factors have higher temperature-dependencies. Thus, at higher temperatures, the abstraction rates will dominate the addition rate, consistent with entropic intuition.

**Table 1.16** – Modified-Arrhenius parameters for H-abstraction rate coefficients<sup>a</sup>.

	$E_0$	$A \left( \frac{T}{1000[\text{K}]} \right)^n = \frac{k_B T}{h} \frac{Q_{TS}}{Q_{AB}}$		TST rate, $n = 2.8$		normalized rate, $n = 2.8$	
		A	n	A	$E_a$	A	$E_a$
propene	6	$9.0 \times 10^{-13}$	2.7	$8.3 \times 10^{-13}$	5.8	$2.8 \times 10^{-13}$	5.8
1-butene	4.1	$1.1 \times 10^{-12}$	2.8	$1.1 \times 10^{-12}$	4.1	$5.6 \times 10^{-13}$	4.1
cis-2-butene	5.1	$1.6 \times 10^{-12}$	2.8	$1.5 \times 10^{-12}$	5	$2.5 \times 10^{-13}$	5
trans-2-butene	5.6	$2.1 \times 10^{-12}$	2.8	$1.9 \times 10^{-12}$	5.5	$3.2 \times 10^{-13}$	5.5
iso-butene	5.4	$1.6 \times 10^{-12}$	2.7	$1.5 \times 10^{-12}$	5.2	$2.5 \times 10^{-13}$	5.2

<sup>a</sup>  $E_0$  is the G3 barrier height at 0 K in units of kilocalories per mole. The columns under TST rate are the Arrhenius parameters for the calculated abstraction rate. A has units of cubic centimeters per molecule per second,  $E_a$  has units of kilocalories per mole. The normalized rates are the TST rates divided by the number of H atoms, which, upon abstraction, yield identical products.

To generate a rate rule for H-abstraction, it is customary to divide by the number of H-atoms that, when abstracted, will yield identical products. For 1-butene, the H-atom comes from the CH<sub>2</sub> group on carbon C3; for the other three alkenes, the H-atoms belong to methyl groups. Thus, propene is normalized by three, 1-butene by two, and 2-butene and isobutene by six. When normalized in this regard, the rates for abstraction from a methyl group are remarkably consistent, as shown in the last two columns of Table 1.16. The abstraction rate from propene has a slightly higher A-factor, consistent with the high rotational constant for propene, and it also has a slightly higher barrier. The rate for abstrac-

tion from 1-butene is roughly a factor of five faster between 500 and 2000 K, as expected, since it is easier to form a secondary radical than a primary radical. Based upon the rates presented in Table 1.16, a generic rule for vinyl H-abstraction is:

For abstraction from CH<sub>3</sub>:  $A = 2.7 \times 10^{-13} \times (T/1000)^{2.8} \text{ cm}^3 \text{ molecule}^{-1} \text{ s}^{-1}$  and  $E_a = 5.4 \text{ kcal/mol}$ .

Of course, one must remember to multiply this rate coefficient by the number of equivalent H atoms (i.e. 3 for each methyl group adjacent to the double-bond group).

For abstraction from CH<sub>2</sub>:  $A = 5.6 \times 10^{-13} \times (T/1000)^{2.8} \text{ cm}^3 \text{ molecule}^{-1} \text{ s}^{-1}$  and  $E_a = 4.1 \text{ kcal/mol}$ .

Again, one must remember to multiply this rate coefficient by the number of equivalent H atoms (i.e. 2 for each CH<sub>2</sub> groups adjacent to the double-bond group).

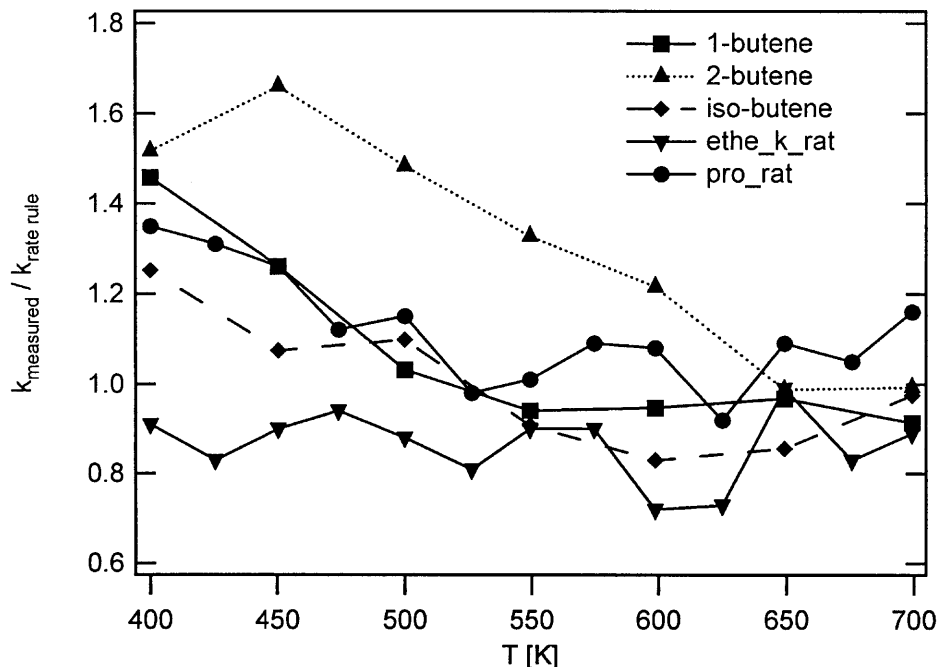
This rate rule agrees very well with the rate coefficients computed from quantum chemistry. From 400 to 850 K, the agreement is within a factor of 2, and from 850 to 2000 K, the agreement is within 25%.

### Rate Rules for Vinyl + Alkenes: Application

Although the major addition channel is the dominant reaction in the experimental temperature range, the H-abstraction channel is not negligible. Indeed, for 1-butene and iso-butene, it can be as much as 25% of the total rate, and even more at combustion-relevant temperatures. Consequently, it is important to include both addition and abstraction reactions when comparing the effectiveness of the new rate rule with the experimental data. The group additivity rate rules for addition and H-abstraction were applied for the five alkenes. The experimentally observed rate coefficients divided by the rate coefficients obtained from the rate rules are plotted versus the temperature in Figure 1-15. With the exception of 2-butene at low temperatures, the rate rules agree with the experimental data to within 40%.

## 1.4.2 Conclusion

The reaction kinetics for the reaction of the vinyl radical with ethene, propene, 1-butene, 2-butene, and iso-butene have been studied over a wide range of temperatures and pres-



**Figure 1-15** – Group additivity rate rule versus experimental data. The dots are the experimental data for vinyl + alkenes divided by the rate rule prediction (sum of the two addition channels plus the dominant H-abstraction channel).

tures. These calculations complement the work in Dr. Ismail’s doctoral thesis. RRKM/ME calculations based on G3 characterization of the  $C_4H_7$ ,  $C_5H_9$ , and  $C_6H_{11}$  potential energy surfaces are presented, and are in excellent agreement with the experimental data. These calculations indicate that at low temperatures, the dominant product for each system will be the collisionally stabilized initial adducts: 3-buten-1-yl for vinyl + ethene; 4-penten-2-yl, 2-methyl-3-buten-1-yl, and 2-methyl-cyclopropylmethyl for vinyl + propene; 5-hexen-3-yl, 2-ethyl-3-buten-1-yl, and 2-ethyl-cyclopropylmethyl for 1-butene; 3-methyl-4-penten-2-yl and 2,3-dimethyl-cyclopropylmethyl for 2-butene; and 2-methyl-4-penten-2-yl, 2,2-dimethyl-3-buten-1-yl, and 2,2-dimethyl-cyclopropylmethyl for iso-butene. At higher temperatures, the addition-isomerization-dissociation channels will yield a mixture of dienes, H atoms, and alkyl radicals, and the direct H-abstraction channels will yield ethene plus allylic radicals. Although several cyclic species are energetically accessible, the yield of cyclic products (with the exception of the cyclopropylmethyl isomers formed via equilibration with the initial adducts) is negligible under the (T,P) conditions considered. The experimental activation energies for the addition reactions do not vary monotonically with

$\Delta H_{rxn}$ ; instead they scale with electrophilicity and steric effects consistent with the present and prior quantum chemical calculations. A new group-additivity based rate rule has been provided for the addition reactions and H-abstraction reaction for the vinyl radical with generic alkenes. This rate rule is in excellent agreement with both the available experimental data and quantum chemical calculations.

## 1.5 Supplemental C<sub>5</sub>H<sub>9</sub> Potential Energy Surfaces

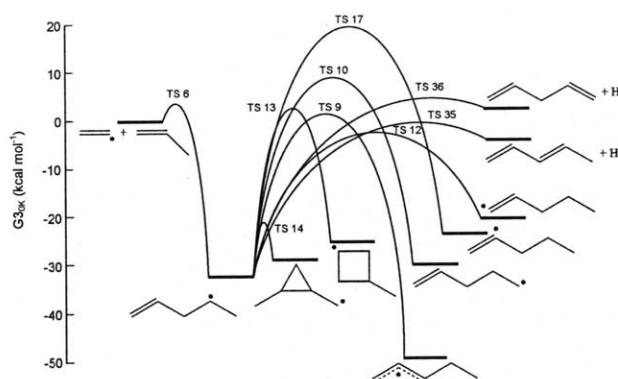


Figure 1-16 – Potential energy surface for 4-penten-2-yl.

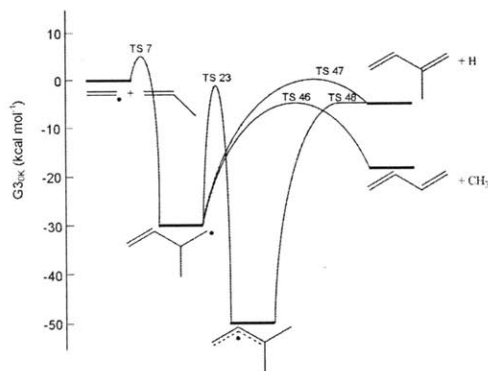


Figure 1-17 – Potential energy surface for 2-methyl-3-buten-1-yl.

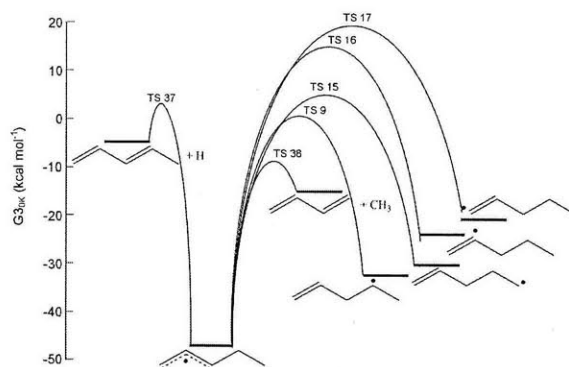


Figure 1-18 – Potential energy surface for 1-ethyl-allyl.

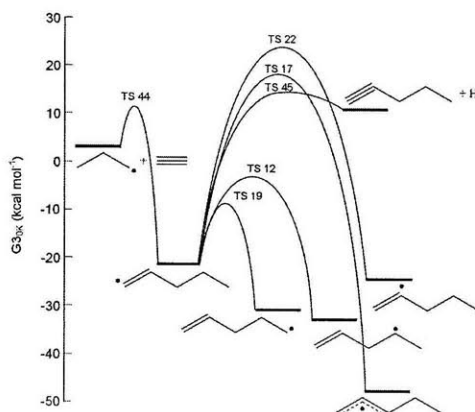


Figure 1-19 – Potential energy surface for 1-penten-1-yl.

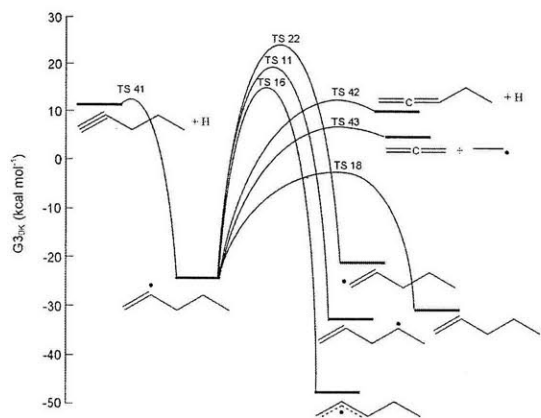


Figure 1-20 – Potential energy surface for 1-penten-2-yl.

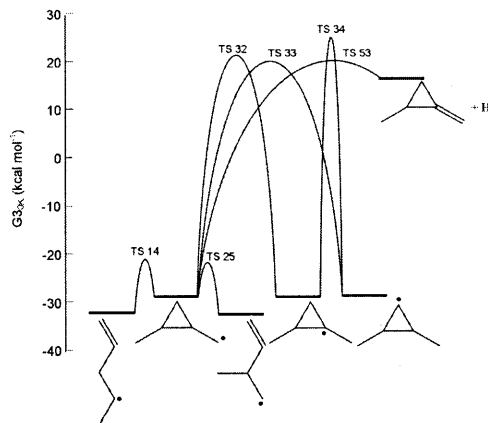


Figure 1-21 – Potential energy surface for 2-methyl-cyclopropylmethyl.

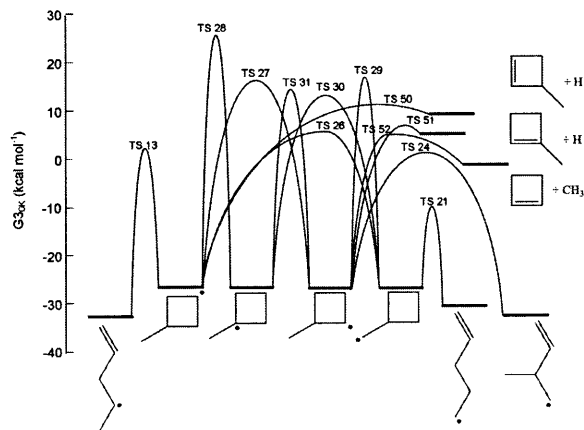


Figure 1-22 – Potential energy surface for 3-methyl-cyclobutyl.

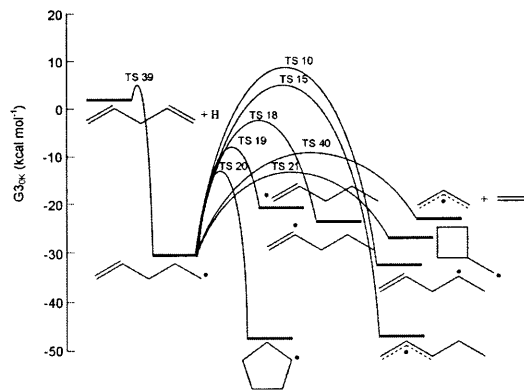


Figure 1-23 – Potential energy surface for 4-penten-1-yl.





# Chapter 2

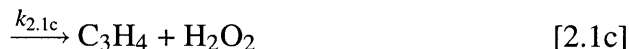
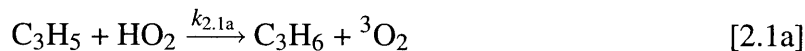
## Allyl + HO<sub>2</sub>

### 2.1 Introduction

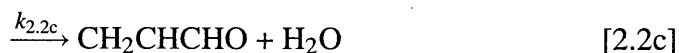
Bimolecular reactions involving HO<sub>2</sub> with other radicals are important in ignition chemistry, particularly at moderate temperatures and high pressures. Although not a chain-branching reaction, R + HO<sub>2</sub> reactions can promote ignition by converting less reactive radicals into more reactive radicals through the following sequence: R + HO<sub>2</sub> → RO + OH → aldehyde + H + OH. Alternatively, the hydroperoxyl radical can transfer the H atom to the other radical, R + HO<sub>2</sub> → RH + O<sub>2</sub>, and thus act as a chain-terminating reaction. The relative rates of these competing chain-branching and chain-terminating reactions are critical for accurate modeling of ignition chemistry. A sensitivity analysis of the reaction rates in the counterflow ignition of methane confirm that CH<sub>3</sub> + HO<sub>2</sub> is among the most important reactions in methane ignition in the temperature range of 1100 to 1400 K [57]. Similarly, Heyberger et al. demonstrated that the induction period of propene ignition in the temperature range of 500 – 800 K is highly sensitive to allyl + HO<sub>2</sub> kinetics, and that omitting this reaction increased the induction period by an order of magnitude [30]. The allyl radical, C<sub>3</sub>H<sub>5</sub>, owing to its resonance stabilization, is less reactive than most radicals and therefore is present in high concentrations in many hydrocarbon flames, so its kinetics with HO<sub>2</sub> will be important for many larger hydrocarbons.

Allyl and HO<sub>2</sub> can react in one of four ways. First, three H-transfer reactions are possible. The allyl radical can abstract the H-atom from hydroperoxyl, forming propene

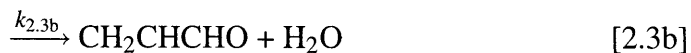
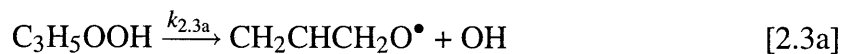
and either singlet or triplet molecular oxygen. Alternatively, HO<sub>2</sub> can abstract the hydrogen from allyl, forming H<sub>2</sub>O<sub>2</sub> + allene:



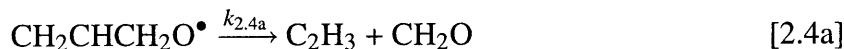
HO<sub>2</sub> can add to either end of the allyl radical. The energized C<sub>3</sub>H<sub>5</sub>OOH adduct is either stabilized via collision or decomposes to two bimolecular channels:



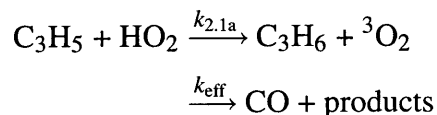
The O-O bond in the collisionally stabilized C<sub>3</sub>H<sub>5</sub>OOH is relatively weak, so this species can decompose to the same two channels:



The sequence Reaction [2.2a] followed by [2.3b] is chain-terminating. Allyloxy, CH<sub>2</sub>CHCH<sub>2</sub>O<sup>•</sup>, can undergo β-scission to form either vinyl + formaldehyde or H + acrolein. Alternatively it can undergo isomerization/decomposition reactions, three of which are listed below:



Despite the importance of the allyl + HO<sub>2</sub> reactions in hydrocarbon combustion, the literature on these reactions is sparse. The only experimental rate coefficients to our knowledge are from Lodhi & Walker [58, 59]. In these experiments, 4,4-dimethyl-pent-1-ene thermally decomposed to t-butyl and allyl in the presence of O<sub>2</sub>. Product yields were monitored by gas chromatography. A complex reaction mechanism is proposed in which the t-butyl radicals are assumed to react exclusively with O<sub>2</sub> to form iso-butene + HO<sub>2</sub>. The mechanism included the following two allyl + HO<sub>2</sub> reactions:



From measured yields of propene and CO they determined  $k_{2.1a}/k_{\text{eff}} = 0.38 \pm 0.18$ . Lodhi & Walker assumed that CO was formed in 100% yield from any species formed via C<sub>3</sub>H<sub>5</sub>OOH, i.e.  $k_{\text{eff}} \approx k_{2.2}$ . The individual rate constants for  $k_{1a}$  and  $k_{\text{eff}}$  were obtained from estimates of the initial allyl and HO<sub>2</sub> concentrations and other rate constants. These results were updated by Baulch et al. [5]. Both Lodhi & Walker and Baulch et al. assumed that the main source of CO is the production and subsequent oxidation of the vinyl radical. Tsang proposed a single-step rate constant for allyl + HO<sub>2</sub> to OH + H + acrolein [97]. The mechanism of Heyberger et al. consisted of three reactions: H-abstraction,  $k_{2.1a}$ ; formation of allylhydroperoxide,  $k_{2.2a}$ ; and a single step for the decomposition of allylhydroperoxide to H + acrolein,  $k_{2.3a-2.4b}$ . The literature rates for Reactions [2.1a] and [2.2] are sum-

marized in Table 2.1. Rauk et al. [84] calculated the high-pressure rate coefficients for the decomposition of allyloxy to vinyl + formaldehyde and acrolein + H using CBS-RAD theory [66]. The related vinyl + formaldehyde  $\rightarrow$  allyloxy potential energy surface was investigated by Xie et al. [105], using G3[11] and CBS-QB3[75] compound methods.

**Table 2.1** – Previous literature values for allyl + HO<sub>2</sub>.<sup>a</sup>

Source	k <sub>2,1a</sub>	k <sub>2,2</sub>
Lodhi and Walker[59] (indirect experiment)	0.31	0.74
Baulch[5] (review)	0.44	1.1
Tsang[97] (estimate)		1.6
Heyberger[30] (modeling)	0.31	0.85
Present work (theory)	0.01	1.2

<sup>a</sup> Rate coefficients are evaluated at 753 K, in units of 10<sup>-11</sup> cm<sup>3</sup> molecule<sup>-1</sup> s<sup>-1</sup>.

The kinetics of the allyl + HO<sub>2</sub> reaction and allyloxy decomposition are considerably more complex than the previous mechanisms suggest. Due to the barrierless entrance channel, the chemically-activated C<sub>3</sub>H<sub>5</sub>OOH adduct can react directly to either allyloxy + OH or acrolein + water on the same time scale as the addition reaction. Thus, the rate coefficients for the reaction of allyl + HO<sub>2</sub> going to products and the subsequent decomposition of allyloxy will be a complex function of temperature and pressure, and the determination of these rate coefficients requires solving the master equation.

The methodology used in this paper is similar to that in Jasper et al. for the CH<sub>3</sub> + HO<sub>2</sub> reactions [38]. Variable reaction coordinate transition state theory (VRC-TST) is used to calculate the E,J-resolved microcanonical rate coefficients for the two barrierless reactions. Temperature and pressure dependence of the C<sub>3</sub>H<sub>5</sub>OOH and C<sub>3</sub>H<sub>5</sub>O addition/isomerization/decomposition rate coefficients are calculated by solving the master equation, using variational transition state theory and rigid-rotor harmonic oscillator (RRHO) approximations.

## 2.2 Theory

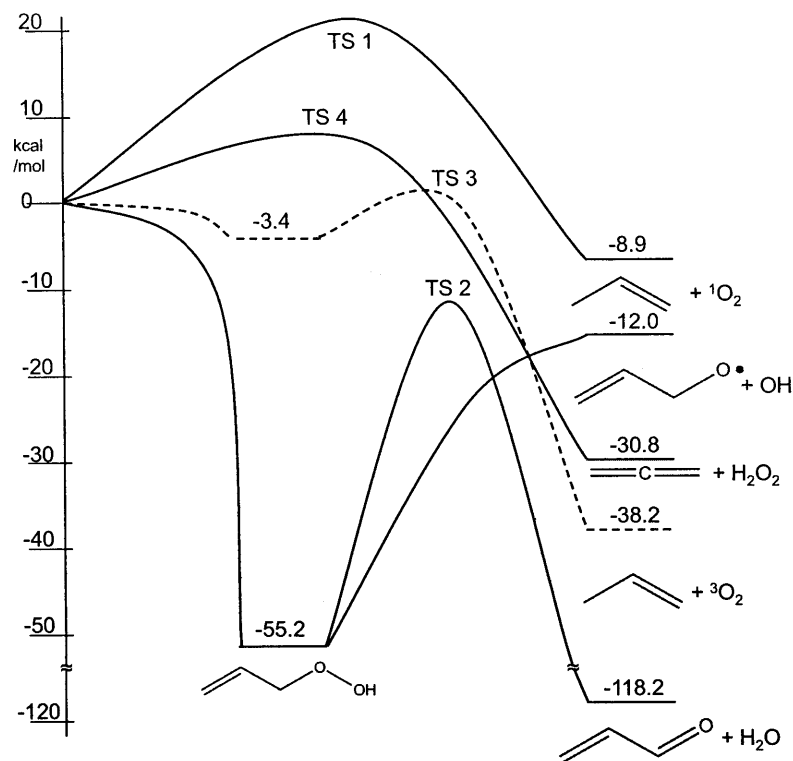
### 2.2.1 Potential Energy Surfaces

For each species and transition state, the  $\sim 3^n$  possible conformers – where  $n$  is the number of torsional modes – were calculated using the CBS-QB3 method. The lowest energy conformer was selected, and this geometry was re-optimized using the B3LYP functional with the MG3S basis set, which was selected for the accuracy of its geometry and frequency calculations[107]. The DFT geometries were used for restricted QCISD(T)/cc-pVTZ and QCISD(T)/cc-pVQZ energies. The QCISD(T) complete basis set limit was extrapolated from the triple and quadruple zeta basis set calculations assuming an inverse power law[64, 14]:

$$E_{\text{QCISD(T)/CBS}} = E_{\text{QCISD(T)/cc-pVQZ}} + \left( E_{\text{QCISD(T)/cc-pVQZ}} - E_{\text{QCISD(T)/cc-pVTZ}} \right) \frac{4^4}{5^4 - 4^4} \quad (2.1)$$

The QCISD(T)/CBS enthalpies at 0 K, including the B3LYP/MG3S zero point energies, for the  $\text{C}_3\text{H}_6\text{O}_2$  potential energy surface (PES) are shown in Figure 2-2 and listed in Tables 2.2 and 2.3; the corresponding values for the  $\text{C}_3\text{H}_5\text{O}$  PES are in Figure 2-2 and Table 2.4 and 2.5. Also included in Tables 2.2 through 2.5 are change in entropy of activation,  $\Delta S$ , as well as the QCISD(T)/cc-pVQZ T1 diagnostic[54] for the equilibrium and saddle point geometries. The T1 diagnostic is a measure of the importance of multi-reference effects. For closed shell species with a T1 diagnostic less than  $\sim 0.02$ , and for radicals with a T1 diagnostic less than  $\sim 0.03$ , the QCISD(T) energies are assumed to be accurate to  $\sim 1$  kcal/mol, and multireference calculations are unnecessary[46]. CASPT2[1] was used for the barrierless reactions. All DFT calculations were done using Gaussian03[17]. All QCISD(T) and CASPT2 calculations were done using MOLPRO[101].

Allyl and  $\text{HO}_2$  can react on both the singlet and triplet potential energy surfaces. On the triplet PES, indicated in Figure 2-1 by the dashed lines, the two doublets form a weakly bound van der Waals complex. The allyl moiety abstracts the H-atom from the  $\text{HO}_2$  via TS



**Figure 2-1** – Allyl + HO<sub>2</sub> potential energy surface.

3, leading to propene + <sup>3</sup>O<sub>2</sub>. On the singlet PES, HO<sub>2</sub> adds to either end of allyl, forming allylhydroperoxide, which dissociates to either allyloxy + OH or to acrolein + water. Two possible H-transfer reactions can occur on the singlet surface: allyl + HO<sub>2</sub> → propene + <sup>1</sup>O<sub>2</sub> via TS 1, and allyl + HO<sub>2</sub> → allene + H<sub>2</sub>O<sub>2</sub> via TS 4. The T1 diagnostic for these reactions are 0.071 and 0.041, respectively, which implies that these transition states are ill-described by single-reference methods. Even if these barriers were off by 5 kcal/mol, they would still be negligible compared to the other two reactions. Therefore, it is assumed that abstraction on the singlet surface can be safely neglected.

The salient features of the C<sub>3</sub>H<sub>5</sub>O PES are shown in Figure 2-2. The lowest decomposition barrier for allyloxy is to acrolein + H via TS 7. Allyloxy can also undergo β-scission to form vinyl + formaldehyde via TS 5. Additionally, allyloxy can isomerize to the vinoxyl-methyl radical, via the oxiranyl-methyl radical, or it can isomerize to 2-formyl-ethyl, via an unusual 1,2-H shift, TS 6. All other competing barriers (e.g. 1,2-H shift to CH<sub>2</sub>CHC•OH) were significantly higher. 2-formyl-ethyl dissociates to HCO + ethene via TS 9. Because this transition state is 13 kcal/mol lower in energy than the preceding isomerization barrier,

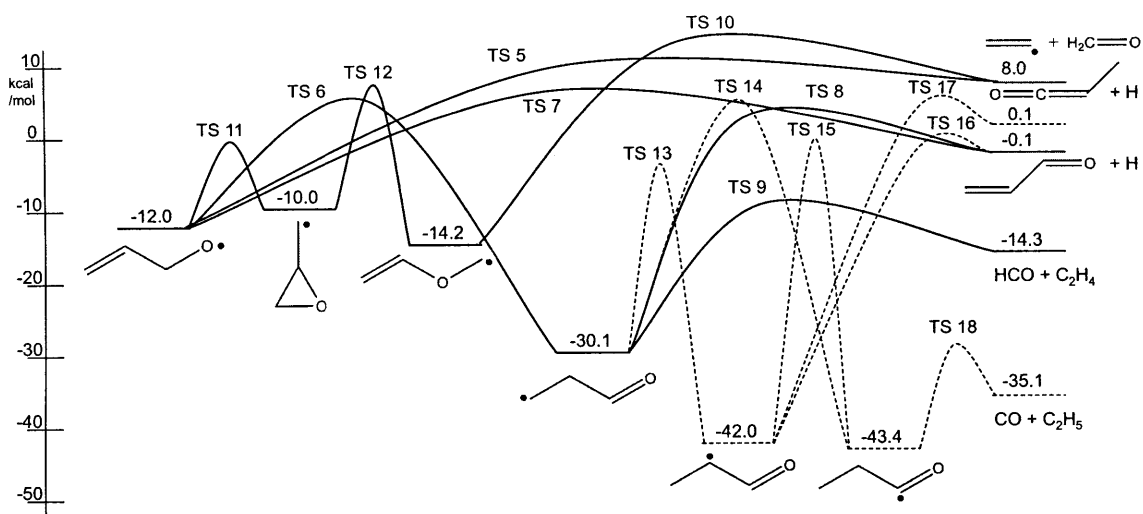
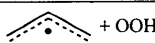
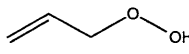
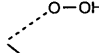
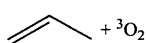
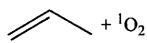
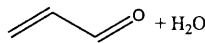
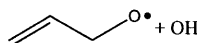



Figure 2-2 – C<sub>3</sub>H<sub>6</sub>O<sub>2</sub> potential energy surface.

it is possible for thermally activated allyloxy to decompose directly to HCO + ethene. Two other wells are available from 2-formyl-ethyl: 2-methyl-vinoxy and propionyl. These two wells and their decomposition channels (shown in the dotted lines in Figure 2-2) were not included in the Master Equation calculations. The transition states leading to these isomers, TS 13 and TS 14, are more than 5 kcal/mol higher than the competing  $\beta$ -scission reaction, TS 9, and have a smaller A-factor. Sample calculations confirm these channels make a negligible contribution to the overall rate coefficients.

Table 2.2 – Species for allyl + HO<sub>2</sub> potential energy surface.

Identifier	Name	Structure	Relative Energy (kcal/mol)	T1 Diagnostic
R1	Allyl + HO <sub>2</sub>	 + OO <sub>2</sub> H	0	0.010, 0.037
W1	Allylhydroperoxide		-55.2	0.012
W2	vdW complex		-3.4	0.030
P1	Propene + <sup>3</sup> O <sub>2</sub>	 + <sup>3</sup> O <sub>2</sub>	-38.2	0.010, 0.007
P2	Propene + <sup>1</sup> O <sub>2</sub>	 + <sup>1</sup> O <sub>2</sub>	-8.9	0.010, 0.015
P3	Acrolein + H <sub>2</sub> O	 + H <sub>2</sub> O	-118.2	0.015, 0.007
P4	Allyloxy + OH	 + OH	-12	0.020, 0.007
P5	Allene + H <sub>2</sub> O <sub>2</sub>	 + H <sub>2</sub> O <sub>2</sub>	-30.7	0.013, 0.011

**Table 2.3** – Transition states for allyl + HO<sub>2</sub> potential energy surface

Identifier	Reaction	Relative Energy (kcal/mol)	$\Delta S$ (cal/mol/K)	T1 Diagnostic
TS 1	R1 to P2	22.8	-34.9	0.071
TS 2	W1 to P3	-9.4	-40.9	0.022
TS 3	R1 to P1	2.6	-43.5	0.035
TS 4	R1 to P5	8.6	-9.2	0.041

**Table 2.4** – Species for C<sub>3</sub>H<sub>5</sub>O potential energy surface

Identifier	Name	Structure	Relative Energy (kcal/mol)	T1 Diagnostic
W3	Allyloxy		-12	0.020
W4	2-formyl-ethyl		-30.1	0.015
W5	Oxiranyl-methyl		-10	0.015
W6	Vinoxyl-methyl		-14.2	0.018
W7	2-methyl-vinoxy		-42	0.020
W8	Propionyl		-43.4	0.019
P6	Acrolein + H		-0.1	0.015, 0.000
P7	C <sub>2</sub> H <sub>4</sub> + HCO		-14.3	0.011, 0.025
P8	C <sub>2</sub> H <sub>3</sub> + CH <sub>2</sub> O		8	0.017, 0.016
P9	Methyl-ketene + H		0.1	0.015, 0.000
P10	CO + ethyl		-35.1	0.018, 0.010

## 2.2.2 Variable Reaction Coordinate TST Calculations

The two barrierless reactions, allyl + HO<sub>2</sub> ↔ allylhydroperoxide, and allylhydroperoxide ↔ allyloxy + OH, were calculated using variable reaction coordinate transition state theory[18, 44, 45]. These calculations were done using the computer code VaReCoF[19]. The degrees of freedom were separated into conserved and transitional modes. The conserved modes were the vibrational modes of the two fragments at their isolated geometries. The transitional modes, which are the coupled, anharmonic modes correlating with the relative orientation and separation of the two fragments, were calculated on-the-fly using



**Table 2.5** – Transition states for C<sub>3</sub>H<sub>5</sub>O potential energy surface.

Identifier	Reaction	Relative Energy (kcal/mol)	$\Delta S$ (cal/mol/K)	T1 Diagnostic
TS 5	W3 to P8	10.3	-34.8	0.019
TS 6	W3 to W4	6.1	-2.2	0.038
TS 7	W3 to P6	6.7	0.6	0.019
TS 8	W4 to P6	3.9	-1.1	0.017
TS 9	W4 to P7	-6.7	0.6	0.023
TS 10	W6 to P8	20.0	-34.1	0.025
TS 11	W3 to W5	-4.5	-3.2	0.026
TS 12	W5 to W6	3.3	-0.8	0.022
TS 13	W4 to W7	-1.7	-3.7	0.018
TS 14	W4 to W8	4.3	-3.9	0.026
TS 15	W7 to W8	-0.4	-0.4	0.024
TS 16	W7 to P6	1.4	2.1	0.016
TS 17	W7 to P9	5.6	1.9	0.019
TS 18	W8 to P10	-29.0	5.9	0.023

multireference perturbation theory (CASPT2). The delocalized  $\pi$ -orbitals in the allyl radical require a minimum active space of three electrons in three orbitals (3e,3o)[20]. Thus, for the allyl + HO<sub>2</sub>  $\leftrightarrow$  allylhydroperoxide reaction, a (4e,4o) active space was chosen. For the allylhydroperoxide  $\leftrightarrow$  allyloxy + OH reaction the minimum active space was (6e,4o), which accounts for the three electrons in two orbitals on each oxygen-centered radical[38]. For each reaction, two sets of CASPT2/cc-pVDZ geometry optimizations were performed along the minimum energy path (MEP) from 1.5 Å to 5 Å. In one set, all of the modes were relaxed; in the other set, the conserved modes were held fixed at their isolated geometries, and only the transitional modes were optimized. The CASPT2/CBS energy was extrapolated from subsequent CASPT2/aug-cc-pVDZ and CASPT2/aug-cc-pVTZ calculations using a formula similar to Equation (2.1). The difference in energy between the constrained and relaxed MEP was added to the CBS correction and used as a 1-D correction to the interaction potential.

### 2.2.3 Master Equation Calculations

The time-dependent master equation was solved using the computer code VariFlex[47]. The torsional modes for each species and transition state were treated as hindered internal rotors. The barriers for internal rotation were calculated by a relaxed scan at the B3LYP/CBSB7 level. The resulting potential was fit to a Fourier series. A rigid-rotor harmonic oscillator model was assumed for all remaining degrees of freedom. In order to reduce the ambiguity regarding low-frequency vibrations and the corresponding torsional modes, the projection of the B3LYP/MG3S force-constant matrix was removed along the vectors corresponding to the torsional modes. This matrix was then diagonalized, which separated the rigid rotor harmonic oscillator frequencies from the torsional modes[91]. These frequencies were then scaled by 0.9983, as recommended by Zhao et al.[107]. A Pitzer-Gwinn-like[80] approximation was made within Variflex for the hindered rotor partition function. The effective moment of inertia for each rotor was  $I^{(2,3)}$ , evaluated at the equilibrium geometry. Tunneling was included for all transition states by use of an Eckart approximation[40]. For energy transfer in the master equation, a singleexponential down model was used. Common literature values were used for the energy transfer parameter[72, 73, 22], with a  $\langle \Delta E_{down} \rangle$  of  $400 \text{ cm}^{-1} (T/298)^{0.8}$  for  $\text{N}_2$ . The collision frequency was estimated using a Lennard-Jones model, with LJ parameters of  $\sigma = 4.42 \text{ \AA}$  and  $\epsilon = 292 \text{ cm}^{-1}$  for  $\text{C}_3\text{H}_5\text{OOH}$  and  $\sigma = 4.40 \text{ \AA}$  and  $\epsilon = 280 \text{ cm}^{-1}$  for all  $\text{C}_3\text{H}_5\text{O}$  isomers. The LJ parameters for the wells were based on group additivity of the functional groups[39]. The  $\text{N}_2$  bath gas LJ-parameters,  $\sigma = 3.74 \text{ \AA}$  and  $\epsilon = 57.0 \text{ cm}^{-1}$ , were taken from literature values[32]. The  $\text{C}_3\text{H}_6\text{O}_2$  and  $\text{C}_3\text{H}_5\text{O}$  master equation calculations were performed at 60 Torr of  $\text{N}_2$  and temperatures between 400 and 2000 K. This pressure was chosen to simulate the experimental conditions of Lodhi & Walker.

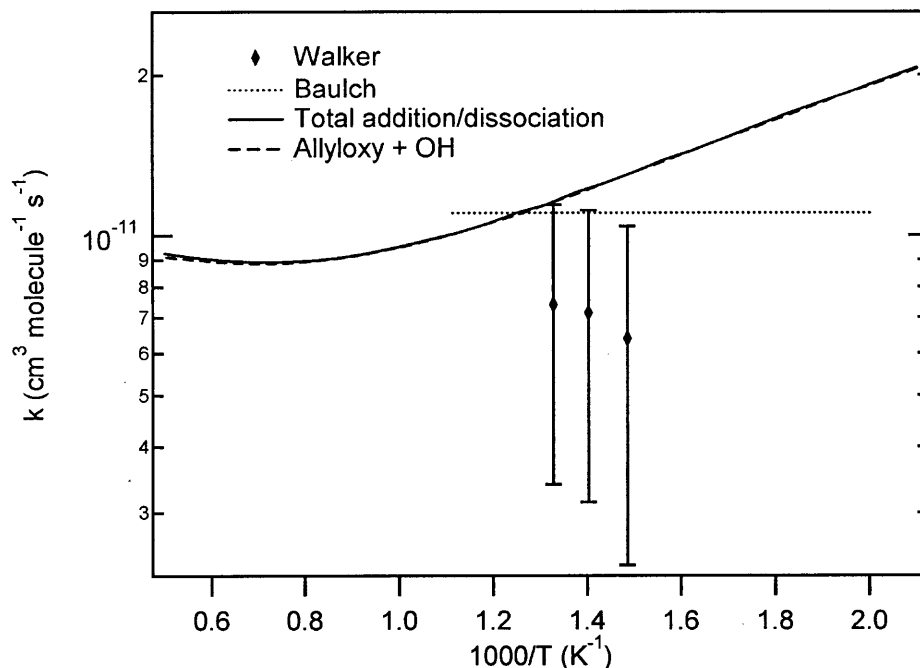


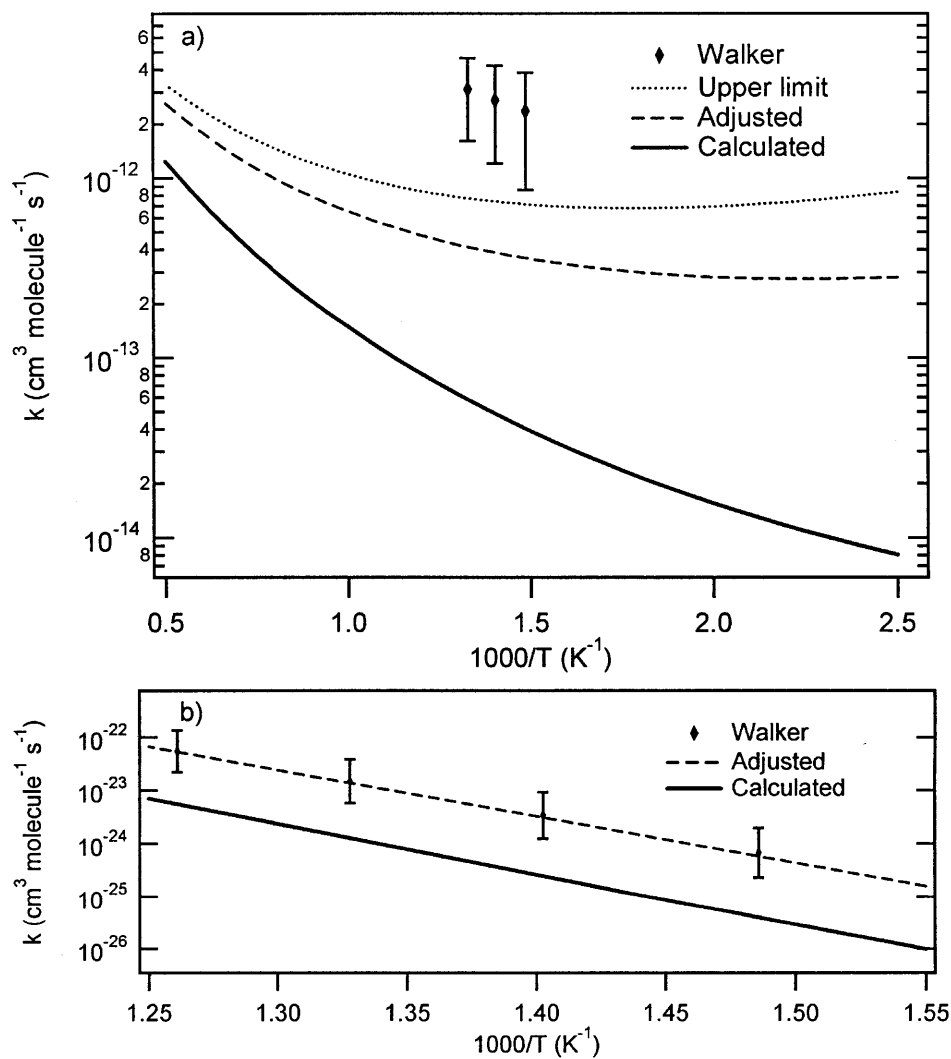
Figure 2-3 – Rate constants for the allyl + HO<sub>2</sub> addition/dissociation reaction.

## 2.3 Results and Discussion

### 2.3.1 Allyl + HO<sub>2</sub> Reaction

The calculated rate coefficients for the addition/dissociation pathway are shown in Figure 2-3 and listed in Table 2.6. The high-pressure limit for the addition reaction,  $k_{2.2a}^{\infty}$ , is within a factor of 2 of the experimental data and is in excellent agreement with the updated results of Baulch. At 400 K and 60 Torr of N<sub>2</sub>, less than 5% of the C<sub>3</sub>H<sub>5</sub>OOH adduct is collisionally stabilized to allylhydroperoxide; for temperatures greater than 600 K more than 99.9% of the energized C<sub>3</sub>H<sub>5</sub>OOH adduct goes directly to allyloxy + OH. The acrolein + water channel is negligible at all temperatures and pressures. Roaming radical reactions[27], which could conceivably increase the acrolein + water channel yield, were not considered in the present work.

The rate for the abstraction reaction on the triplet surface is shown in Figure 2-4a and listed in Table 2.6. The computed rate coefficient is nearly a factor of 30 slower than that inferred by Lodhi & Walker from experimental data. The T1 diagnostic for H abstraction on the triplet surface is 0.035, which suggests minor uncertainty due to multireference



**Figure 2-4** – Rate constants for the allyl + HO<sub>2</sub> H-abstraction reaction. (a) The rate coefficients for allyl + HO<sub>2</sub> → C<sub>3</sub>H<sub>6</sub> + <sup>3</sup>O<sub>2</sub>. The solid line is the original computed rate; the dashed line is the rate coefficient when the transition state is reduced by 3.0 kcal/mol; the dotted line is the rate coefficient when the transition state is reduced by 3.0 kcal/mol and ΔH<sub>0</sub> is decreased by 1.0 kcal/mol. (b) the rate coefficients for C<sub>3</sub>H<sub>6</sub> + <sup>3</sup>O<sub>2</sub> → allyl + HO<sub>2</sub>. The solid line is the original computed rate; the dashed line is the rate coefficient when the transition state is reduced by 3.0 kcal/mol.

**Table 2.6** – Calculated rate coefficients for allyl + HO<sub>2</sub> in 60 Torr of N<sub>2</sub>.<sup>a</sup>

Reaction		A	n	E <sub>a</sub>
allyl + HO <sub>2</sub>	$\xrightarrow{k_{2.1a}}$ propene + <sup>3</sup> O <sub>2</sub>	(9.3 ± 0.1) × 10 <sup>-15</sup>	2.7	490 ± 10
	$\xrightarrow{k_{2.1a}^{\text{adjusted}}}$ propene + <sup>3</sup> O <sub>2</sub>	(7.4 ± 0.1) × 10 <sup>-15</sup>	2.8	-1100 ± 10
	$\xrightarrow{k_{2.1a}^{\text{upper limit}}}$ propene + <sup>3</sup> O <sub>2</sub>	(7.6 ± 0.1) × 10 <sup>-15</sup>	2.8	-1540 ± 10
	$\xrightarrow{k_{2.2a}^{\infty}}$ allylhydroperoxide	(1.7 ± 0.1) × 10 <sup>-12</sup>	0.6	-1060 ± 10
	$\xrightarrow{k_{2.2a}}$ allylhydroperoxide	(8.7 ± 0.9) × 10 <sup>-14</sup>	-3.7	-650 ± 50
	$\xrightarrow{k_{2.2b}}$ allyloxy + OH	(2.0 ± 0.5) × 10 <sup>-12</sup>	0.5	-990 ± 10
	$\xrightarrow{k_{2.2c}}$ acrolein + H <sub>2</sub> O	(9.5 ± 0.2) × 10 <sup>-18</sup>	3.4	-1390 ± 30

<sup>a</sup> The error limits in the Arrhenius parameters are the 95% confidence intervals and do not include uncertainties in the thermochemistry. The superscript <sup>∞</sup> refers to the high-pressure limit for the reaction. The units for A are in cm<sup>3</sup> molecule<sup>-1</sup> s<sup>-1</sup> and for E<sub>a</sub> in Kelvin. The rate coefficient is  $k = A(T/298)^n \exp[-E_a/T]$ .

effects. The transition state geometry was re-optimized using the (6e,6o)-CASPT2/cc-PVTZ method, and the CASPT2/CBS energy was estimated from subsequent CASPT2 calculations using the cc-pVTZ and cc-pVQZ basis sets. The CASPT2/CBS barrier is 1.0 kcal/mol lower than the QCI/CBS barrier. Thus, the uncertainty in this transition state is assumed to be ~ 2 kcal/mol. Stothard & Walker measured the rate coefficient for the reverse reaction,  $k_{-2.1a}$ , C<sub>3</sub>H<sub>6</sub> + <sup>3</sup>O<sub>2</sub> allyl + HO<sub>2</sub>[94]. The present thermochemistry was used to calculate the rate coefficient for this reaction, shown in Figure 2-4b. The calculated rate coefficient using the QCI/CBS energy is a factor of five too slow. If the barrier is decreased by 2 kcal/mol, the calculated rate coefficient is within the experimental error; if the barrier is decreased by 3.0 kcal/mol (i.e. ΔE<sub>0</sub> = 37.8 kcal/mol relative to propene + <sup>3</sup>O<sub>2</sub>, instead of ΔE<sub>0</sub> = 40.8 kcal/mol), the calculated rate coefficient agrees with the data to within 25% (see inset). If this new barrier is used for the forward reaction (i.e. ΔE<sub>0</sub> = - 0.4 instead of 2.6 kcal/mol), the calculated rate coefficient remains too slow by a factor of ten. If the uncertainty in the thermochemistry for allyl + HO<sub>2</sub> relative to propene + <sup>3</sup>O<sub>2</sub> is ~1 kcal/mol, and if ΔH<sub>0</sub> is thereby decreased from -38.2 to -39.2 kcal/mol, while holding the transition state barrier at ΔE<sub>0</sub> = 37.8 kcal/mol relative to propene + <sup>3</sup>O<sub>2</sub>, the adjusted rate coefficient is within a factor of four of the experimental data. This adjusted rate coefficient

(the dotted line in Figure 2-4a) is an upper bound for  $\text{allyl} + \text{HO}_2 \rightarrow \text{C}_3\text{H}_6 + {}^3\text{O}_2$ . To match the data to within 25%,  $\Delta H_0$  would need to be decreased by 3.3 kcal/mol, which correlates to an unrealistically large decrease of 6 kcal/mol in the forward barrier height. Since the experimental rate coefficients for  $k_{-1a}$  are less errorprone than the forward rate, and since the calculated thermochemistry for the stable species should be accurate to  $\sim 1$  kcal/mol, the present results suggest that the previous rate coefficient for  $\text{allyl} + \text{HO}_2 \rightarrow \text{C}_3\text{H}_6 + {}^3\text{O}_2$  is at least a factor of four too fast. In all likelihood, it is an order of magnitude off, and may possibly be off by as much as a factor of thirty. The experimental results suggest that a larger mechanism, possibly one including heterogeneous effects, is needed to explain some of the observed species.

### 2.3.2 Allylhydroperoxide Dissociation

At high pressures and low-to-moderate temperatures, the activated  $\text{C}_3\text{H}_5\text{OOH}$  adduct is collisionally stabilized to allylhydroperoxide. The stabilized product will then dissociate to form allyloxy + OH. The rate coefficients for allylhydroperoxide dissociation are listed in Table 2.7. At 60 Torr of  $\text{N}_2$ , the rate constant is roughly an order of magnitude slower than the high pressure limit. The other two unimolecular channels available to allylhydroperoxide are four orders of magnitude slower than dissociation to allyloxy + OH at all temperatures and pressures.

**Table 2.7** – Calculated rate coefficients for allyl-hydroperoxide dissociation in 60 Torr of  $\text{N}_2$ .<sup>a</sup>

Reaction		$A$	$n$	$E_a$
allylhydroperoxide	$\xrightarrow{k_{2.3a}}$ allyloxy + OH	$(5.9 \pm 0.3) \times 10^{16}$	-7.2	$19560 \pm 110$
	$\xrightarrow{k_{2.3a}^\infty}$ allyloxy + OH	$(3.1 \pm 0.1) \times 10^{16}$	-1.5	$21580 \pm 10$
	$\xrightarrow{k_{2.3b}}$ acrolein + $\text{H}_2\text{O}$	$(1.4 \pm 0.1) \times 10^{12}$	-7.0	$20740 \pm 50$

<sup>a</sup> The error limits in the Arrhenius parameters are the 95% confidence intervals and do not include uncertainties in the thermochemistry. The superscript  $\infty$  refers to the high-pressure limit for the reaction. The units for  $A$  are in  $\text{s}^{-1}$  and for  $E_a$  in Kelvin. The rate coefficient is  $k = A(T/298)^n \exp[-E_a/T]$ .

### 2.3.3 Allyloxy Kinetics

Whether formed directly via chemical activation or indirectly via collisional stabilization and subsequent thermal dissociation of allylhydroperoxide, the dominant product in the allyl + HO<sub>2</sub> reaction is allyloxy + OH. The results of master equation simulations of allyloxy dissociation in 60 Torr of N<sub>2</sub> are shown in Figure 2-5; the corresponding rate coefficients are listed in Table 2.8. At this pressure, the two  $\beta$ -scission channels are several orders of magnitude below their high-pressure limits. The largest rate coefficient is isomerization to vinoxyl-methyl. Kinetic simulations suggest that allyloxy and vinoxyl-methyl rapidly equilibrate, followed by decomposition. Below 600 K, HCO + ethene is computed to be the dominant bimolecular product. Above 600 K, acrolein + H is the dominant bimolecular product, but the HCO + ethene channel is within a factor of three for all temperatures. This important channel has been neglected in all previous mechanisms, even though ethene production was observed experimentally. In the temperature range of the experiments, the rate of production of vinyl + formaldehyde is less than 2% of the total rate of allyloxy decomposition to bimolecular products. Thus, it is unlikely that the dominant source of CO in the experiments is from this channel. Instead, the CO probably resulted from (i) HCO decomposition and (ii) H-abstraction from acrolein to form an unsaturated acyl radical, CH<sub>2</sub>=CHC(=O), which decomposes to vinyl + CO[68, 95, 52]. Although allyl + HO<sub>2</sub> can go directly to allyloxy + OH via chemical activation, it is unlikely that the allyloxy fragment will have sufficient internal energy to fragment immediately on the same time scale, since the barrier for decomposition to acrolein + H is  $\sim 7$  kcal/mol above allyl + HO<sub>2</sub> in energy. Thus, modeling the kinetics by a single step reaction that omits the allyloxy intermediate is not advised.

Transition state TS 6 determines the branching fraction between HCO + ethene versus acrolein + H. The T1 diagnostic for this transition state is 0.038. Consequently, there is some uncertainty in this barrier height due to multireference effects. Subsequent (5e,5o)-CASPT2/CBS//CASPT2/aug-cc-pVDZ calculations lowered the barrier from  $\Delta E_0 = 18.1$  kcal/mol to  $\Delta E_0 = 16.6$  kcal/mol, and CI+QC/CBS corrections to the CASPT2 19 geometry increased the barrier from  $\Delta E_0 = 18.1$  kcal/mol to  $\Delta E_0 = 20.5$  kcal/mol. In order to test the

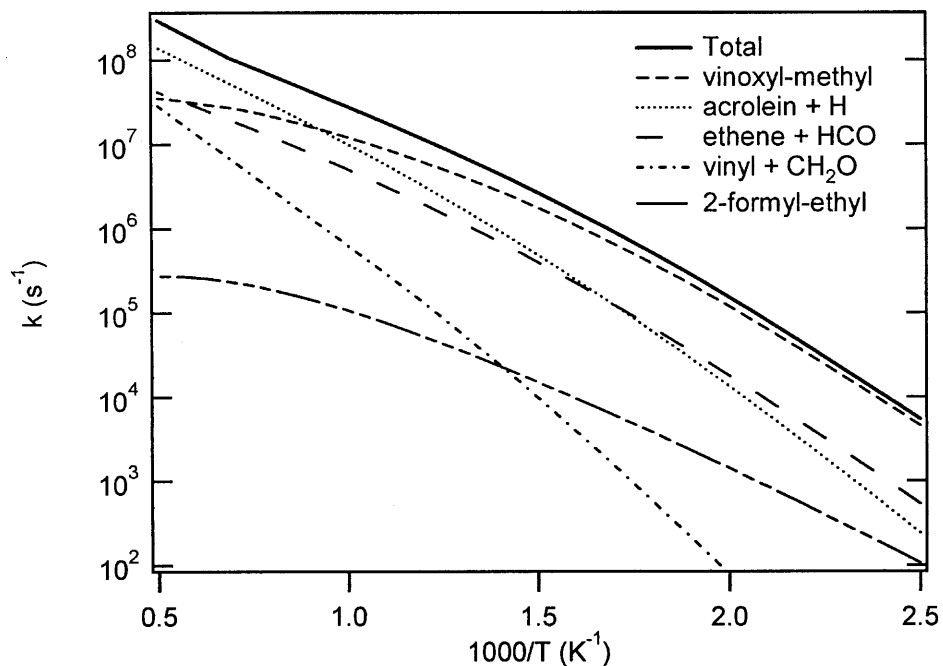


Figure 2-5 – Rate constants for allyloxy decomposition.

sensitivity of the total branching fractions to this transition state, the RRKM/ME results were repeated with the barrier height altered  $\pm 2$  kcal/mol. Increasing the barrier by 2 kcal/mol increased the rate of acrolein + H by  $\sim 20\%$  and decreased the rate of HCO + ethene by a factor of 5. Similarly, decreasing the barrier by 2 kcal/mol decreased the rate of acrolein + H by a factor of 2 and increased the rate of HCO + ethene by a factor of 3.

## 2.4 Kinetic Model

As detailed in the Section 2.1, the kinetics of the allyl + HO<sub>2</sub> reaction are considerably more complex than previous models have considered. In order to test the significance of the present work, a simple kinetic model was developed, which included the major channels shown in Figures 2-1 and 2-2: allyl + HO<sub>2</sub>, allylhydroperoxide, propene + <sup>3</sup>O<sub>2</sub>, allyloxy + OH, 2-formyl-ethyl, vinoxyl-methyl, acrolein + H, ethene + HCO, and vinyl + CH<sub>2</sub>O. The model was compared to the previously most detailed mechanism, that of EXGAS by Battin-Leclerc and coworkers [30]. The model assumes an initial mole fraction of allyl and HO<sub>2</sub> of 5 ppm at 600 K. To illustrate the impact of the pressure dependence of the rate



**Table 2.8** – Calculated rate coefficients for allyloxy decomposition in 60 Torr of N<sub>2</sub>.<sup>a</sup>

	Reaction	<i>A</i>	<i>n</i>	<i>E<sub>a</sub></i>
allyloxy	$\xrightarrow{k_{2.4a}}$ vinyl + CH <sub>2</sub> O	$(2.1 \pm 0.1) \times 10^{10}$	-1.0	9380 ± 40
	$\xrightarrow{k_{2.4a}^{\infty}}$ vinyl + CH <sub>2</sub> O	$(2.7 \pm 0.1) \times 10^{14}$	0.0	12030 ± 10
	$\xrightarrow{k_{2.4b}}$ acrolein + H	$(1.8 \pm 0.1) \times 10^{11}$	-1.7	7880 ± 50
	$\xrightarrow{k_{2.4b}^{\infty}}$ acrolein + H	$(3.5 \pm 0.1) \times 10^{12}$	1.0	9340 ± 20
	$\xrightarrow{k_{2.4c}}$ ethene + HCO	$(3.9 \pm 0.1) \times 10^{10}$	-1.8	6860 ± 40
	$\xrightarrow{k_{2.4d}}$ 2-formyl-ethyl	$(6.2 \pm 0.1) \times 10^9$	-3.5	6740 ± 10
	$\xrightarrow{k_{2.4e}}$ vinoxyl-methyl	$(8.5 \pm 0.2) \times 10^{11}$	-3.5	6950 ± 40

<sup>a</sup> The error limits in the Arrhenius parameters are the 95% confidence intervals and do not include uncertainties in the thermochemistry. The superscript <sup>∞</sup> refers to the high-pressure limit for the reaction. The units for *A* are in s<sup>-1</sup> and for *E<sub>a</sub>* in Kelvin. The rate coefficient is  $k = A(T/298)^n \exp[-E_a/T]$ .

coefficients, the simulation was repeated for 0.8 atm and 10 atm. 0.8 atm was chosen to match the experimental data from [30]. The results are shown in Figure 2-6.

As seen in the first pane of Figure 2-6, the two models are in close agreement in the predicted profiles of the allyl radical; the mole fractions of allylhydroperoxide are qualitatively similar as well. For the remaining species, however, the mole fractions predicted by new rate coefficients differ significantly from those predicted by EXGAS. First, the oxygen profiles differ by nearly two orders of magnitude. The EXGAS code fit their rate expression to the experimental data from Lodhi and Walker, which as detailed above is arguably too fast. This difference is important for two reasons. First, this reaction is chain terminating. Since their mechanism was fit to the experimental data, it assumed a ratio of  $k_{2.1a}/k_{2.2} \approx 0.4$ , whereas the current results suggest  $k_{2.1a}/k_{2.2} \approx 0.02$ . Second, the reaction sequence allyl + HO<sub>2</sub> → C<sub>3</sub>H<sub>5</sub>OOH<sup>‡</sup> → products is largely thermoneutral (for example, relative to allyl + HO<sub>2</sub>, acrolein + H + OH is ΔH<sub>0 K</sub> = -0.1 kcal/mol, ethene + formyl + OH is ΔH<sub>0 K</sub> = -14.3 kcal/mol, and vinyl + formaldehyde + OH is ΔH<sub>0 K</sub> = 8.0 kcal/mol. Allyl + HO<sub>2</sub> → propene + <sup>3</sup>O<sub>2</sub> is considerably more exothermic, with ΔH<sub>0 K</sub> = -38.2 kcal/mol. Thus, the EXGAS mechanism (i) is significantly more chain terminating and (ii) has significantly more heat release than the present work.

The difference in mole fraction profiles is even more pronounced for the radical species.

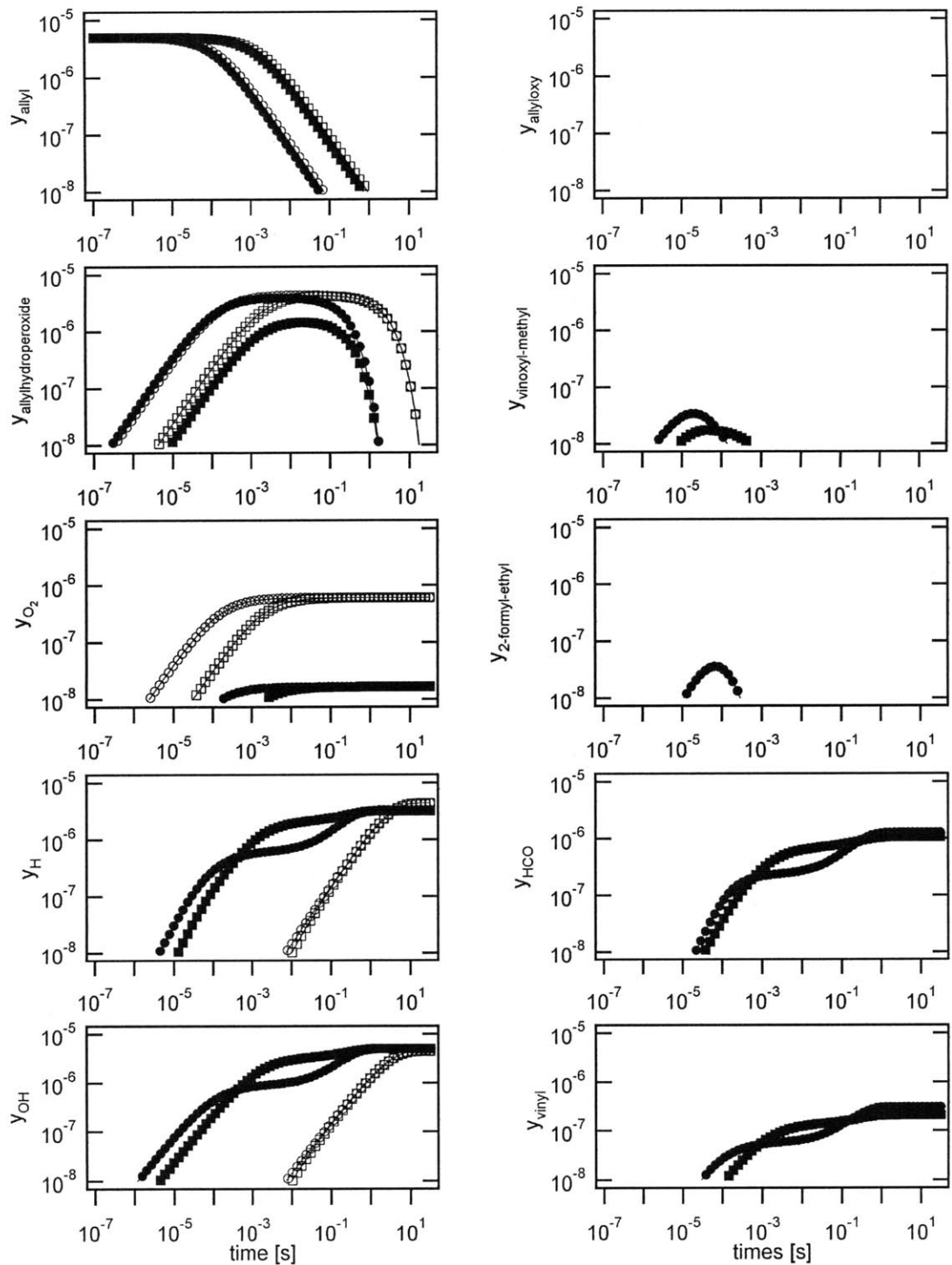


Figure 2-6 – Mole fractions of the major species in the allyl + HO<sub>2</sub> kinetic model.

Because the EXGAS mechanism does not account for chemical activation, all the H and OH molecules must be formed by the thermal decomposition of collisionally stabilized allylhydroperoxide. In the current work, the vast majority of the activated  $C_3H_5OOH^\ddagger$  complex goes directly to allyloxy + OH. As a consequence, the rate of product of H and OH radicals is orders of magnitude faster and larger. Since these two radicals are among the most aggressive in oxidation chemistry, the increased rate and yield predicted by the current work will have a profound impact on larger mechanisms. Furthermore, as noted by the panes on the right-hand side of Figure 2-6, the present work predicts significant mole fractions of both formyl and vinyl radicals, which EXGAS completely omits. As detailed in Chapter 1, the vinyl radical plays an important role in oxidation chemistry, since it helps to determine when a fuel is completely oxidized and when it forms soot precursors.

## 2.5 Conclusion

A theoretical investigation of the kinetics of the allyl + HO<sub>2</sub> bimolecular reaction and subsequent kinetics of allyloxy decomposition have been performed over a wide range of temperatures and pressures relevant for combustion modeling. This study presents for the first time a set of comprehensive pressure-dependent rate coefficients. Rate coefficients were calculated using *ab initio* theory, variable reaction coordinate transition state theory, variational transition state theory, and master equation simulations. The present calculations are in good agreement with available experimental data for the addition reaction. The calculations for the abstraction reaction on the triplet surface are slower than the experimentally determined rates by a factor of 30, but agree with the reverse reaction 20 within a factor of five. Some of this discrepancy may be attributed to minor multireference effects in the transition state, but mostly it is due to the indirect methods used to measure the rate constant. At lower pressures and/or higher temperatures, most of the allyl + HO<sub>2</sub> goes directly to allyloxy + OH via chemical activation. Rate coefficients for allyloxy decomposition are also presented. Allyloxy will decompose to H + acrolein, HCO + ethene, and vinyl + CH<sub>2</sub>O. The prompt formation of OH, and the slower rate of formation of propene + O<sub>2</sub>, suggest that this reaction can promote chain branching significantly more than previous

models suggest.

# Chapter 3

## Frequency Estimation in RMG

### 3.1 Introduction

This chapter presents a new method for estimating the vibrational frequencies for hydrocarbons. This method, which is inspired by infrared spectroscopy, assigns vibrational frequencies to functional groups. The first section of this chapter details the background of the project. The second section describes how the new method works. The final section uses the acetyl + O<sub>2</sub> reaction as a test case.

### 3.2 Background

A detailed description of combustion chemistry composed of elementary reactions can require hundreds of species and thousands of reactions. In order to simplify this process, former group members have developed a tool for automatically generating complex reaction mechanisms, RMG [93]. As detailed in Chapters 1 and 2, rate coefficients for unimolecular reactions, as well as bimolecular reactions that pass through a unimolecular intermediate, can be a function of pressure, particularly under combustion relevant conditions. Thus, in order for RMG to be useful in generating mechanisms for hydrocarbon combustion, it must be able to compute the pressure dependence of rate coefficients. The implementation of pressure dependence in RMG was first accomplished by David M. Matheu for his Ph.D. thesis [65]. This approach combined Quantum-Rice-Ramsperger-Kassel (QRRK) theory

for estimation of the density of states, Inverse Laplace Transform (ILT) for calculating the microcanonical rate coefficients, and the Modified Strong Collision (MSC) assumption to collisional energy transfer, as implemented in the software CHEMDIS [10]. This approach had the benefit of being computationally efficient and numerically robust. However, QRRK/MSC has been criticized for being too simplistic, particularly compared to Rice-Ramsperger-Kassel-Marcus (RRKM) Master Equation (ME) [85, 42, 63] theory. To facilitate the discussion, I will present a brief summary of the master equation and three solution techniques.

### 3.2.1 Formulation of the Master Equation

Begin with the number density of species  $i$  with energy between  $E$  and  $E + dE$ ,  $n_i(E) dE$ . In a thermally activated (i.e. unimolecular) or a chemically activated (i.e. bimolecular) system, the energy-dependent population can undergo the following possibilities: it can gain or lose energy by colliding with other molecules, it can be formed by the association reaction of the reactants, it can decompose back to the reactants, it can isomerize to form other well species, or it can decompose to form bimolecular products. Thus,

$$\begin{aligned} \frac{dn_i(E)}{dt} = & \text{Gain to } n_i(E) \text{ via collisional energy transfer from } n_i(E') \\ & - \text{loss from } n_i(E) \text{ via collisional energy transfer to all other } n_i(E') \\ & + \text{gain to } n_i(E) \text{ via association of reactants } n_R, n_m \\ & - \text{loss from } n_i(E) \text{ via decomposition back to reactants } n_R, n_m \\ & + \text{gain to } n_i(E) \text{ via isomerization from } n_j(E) \\ & - \text{loss from } n_i(E) \text{ via isomerization to } n_j(E) \\ & - \text{loss from } n_i(E) \text{ via decomposition to bimolecular products } p_i \end{aligned}$$

Mathematically, we have

$$\begin{aligned}
\frac{dn_i(E)}{dt} = & \omega \int_0^\infty P_i(E, E') n_i(E') dE' - \omega n_i(E) \\
& + n_R n_m K_{eq} k_{dis}(E) F_i(E) \delta_{Rmi} - k_{dis}(E) n_i(E) \delta_{Rmi} \\
& + \sum_{j \neq i}^{N_{wells}} k_{ij}(E) n_j(E) - \sum_{j \neq i}^{N_{wells}} k_{ji}(E) n_i(E) \\
& - \sum_{P_j}^{N_{prod}} k_{pji}(E) n_i(E)
\end{aligned} \tag{3.1}$$

The corresponding equations for the reactants are:

$$\begin{aligned}
\frac{dn_R}{dt} = \frac{dn_m}{dt} = & \sum_{i=1}^{N_{wells}} \delta_{Rmi} \int_{E_{i0}}^\infty k_{dis}(E) n_i(E) dE \\
& - \sum_{i=1}^{N_{wells}} \delta_{Rmi} \int_{E_{i0}}^\infty K_{eq} k_{dis}(E) F_i(E) n_R n_m dE
\end{aligned} \tag{3.2}$$

The units of the number density  $n_i(E) dE$  are [particle/volume].  $\omega$  is the collision frequency [ $s^{-1}$ ],  $P_i(E, E') dE$  is the probability that a particle with energy  $E'$  will have energy  $E$  after collision [unitless],  $k_{ij}(E)$  is the microcanonical rate constant for the isomerization from well  $j$  to well  $i$  [ $s^{-1}$ ],  $K_{eq}$  is the equilibrium constant between the reactants  $R$  and  $m$  and the  $i^{th}$  well [volume/particle],  $k_{dis}(E)$  is the microcanonical rate constant for the dissociation back to the reactants [ $s^{-1}$ ],  $\rho_i(E)$  is the density of states [ $energy^{-1}$ ],  $Q_i(T)$  is the partition function for the active degrees of freedom [unitless],  $n_R$  and  $n_m$  are the number density of the reactants [particle/volume], and  $k_{pji}(E)$  is the microcanonical rate constant for the dissociation from well  $i$  to the  $j^{th}$  product channel [ $s^{-1}$ ]. The delta function  $\delta_{Rmi}$  is there to ensure that only wells with direct access to the reactants can be formed from or dissociate back to the reactants. In principle, the energy-dependent populations are a series of delta peaks and not a continuous function; in practice, however, at energy levels relevant for our calculations, the spacing between delta functions is so small that the populations can be approximated by a continuous function.

At this point we have  $N_{wells} + 2$  coupled, non-linear integro-differential equations. We

would prefer a system of linear ODEs. To simplify the system of equations, we make two assumptions:

1. Energy is discretized
2.  $n_m$  is constant

The first assumption makes the system of equations numerically tractable; by discretizing the energy, we replace the integrals with summations, which yields  $N_{\text{energy levels}} \times N_{\text{wells}} + 2$  coupled, non-linear ordinary differential equations. The second assumption assumes that one of the reactants is in great excess over the other (e.g. a stable species rather than a radical). This assumption linearizes the system of equations, yielding  $N_{\text{energy levels}} \times N_{\text{wells}} + 1$  coupled linear ODEs. Although currently asymmetric, a choice of a cleverly chosen normalization scheme will yield a symmetric system of equations. Broadly speaking, there are four ways to solve the master equation: (i) direct integration with an ODE solver, (ii) kinetic Monte Carlo (e.g. MultiWell [3]), (iii) eigenvalue decomposition (e.g. VariFlex [47]), and (iv) steady-state approximation (e.g. CHEMDIS [10]). Using an ODE solver may provide the time-dependent populations of the species, but it does not provide a clear rate constant. For minor channels the stochastic methods require a long time to obtain decent sampling statistics. The eigenvalue and steady-state methods, in contrast, offer a closed-form solution for computing the rate coefficients.

### Eigenvalue Decomposition

Before we form the matrix equation, we normalize the variables as follows:

$$y_i(E) \equiv \frac{n_i(E)}{n_R(0) \sqrt{\rho_i(E)} e^{-\beta E}}$$
$$x_R \equiv \frac{n_R}{n_R(0)}$$

Now group like terms:



$$\begin{aligned}
\frac{dy_i(E)}{dt} = & - \left[ \omega + \sum_{j \neq i}^{N_{wells}} k_{ji}(E) + k_{di}(E) \delta_{Ri} + \sum_{p_j}^{N_{prod}} k_{pji}(E) \right] y_i(E) \\
& + \left[ \omega \sum_{E_{i0}}^{E_{i\infty}} P_i(E, E') \frac{\sqrt{\rho_i(E') e^{-\beta E'}}}{\sqrt{\rho_i(E) e^{-\beta E}}} \right] y_i(E') \\
& + \left[ \sum_{j \neq i}^{N_{wells}} k_{ij}(E) \frac{\sqrt{\rho_j(E) e^{-\beta E}}}{\sqrt{\rho_i(E) e^{-\beta E}}} \right] y_j(E) \\
& + \left[ K_{eq} k_{di}(E) \frac{\sqrt{\rho_i(E) e^{-\beta E}}}{Q_i(T)} n_m \delta_{ir} \right] x_R
\end{aligned}$$

$$\begin{aligned}
\frac{dx_R}{dt} = & \left[ \sum_{i=1}^{N_{wells}} \delta_{Ri} \sum_{E_{i0}}^{E_{i\infty}} k_{di}(E) \sqrt{\rho_i(E) e^{-\beta E}} \right] y_i(E) \\
& - \left[ \sum_{i=1}^{N_{wells}} \delta_{Ri} \sum_{E_{i0}}^{E_{i\infty}} K_{eq} k_{di}(E) \frac{\rho_i(E) e^{-\beta E}}{Q_i(T)} n_m \right] x_R
\end{aligned}$$

Regarding the equation for  $dy_i(E)dt$ , the first line on the right-hand side is the loss term, which contains the loss in population due to collision, isomerization, and dissociation; it forms the diagonal elements of the transition matrix. The second line on the right-hand side couples  $y_i(E)$  to all the other energy levels of the  $i^{th}$  (i.e. the same) well,  $y_i(E')$ . The third line on the right-hand side couples  $y_i(E)$  to the other wells, and the final line on the right-hand side couples  $y_i(E)$  to the radical population  $x_R$ .

The energy-dependent populations and the reactant species are grouped into a single vector:

$$\mathbf{n} = \left[ y_1(E_{10}), y_1(E_{11}), \dots, y_1(E_{1\infty}), \dots, y_i(E_{i0}), y_i(E_{i1}), \dots, y_i(E_{i\infty}), \left( \frac{n_M}{Q_{Rm} \Delta E} \right)^{1/2} x_R \right]$$

Thus, the  $N + 1$  ODEs become a single matrix equation:

$$\frac{d\mathbf{n}}{dt} = \mathbf{M}\mathbf{n}$$

where  $\mathbf{M}$  is the real, symmetric transition matrix. The matrix is block diagonal. The principle diagonal is the loss term. The large blocks are the coupling within each well of all the energy bins, due to collisional energy transfer. The off diagonal elements are the coupling between wells at the same energy level. The very last row and column couple the reactant species with the wells.

Since  $\mathbf{M}$  is real and symmetric, it can be factored into  $\mathbf{M} = \mathbf{Q}\Lambda\mathbf{Q}^T$ , where  $\mathbf{Q}$  is the matrix of orthonormal eigenvectors, and  $\Lambda$  is the diagonal matrix of eigenvalues. The solution to the matrix equation is:

$$\begin{aligned}\mathbf{n}(t) &= \mathbf{Q}e^{\Lambda t}\mathbf{Q}^T\mathbf{n}_0 \\ &= \sum_{j=1}^{N+1} e^{\lambda_j t} \mathbf{c}_j\end{aligned}$$

where  $\mathbf{n}_0$  is the vector of initial conditions,  $\mathbf{q}_j$  is the  $j^{\text{th}}$  column vector of the matrix  $\mathbf{Q}$ , and  $\mathbf{c}_j \equiv \mathbf{q}_j\mathbf{q}_j^T\mathbf{n}_0$ . Since  $\mathbf{M}$  is real and symmetric, it follows that all its eigenvalues are real. A physical constraint on the system is that all the eigenvalues must be less than or equal to zero. Positive eigenvalues would be unphysical, since the population system would grow exponentially with time. The zero eigenvalue, if it exists, corresponds to the steady-state population distribution.

Although  $N$  eigenvalues is quite large (order thousands, possibly tens of thousands), only a few eigenvalues are useful. Following Widom [102, 103, 104, 4], most eigenvalues correspond to the relaxation of internal degrees of freedom, with the remaining eigenvalues corresponding to the rearrangement of bonds. Let  $N_{chem} \equiv N_{species} - 1 = N_{wells}$ . If we assume that the relaxation of internal degrees of freedom is significantly faster than the chemical reaction, then the  $N_{chem}$  eigenvalues closest to zero (i.e. smallest order of magnitude) correspond to the chemical reactions. The remaining  $N - N_{chem}$  eigenvalues are

associated with the rapid redistribution of energy and are discarded. Once the key eigenvalues have been determined, the time-dependent solution for the  $i^{th}$  well at its  $k^{th}$  energy level is given by:

$$y_i(E_{ik}, t) = \sum_{j=1}^{N_{chem}+1} e^{\lambda_j t} c_{jik}$$

where the scalar  $c_{jik}$  is the  $ik^{th}$  component of  $\mathbf{c}_j$ , which corresponds to the  $j^{th}$  eigenvector coefficient of the  $i^{th}$  species in the  $k^{th}$  energy level.

The time-dependent (and energy-independent) population of the entire well is obtained by summing over the energy-dependent bins:

$$\begin{aligned} Y_i(t) &= \sum_{k=1}^{N_i} y_i(E_{ik}, t) \Delta E \\ &= \sum_{k=1}^{N_i} \sum_{j=1}^{N_{chem}+1} e^{\lambda_j t} c_{jik} \Delta E \\ &= \sum_{j=1}^{N_{chem}+1} \underbrace{\sum_{k=1}^{N_i} c_{jik} \Delta E}_{a_{ij}} e^{\lambda_j t} \\ &= \sum_{j=1}^{N_{chem}+1} a_{ij} e^{\lambda_j t} \end{aligned}$$

Next, the product channels are lumped together into a single channel:  $X_P = \sum_{i=1}^{N_{prod}} X_{Pi}$ . It is assumed that the total product channel population may be written as a sum of exponentials, similar to the reactant and well species:  $X_P = \sum_{j=1}^{N_{chem}+1} a_{Pj} e^{\lambda_j t}$ . From the mass balance, the infinite-sink assumption, and the orthonormality of the eigenvectors, it follows that  $a_{P1} = 1$ ,  $a_{R1} = 0$ ,  $a_{j1} = 0$ , and  $a_{Pj} = -a_{Rj} - a_{ij}$  for  $j > 1$ .

The  $a_{ij}$ ,  $a_{Rj}$ , and  $a_{Pj}$  coefficients are grouped together into a matrix  $\mathbf{A}$ .  $\mathbf{A}$  is square and non-singular, with  $N_{wells} + 2$  rows corresponding to the coefficients for the reactant, intermediates and product channels, and  $N_{chem} + 1$  columns corresponding to the exponential decays. The total population vector may be written as:

$$\mathbf{X} = \mathbf{A}e^{\Lambda t}$$

Since  $\mathbf{A}$  is square and non-singular, it is invertible:  $\mathbf{B} = \mathbf{A}^{-1}$ . It follows then that  $e^{\Lambda t} = \mathbf{B}\mathbf{X}$ , and

$$e^{\lambda_j t} = \sum_{l=1}^{N_{wells}+2} b_{jl} X_l$$

The final task is to calculate the phenomenological rate constant. Since  $Y_i(t) = \sum_{j=1}^{N_{chem}+1} a_{ij} e^{\lambda_j t}$ , it follows that the rate of change is:

$$\begin{aligned} \frac{dY_i}{dt} &= \sum_{j=1}^{N_{chem}+1} \lambda_j a_{ij} e^{\lambda_j t} \\ &= \sum_{j=1}^{N_{chem}+1} \lambda_j a_{ij} \sum_{l=1}^{N_{wells}+2} b_{jl} X_l \\ &= \sum_{l=1}^{N_{wells}+2} \sum_{j=1}^{N_{chem}+1} \lambda_j a_{ij} b_{jl} X_l \\ &= \sum_{l \neq i}^{N_{wells}+2} \underbrace{\sum_{j=1}^{N_{chem}+1} \lambda_j a_{ij} b_{jl} X_l}_{k_{il}(T,P)} - \underbrace{\sum_{j=1}^{N_{chem}+1} \lambda_j a_{ij} b_{ji} X_i}_{k_{Ti}(T,P)} \\ &= \sum_{l \neq i}^{N_{wells}+2} k_{il}(T,P) X_l - k_{Ti}(T,P) X_i \end{aligned}$$

Thus,  $k_{il}(T,P)$  is the phenomenological (i.e. temperature and pressure dependent) rate constant for the isomerization from well  $l$  to well  $i$ , and  $k_{Ti}(T,P)$  is the total rate of removal for well  $i$ . The phenomenological rate constants for the reactants and products can be obtained similarly.

## Difficulties with Eigenvalue Decomposition

Two issues prevented an automatic implementation of eigenvalue decomposition within RMG: one complication at low temperatures, and one complication at high temperatures. First, it is quite common for the eigenvalue decomposition to return a positive eigenvalue at low temperatures [71, 72], even for small systems, presumably due to stiffness. For the vinyl + alkenes and allyl + HO<sub>2</sub> systems, positive eigenvalues always occurred below 400 K. While these low temperatures may not pose such a problem for combustion, they are critical for atmospheric chemistry, as well as modeling room temperature experiments. One solution to this problem is to perform the eigenvalue decomposition using quadruple precision arithmetic. I tested this solution on the vinyl + ethene reaction, and the results were discouraging. For this small, three-well system, each eigenvalue step took several hours. For the six-wells system in vinyl + propene, each step took nearly a day. Since we would like for RMG to (i) be able to handle arbitrarily large systems, and (ii) return a matrix of temperature- and pressure-dependent rate constants in seconds if not minutes, it was clear that eigenvalue decomposition in quadruple precision was not a feasible approach.

The second problem for eigenvalue decomposition occurs at high temperatures. The difficulty with high-temperature chemistry is more subtle, since the computer code has no difficulty in obtaining all negative eigenvalues. The problem is that one or more of the chemically significant eigenvalues crosses into the continuum. The physical interpretation of this phenomena is that two or more of the well species equilibrate on a time scale faster than the kinetics of the chemical reactions. In other words, the assumption that the relaxation of internal energy is significantly faster than this isomerization reaction is no longer valid. When performing calculations “by hand” – as was the case in Chapters 1 and 2 – This problem can be overcome. First, I determined the temperature at which the wells equilibrate (i.e. the temperature at which the eigenvalue crossed into the continuum). Next I determined which two wells equilibrated and combined their density of states into a single new admixture. The simulation was rerun, now with one fewer chemically significant eigenvalues. Currently there is no simple, robust method for handling this situation automatically. Although it is possible to analyze the eigenvalues and determine when the

number of chemically significant eigenvalues has been reduced by one, it is not a straightforward task to determine which wells to lump together. A general strategy would be to pair wells with the lowest isomerization barriers, but this strategy needs further development before it can be implemented automatically. An alternate strategy, more easily implemented, is to continue with the original potential energy surface but include one fewer eigenpairs in the solution. However, this method frequently failed, often returning negative rate coefficients for minor channels, and therefore cannot be recommended as robust enough.

The combination of these two problems – positive eigenvalues at low temperatures, equilibration of wells at high temperatures – convinced us that time-dependent eigenvalue decomposition is not fast and robust enough to meet the needs of RMG. Simply put, this method cannot be treated like a black box. Each chemical system requires both coaxing and chemical intuition.

### **Modified Strong Collision**

The Modified Strong Collision model makes three additional assumptions:

3. The  $d/dt$  is equal to zero
4.  $n_R$  is constant
5. The collisional energy transfer,  $\omega \int_0^\infty P_i(E, E') n_i(E') dE'$ , is replaced by a modified strong collision,  $\omega\beta$ .

The third assumption assumes that the lifetime of the vibrationally excited intermediates is significantly less than the phenomenologically relevant time scale of the reaction. This assumption converts the system of ODEs into a single matrix equation of rank  $N_{\text{energy levels}} \times N_{\text{wells}} + 1$ . The fourth assumption reduces the order of the rank by one, and more importantly it ensures that the matrix equation has a non-zero solution. Conceptually, it suggests that the reaction could be modeled as a perfectly stirred reactor with a constant inlet stream, rather than as a batch reactor. With these two additional assumptions, we now have a steady-state master equation. The final assumption is the most drastic. It assumes that a certain fraction,  $\beta$ , of all collisions will quench the vibrationally excited adducts.

This assumption decouples all the energy levels for a given well, thereby reducing the large matrix equation into  $N_{\text{energy}}$  levels individual matrix equations of rank  $N_{\text{wells}}$ . With these three additional assumptions, the individual equations simply to:

$$S_i(E) = \left[ \beta\omega + \sum_{j \neq i}^{N_{\text{wells}}} k_{ji}(E) + \delta_{Rmi} k_{dis}(E) + \sum_{p_j}^{N_{\text{prod}}} k_{pji}(E) \right] n_i(E) - \sum_{j \neq i}^{N_{\text{wells}}} k_{ij}(E) n_j(E) \quad (3.3)$$

where  $S_i(E) \equiv K_{eq} k_{dis}(E) n_{Rn_m} \delta_{Rmi} \frac{\rho_i(E) e^{-\beta E}}{Q_i(T)}$  is the source term, which is the product of the association rate,  $K_{eq} k_{dis}(E) n_{Rn_m} \delta_{Rmi}$ , and the equilibrium energy distribution  $\frac{\rho_i(E) e^{-\beta E}}{Q_i(T)}$ .

The terms in square brackets on the right-hand side are the loss channels; these terms appear in the diagonal of the matrix. The other term on the right-hand side is the gain to a well from the other wells; these rates appear in the off-diagonal positions. To calculate the phenomenological rate constants, Equation (3.3) is solved for each energy level. The phenomenological rate constant for a particular channel is the dot product of the steady-state population vector and the vector containing the microcanonical rate constant for that channel.

### Steady-State Master Equation

As mentioned at the beginning, the modified strong collision approach has been criticized frequently for being too simplistic: Replacing the complex, stepwise activation and deactivation energy transfer function with a single deactivation step is not physically realistic. If the full-blown time-dependent eigenvalue decomposition is not robust enough, and if the robust modified strong collision model is too simplistic, a suitable intermediate would be to relax the fifth assumption. The result would be a steady-state master equation.

$$\begin{aligned}
S(E) = & -\omega \sum_{E'=E_{i0}}^{E_{i,max}} P_i(E, E') n_i(E') \Delta E \\
& + \left[ \omega + \sum_{j \neq i}^{N_{wells}} k_{ji}(E) + k_{di}(E) \delta_{R,m,i} + \sum_p^{N_{prod}} k_{pi}(E) \right] n_i(E) \\
& - \sum_{j \neq i}^{N_{wells}} k_{ij}(E) n_j(E)
\end{aligned}$$

where the left-hand side  $S(E)$  is the same source term from Equation (3.3). I began to develop a new code for RMG that would replace the modified strong collision subroutine with a steady-state master equation solver. The beta version of the code was named MESS (Master Equation at Steady State). In the process, however, I realized that a potentially significant source of error was how RMG computed the density of states. Thus, I postponed development on MESS until I could develop a more accurate method for estimating the parameters used to compute the density of states. This new method is described in the remainder of this chapter. By the time I finished the new code for density of states, N.J.B. Green published a paper on steady-state master equation techniques [25], and Joshua W. Allen joined our group. He implemented a modified version of Green's Reservoir State method, and so I abandoned my previous efforts on MESS and left the project in J.W. Allen's more capable hands. Together we worked on an improved system for pressure dependent rate calculations in RMG. I focused on improving RMG's ability to compute the density of states, and J.W. Allen focused on the implementation of a steady-state master equation solver. This collaboration culminated in a paper comparing the improved methods with the QRRK/MSC approach [REF]. To test our improvements, we focused on the reaction of acetyl + molecular oxygen. At the conclusion of this chapter, I summarize our results on the improved density of states calculations for acetyl + O<sub>2</sub>.



### 3.3 Method for Estimating Density of States

To summarize everything up to this point: Our objective is to calculate pressure dependent rate constants for chemically-activated reactions. To calculate these rate constants, we must solve the master equation. In order to solve this system of equations, we need the micro-canonical rate constants for the association, isomerization, and dissociation channels. These rate constants, in turn, require the rovibrational density of states. The rovibrational degrees of freedom are those degrees of freedom in which the energy of the excited species can be randomized. Normally, the parameters used to compute the density of states would be determined from a 3D model of the molecule. Unfortunately, RMG does not have access to 3D structure models at this time. The current version of RMG represents each molecule solely by its connectivity. The connectivity diagram for each species is used to calculate the heat capacity at seven temperatures (300, 400, 500, 600, 800, 1000, 1500 K), based upon the group additivity theories developed by Benson [6]. Thus, we need some other method for estimating these physical parameters. In RMG, the rovibrational degrees of freedom are taken to be the harmonic-oscillator vibrational frequencies, hindered internal rotors, and a one-dimensional external rotation (i.e. the K-rotor for a symmetric top approximation). Furthermore, it is assumed that the degrees of freedom are independent. RMG assumes that each molecule may be approximated as a symmetric top; the density of states for the one-dimensional K-rotor is:

$$\rho_r(E) = \frac{1}{\sigma} \left( \frac{1}{|A - \bar{B}| E} \right)^{1/2} \quad (3.4)$$

where  $\sigma$  is the rotational symmetry number for this rotor,  $A$  is the unique rotational constant, and  $\bar{B}$  is the average of the two most similar rotational constants. The density of states for hindered internal rotors is given by the Laplace transform of the hindered-rotor partition function. RMG assumes a semi-classical approximation for the hindered-rotor partition function:

$$\begin{aligned}
Q_{\text{HR}_{\text{semi}}} &= Q_{\text{HR}_{\text{classical}}} \frac{Q_{\text{HO}_{\text{quantum}}}}{Q_{\text{HO}_{\text{classical}}}} \\
&= \left( \frac{V_0 \pi}{2\sigma^2 B_r} \right)^{1/2} u^{1/2} e^{-u} I_0(u) \frac{e^{-\alpha u}}{1 - e^{-2\alpha u}} 2\alpha
\end{aligned} \tag{3.5}$$

where  $B_r$  is the rotational constant corresponding to the reduced moment of inertia,  $V_0$  is the rotational barrier height assuming a single cosine potential,  $\sigma$  is the symmetry number of the internal rotor,  $\nu$  is the normal mode frequency corresponding to the torsion,  $I_0$  is the modified Bessel function of the first kind, and  $u \equiv V_0/2k_B T$ , and  $\alpha \equiv \nu/V_0$ . The density of states corresponding to the classical hindered rotor partition function was described by Knyazev [49].

$$\rho_{\text{HR}_{\text{classical}}}(E) = \begin{cases} \frac{2\mathbf{K}(\sqrt{E/V_0})}{\pi\sigma\sqrt{B_r V_0}} & \text{for } E < V_0 \\ \frac{2\mathbf{K}(\sqrt{V_0/E})}{\pi\sigma\sqrt{B_r E}} & \text{for } E > V_0 \end{cases} \tag{3.6}$$

where  $\mathbf{K}$  is the complete elliptical integral of the first kind. No analytical expression exists for the density of states for the semi-classical partition function, since there is no analytical inverse Laplace transform for the quantum harmonic oscillator partition function. To compute the density of states for the semi-classical partition function one must perform the inverse Laplace transform numerically (e.g. via steepest descents, see Forst [16]). Alternatively, if we replace the exponential term in the denominator in the quantum harmonic oscillator partition function with a Taylor series expansion, truncated after the second term, we can reduce the ratio of harmonic oscillator partition functions to a simple zero-point energy offset:

$$\begin{aligned}
\frac{Q_{\text{HO}_{\text{quantum}}}}{Q_{\text{HO}_{\text{classical}}}} &= \frac{\frac{e^{-h\nu/2k_B T}}{1 - e^{-h\nu/k_B T}}}{\frac{k_B T}{h\nu}} \\
&= \frac{e^{-h\nu/2k_B T}}{1 - \sum_{j=0}^{\infty} \frac{1}{j!} \left(\frac{-h\nu}{k_B T}\right)^j} \\
&\approx \frac{k_B T}{h\nu} \\
&\approx e^{-h\nu/2k_B T}
\end{aligned}$$

This approximation works well for lower frequencies and higher temperatures, which is precisely when hindered rotors are significant. The inclusion of this term simply shifts Equation (3.6) by the zero-point energy:

$$\rho_{\text{HR}_{\text{semi}}}(E) = \begin{cases} \frac{2\mathbf{K}\left(\sqrt{\tilde{E}/V_0}\right)}{\pi\sigma\sqrt{B_r V_0}} & \text{for } E < \max(V_0, h\nu/2) \\ \frac{2\mathbf{K}\left(\sqrt{V_0/\tilde{E}}\right)}{\pi\sigma\sqrt{B_r \tilde{E}}} & \text{otherwise} \end{cases} \quad (3.7)$$

where  $\tilde{E} = E - h\nu/2$ . Equation (3.7) is calculated for each hindered rotor. The density states for multiple hindered internal rotors is calculated by repeated application of the convolution integral. Similarly, the density of states for internal rotors and active external rotation is calculated by convoluting the density of states for the active K-rotor with the density of states for all the hindered rotors, [16]. Finally, following the method of Astholz [2, 21], the Beyer-Swinehart algorithm [7] is initialized with the K-rotor/hindered-rotor density of states, which convolutes this density of states with the vibrational modes. The result is the complete rovibrational density of states,  $\rho(E)$ .

As mentioned in the introduction, RMG cannot currently generate 3D structures, and therefore is required to estimate vibrational frequencies and hindered rotor parameters from the heat capacity. The heat capacity may be separated into contributions from external

translation, external rotation, and the internal rovibrational degrees of freedom:

$$C_V^{\text{total}} = C_V^{\text{translation}} + C_V^{\text{rotation}} + C_V^{\text{rovibration}}$$

In this presentation, the K-rotor is included in the external rotation. The vibrational frequencies and hindered rotor parameters can be calculated by fitting a function to the rovibrational contribution to the heat capacity. In most cases, however, the number of vibrational modes exceeds number of known values of the heat capacity as a function of temperature, and therefore these frequencies cannot be determined uniquely. Two methods for approximating the vibrational frequencies are described below.

### 3.3.1 The Three-Frequency Model

The three frequency model was proposed by Bozzelli, Chang, and Dean [10]. This approach assumes that the molecule can be described by the HO model. The heat capacity as a function of HO frequencies is given by the following formula from statistical mechanics:

$$\frac{C_V^{\text{HO}}(T; \nu_i)}{R} = e^{\nu_i/k_B T} \left( \frac{\nu_i/k_B T}{e^{\nu_i/k_B T} - 1} \right)^2 \quad (3.8)$$

where  $\nu_i$  is the vibrational frequency for the  $i^{\text{th}}$  mode. Bozzelli et al. fit three vibrational frequencies to the heat capacity at seven temperatures (300, 400, 500, 600, 800, 1000, 1500 K), using the following formula:

$$C_V^{\text{rovibration}}(T) = \sum_{i=1}^3 g_i C_V^{\text{HO}}(T; \nu_i) \quad (3.9)$$

$$g_3 = s - g_1 - g_2$$

where  $s$  is the number of vibrational modes (e.g.  $3N - 6$  for a nonlinear molecular with no internal rotors). In the original implementation, the three degeneracies  $g_i$  were allowed

to be non-integers. Later implementations of this approach forced the degeneracies to be integers, so  $\rho(E)$  could be computed efficiently using the Beyer-Swinehart algorithm, and that is what was previously implemented in RMG [65]. Thus, five parameters are fit to the heat capacity data: three frequencies and two degeneracies. This method is simple and computationally efficient. There are two problems with this approach. First, the resulting pseudo-frequencies may not be physically realistic. Second, it assumes that the heat capacity necessarily increases monotonically with temperature. For molecules with hindered internal rotors, the heat capacity may actually have a local maximum with respect to temperature.

### 3.3.2 The Functional-Group Frequency Model

An alternative to the three-frequency model, inspired by IR spectroscopy, is to assign frequencies to functional groups. For each functional group, the number of characteristic frequencies is limited to  $3N_{atoms} - N_{rotors} - 6$ . For example, a heavy atom, R, attached to a methyl group contains 5 atoms and one single bond between heavy atoms and has 9 characteristic frequencies: 3 C-H stretches, 1 R-C stretch, 2 R-C-H bending modes, 2 R-C-H rocking mode, and 1 umbrella mode; however, to avoid the possibility of double counting, the R-C stretch mode is omitted from the frequency prediction. The frequency group method also allots one internal rotor. To see why the R-C mode must be removed, consider ethane. Ethane has 18 frequencies, including 1 C-C stretch and 1 torsional mode. If we include the R-C stretch in the methyl group count, then the result would correctly predict 18 frequencies, but it would incorrectly predict two C-C stretches, and therefore would not allow any torsional modes. Instead, the new way correctly predicts 16 of the 18 frequencies, and the C-C stretch and hindered rotor are then fit from the heat capacity. Each vibrational mode is associated with a range of frequencies, and RMG automatically selects the appropriate number of frequencies, taking them to be evenly spaced between the two bounds. Thus, for a molecule with two methyl groups, RMG would assume 6 C-H stretching frequencies that are evenly spaced between 2750 - 2850  $\text{cm}^{-1}$ . A list of the functional groups, the corresponding range of frequencies, and the number of frequencies per group

are provided in Table 3.4. By summing over the functional groups, the model predicts the majority of the HO vibrational frequencies. The heat capacity for the remaining degrees of freedom (e.g. vibrational frequencies not explicitly accounted for, as well as hindered rotors) is obtained by subtracting the heat capacity of the functional group frequencies from the rovibrational heat capacity:

$$C_V^{\text{remaining degrees of freedom}}(T) = C_V^{\text{rovibration}}(T) - \sum_{i=1}^{N_{\text{functional group frequencies}}} C_V^{\text{HO}}(T; \nu_i) \quad (3.10)$$

The remaining vibrational frequencies and the parameters for hindered internal rotors are determined from this heat capacity data. Unlike the three frequency model, this method includes a function for hindered internal rotors and therefore can accommodate heat capacities with a local maximum.

$$C_V^{\text{remaining degrees of freedom}} = \sum_{i=1}^{N_{\text{remaining}}} C_V^{\text{HO}}(T; \nu_i) + \sum_{j=1}^{N_{\text{rotors}}} C_V^{\text{HR}}(T; V_{0,j}, \nu_j)$$

where  $N_{\text{remaining}} \equiv 3N - 6 - N_{\text{rotors}} - N_{\text{functional group frequencies}}$ . The heat capacity of a hindered internal rotor is derived from the semi-classical model for the hindered rotor partition function, Equation (3.5). The heat capacity for this partition function is:

$$\begin{aligned} \frac{C_V^{\text{HR}}(T; V_0, \nu)}{R} &= \frac{d}{dT} \left( T^2 \frac{d \ln Q_{\text{HR}}}{dT} \right) \\ &= u^2 \frac{d^2 \ln Q_{\text{HR}}}{du^2} \\ &= -\frac{1}{2} + u \left[ u - \frac{I_1(u)}{I_0(u)} - u \left( \frac{I_1(u)}{I_0(u)} \right)^2 \right] + \left( \frac{2u\alpha e^{-\alpha u}}{1 - e^{-2\alpha u}} \right)^2 \\ &= -\frac{1}{2} + \frac{V_0}{2k_B T} \left[ \frac{V_0}{2k_B T} - \frac{I_1\left(\frac{V_0}{2k_B T}\right)}{I_0\left(\frac{V_0}{2k_B T}\right)} - \frac{V_0}{2k_B T} \left( \frac{I_1\left(\frac{V_0}{2k_B T}\right)}{I_0\left(\frac{V_0}{2k_B T}\right)} \right)^2 \right] + \left( \frac{\frac{\nu}{k_B T} e^{-\frac{\nu}{2k_B T}}}{1 - e^{-\frac{\nu}{k_B T}}} \right)^2 \end{aligned} \quad (3.11)$$

Some rotor parameters, such as the reduced moment of inertia and the symmetry number, are multiplicative constants of the partition function, Equation (3.5), and corresponding density of state, Equation (3.6). Consequently, these parameters do not appear in the heat capacity formulation and thus cannot be determined from the heat capacity data. Fortunately, this problem is not critical. Since RMG currently uses the Inverse Laplace Transform method to compute the microcanonical rate coefficients, these multiplicative constants will cancel in the final rate formulation. Similarly, in the detailed balance equation for collisional energy transfer, the ratio of density of state to partition function ensures that these parameters will cancel. The one significant equation for which these parameters will not cancel is the detailed balance equation for isomerization between two isomers:  $k_{ij}\rho_j = k_{ji}\rho_i$ . In these instances, the rate coefficient for the reverse direction will be off by a factor equal to the ratio of multiplicative prefactors. In most instances, the rotational parameters will be similar, and thus the error will be small. For ring closing reactions, however, this error may be larger. Unfortunately, until RMG is able to estimate 3D geometries, there is no solution to this problem.

Although the functional group method will estimate most of the frequencies, it may be the case that not all of the remaining parameters can be determined uniquely from the heat capacity data. For example, if there are more than six unknown parameters, then some of the rigid-rotor harmonic-oscillator frequencies or the hindered rotors (or in some cases both) may be lumped into a single frequency or hindered rotor, respectively, so that no more than six parameters are fitted:

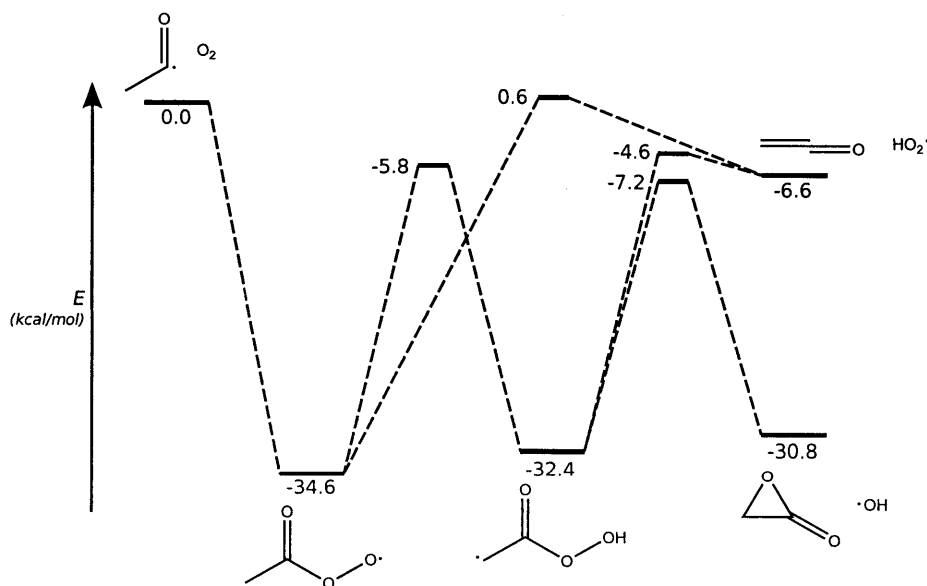
$$\sum_{i=1}^N C_V^{\text{HO}}(T; \nu_i) \rightarrow N C_V^{\text{HO}}(T; \nu)$$

$$\sum_{j=1}^N C_V^{\text{HR}}(T; V_{0,j}, \nu_j) \rightarrow N C_V^{\text{HR}}(T; V_0, \nu)$$

Depending upon the exact number of unknown frequencies and rotors, the code will call 26 possible fitting subroutines. These 26 cases, as well as the fitting functions, are described in Table 3.5. In order to make the resulting parameters as realistic as possible,

the fitted parameters are given physically meaningful constraints: the harmonic oscillator frequencies are bound between 180 and 4000  $\text{cm}^{-1}$ , the hindered rotor torsional frequencies are bound between 40 and 600  $\text{cm}^{-1}$ , and the hindered rotor barrier heights are bound between 10 and 10000  $\text{cm}^{-1}$ . The FORTRAN 90 code DQED [26, 9] was used for the bounded, constrained, non-linear least-squares fitting procedure. To improve the speed and accuracy of the fitting procedure, I supplied DQED with analytical first derivatives for the Jacobian matrix.

### 3.4 Case Study: The Acetyl + Oxygen System



**Figure 3-1** – The potential energy surface for the acetyl oxidation network. Energies are listed in kcal/mol.

As mentioned in the introduction, I collaborated with J.W. Allen on a project to improve RMG's ability to compute pressure-dependent rate coefficients. We used the reaction of acetyl radical with molecular oxygen as a test case. This system is important to atmospheric chemistry as a step in the conversion of acetaldehyde to peroxyacetyl nitrate (PAN), the latter of which is a secondary air pollutant [88]. The potential energy surface for this reaction was computed originally by Lee, Chen, and Bozzelli [53]. The values in Figure



3-1 are updated results, described below.

Michael, Keil, and Klemm demonstrated that the acetyl radical is a major product of the reaction of acetaldehyde with OH radical, which preferentially abstracts the weakly-bonded aldehydic hydrogen. They also observed pressure-dependent regeneration of OH radical when acetyl radical is reacted with oxygen, ranging from nearly complete regeneration at low pressures to minimal regeneration at high pressures [69]. Later experimental efforts generally agree on the relevant pressure range being about 0.001 to 1 bar at 300 K [100, 8, 33, 96, 51].

On the theoretical side, this system was previously studied by Lee, Chen, and Bozzelli using a three-frequency model to estimate the density of states and the modified strong collision method to estimate the phenomenological rate coefficients. Their calculations significantly underpredicted the regeneration of the OH radical [53]. More recently Maranzana, Barker, and Tonachini studied the system using quantum chemistry calculated modes as input to the density of states and the MultiWell stochastic master equation solver. They allowed the exponential down parameters to vary so as to match the experimental data, and thus were able to match the regeneration of OH [62].

The potential energy surface developed by Bozzelli and coworkers has some serious flaws. Specifically, they predicted that the dominant bimolecular product channel was a biradical + OH. The existence of this biradical is highly dubious. I was able to find a stable geometry for the triplet species, but the zero-point corrected electronic energy for this species is 46 kcal/mol above hydroperoxyl-vinoyl, whereas the species on their PES is 28 kcal/mol above the same species. Similarly, I was able to find a minimum for the geometry optimization for the singlet, but only if I forced the symmetry to a C<sub>2</sub> point group, and even then it always had at least one negative frequency, which suggests that it is not a stable species.

To correct for these errors, I recomputed the potential energy surface, using methods similar to those discussed in Chapters 2 and 4. All DFT calculations were done using Gaussian03[17]. All MP2 and QCISD(T) calculations were done using MOLPRO[101]. For each species in the library, the  $\sim 3^n$  possible conformers – where  $n$  is the number of torsional modes – were calculated using the CBS-QB3 method. The lowest energy con-

former was selected, and this geometry was re-optimized using the B3LYP functional with the MG3S basis set [107]. The torsional modes for each species were treated as internal rotors. The barriers for internal rotation were calculated by a relaxed scan at the B3LYP/6-31+G(d,p) level. The resulting potential was fit to a Fourier series. A rigid-rotor harmonic oscillator model was assumed for all remaining degrees of freedom. In order to reduce the ambiguity regarding low-frequency vibrations and the corresponding torsional modes, the projection of the B3LYP/6-311++G(d,p) force-constant matrix was removed along the vectors corresponding to the torsional modes. This matrix was then diagonalized, which separated the rigid rotor harmonic oscillator frequencies from the torsional modes[91]. For all hindered rotors, it is assumed that the torsional modes can be separated and approximated by a one-dimensional rotation, which is fit to a by the Fourier series. A Hamiltonian is formed from this potential, and the corresponding 1D Schrödinger equation is solved for the energy levels,  $\epsilon_j$ . The partition function is the calculated by summing over the energy levels,  $Q = \sum_j \exp[-\epsilon_j/k_B T]$ , and the enthalpy, entropy, and heat capacity are computed accordingly. The effective moment of inertia for each rotor was  $I^{(2,3)}$ , evaluated at the equilibrium geometry. For internal rotors with a barrier below 0.5 kcal/mol, the rotor was treated as a free rotor.

The DFT geometries were used for restricted RQCISD(T)/cc-pVTZ and RQCISD(T)/cc-pVQZ energies. To avoid spin contamination, all calculations were spin restricted. The RQCISD(T) complete basis set limit was extrapolated from the triple and quadruple zeta basis set calculations assuming an inverse power law[64, 14]:

$$E_{\text{QCISD(T)/CBS}} = E_{\text{QCISD(T)/cc-pVQZ}} + \left( E_{\text{QCISD(T)/cc-pVQZ}} - E_{\text{QCISD(T)/cc-pVTZ}} \right) \frac{4^4}{5^4 - 4^4} \quad (2.1)$$

The updated PES is shown in 3-1. Based upon these results, I recomputed the high-pressure limit for the rate coefficients in Variflex. These results are provided in Table 3.1.

**Table 3.1** – Calculated high-pressure limit rate coefficients for acetyl + O<sub>2</sub>.

Reaction		<i>A</i>	<i>n</i>	<i>E<sub>a</sub></i>
acetylperoxy	→ hydroperoxyl-vinoxy	2.3×10 <sup>9</sup>	0.75	23.2
acetylperoxy	→ ketene + HO <sub>2</sub>	2.6×10 <sup>9</sup>	1.2	34.1
hydroperoxyl-vinoxy	→ ketene + HO <sub>2</sub>	5.3×10 <sup>16</sup>	-1.0	29.5
hydroperoxyl-vinoxy	→ lactone + OH	1.9×10 <sup>17</sup>	-1.1	27.2

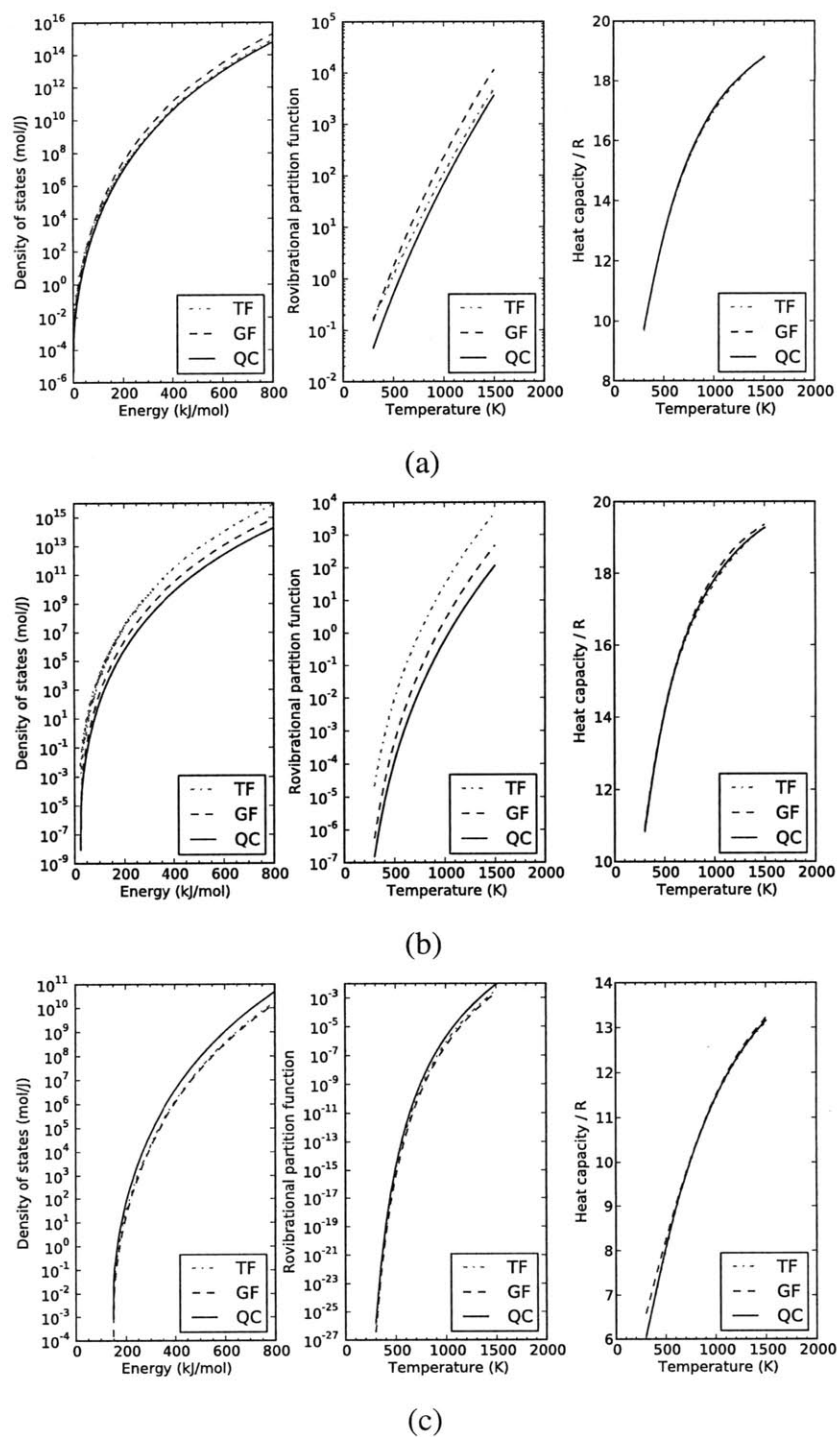
As for the initial association reaction, we decided to use the high-pressure limit provided by Bozzelli and coworkers. Hou and coworkers claimed to have found a transition state for this reaction [33]. However, this result is suspect. First, depending upon which method they chose – MP2, CCSD, G3MP2, CASPT2 – the barrier height varied between +13 kcal/mol and -1 kcal/mol, relative to the reactants. The location of the saddle point had the C–O bond distance of 2.5 Å. At these bond lengths, single reference methods will have considerable uncertainty. Thus, the CASPT2(7,7) energies are the most realistic. More importantly, at these distances the modes between the two reacting moieties will be highly anharmonic, and a rigid-rotor harmonic oscillator model should not be used for the transition state. Using DFT, I was able to locate a saddle point for this reaction, but there were four vibrational modes with frequencies less than 20 cm<sup>-1</sup>. The proper way to treat this entrance channel would be to use variable reaction coordinate transition state theory, as was done in Chapter 2. Ideally the interaction potential would be computed at the CASPT2 level, with an active space of at least 7 electrons and five orbitals – six electrons in four orbitals for O<sub>2</sub>, and one electron in one orbital for the unpaired electron in acetyl, with the possibility of adding additional electrons and orbitals to account for the C=O π-bond and/or any oxygen lone pair electrons in acetyl. However, these calculations are beyond the scope of this work. Thus, for simplicity, we have adopted the high-pressure limit recommended by Bozzelli.

**Table 3.2** – Harmonic oscillator degrees of freedom using various methods.

Species	Method	Frequency (degeneracy) ( $\text{cm}^{-1}$ )
	Three frequency	467.3 (8), 1443.0 (7), 4069.3 (3)
	Group frequency	463.6 (3), 492.5, 750, 1050, 1135, 1185.3 (3), 1350, 1375, 1500, 2570, 2800, 2850
	Quantum chemistry	321.6, 503.5, 539.9, 547.1, 731.5, 979.2, 1044.0, 1126.4, 1188.6, 1399.4, 1458.2, 1463.4, 1881.7, 3055.3, 3115.4, 3155.1
	Three frequency	391.4 (8), 1172.3 (7), 3800.5 (3)
	Group frequency	387.5, 400.0, 440, 815, 850, 955.0 (5), 1310, 1455, 3000, 3100, 3615
	Quantum chemistry	320.7, 423.4, 670.2, 680.0, 757.3, 869.8, 1004.4, 1025.6, 1243.6, 1446.5, 1494.6, 1698.0, 3164.2, 3282.4, 3454.9
	Three frequency	628.5 (4), 1777.0 (6), 4513.8 (2)
	Group frequency	455, 750, 1050, 1350, 1375, 1500, 1855, 2264.1, 2750, 2800, 2850
	Quantum chemistry	468.7, 850.5, 1019.8, 1047.6, 1356.5, 1447.0, 1455.5, 1918.0, 3010.3, 3099.4, 3102.2

**Table 3.3** – Hindered-rotor degrees of freedom using various methods.

Species	Method	(Frequency, Barrier height) ( $\text{cm}^{-1}$ , $\text{cm}^{-1}$ )
	Three frequency	n/a
	Group frequency	(40.0, 326.1), (150.0, 915.6)
	Quantum chemistry	(139.4, 2139.3), (159.2, 425.8)
	Three frequency	n/a
	Group frequency	(100.0, 415.1), (300.0, 3307.1), (300.0, 3307.1)
	Quantum chemistry	(336.8, 2189.5), (205.3, 5153.4), (321.9, 1672.3)
	Three frequency	n/a
	Group frequency	(600.0, 1041.7)
	Quantum chemistry	(112.4, 176.4)



**Figure 3-2** – Comparison of densities of states, partition functions, and heat capacities for the (a) acetylperoxy, (b) hydroperoxylvinoy, and (c) acetyl species using a three-frequency model (TF), group frequency model (GF), and quantum chemistry calculations (QC). Both the TF and GF models reproduce the QC heat capacity data, but the latter more consistently reflects the density of states than the former.

### 3.4.1 Density of States Comparison

Figure 3-2 shows the density of states, partition function, and heat capacity for acetylperoxy, hydroperoxylvinoxy, and acetyl as calculated from data estimated using the three-frequency and group frequency approaches and calculated from quantum chemistry, with the goal of judging how the two approximate models compare to the detailed quantum chemistry model. For the purposes of this comparison the external rotational modes from the quantum chemistry calculations were discarded to make the comparison equivalent to the three-frequency and group-frequency methods, which only estimate the internal (vibrational and hindered rotor) modes. However, a single arbitrary active K-rotor was included. The parameters for the internal modes as determined for each model are given in Tables 3.2 and 3.3.

The performance of the three frequency method in approximating the density of states is erratic, sometimes doing very well (acetylperoxy) and other times doing poorly (hydroperoxylvinoxy). This is due to the fact that the method is purely focused on fitting to the heat capacity data, which is only indirectly related to the density of states via the molecular degrees of freedom. Even with hydroperoxylvinoxy, which has a poor density of states approximation, the fit to the heat capacity is very good. By contrast, the characteristic frequencies used in the group frequency approach are an effort to also fit the molecular degrees of freedom, and this results in a much more consistent density of states estimation, usually within an order of magnitude or better. Furthermore, the use of characteristic frequencies does not significantly affect the fit to the heat capacity data.

Note that the deviation of the approximate density of states from the true (quantum chemistry-based) density of states appears to be somewhat consistent; that is, the density of states is always overpredicted or underpredicted by roughly the same ratio. As noted before, constant factors in densities of states are cancelled out when using the inverse Laplace transform method of estimating microcanonical rate coefficients, when using detailed balance within the collisional transfer probabilities model, and when calculating the normalized equilibrium distributions. Thus, much of the master equation model only depends on the *relative* density of states rather than the *absolute* density of states. How-

ever, there are other parts of the model that do depend on the absolute density of states, such as detailed balance for isomerization and association reactions. Furthermore, getting the absolute density of states correct becomes more important when using another microcanonical rate method, such as RRKM. RRKM, however, requires detailed knowledge of the transition state geometry, and thus cannot be implemented in the current version of RMG.

### 3.5 Recommendations for Future Work

Improvements to RMG's ability to compute the pressure dependence of rate coefficients will be an ongoing work. Generally speaking, there are four areas of improvement: (i) the density of states, (ii) the collisional energy transfer model, (iii) the microcanonical rate coefficients, and (iv) solving the master equation. Of the four areas, the second – collisional energy transfer – is the most poorly understood on a theoretical level. Within the context of RMG, the third area – computing the microcanonical rates – is the most difficult. Currently RMG uses the Inverse Laplace Method to calculate the microcanonical rate coefficients, which requires the density of states for the reactant and the high-pressure limit Arrhenius parameters. The next “step up” in theory or complexity would be to implement an RRKM treatment. However, this treatment requires detailed data for the transition-state geometry. Since finding the correct saddle point on a potential energy surface is a difficult process to automate with reliable results, it is safe to assume that RMG will continue to use ILT for the immediate future. Regarding the solution to the master equation: Joshua Allen has made considerable progress in implementing the steady-state master equation solver into RMG. He has also implemented a time-dependent eigenvalue solution method. However, as discussed in Section 3.2.1, the eigenvalue technique is not robust enough for automation. Future work could be to develop a method for automatically adjusting the system of equations to account for the rapid equilibration between wells at high temperatures. This would extend the feasible temperatures at which the eigenvalue method could be utilized. As for the density of states, I would recommend the creation of a Primary Frequency Library (PFL). RMG is already equipped to use pre-calculated entropy, enthalpy,

and heat capacities for certain species in its Primary Thermo Library. For species for which the rovibrational parameters are already known – either from experiment or computational quantum chemistry – those parameters should be used. For example, XML could be used to tag the relevant data. Vibrational frequencies could be given one tag; hindered rotor barrier heights, reduced moments of inertia, rotational symmetry numbers, etc, could be given their own tags. Each time quantum calculations are performed for some molecule, the rovibrational parameters could be added to the database. This database would not replace the group-frequency estimation method, since RMG will always generate new and unusual species; rather, it would simply provide more accurate parameters for the most common (and presumably most important) species.

### 3.6 Conclusion

A new framework for estimating vibrational frequencies and hindered internal rotor parameters has been developed. The new method separates a molecule into its functional groups and assigns frequencies accordingly. The remaining frequencies are fit from heat capacity data. The new method is more accurate than the pre-existing three-frequency model in approximating the density of states obtained by detailed quantum calculations. This new approach should improve the accuracy of pressure-dependent rate coefficients calculated within RMG.

### 3.7 Appendix: Tables

**Table 3.4** – List of the group types and the corresponding frequency range for each mode.

Name	Description	Mode	freq. range	# of modes
RsCH3	5 atoms	C-H stretch	2750 - 2850	3
<i>Alkane end group</i>	1 rotor	R-C-H bend	1350 - 1500	2
	Terminal	R-C-H rock	700 - 800	1



Table 3.4 – Continued

Name	Description	Mode	freq. range	# of modes
		R-C-H rock	1000 - 1100	1
		Umbrella	1350 - 1400	1
RdCH <sub>2</sub>	4 atoms	C-H stretch	2950 - 3100	2
<i>Alkene end group</i>	no rotor	R-C-H scissor	1330 - 1430	1
	Terminal	R-C-H swing	900 - 1050	1
		R-C-H rock	1000 - 1050	1
CtCH	3 atoms	R-C-H bend	750 - 770	2
<i>Alkyne end group</i>	no rotor	C-H stretch	3350 - 3450	1
	Terminal			
RsCH <sub>2</sub> sR	5 atoms	C-H stretch	2750 - 2850	2
<i>saturated carbon with</i>	2 rotors	H-C-H scissor	1425 - 1450	1
<i>two single bonds</i>	non-terminal	R-C-H symmetric	1225 - 1275	1
		R-C-H asymmetric	1270 - 1340	1
		H-C-H side rock	700 - 800	1
		R-C-R scissor	300 - 400	1
CdCHsR	4 atoms	C-H stretch	2995 - 3025	1
<i>carbon with double</i>	1 rotors	R-C-H bend	975 - 1000	1
<i>bond to carbon and</i>	non-terminal	R-C-H bend	1300 - 1375	1
<i>single bond to R</i>		CdC-R scissor	400 - 500	1
		CdC stretch	1630 - 1680	1
Aldehyde	4 atoms	C-H stretch	2695 - 2870	1
<i>carbon with double</i>	1 rotors	R-C-H bend	700 - 800	1
<i>bond to oxygen and</i>	non-terminal	R-C-H bend	1380 - 1410	1
<i>single bond to R</i>		OdC-R scissor	450 - 500	1
		OdC stretch	1750 - 1800	1
Cumulene	3 atoms	C-C-C scissor	540 - 610	2

Table 3.4 – Continued

Name	Description	Mode	freq. range	# of modes
<i>carbon with two double bonds to carbon</i>	no rotor non-terminal	C-C-C asymmetric	1970 - 2140	1
Ketene	3 atoms	OdC stretch	2110 - 2130	1
<i>carbon with one carbon double bond and one oxygen double bond</i>	no rotor non-terminal	OdCdC bend OdCdC bend	495 - 530 650 - 925	1 1
CtCsR	3 atoms	CtC stretch	2100 - 2250	1
<i>carbon with one triple bond and one single bond</i>	1 rotor non-terminal	CtC-C bend	500 - 550	1
RsCHsR2	5 atoms	R-C-H bend	1380 - 1390	2
<i>carbon with three single bonds</i>	3 rotors non-terminal	C-C-C scissor C-H stretch Umbrella	370 - 380 2800 - 3000 430 0 440	2 1 1
CdCsR2	4 atoms	R-C-R scissor	325 - 375	1
<i>carbon with one carbon double bond and two single bonds</i>	2 rotors non-terminal	CdC-R scissor Umbrella CdC stretch	415 - 465 420 - 450 1700 - 1750	1 1 1
Ketone	4 atoms	R-C-R scissor	365 - 385	1
<i>carbon with one oxygen double bond and two single bonds</i>	2 rotors non-terminal	OdC-R scissor Umbrella OdC stretch	505 - 600 445 - 480 1700 - 1720	1 1 1
RsCsR3	5 atoms	C-C-C scissor	350 - 400	2
<i>carbon with four single bonds</i>	4 rotors non-terminal	C-C-C bend Umbrella	1190 - 1240 400 - 500	2 1
RsCH2r	4 atoms	C-H stretch	3000 - 3100	2

Table 3.4 – Continued

Name	Description	Mode	freq. range	# of modes
<i>carbon radical with one single bond</i>	1 rotor	R-C-H swing	415 - 465	1
	terminal	R-C-H rock	780 - 850	1
		R-C-H scissor	1435 - 1475	1
RdCHr	3 atoms	C-H stretch	3115 - 3125	1
<i>carbon radical with one double bond</i>	no rotors	CdC-H bend	620 - 680	1
	terminal	CdC-H bend	785 - 800	1
RsCHrsR	4 atoms	C-H stretch	3000 - 3050	1
<i>carbon radical with two single bonds</i>	2 rotors	R-C-H bend	390 - 425	1
	non-terminal	R-C-H bend	1340 - 1360	1
		R-C-R scissor	335 - 370	1
CdCrSR	3 atoms	CdC stretch	1670 - 1700	1
<i>carbon radical with one carbon double bond and one single bond</i>	1 rotor	CdC-R bend	300 - 440	1
	non-terminal			
OdCrSR	3 atoms	OdC stretch	1850 - 1860	1
<i>carbon radical with one oxygen double bond and one single bond</i>	1 rotor	OdC-R bend	440 - 470	1
	non-terminal			
RsCrSR2	4 atoms	C-C-C scissor	360 - 370	2
<i>carbon radical with three single bonds</i>	3 rotors	Umbrella	300 - 400	1
	non-terminal			
Alcohol	3 atoms	O-H stretch	3580 - 3650	1
<i>hydrogen bond and</i>	terminal	R-O-H bend	1210 - 1345	1
Ether	3 atoms	C-O-C scissor	350 - 500	1
<i>oxygen with two single carbon bonds</i>	2 rotors			
	non-terminal			

Table 3.4 – Continued

Name	Description	Mode	freq. range	# of modes
ROOH	4 atoms	O-H stretch	3580 - 3650	1
	terminal	O-O-H bend	1300 - 1320	1
		C-O-O scissor	350 - 425	1
		O-O stretch	825 - 875	1
ROOR <i>peroxide</i>	4 atoms	C-O-O scissor	350 - 500	1
	3 rotors non-terminal	O-O stretch	795 - 815	1
peroxy	3 atoms	C-O-O scissor	470 - 515	1
	terminal	O-O stretch	1100 - 1170	1

**Table 3.5** – The possible cases RMG will use to solve the unknown parameters. The variable  $f(x_i)$  corresponds to the heat capacity for the rigid-rotor harmonic-oscillator,  $C_V^{\text{RRHO}}(v_i)$ . The variable  $g(x_i, y_i)$  corresponds to the heat capacity for the hindered rotor,  $C_V^{\text{HR}}(V_0, v)$ . In both equations, the temperature dependence has been suppressed for clarity.

Cases	$N_{\text{RRHO}}$	$N_{\text{HR}}$	unknown heat capacity
Case 0	0	0	0
Case 1	1	0	$f(x_1)$
Case 2	2	0	$f(x_1) + f(x_2)$
Case 3	3	0	$f(x_1) + f(x_2) + f(x_3)$
Case 4	4	0	$\sum_{i=1}^4 f(x_i)$
Case 5	5	0	$\sum_{i=1}^5 f(x_i)$

Table 3.5 – Continued

Cases	$N_{RRHO}$	$N_{HR}$	unknown heat capacity
Case 6	6	0	$\sum_{i=1}^6 f(x_i)$
Case 7	$\geq 7$	0	$f(x_1) + x_2 f(x_3) + x_4 f(x_5)$ $+ (N_{RRHO} - 1 - x_2 - x_4) f(x_6)$
Case 8	0	1	$g(x_1, x_2)$
Case 9	1	1	$f(x_3) + g(x_1, x_2)$
Case 10	2	1	$f(x_3) + f(x_4) + g(x_1, x_2)$
Case 11	3	1	$\sum_{i=3}^5 f(x_i) + g(x_1, x_2)$
Case 12	4	1	$\sum_{i=3}^6 f(x_i) + g(x_1, x_2)$
Case 13	$\geq 5$	1	$f(x_3) + x_4 f(x_5) + (N_{RRHO} - 1 - x_4) f(x_6)$ $+ g(x_1, x_2)$
Case 14	0	2	$g(x_1, x_2) + g(x_3, x_4)$
Case 15	1	2	$f(x_5) + g(x_1, x_2) + g(x_3, x_4)$
Case 16	2	2	$f(x_5) + f(x_6) + g(x_1, x_2) + g(x_3, x_4)$
Case 17	3	2	$f(x_1) + f(x_2) + f(x_3)$ $+ g(x_4, x_5) + g(x_6, v_{mid})$
Case 18	$\geq 4$	2	$x_1 f(x_2) + (N_{RRHO} - x_1) f(x_3)$ $+ g(x_4, x_5) + g(x_6, v_{mid})$

Table 3.5 – Continued

Cases	$N_{RRHO}$	$N_{HR}$	unknown heat capacity
Case 19	0	3	$g(x_1, x_2) + g(x_3, x_4) + g(x_5, x_6)$
Case 20	1	3	$f(x_1)$ $+g(x_3, x_2) + g(x_5, x_4) + g(x_6, v_{mid})$
Case 21	2	3	$f(x_1) + f(x_2)$ $+g(x_4, x_3) + g(x_5, v_{low}) + g(x_6, v_{high})$
Case 22	3	$\geq 3$	$f(x_1) + f(x_5) + f(x_6)$ $+x_2g(x_3, v_{low}) + (N_{HR} - x_2)g(x_4, v_{high})$
Case 23	$\geq 4$	$\geq 3$	$x_1f(x_2) + (N_{RRHO} - x_1)f(x_3)$ $+x_4g(x_5, v_{low}) + (N_{HR} - x_4)g(x_6, v_{high})$
Case 24	0	$\geq 4$	$g(x_1, x_2) + x_3g(x_4, x_6) +$ $(N_{HR} - x_3 - 1)g(x_5, v_{mid})$
Case 25	1	$\geq 4$	$f(x_6) + g(x_1, x_2) + x_3g(x_4, v_{low}) +$ $(N_{HR} - x_3 - 1)g(x_5, v_{high})$
Case 26	2	$\geq 4$	$f(x_1) + f(x_2) + x_3g(x_4, x_5) +$ $(N_{HR} - x_3)g(x_6, v_{mid})$

## Chapter 4

# Primary Thermo Library for Oxidation Chemistry of Light Alkanes

### 4.1 Introduction

The two most important components to a chemical kinetics mechanism are the rate coefficients and the thermodynamic parameters. Because RMG generates thousands of possible species in the process of generating a mechanism, many of which have never been considered before, it is not possible to tabulate the thermodynamic parameters for all possible species. Therefore RMG must be able to estimate thermodynamic properties quickly for any arbitrary species. RMG estimates the enthalpy, entropy, and heat capacity for a given molecule based upon its functional groups [6]. This method is surprisingly accurate, at least for non-cyclic species. However, it is not perfect. To calculate the enthalpy and entropy at higher temperatures, RMG requires the heat capacity as a function of temperature. The difficulty is that the group-additivity scheme only has seven temperatures from which to fit the parametrization: 300, 400, 500, 600, 800, 1000, & 1500 K. Since combustion temperatures frequently exceed 1500K, RMG is forced to extrapolate to higher temperatures. To complicate matters, the heat capacity is not necessarily monotonically increasing. For molecules with hindered internal rotors, the heat capacity will reach a maximum at a certain temperature and decrease thereafter. The temperature corresponding to the maximum heat capacity depends upon the barrier to internal rotation. To account for the non-monotonic nature of

the heat capacity, RMG uses a Wilhoit polynomial for the heat capacity extrapolation. This polynomial works well, since it correctly predicts the limiting behavior.

$$C_P^{\text{Wilhoit}}(T) = C_P^0 + (C_P^\infty - C_P^0) y^2 [1 + (y - 1)(a + by + cy^2 + dy^3)] \quad (4.1)$$

$$y = \frac{T}{T + B}$$

where the parameters  $C_P^0$  and  $C_P^\infty$  are known from statistical mechanics, and the parameters  $a$ ,  $b$ ,  $c$ ,  $d$ , and  $B$  are fit to the data. One difficulty with this approach is that the Wilhoit polynomial is infrequently used in the combustion community. The two most commonly used software packages for chemically reacting flow – CHEMKIN and Cantera – both require the fourteen-coefficient NASA polynomial.

$$\frac{C_P^{\text{NASA}}(T)}{R} = \sum_{i=1}^5 a_{i,j} T^{i-1} \quad (4.2)$$

$$\frac{H^{\text{NASA}}(T)}{RT} = \sum_{i=1}^5 \frac{a_{i,j}}{i} T^{i-1} + \frac{a_{6,j}}{T} \quad (4.3)$$

$$\frac{S^{\text{NASA}}(T)}{R} = a_{1,j} \ln T + \sum_{i=2}^5 \frac{a_{i,j}}{i-1} T^{i-1} + a_{7,j} \quad (4.4)$$

$$j = \begin{cases} 1 & \text{if } T \leq T_{inter} \\ 2 & \text{otherwise} \end{cases}$$

where the seven  $a_i$ 's are computed for each of two temperature ranges. Since it is obviously not possible to fit fourteen coefficients directly to the seven  $C_p$  data, RMG uses the Wilhoit polynomial to compute the heat capacity at numerous temperatures, and then it fits the NASA coefficients to the computed values. A further complication is that RMG's estimates for the heat capacity at 1500 K are not always accurate. For many functional groups, the value at 1500 K is equal to the value at 1000 K, simply because no better value was available. In these instances RMG's ability to extrapolate the heat capacity to higher temperatures is less reliable. In order to address this latter problem, RMG has a Primary



Thermo Library. This library is a list of the heat capacity at the seven Benson temperatures. These heat capacities are well known, either from experiment or (more likely) from statistical mechanics calculations. Although the Primary Thermo Library removes the uncertainty associated with the group additivity scheme, it does not remove the uncertainty associated with fitting one polynomial to the output of another polynomial.

One solution to this problem would be to expand the information contained in the Primary Thermo Library. For example, in addition to the heat capacities at seven temperatures, the expanded library could include Wilhoit and NASA polynomial coefficients directly. It could also include spectroscopic data, such as the vibrational frequencies, rotational constants, as well as internal rotor parameters.

As one part of my thesis, I created a new library for thermodynamic data. This library contains all the information RMG would need to improve its thermodynamic estimates. The library currently contains more than 170 molecules. The selection of molecules is geared towards the oxidation chemistry of light alkanes. To generate the list of molecules, I ran RMG over a wide range of temperatures and pressure for fuel-lean propane combustion, as part of an on-going collaboration with Dr. Stephen Klippenstein at Argonne National Lab and Dr. Craig Taatjes at Sandia National Lab. I also collaborated with Dr. Richard West, a post-doctoral associate in our group, on a mechanism for methyl-formate oxidation over a similarly wide range of conditions. Additionally, I looked at two distinct, detailed mechanisms from the literature: The recommended values of Baulch et al [5], and the more recent C3 mechanism of Glarborg et al [60, 82, 83]. The union of these four mechanisms is the core of the new library. Not all of the species in the list were analyzed with the intent that they would or should be included in a final model (e.g. many bi-radicals and species in their first electronic excited state are included). In many instances, RMG included a dubious species in the final mechanism because its thermochemistry estimate was off by a considerable margin. I have included these species in the library not because they are significant, but because they might be used in the future to retrain RMG's thermo estimates.

There are two advantages to the new thermo library. First, the polynomial coefficients should be significantly more accurate than was is currently available. Given the hierarchical nature of combustion mechanisms, these species are likely to appear in almost any

oxidation mechanism, so all future work will be improved by their presence. Second, it is systematic. Since all of these species were calculated using the same detail with the same level of theory, any errors will be systematic. Consequently, some of these errors may cancel in the final mechanism.

In the next section, I describe the software I used to compute the thermodynamic parameters, CanTherm, as well as improvements to the code I made. In the following section, I detail the computational quantum chemistry methods I used. The final section is a recommendation for future work, in which I describe three short projects for using and developing this library within RMG. The results are included in the appendix at the end of the chapter.

## 4.2 Improvements to CanTherm

CanTherm is an open-source software package for calculating thermodynamic quantities [90]. It was written by a former group member, Dr. Sandeep Sharma and is presently under development by a current group member, Michael Harper. I contributed three small changes to the code. First, I improved CanTherm’s method for fitting a hindered rotor barrier to a Fourier series; second, I added the ability to treat some internal rotors as free rotors; and third, I added a module for providing heat capacity parameters for the four most commonly used parametrization methods: Benson, Wilhoit, NASA, and Shomate.

### 4.2.1 Hindered Rotor Potentials

For each hindered rotor, CanTherm reads an input file which contains the rotational potential as a function of dihedral angle. In most instances, the potential is generated from Gaussian03 calculations, in which a relaxed optimization scan is performed as the dihedral angle is incrementally rotated[17]. This potential is then fit to a Fourier series using a linear least squares method.

$$V(\phi) = V_0 + \sum_{i=1}^5 a_i \cos i\phi + \sum_{i=1}^5 b_i \sin i\phi \quad (4.5)$$

In the original method, eleven coefficients were fit:  $V_0$  and the five  $a_i$ 's and  $b_i$ 's. Michael Harper and I modified the code so that only the five  $a_i$ 's and  $b_i$ 's are treated as fitting parameters; the parameter  $V_0$  is therefore defined in terms of the other ten. (My justification for modifying the code is as follows: The software package VariFlex, which I use to calculate pressure-dependent rate coefficients, defines  $V_0$  this way, and so I wanted to make sure the Fourier coefficients I computed in CanTherm could be used by VariFlex.) In order to remove  $V_0$  as a fitting parameter, I coded  $V_0 = -\sum_{i=1}^5 a_i$ . This is equivalent to the constraint that the potential is zero at  $\phi = 0$ :

$$V(\phi)|_{\phi=0} = 0$$

Additionally, I added a second constraint:  $\sum_{i=1}^5 ib_i = 0$ , which is equivalent to the requirement that the first derivative of the potential to be zero at  $\phi = 0$ :

$$\left. \frac{dV(\phi)}{d\phi} \right|_{\phi=0} = 0$$

The resulting Fourier Series requires fewer parameters, and it is physically more realistic.

## 4.2.2 Free Rotors

For some molecules, the barrier for internal rotation is so low that it behaves like a free rotor. For example, the ethyl radical has a barrier for rotation along the H-C-C-H dihedral angle that is less than 0.1 kcal/mol, which corresponds to a  $k_B T$  of  $\sim 50$  K. Instead of treating this rotor as a hindered rotor, it makes more sense to treat it as a free internal rotor. I added the option within CanTherm to treat such modes as free rotors. If a maximum barrier height is below a threshold value,  $V_{minimum}$ , then CanTherm will treat that internal rotor as a free rotor. The default threshold value is  $V_{minimum} = 0.5$  kcal/mol, which corresponds to  $k_B T$  of  $\sim 250$  K. In other words, if a molecule at room temperature has more than enough

energy to exceed the barrier, it can be modeled as a free rotor. I tested this assumption for a wide range of molecules. According to the molecules I considered, the species with the lowest reduced moment of inertia is hydrogen-peroxide,  $\text{H}_2\text{O}_2$ , with  $I_r = 0.42$  [ $\text{amu}/\text{\AA}^2$ ], and the species with the largest reduced moment of inertia is acetyl-methyl-hydroperoxide,  $\text{C}_3\text{H}_6\text{O}_3$ , with  $I_r = 19.26$  [ $\text{amu}/\text{\AA}^2$ ]. For these two species, I replaced the corresponding potential with a potential with a maximum barrier of 0.5 kcal/mol. In both cases, the heat capacity for that mode was  $\sim 0.5 R$  ( $\pm 8\%$ ) at 300 K and rapidly approached 0.5 R for  $T > 300$  K. In order to keep the low-temperature error below 10%, I would not advise using a  $V_{\text{minimum}} > 0.5$  kcal/mol.

The equations for a free rotor are taken from the works of Pitzer [80, 79, 81]:

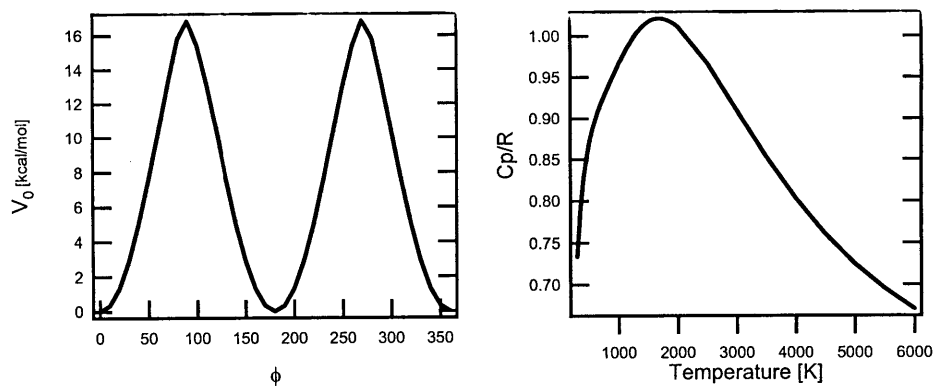
$$Q(T) = \frac{(8\pi^3 I_r k_B T)^{1/2}}{\sigma_r h}$$

$$C_p(T) = \frac{1}{2}R$$

$$S(T) = R \ln[Q] + \frac{1}{2}R$$

### 4.2.3 Barrier Heights

Having established that  $V_{\text{minimum}} \leq 0.5$  kcal/mol is a suitable threshold for free rotors, my next question was to determine if there is a corresponding  $V_{\text{maximum}}$ , such that barriers greater than this value can safely be modelled as harmonic oscillators. Specifically, I wanted to treat allylic radicals properly. In allylic radicals, the radical site is adjacent to a double bond; the unpaired electron is delocalized by the neighboring  $\pi$ -orbitals, and the resulting resonance-enhanced stability makes these radicals of particular importance in combustion chemistry. Since  $\pi$ -orbital resonance is destroyed in rotating the  $-\text{CH}_2^\bullet$  moiety relative to the double-bond, this torsional mode normally has a high barrier to rotation. Consequently, I have assumed that allylic radicals should not be treated as hindered rotors. To test this assumption, I computed the potential to rotation for allyl,  $\text{C}_3\text{H}_5$ , and then computed the heat capacity, first assuming a rigid-rotor harmonic oscillator model, and then using the hindered rotor model. The rotational barrier and corresponding heat capac-



**Figure 4-1** – Rotational barrier and heat capacity for the hindered internal rotor in allyl,  $C_3H_5$ .

ity are shown in Figure 4-1. On the one hand, the torsional mode clearly shows the classic behavior of a hindered rotor, with a heat capacity that begins like a harmonic oscillator as  $C_p \rightarrow R$ , peaks, then asymptotically approaches  $C_p \rightarrow \frac{1}{2}R$ . On the other hand, for  $300 \leq T \leq 2500$  K, the RRHO and hindered rotor models agree with a couple of percent. Therefore, the total error in treating this torsional mode as an harmonic oscillator over the temperature range of interest is negligible, and is certainly within the uncertainty of the computed vibrational frequencies. Consequently, for all the resonantly enhanced (allylic) radicals in the new thermo library, I have treated the corresponding torsional mode as an harmonic oscillator. All other single bonds between heavy atoms – except those in cyclic structures – are modeled using the hindered rotor approximation.

#### 4.2.4 Heat Capacity Routines

The final modification to CanTherm was to fit the coefficients for the Wilhoit and NASA polynomials. CanTherm will compute the heat capacity in 50 degree increments from 300 K to 2000 K, and then in 500 degree increments from 2000 K to 6000 K. For Equation (4.1), I used the nonlinear bounded solver in SciPy, `fminbound`, to determine the optimum value for the parameter  $B$ . For a given value of  $B$ , the remaining four parameters were determined by a linear least squares regression. Similarly, for Equation (4.2) I used `fminbound` to determine the optimum switching temperature  $T_{inter}$  for the NASA polynomial; the other fourteen parameters were determined via a linear least squares regression. For the NASA fit, I also supplied three constraints, requiring that the function and its first and second

derivatives be equal at  $T_{inter}$ . These constraints ensure that the heat capacity remains a smooth function across the switching temperature.

$$\begin{aligned}\sum_{i=1}^5 a_{i,1} T_{iter}^{i-1} &= \sum_{i=1}^5 a_{i,2} T_{iter}^{i-1} \\ \sum_{i=2}^5 (i-1) a_{i,1} T_{iter}^{i-2} &= \sum_{i=2}^5 (i-1) a_{i,2} T_{iter}^{i-2} \\ \sum_{i=3}^5 (i-2) a_{i,1} T_{iter}^{i-3} &= \sum_{i=2}^5 (i-2) a_{i,2} T_{iter}^{i-3}\end{aligned}$$

### 4.3 Computational Methods

The computation methods I used are similar to those described in Chapters 2 and 3. All DFT calculations were done using Gaussian03[17]. All MP2 and QCISD(T) calculations were done using MOLPRO[101]. For each species in the library, the  $\sim 3^n$  possible conformers – where  $n$  is the number of torsional modes – were calculated using the CBS-QB3 method. The lowest energy conformer was selected, and this geometry was re-optimized using the B3LYP functional with the 6-311++G(d,p) basis set. The torsional modes for each species were treated as internal rotors. The barriers for internal rotation were calculated by a relaxed scan at the B3LYP/6-31+G(d,p) level. The resulting potential was fit to a Fourier series. A rigid-rotor harmonic oscillator model was assumed for all remaining degrees of freedom. In order to reduce the ambiguity regarding low-frequency vibrations and the corresponding torsional modes, the projection of the B3LYP/6-311++G(d,p) force-constant matrix was removed along the vectors corresponding to the torsional modes. This matrix was then diagonalized, which separated the rigid rotor harmonic oscillator frequencies from the torsional modes[91]. For all hindered rotors, it is assumed that the torsional modes can be separated and approximated by a one-dimensional rotation, given by the Fourier series in Equation (4.5). A Hamiltonian is formed from this potential, and the corresponding 1D Schrödinger equation is solved for the energy levels,  $\epsilon_j$ . The partition function is calculated by summing over the energy levels,  $Q = \sum_j \exp[-\epsilon_j/k_B T]$ , and the enthalpy, entropy, and heat capacity are computed accordingly. The effective moment

of inertia for each rotor was  $I^{(2,3)}$ , evaluated at the equilibrium geometry. For internal rotors with a barrier below 0.5 kcal/mol, the rotor was treated as a free rotor, as described above; for internal rotors with a barrier greater than 0.5 kcal/mol, the rotor is treated as a hindered rotor. For all allylic radicals, the rotation along the resonantly stabilized single bond was treated as an harmonic oscillator, as described above.

The DFT geometries were used for restricted RQCISD(T)/cc-pVTZ and RQCISD(T)/cc-pVQZ energies. To avoid spin contamination, all calculations were spin restricted. For open shell species, the MOLPRO's initial guess for the  $\alpha$  and  $\beta$  spin electrons in the restricted Hartree-Fock calculation is sometimes inaccurate, and the resulting post-Hartree-Fock calculations were off by  $\sim 30$  kcal/mol. To prevent this, I preceded the RHF calculation with a UHF calculation for open-shell species; the spin unrestricted calculations provide a better guess for the open-shell spin restricted calculation. Additionally, for molecules with an Abelian point group other than C1, MOLPRO does not always find the lowest symmetry. To test for this, I screened all the molecules for the point group. For molecules with some symmetry element, I repeated the calculation – usually at a lower level of theory, e.g. RMP2/cc-pVDZ – to determine the symmetry orientation with the lowest energy. The RQCISD(T) complete basis set limit was extrapolated from the triple and quadruple zeta basis set calculations assuming an inverse power law[64, 14]:

$$E_{\text{QCISD(T)/CBS}} = E_{\text{QCISD(T)/cc-pVQZ}} + (E_{\text{QCISD(T)/cc-pVQZ}} - E_{\text{QCISD(T)/cc-pVTZ}}) \frac{4^4}{5^4 - 4^4} \quad (2.1)$$

Tables 4.2 through 4.5 contains the standard state heat of formation and entropy for the species. Also included in these tables is the RQCISD(T)/cc-pVQZ T1 diagnostic[54]. The T1 diagnostic is a measure of the importance of multi-reference effects. For closed shell species with a T1 diagnostic less than  $\sim 0.02$ , and for radicals with a T1 diagnostic less than  $\sim 0.03$ , the RQCISD(T) energies are assumed to be accurate to  $\pm 1$  kcal/mol, and multi-reference calculations are unnecessary[46]. For the vast majority of species considered, a single-electron wave function appears to be sufficient. For many of the peroxy compounds

the T1 diagnostic was between 0.03 and 0.037, which suggests an uncertainty in the energy of  $\pm 2$  kcal/mol; for ketylperoxy, the T1 diagnostic was 0.042, so the uncertainty is larger, probably  $\pm 5$  kcal/mol.

### 4.3.1 Benchmark Study of Computational Methods

A full benchmark analysis of this method is well beyond the scope of this chapter. As a simpler task, I wanted simple confirmation that these methods are roughly accurate to within  $\pm 1$  kcal/mol of some species for which the thermochemistry is accurately known. I looked at several papers on benchmarks for more detailed computational quantum methods [64, 14, 48, 11]. From those papers, I compiled a short list of test cases. As seen in Table 4.1, the present method is quite good. The average of the absolute value of the difference between the present work and the literature value is 0.74 kcal/mol. The worst case is for benzene, for which the present work is off by nearly 2.5 kcal/mol. This result is not entirely surprising, since the electrons in benzene are highly delocalized and are not well described by the RQCISD(T) [31]. However, the present work does not include any aromatic species, so this behavior is not too discouraging. Although the sample calculations below are clearly too small for conclusive statistics, they nonetheless support the assertion that the uncertainties in our method are roughly  $\pm 1$  kcal/mol.

## 4.4 Recommendation for Future Work

I have three recommendations for the future development of the library and its relation to RMG, ranked in difficulty. The easiest recommendation would be to have RMG read that NASA polynomial coefficients directly from a file, much as it currently does for the pre-computed heat capacity at seven temperatures. This simple implementation would significantly improve the final thermochemistry that RMG provides in its CHEMKIN mechanism. The second recommendation would be to create a primary spectroscopic library, analogous to the thermo library. This would include the rotational constants, the vibrational frequencies, the reduced moments of inertia for internal rotors, and the Fourier coefficients for internal rotors. These data would then be passed to the subroutine that calculates the density



**Table 4.1** – Simple benchmark study of the computational methods used in the thermo library.

Species	Experimental $\sum D_e^a$ kcal/mol	Computed $\sum D_e$ [kcal/mol]	$\Delta E$ [kcal/mol]	Reference
H <sub>2</sub>	109.43	109.97	-0.54	[64]
H <sub>2</sub> O	232.42	233.86	-1.44	[64]
CH <sub>4</sub>	420.12	420.42	-0.3	[64]
CH <sub>2</sub> O	373.65	374.46	-0.81	[64]
CO	259.19	259.57	-0.38	[64]
CO <sub>2</sub>	388.98	389.73	-0.75	[64]
C <sub>2</sub> H <sub>2</sub>	403.59	404.25	-0.66	[64]
C <sub>2</sub> H <sub>4</sub>	563.4	563.24	0.16	[11]
C <sub>2</sub> H <sub>6</sub>	712.34	712.66	-0.32	[11]
HOOH	268.47	269.45	-0.98	[11]
CH <sub>3</sub> OH	512.41	513.82	-1.41	[11]
HCO	278.61	278.97	-0.36	[28]
CH <sub>3</sub>	307.29	307.68	-0.39	[28]
OH	106.89	107.56	-0.67	[28]
HO <sub>2</sub>	174.62	174.89	-0.27	[28]
O <sub>2</sub>	120.23	119.85	0.38	[28]
allene	703.11	702.4	0.71	[14]
propyne	704.86	703.87	0.99	[14]
allyl	766.22	765.07	1.15	[14]
cyclopropane	853.03	852.54	0.49	[14]
propene	860.01	860.24	-0.23	[14]
propane	1006.33	1007.05	-0.72	[14]
furan	993.82	992.6	1.22	[14]
benzene	1367.77	1365.36	2.41	[14]
Mean absolute deviation:			0.74	
Mean absolute deviation (without benzene):			0.67	

<sup>a</sup>  $\sum D_e$  is the atomization energy.

of states. This should improve the accuracy of RMG's ability to compute pressure dependent rate coefficients. The final recommendation would be to use this database to retrain or refit the parameters RMG uses for estimating the thermochemistry from functional groups. As mentioned in the introduction, RMG will always need a method for rapidly estimating the thermochemistry of new species. With appropriate data-mining techniques, it should be possible to use this database to develop new and more accurate group-additivity predictions. Instead of limiting RMG to the heat capacity at seven temperatures below 1500 K, the new group estimates could be valid over a much larger temperature range. RMG could then fit the NASA polynomial coefficients to these higher-temperature predictions. In principle, this should be more accurate than the current method of fitting a Wilhoit polynomial to the seven heat capacity values, using this polynomial to compute a Cp array, and then fit the NASA polynomials to this array.

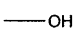
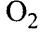
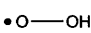
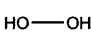
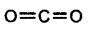
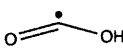
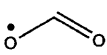
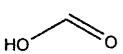
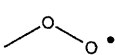
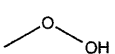
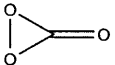
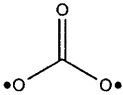
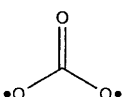
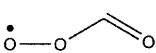
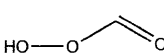
Fortunately, the library is structured in such a way that should simplify this process. Each species has its own directory, with subdirectories for the Gaussian03 and MOLPRO files. More importantly, each directory contains a CanTherm input and output file. The output file already contains everything necessary for the first two recommendations – the NASA polynomial coefficients and the spectroscopic data. If desired, it would be a trivially simple task to have CanTherm return the Cp values directly. These Cp values could then be collected and mined for an updated group-additivity scheme. Because each molecule has a CanTherm input file, and since CanTherm is written in Python and therefore easy to modify, it will be simple generate new values.

## **Appendix: Tabulated Results**

Table 4.2 – C1 species in new primary thermo library.

Number	Structure	Name	$\Delta_f H_{298}^0$	$S_{298}^0$	T1
			[kcal/mol]	[cal/mol/K]	
1	H	H	52.1	27.36	
2	H <sub>2</sub>	H <sub>2</sub>	-0.01	31.09	0.006
3	C	C	171.29	35.54	
4	CH	CH (doublet)	142.34	42.27	0.009
5	<sup>1</sup> CH <sub>2</sub>	CH <sub>2</sub> (singlet)	102.52	45.14	0.009
6	<sup>3</sup> CH <sub>2</sub>	CH <sub>2</sub> (triplet)	93.85	46.59	0.012
7	CH <sub>3</sub>	methyl	35.25	46.44	0.005
8	CH <sub>4</sub>	methane	-17.53	44.41	0.008
9	O	O	59.64	36.4	
10	OH	OH	8.69	42.53	0.007
11	H <sub>2</sub> O	H <sub>2</sub> O	-58.46	45.02	0.007
12	CO	CO	-26.44	47.14	0.019
13	$\bullet \equiv \text{O}$	HCO	10.08	53.51	0.026
14	$\equiv \text{O}$	formaldehyde	-26.22	52.16	0.016
15	$\text{—O} \bullet$	methoxy	4.87	54.42	0.021
16	$\bullet \text{—OH}$	hydroxymethyl	-3.84	58.19	0.018

Table 4.2 – Continued

Number	Structure	Name	$\Delta_f H_{298}^0$	$S_{298}^0$	T1
			[kcal/mol]	[cal/mol/K]	
17		methanol	-48.47	57.18	0.009
18		O <sub>2</sub>	0.68	46.74	0.007
19		HO <sub>2</sub>	3.07	54.61	0.037
20		HOOH	-32.55	55.78	0.011
21		CO <sub>2</sub>	-94.36	50.99	0.018
22		HOCO	-44.11	60.19	0.024
23		formyloxy	-29.51	59.94	0.024
24		formic acid	-90.87	59.46	0.017
25		methylperoxy	3.82	64.41	0.036
26		methyl-hydroperoxide	-30.39	67.11	0.011
27		cCO <sub>3</sub>	-38.79	60.99	0.02
28		CO <sub>3</sub> (singlet)	-33.39	62.94	0.024
29		CO <sub>3</sub> (triplet)	-16.99	65.76	0.069
30		formylperoxy	-24.8	66.19	0.031
31		formylhydroperoxide	-68.9	67.24	0.019

**Table 4.3** – C2 species in new primary thermo library.

Number	Structure	Name	$\Delta_f H_{298}^0$	$S_{298}^0$	T1
			[kcal/mol]	[cal/mol/K]	
32	$\equiv\equiv$	C <sub>2</sub> (singlet)	197.56	45.46	0.041
33	$\bullet\equiv\equiv\bullet$	C <sub>2</sub> (triplet)	200.8	47.81	0.020
34	HC <sub>2</sub>	HC <sub>2</sub>	137.14	51.64	0.017
35	$\equiv$	acetylene (singlet)	56.1	47.73	0.013
36	$\bullet\equiv\bullet$	acetylene (triplet)	159.03	54.26	0.011
37	${}^1\text{H}_2\text{CC}$	H <sub>2</sub> CC (singlet)	99.43	54.47	0.018
38	${}^3\text{H}_2\text{CC}$	H <sub>2</sub> CC (triplet)	146.96	55.63	0.021
39	$\equiv\bullet$	vinyl	72.2	55.78	0.017
40	$\equiv$	ethene (singlet)	13.55	52.25	0.011
41	$\bullet\text{---}\bullet$	ethene (triplet)	79.58	57.01	0.011
42	$\text{---}\bullet$	ethyl	29.43	59.12	0.010
43	$\text{---}$	ethane	-19.5	54.73	0.008
44	${}^1\text{C}_2\text{O}$	C <sub>2</sub> O (singlet)	110.61	53.61	0.023
45	${}^3\text{C}_2\text{O}$	C <sub>2</sub> O (triplet)	91.89	55.84	0.028
46	$\bullet\equiv\text{c}=\text{o}$	ketenyl	37.64	58.80	0.026

Table 4.3 – Continued

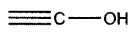
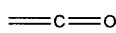

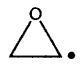
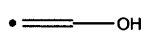
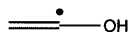

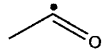

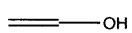
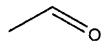
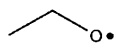
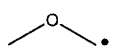
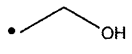
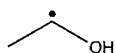
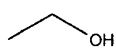
Number	Structure	Name	$\Delta_f H_{298}^0$	$S_{298}^0$	T1
			[kcal/mol]	[cal/mol/K]	
47		ethynol	23.15	59.10	0.013
48		ketene	-10.78	57.63	0.017
49		oxirene	65.92	60.48	0.014
50		oxiranyl	40.22	60.35	0.022
51		2-hydroxyl-vinyl	32.17	62.75	0.016
52		1-hydroxyl-vinyl	28.54	64.12	0.019
53		vinoxy	4.75	61.85	0.023
54		acetyl	-1.95	-1.95	0.022
55		oxirane	-12.07	57.94	0.011
56		ethenol	-29.12	62.18	0.013
57		acetaldehyde	-39.24	62.99	0.015
58		ethoxy	-2.66	66.84	0.020
59		methoxy-methyl	0.73	67.32	0.017
60		2-hydroxyl-ethyl	-5.79	69.42	0.012
61		1-hydroxyl-ethyl	-12.92	68.09	0.015
62		ethanol	-56.24	66.77	0.009

Table 4.3 – Continued

Number	Structure	Name	$\Delta_f H_{298}^0$	$S_{298}^0$	T1
			[kcal/mol]	[cal/mol/K]	
63		dimethyl-ether	-43.93	63.86	0.010
64	$\text{o}=\text{c}=\text{c}=\text{o}$	ethenedial (singlet)	18.31	90.63	0.021
65	$\bullet\text{o}-\text{c}\equiv\text{c}-\text{o}\bullet$	ethenedial (triplet)	5.6	61.18	0.026
66		1,2-dionyl-ethyl	-14.75	67.19	0.020
67		1-hydroxyl-ketenyl	4.91	65.75	0.020
68		glyoxal	-50.74	64.55	0.016
69		vinylperoxy	28.07	68.05	0.035
70		2-hydroperoxyl-vinyl	54.77	74.80	0.016
71		formyl-methoxy	-18.04	70.09	0.029
72		formyloxy-methyl	-37.47	70.12	0.019
73		methoxyl-formyl	-37.83	70.50	0.023
74		oxiranyloxy	-8.75	66.41	0.035
75		acetyloxy	-44.66	67.74	0.021
76		2-hydroxyl-vinoxy	-55.81	67.80	0.018
77		vinyl-hydroperoxide	-7.9	73.04	0.014

Table 4.3 – Continued

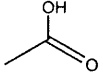
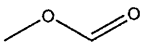
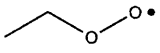
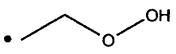
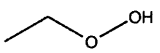
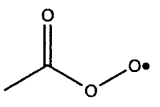
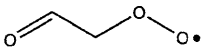
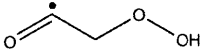
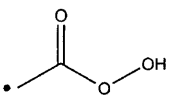
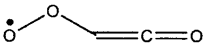
Number	Structure	Name	$\Delta_f H_{298}^0$	$S_{298}^0$	T1
			[kcal/mol]	[cal/mol/K]	
78		acetic acid	-103.24	68.19	0.015
79		methyl formate	-85.78	69.00	0.016
80		ethylperoxy	-4.07	74.15	0.032
81		hydroperoxyl-ethyl	12.88	79.03	0.013
82		ethyl-hydroperoxide	-37.78	75.15	0.012
83		acetylperoxy	-36.67	76.21	0.029
84		vinoxperoxy	-18.09	77.55	0.031
85		hydroperoxyl-acetyl	-17.2	79.32	0.020
86		hydroperoxyl-vinoxy	-34.67	73.73	0.021
87		ketenylperoxy	20.5	75.79	0.043



Table 4.4 – C3 species in new primary thermo library.

Number	Structure	Name	$\Delta_f H_{298}^0$	$S_{298}^0$	T1
			[kcal/mol]	[cal/mol/K]	
88		propargyl	86.21	60.63	0.023
89		allene	47.11	59.34	0.013
90		propyne	46.16	58.99	0.012
91		cyclopropene	69.38	58.01	0.010
92		allyl	42.04	61.54	0.011
93		cyclopropyl	71.09	61.58	0.012
94		1-methyl-vinyl	61.96	65.41	0.015
95		2-methyl-vinyl	65.51	64.88	0.015
96		cyclopropane	14.26	59.42	0.008
97		propene (singlet)	6.24	63.59	0.010
98		propene (triplet)	72.5	70.43	0.012
99		n-propyl	25.18	69.28	0.010
100		i-propyl	26.01	68.90	0.011
101		propane	-24.27	66.07	0.008
102		propynal	33.48	65.54	0.016
103		propadienal	33.02	66.05	0.019

Table 4.4 – Continued



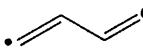
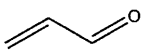

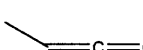
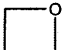
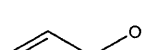
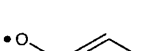
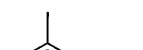
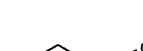




Number	Structure	Name	$\Delta_f H_{298}^0$	$S_{298}^0$	T1
			[kcal/mol]	[cal/mol/K]	
104		vinyl-formyl	24.52	67.91	0.022
105		1-formyl-vinyl	46.45	70.26	0.019
106		2-formyl-vinyl	45.67	67.33	0.019
107		acrolein (singlet)	-14.2	65.35	0.015
108		acrolein (triplet)	47.18	69.68	0.021
109		methyl-ketene	-13.82	68.58	0.016
110		oxetene	13.88	62.93	0.015
111		allyloxy	25.06	72.63	0.020
112		propen-1-oxy	-4.44	71.94	0.020
113		propen-2-oxy	-6.16	72.93	0.019
114		2-formyl-ethyl	7.36	75.41	0.015
115		oxiranyl-methyl	26.63	68.55	0.015
116		vinoxyl-methyl	22.8	72.91	0.018
117		2-methyl-vinoxy	-4.96	71.27	0.020
118		propionyl	-6.18	74.68	0.019

Table 4.4 – Continued

Number	Structure	Name	$\Delta_f H_{298}^0$	$S_{298}^0$	T1
			[kcal/mol]	[cal/mol/K]	
119		acetone	-51.21	70.90	0.014
120		propanal	-43.67	73.50	0.014
121		propen-1-ol	-34.7	70.85	0.012
122		propen-2-ol	-39.44	69.60	0.012
123		propene oxide	-21.56	67.16	0.011
124		allyl-alcohol	-28.99	72.64	0.011
125		n-propoxy	-7.25	106.11	0.018
126		i-propoxy	-9.85	72.53	0.018
127		3-hydroxyl-1-propyl	-10.69	79.48	0.011
128		1-hydroxyl-1-propyl	-17.02	78.74	0.014
129		1-methyl-2-hydroxyl-ethyl	-12.95	80.42	0.012
130		2-hydroxyl-1-propyl	-14.14	76.56	0.011
131		1-methyl-1-hydroxyl-ethyl	-22.33	74.56	0.014
132		ethoxymethyl	-6.92	76.06	0.016

Table 4.4 – Continued

Number	Structure	Name	$\Delta_f H_{298}^0$	$S_{298}^0$	T1
			[kcal/mol]	[cal/mol/K]	
133		2-methoxyethyl	-0.95	77.59	0.011
134		1-methoxyethyl	-8.27	75.54	0.016
135		n-propanol	-60.69	76.31	0.009
136		i=propanol	-64.83	74.20	0.010
137		ethyl-methyl-ether	-51.54	73.52	0.010
138		allylperoxy	24.09	80.56	0.030
139		propen-1-peroxy	21.11	76.70	0.033
140		propen-2-peroxy	17.91	76.20	0.033
141		2-formyl-ethoxy	-26.05	82.32	0.019
142		1-formyl-ethoxy	-28.15	78.17	0.026
143		acetyl-methoxy	-32.35	78.33	0.033
144		allyl-hydroperoxide	-11.23	82.03	0.012
145		propen-1-hydroperoxide	-15.29	81.56	0.013
146		propen-2-hydroperoxide	-19.92	78.90	0.013

Table 4.4 – Continued

Number	Structure	Name	$\Delta_f H_{298}^0$	$S_{298}^0$	T1
			[kcal/mol]	[cal/mol/K]	
147		1-formyl-ethyl-hydroperoxide	-65.73	85.49	0.014
148		2-formyl-ethyl-hydroperoxide	-63.09	89.68	0.014
149		acetyl-methyl-hydroperoxide	-70.08	85.82	0.014
150		oxiranyl-methyl-hydroperoxide	-42.37	80.91	0.013
151		n-propylperoxy	-8.38	83.49	0.029
152		i-propylperoxy	-12.99	80.87	0.029
153		3-hydroperoxyl-1-propyl	7.26	88.49	0.012
154		3-hydroperoxyl-2-propyl	5.1	88.21	0.013
155		2-methyl-2-hydroperoxyl-ethyl	4.5	85.49	0.013
156		n-propyl-hydroperoxide	-43.76	84.19	0.011
157		i-propyl-hydroperoxide	-48.3	82.43	0.011

**Table 4.5** – C4 species in new primary thermo library.

Number	Structure	Name	$\Delta_f H_{298}^0$	$S_{298}^0$	T1
			[kcal/mol]	[cal/mol/K]	
158		1,3-butadiyne	113.13	59.15	0.014
159		but-3-yn-1-en-1-yl	132.99	67.35	0.016
160		but-1-yn-3-en-1-yl	121.56	70.27	0.021
161		1-buten-3-yne	71.86	66.24	0.013
162		1,2,3-butatriene	79.7	65.15	0.015
163		1,2-butadien-1-yl	79.11	71.83	0.020
164		1,3-butadien-2-yl	86.31	99.28	0.015
165		1-butyne	42.02	69.18	0.011
166		1,2-butadiene	40.97	69.71	0.012
167		1,3-butadiene	28.95	65.82	0.012
168		1-methyl-allyl	33.82	71.99	0.013
169		2-methyl-allyl	34.07	70.24	0.020
170		1-butyl	20.65	78.53	0.010
171		2-butyl	18.34	78.98	0.011
172		n-butane	-28.28	76.34	0.009

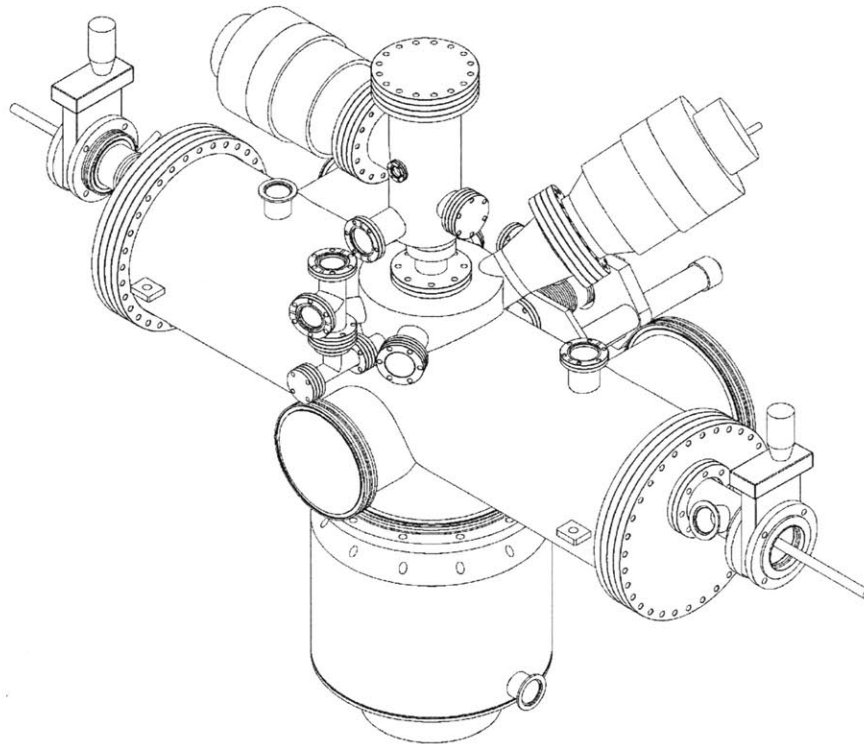






## Chapter 5

# Design of Time-of-Flight Mass Spectrometer Gas Sampling System



## 5.1 Introduction

This chapter details the contributions I made towards the design of a novel experimental apparatus. The new design will modify the existing laser flash-photolysis absorption-spectroscopy system to include simultaneous measurement of species concentrations via time-of-flight mass spectrometry. My work was focused primarily on the gas dynamics of the design, i.e. getting the sample gas from the photolysis region to the detector as quickly as possible with as few collisions as possible.

### 5.1.1 Motivation: Vinyl + O<sub>2</sub>, and the need for a new way to measure radical kinetics

Large scale kinetic models require thousands of elementary rate coefficients. Some reactions are more important than others, and it is critical that these rate coefficients be determined as accurately as possible. An ideal method for validating the accuracy of the rate coefficients is to combine experimentally measured rates with theoretical calculations obtained from computational quantum chemistry. If the two methods agree to within statistical uncertainty, then we can feel confident that the rate coefficients are suitably accurate. An example of this agreement between experiment and theory is the work I did with Dr. Huzeifa Ismail on the kinetics of the vinyl radical with alkenes, as detailed in Chapter 1. Because the computational methods I used to compute the rate coefficients were in excellent agreement with the measured rates of Dr. Ismail, I was able to use those same methods to estimate the rate coefficients for previously unmeasured systems.

Although the current spectroscopy lab can provide highly accurate measurement of reaction rates, it is nonetheless limited in the number of species it can study. In order for the current system to work, we need to insure that (i) we know the UV-vis absorption features of the radical in question (typically – though not necessarily – a reactant produced from the photolysis shot), (ii) we can access the appropriate absorption bands with our probe laser, and (iii) no other species are produced that have strong absorption cross sections at the same wavelength.

As detailed in Dr. Ismail's thesis [35], the third condition was not satisfied for the

reaction of the vinyl radical with molecular oxygen. The precursor used to generate the vinyl radical, vinyl iodide, creates I atoms upon photolysis. A small fraction of these I atoms reacted with some oxygenated intermediates – presumably vinylperoxy – to form iodine monoxide, IO. The absorption cross section of iodine monoxide at 423 nm is more than one order of magnitude larger than the cross section of the vinyl radical at the same wavelength. Even though the total concentration of iodine monoxide formed is quite small (e.g. less than one percent of the vinyl), it was sufficiently large to swamp the signal. Thus, it was not possible to measure this important reaction using the current system.

Early on, I searched for alternate methods for measuring this reaction rate. One alternative would have been to measure the rate of production of one of the products. The main bimolecular channel in this reaction is  $\text{vinyl} + \text{O}_2 \rightarrow \text{HCO} + \text{CH}_2\text{O}$  [67]. It should be possible to measure the rise time – and therefore reaction time constant – of HCO by absorption spectroscopy. The Ti:Sapphire laser is tunable between 690 - 1080 nm, and using an external doubler or tripler allows us to extend this range to 230 - 540 nm. Although HCO has a strong absorption peak at 614.5 nm [55], this wavelength is squarely in the gap of our current system, 540 - 690 nm. Thus, using HCO as our species for detection failed to satisfy the second criterion from above and would necessitate the procurement of a new probe laser.

A second alternative I considered was to look for a non-iodinated precursor. I considered two possible precursors: vinyl bromide ( $\text{C}_2\text{H}_3\text{Br}$ ) and methyl vinyl ketone (MVK). Since the analogous monoxide for vinyl bromide, bromide monoxide, does not have an absorption feature at 423 nm, its formation should not affect our signal. There were two problems with  $\text{C}_2\text{H}_3\text{Br}$  that discouraged us from trying it. The first difficulty with  $\text{C}_2\text{H}_3\text{Br}$  is that it requires a photolysis wavelength of 248 nm, rather than the 266 nm we had at the time. Generating a photolysis pulse at 248 nm would require borrowing or purchasing an excimer laser. Even if we could have used an excimer, the resulting vinyl radicals would be “hot”, since they will absorb some of the higher-energy UV light [108]. These hot reactants could influence the kinetics, and we were interested in producing vinyl with longer wavelength photolysis beams to avoid this issue.

The other alternate, MVK, also did not work. MVK is frequently photolyzed at 193

nm as a source for vinyl radicals. Dr. Ismail and I tried to photolyze MVK at 266 nm, but we were unable to detect any vinyl. The vapor pressure of MVK is 71 Torr at room temperature. We used a bubbler to increase the partial pressure of MVK, allowing us to increase the reactor pressure to 100 Torr. Nonetheless, we never observed a vinyl signal. The most likely reason that we didn't see any signal is that MVK has a low absorption cross section at 266 nm, and that absorption at this wavelength might not necessarily lead to photodissociation. The absorption cross section of MVK increases by more than an order of magnitude as the wavelength is increased from 266 nm to  $\sim 360$  nm. At the time, it was not known if absorption at 355 nm would necessarily lead to radical fragmentation. Furthermore, replacing the external doubling crystal with the tripling crystal for the old Nd:YAG laser was a time-consuming and laborious process. Since we needed the 266 nm laser for other experiments (e.g. vinyl + vinyl), we did not attempt to photolyze MVK at 355 nm. As it turns out, converting the Nd:YAG to produce 355 nm light would have been a waste of time. A recent experimental and theoretical analysis concluded that photolysis of MVK at 308 nm does not produce vinyl radicals [12]. Photolysis at 193 nm promotes the  $\pi \rightarrow \pi^*$  transition, whereas photolysis at 308 nm promotes the  $n \rightarrow \pi^*$  transition. The authors were unable to detect ethane or 1,3-butadiene after each photolysis shot, thereby suggesting that methyl and vinyl were not formed. Presumably photolysis at 355 nm would be no different than 308 nm.

My experience troubleshooting the vinyl + O<sub>2</sub> system led me to consider using mass spectrometry as a compliment to our absorption spectroscopy apparatus. Time-of-flight mass spectrometry seemed like a natural measurement technique for a pulsed system; it captures the entire mass spectra following each photolysis pulse, so we would not be limited to tracking only one mass per event. Furthermore, thanks to advances in high-voltage electronics, it is now possible to pulse the egun used in electron impact ionization at a frequency fast enough to resolve the kinetics of each photolysis shot (e.g.  $>100$  kHz). By capturing a snapshot of all the mass spectrum every  $<50 \mu\text{s}$ , we can measure the rise or decay of each mass following a photolysis shot.

Mass spectrometry is not without its shortcomings. Unlike spectroscopic techniques, which allow us to measure changes in the gas composition *in situ*, mass spectrometry re-

quires that the gas be removed from the reactor and transported to an ionization region before it can be detected. Unless great care is taken with the design of this gas sampling system, the gas will continue to react, potentially rendering it useless for kinetic studies. Thus, the primary challenge in using mass spectrometry to measure chemical kinetics is ensuring that the gas composition does not change significantly from the time it is sampled to the time it is measured. In order to learn more about (i) time-of-flight mass spectrometry for kinetic studies, and (ii) equipment design for molecular beam gas sampling, I went to Argonne National Laboratory.

## **5.1.2 Argonne National Laboratory**

I spend six months in 2008 at Argonne National Laboratory as a Thesis-Parts Fellow, working under the tutelage of Dr. Robert Tranter in the Chemical Science and Engineering Division. Dr. Tranter has two labs at Argonne devoted to measuring rate coefficients for combustion chemistry. One lab uses a shock tube. The second lab – currently under construction – will use a fast-flow reactor. I performed experiments in the shock tube lab, and I helped design and construct components of the flow reactor.

### **Shock Tube Studies of Methyl-Iodide Decomposition and Vibrational Relaxation and Subsequent Methyl Radical Recombination**

In order to learn more about time-of-flight mass spectrometry (TOF-MS), I assisted a post-doc in Dr. Tranter's lab, Xueliang Yang, in shock tube experiments. Dr. Tranter has developed a detailed mechanism for methyl radical pyrolysis. In order to make the mechanism as valid as possible, he has considered several precursors for methyl radicals, most recently acetaldehyde and diacetyl. The purpose of these experiments was to characterize methyl iodide,  $\text{CH}_3\text{I}$ , as a new and clean source for methyl radicals in shock tubes. Dr. Yang and I performed 108 experiments between 630 - 2200 K at pressures of 20, 66, 148, and 280 Torr. Measurements were performed using two techniques. First, a TOF-MS was used to measure the mass spectrum in the reflected shock wave. Second, laser Schlieren (LS) densitometry was used to measure the density gradient in the incident shock wave.

Based upon these experiments, we were able to refine and improve the methyl pyrolysis mechanism [106]. The TOF-MS was custom built by Dr. Tranter, using parts from R. M. Jordan Time of Flight Products. The gas was sampled from the shock tube via a small pin hole in the center of the end wall. This effluent was collimated by a nickel skimmer before reaching the high-voltage plate. The gas stream was ionized using electron impact. Although the egun was capable of firing at rates faster than 100 kHz, the TOF-MS was used as a supplement to the laser Schlieren, rather than a primary source of kinetic data. At 100 kHz, the sampling rate (i.e. every 50  $\mu$ s) was too slow to get reliable time constants for the high temperature experiments. Although the electronics could handle a faster egun frequency, in practice this was not helpful. If the ionization frequency is too fast, then the ionization packets will overlap. In other words, the fastest (i.e. lightest) species from one pulse will reach the detector before the slowest species from the previous pulse. These slower, heavier species from previous pulses would appear as phantom species, suggesting the presence of species with a certain mass/charge ratio that is not in fact present. Although it is possible to deconvolute overlapping mass spectra, it is a difficult and error-prone process. Thus, in order to avoid packet overlap, the range of masses in the gas – and thus the difference in time between the fastest and slowest masses – sets an upper limit on the ionization frequency. At the highest temperatures of the shock tube, this rate was too slow to resolve the kinetics. Hence, laser Schlieren densitometry. The LS technique measures the rate of change in the density gradient in the incident shock. This density gradient is related in turn to the change in chemical composition of the gas mixture. Measuring the cumulative effect of all the chemical reactions on the rate of change of the density gradient is an excellent experimental technique for validating kinetic mechanisms.

### **Construction of a Fast-Flow Reactor**

In addition to performing the shock tube experiments, I assisted in the construction of a new reactor. The purpose of this project was to familiarize myself with vacuum technology, differential pumping, and the fundamentals of molecular beams. It also provided an opportunity to work with and create 2D CAD drawings to be supplied to a machinist.

## 5.2 Design of the TOF-MS Reactor

### 5.2.1 Comparison with other TOF-MS Reactors

When I returned to MIT, I began to work with a colleague, Joshua Middaugh, on the design of the new reactor. Our objective was to design a new laser flash photolysis reactor that would allow us to use a time-of-flight mass spectrometer to measure chemical kinetics while preserving the preexisting multi-pass laser absorption spectroscopy (LAS) capability. This simultaneous TOF-MS/LAS system would be a one-of-a-kind reactor for measuring reactions under combustion relevant conditions: The LAS would continue to provide high-accuracy measurements of the reaction rates, and the TOF would provide concentration profiles of all the product channels. The combination of these two pieces of information would provide unprecedented data for complex reactions. A second object in our design was to provide some flexibility with respect to ionization sources. Specifically, we wanted the ability to use either electron impact (EI) or laser photoionization (PI). Although we worked closely together on all aspects of the design, we settled on a natural division of labor: I would focus on the gas dynamics aspects of the design, and Josh would focus on the photoionization process.

Although using mass spectrometry with laser flash photolysis in a slow flow or static reactor for kinetics is not new, combining this technique with multi-pass absorption spectroscopy is. The incorporation of the LAS system into the reactor presented some unique design challenges. All the previous reactors in the literature have one thing in common: the gas is sampled from a small pinhole in the side of the reactor tube. Because the pinhole is typically on the order of 200  $\mu\text{m}$  in diameter, the volume of gas that is sampled is quite small and is limited to the area near the surface of the tube. In these experiments, the entire cross-section of the tube is photolyzed, thereby ensuring that the reactive gas is sampled. However, because the photolysis beam is in contact with the inner surface of the reactor, there is concern that the UV radiation may cause the surface to become catalytically active, particularly for reactors made of stainless steel.

In the current LAS reactor, only a narrow annular region is photolyzed and probed (e.g. a 1.5 cm diameter photolysis beam centered in a 2.5" diameter tube). Heterogeneous

contamination is not a concern, since neither the photolysis beam nor probe beam is in contact with the wall. Clearly adding a simple pinhole to the current reactor would not work, since the mass spectrometer would only sample unphotolyzed gas. The other alternative – increasing the photolysis beam diameter – would not work with the multi-pass cell. It would be possible to combine a full-bore photolysis pulse with a single-pass probe beam, but this system would severely decrease our LAS signal-to-noise. The multi-pass Harriott cell – shown in Figure 5-1 – increases the overlap pathlength by up to a factor of forty, which permits detection of species at much lower absorption cross sections  $\times$  concentration values, and it is this level of detection that we wanted to preserve. The challenge, then, amounts to this: how can we sample the gas from within the annular photolyzed region, quench the gas so that all reactions cease and the composition is frozen, transport it through the unphotolyzed region to the ionization chamber and thence to the detector, while simultaneously not interfering with the laser absorption measurements?

## 5.2.2 Gas Sampling System Overview

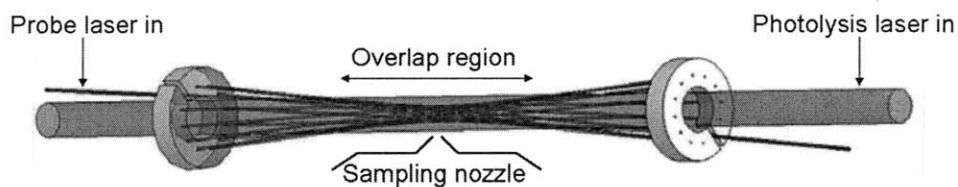
An isometric projection of the new reactor is shown on the chapter title page. From the gas dynamics perspective, the new reactor has three regions: a high-pressure reactor cell, a low-vacuum region, and a high-vacuum region. The high-pressure reactor cell will replace the current reactor tube; it is shown in Figure 5-2 and is described in greater detail in the next section. The low-vacuum region is a larger tube, 10" in diameter, that surrounds the reactor cell. This volume is the first stage in the differential pumping system and is maintained between  $10^{-3}$  and  $10^{-4}$  Torr by a 2000 L/s turbomolecular pump. The gas is ionized in the high-vacuum chamber. The high-vacuum chamber is the second stage in the differential pumping system and is maintained between  $10^{-6}$  and  $10^{-7}$  Torr by a 350 L/s turbomolecular pump. Gas is sampled from the reactor cell via a 200  $\mu\text{m}$  orifice. The gas expands into low-vacuum chamber, where it is collimated by a nickel skimmer into the high-vacuum chamber. In the new design, the total distance from the nozzle orifice to the snout is 6.1 cm. After several rounds of consultation with the design teams at Kurt J. Lesker – the company we chose to manufacture the new reactor – we determined what was



feasible from the metal fabrication standpoint. A blow-up of the gas sampling system is shown in Figure 5-3.

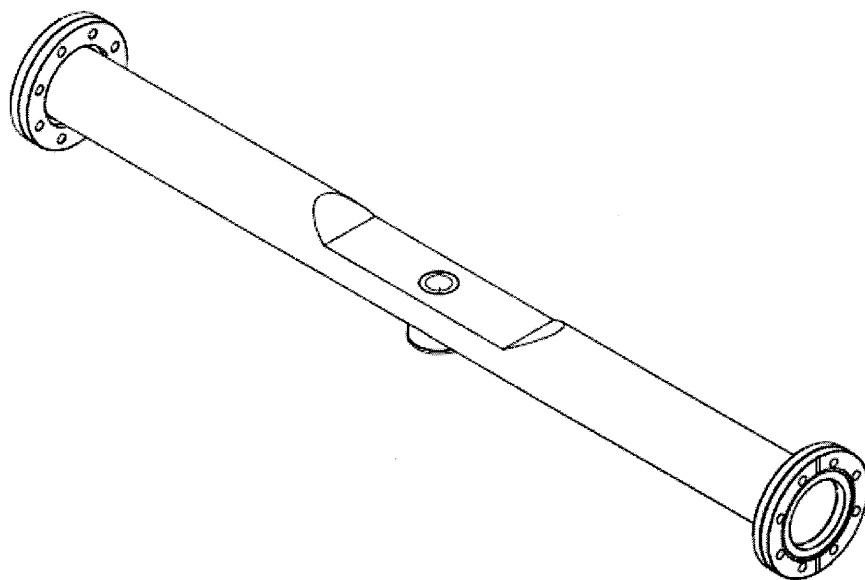
### 5.2.3 Interference with Laser Absorption Spectroscopy

The LAS probe beam forms a narrow waist as it passes back and forth between the two Harriott mirrors, as seen in Figure 5-1. The overlap region between the wider photolysis beam and the narrow probe beam is roughly 60 cm in length, depending upon the width of the photolysis beam and the initial angle of the probe beam.

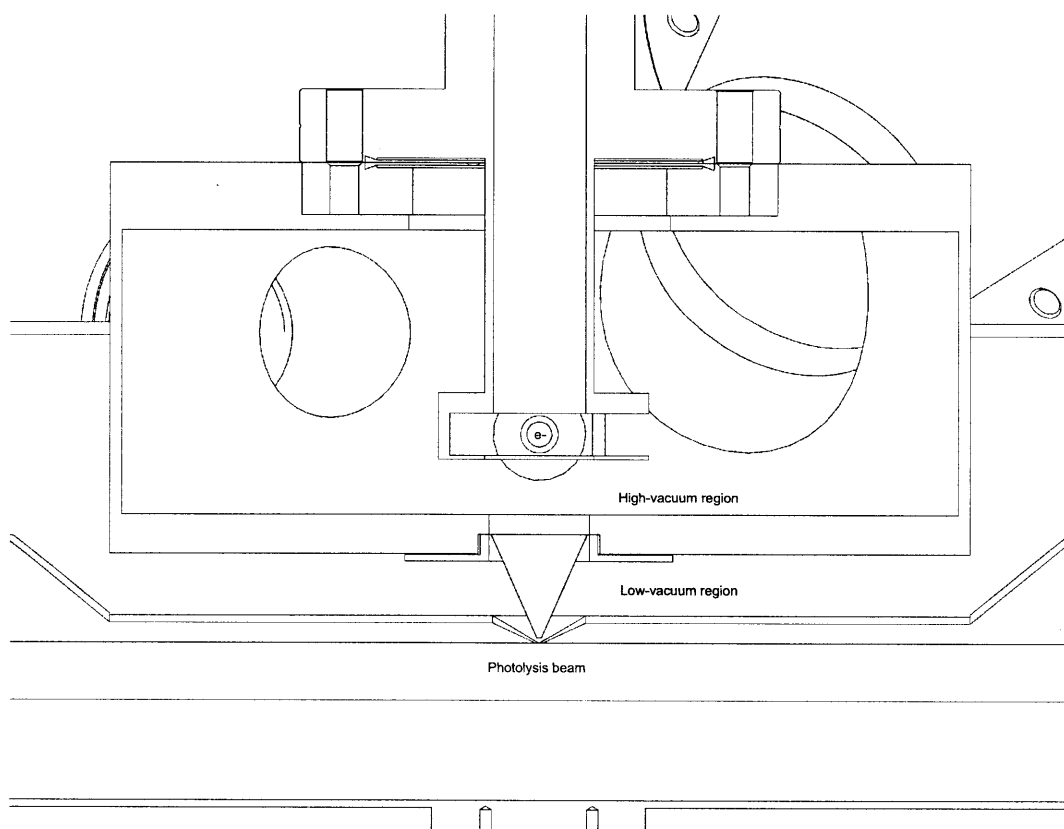


**Figure 5-1** – Location of sampling nozzle in the Herriott multi-pass cell

Our design is to sample from the center of the overlap region. As long as the width of the sampling mechanism is less than the width of the overlap region, the sampling mechanism will not interfere with the path of the probe laser. To achieve this goal, we redesigned the flow tube so that a central section of the tube is replaced by a flat plate. This plate is 8 inches long and is recessed 1.1 inches deep, shown in Figure 5-2. A small cone protrudes from the center of the plate into the reactor tube. This cone is 5 mm high, 1.7 mm wide at the tip, and 22 mm wide at the base; the outer angle of the cone is  $130^\circ$ , and the inner angle of the cone is  $120^\circ$ . At the tip of the cone is a  $200\ \mu$  orifice. This cone forms the sampling nozzle. The tip of the cone is positioned against the edge of the photolysis beam. Gas is sampled through the orifice and expands outside the reactor tube. A cartoon of this nozzle relative to the two laser beams – not drawn to scale – is shown in the bottom of Figure 5-1. There are two issues regarding this design that needed to be resolved: first, we had to ensure the nozzle samples gas only from within the photolysis region, and second, we had to ensure that the flow constriction caused by the sampling apparatus does not substantially decrease the pressure at the sampling tip.



**Figure 5-2** – The new reactor tube. The sampling orifice is located within the small circle on the top of the flat region. (image courtesy of Joshua Middaugh)



**Figure 5-3** – Cross section of the new reactor, illustrating the high-pressure reactor cell, the low-vacuum chamber, and the high-vacuum chamber. (image courtesy of Joshua Middaugh)

## 5.2.4 Volume of Sample Gas

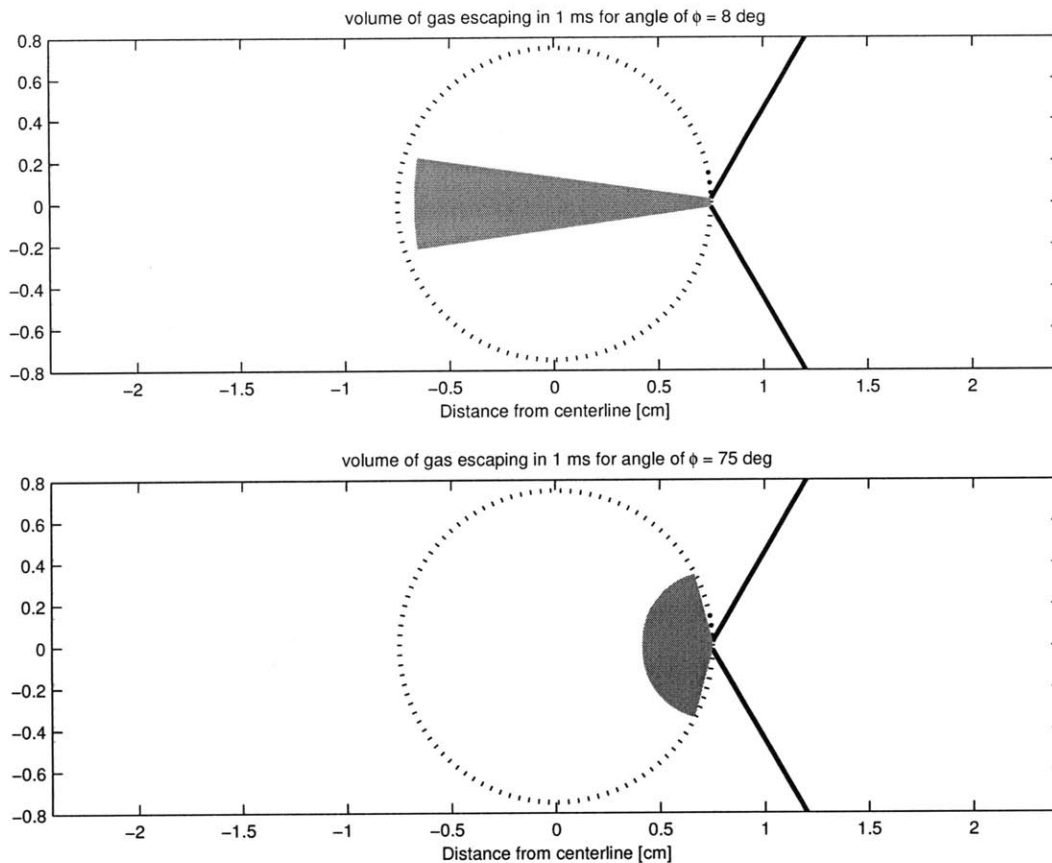
It is not possible to predict exactly the flow profile of the gas leaving the reactor cell and flowing out the orifice. Nonetheless some reasonable estimates can be made to ensure that only photolyzed gas enters the nozzle. In these calculations, I have assumed (i) that the nozzle is positioned to within a few tens of microns of the photolysis pulse, and (ii) that the gas exits the orifice at the speed of sound. The first assumption is reasonable, since we can adjust the position of the nozzle relative to photolysis laser with a micrometer-scaled XYZ translation stage. The second assumption is reasonable, since, as will be detailed in a later section, the pressure drop between the reactor tube and the first stage of the differential pumping is large enough to ensure a supersonic gas expansion.

The volume of gas inside the reactor that will exit through the orifice can be approximated as a spherical cone. The exact angle of this cone is not precisely known, since it depends upon the surface features and the angle of nozzle, as well as the boundary layers created by the flow fields. As shown below, as long as this angle is within some reasonable estimate, the nozzle should only sample gas from within the photolysis region.

To estimate the volume of gas that leaves the cell, I assumed that the volumetric flow rate of gas leaving the cell is equal to the area of the orifice,  $A_{\text{orifice}}$ , times the speed of sound for the gas,  $v_{\text{sound}}(T; \text{gas})$ , and I multiplied this volumetric flow rate by a time,  $\tau$ . Since most of our kinetics occur on a microsecond time scale, I chose 1 ms as an upper limit. Next, I calculated the volume of a spherical cone of fixed angle  $\phi$  and unknown height,  $h$ . I set these two volumes equal, and I solved for the height,  $h$ .

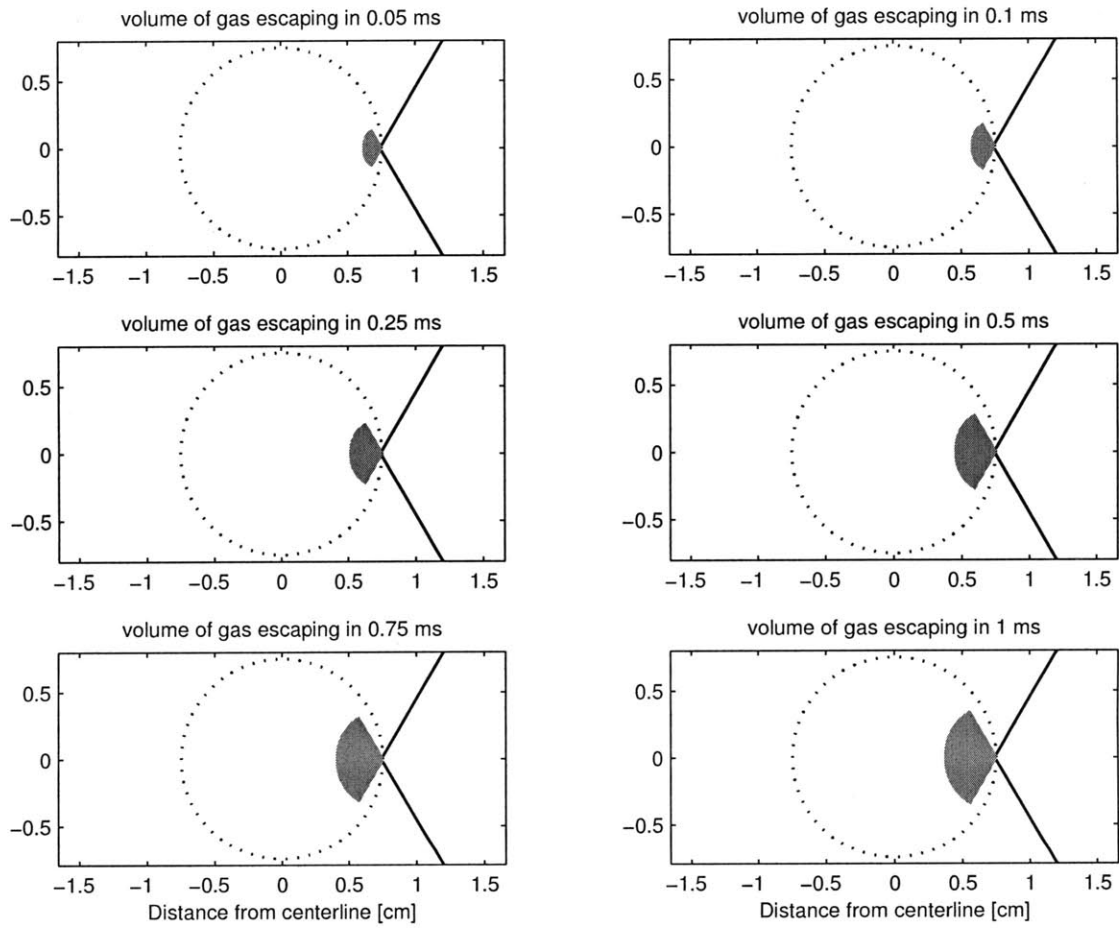
$$V_{\text{spherical cone}}(\phi, h) = A_{\text{orifice}} v_{\text{sound}}(T; \text{gas}) \tau \quad (5.1)$$

The results of this analysis are shown in Figure 5-4. Each plot is oriented looking down the barrel of the tube. The dotted line represents the diameter of the photolysis beam, here assumed to be 1.5 cm. The solid black line is the sampling nozzle, assuming an angle of 120°. The gray area represents the projection of the volume in the 2D plane. If the angle of the spherical cone is between 8 degrees and 75 degrees, then > 99.9% of the volume



**Figure 5-4 – Limiting cases for gas sampling cone**

of gas sampled in 1 ms will come from within the photolysis region. If we assume that the angle of the spherical cone is roughly equal to the inner angle of the nozzle,  $60^\circ$ , then we can plot how the volume evolves as a function of time. Figure: 5-5 illustrates how the sample gas volume would grow if gas were sampled every  $50 \mu\text{s}$ , (corresponding to a ionization rate of 100 kHz in an electron impact experiment). In both Figures 5-4 and 5-5, I have assumed a gas of pure Helium at 1,000 K, since this represents the worst possible case. Most experiments will involve heavier gases at cooler temperatures, and therefore the results will be even better. As a result of this study, we feel confident that the nozzle design will not pull in a significant volume of unphotolyzed gas.



**Figure 5-5** – Time evolution of the sample gas volume for  $\phi = 60^\circ$

## 5.2.5 Pressure Increase Around the Nozzle

As detailed above, the plate that supports the sampling nozzle is recessed into the flow tube. Consequently, the cross-sectional area of the tube is reduced, which leads to a pressure drop as the constrained gas accelerates around the plate. To estimate the severity of the pressure drop, I began with the energy balance, mass balance, and equation of state:

$$\frac{1}{2} (v_2^2 - v_1^2) + \int_{P_1}^{P_2} \frac{1}{\rho} dP = 0 \quad (5.2)$$

$$\rho_1 v_1 A_1 = \rho_2 v_2 A_2 \quad (5.3)$$

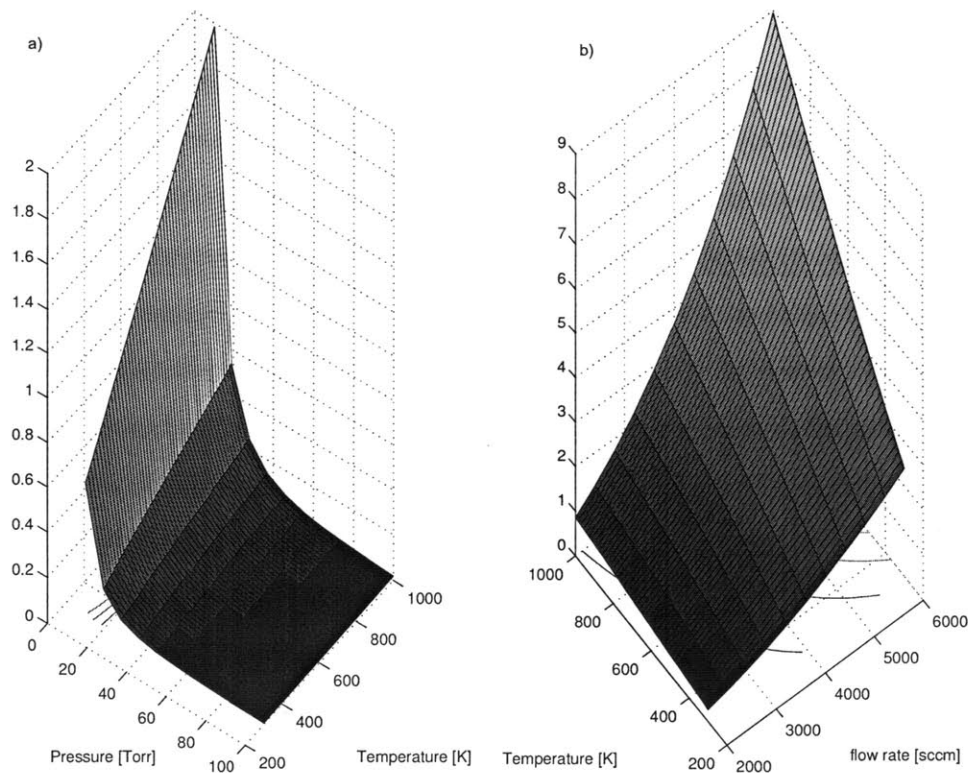
$$\rho = MW \frac{P}{RT} \quad (5.4)$$

where  $v$  is the velocity,  $P$  is the pressure,  $\rho$  is the density,  $A$  is the cross-sectional area, the subscript 1 refers to the region upstream of the plate, and the subscript 2 refers to the region of the plate. Assuming that the system is isothermal, these three equations can be combined to yield a single equation for the pressure drop:

$$\frac{1}{2} v_1^2 \left( \left( \frac{P_1}{P_2} \right)^2 \left( \frac{A_1}{A_2} \right)^2 - 1 \right) - RT \ln \left( \frac{P_1}{P_2} \right) = 0 \quad (5.5)$$

According to Equation (5.5), the pressure drop will increase as (i) the initial temperature is increased, (ii) the initial pressure is decreased, or (iii) the initial flow rate is increased. Equation (5.5) was solved for a broad range of temperatures, pressures, and flow rates. All of the previous experiments were performed between 10 and 100 Torr, 300 and 700 K, and with flow rates roughly of 3000 sccm (the fastest being 4500 sccm), so similar values were chosen here. It is unlikely that the pressures will change much outside of the 10 - 100 Torr range in the new reactor, based upon the pumping system. The new reactor is designed to be heated up to 1000 K, although in practice it is unlikely that we will be able to go much beyond 800 K. The flow rate will not deviate much beyond 3000 sccm, based upon the flow meters we have in place, so I chose a range of 2000 to 6000 sccm. The results

of this parametric analysis are shown in the following two figures. Figure 5-6a plots the percentage change in pressure under normal operating conditions: initial flow rate of 3000 sccm,  $10 < P < 100$  Torr, and  $300 < T < 1000$  K. The maximum change in pressure occurs at 10 Torr and 1000 K, but the pressure drop is still less than 2% the initial pressure. Figure 5-6b plots the percentage change in pressure at 10 Torr as a function of flow rate and temperature. As the flow rate is increased to 6000 sccm, the pressure drop increases to 9% at 1000 K. However, these conditions do not present a particularly realistic scenario. If the flow rate is kept below 4500 sccm, the temperature below 900 K, and the pressure above 10 Torr, then the pressure drop never rises above 4%. If the flow rate does need to exceed 4500 sccm, or if pressures below 10 Torr are required, then care must be made to ensure that the pressure drop does not exceed the tolerated range. Since the rate coefficients are expected to be a weak function of pressure under the stated range of operating conditions, a pressure drop of 5% is acceptable. Indeed, pressure fluctuations in this range are not significantly larger than the error in the capacitance manometers used to control the pressure.



**Figure 5-6** – Percent pressure drop at sample nozzle. (a) at 3000 sccm, (b) at 10 Torr.

## 5.2.6 Formation of the Supersonic Expansion

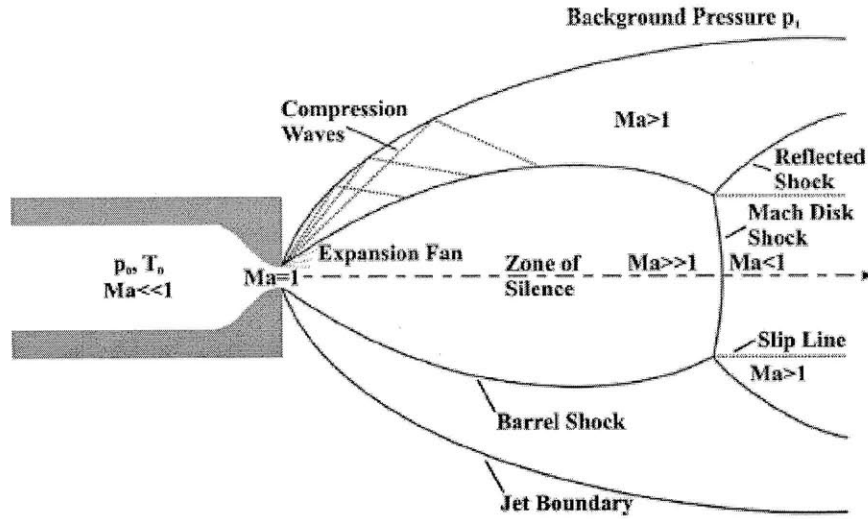


Figure 5-7 – Continuum free jet expansion, taken from [70].

Having established that the nozzle samples gas from within the photolysis region without perturbing either the flow field or the absorption probe laser, the next step is to quench the sampled gas. This quenching is accomplished by the rapid pressure drop between the reactor cell and low-vacuum region surrounding it. As the gas emerges from the nozzle, it expands supersonically. I have based the gas dynamics calculations in this section on three standard texts on the design of supersonic free jet expansions [70, 77, 76]. In instances where the three text gave slightly different parameters, I chose the parameters that would yield the most pessimistic result. The following analysis assumes that the gas expansion behaves ideally, which is to say that the gases are ideal, the flow is isentropic and compressible, and that viscous flow and heat conduction effects are negligible. The analysis begins with the energy balance per unit mass along a streamline:

$$\begin{aligned} v^2 &= 2(h_0 - h) \\ &= 2 \int_T^{T_0} \hat{C}_p dT \end{aligned} \quad (5.6)$$

Next I calculated the Mach number as the gas expands away from the orifice, using the



following empirical formula for axisymmetric expansion:

$$M = \begin{cases} 1.0 + A \left(\frac{x}{d}\right)^2 + B \left(\frac{x}{d}\right)^3 & \text{if } \frac{x}{d} < 1.0 \\ \left(\frac{x}{d}\right)^{\gamma-1} \left[ C_1 + \frac{C_2}{x/d} + \frac{C_3}{(x/d)^2} + \frac{C_4}{(x/d)^3} \right] & \text{otherwise} \end{cases} \quad (5.7)$$

where  $\gamma$  is the isentropic expansion factor (i.e. ratio of heat capacities),  $x$  is the position away from the orifice,  $d$  is the orifice diameter, and  $A$ ,  $B$ ,  $C_1$ ,  $C_2$ ,  $C_3$ , and  $C_4$  are constants tabulated in reference [70]. Once the Mach number was estimated, I computed the temperature, pressure, density, and velocity downstream of the orifice:

$$\frac{T}{T_{\text{reactor}}} = \left( 1 + \frac{\gamma-1}{2} M^2 \right)^{-1} \quad (5.8)$$

$$\frac{P}{P_{\text{reactor}}} = \left( 1 + \frac{\gamma-1}{2} M^2 \right)^{-\gamma/(\gamma-1)} \quad (5.9)$$

$$\frac{\rho}{\rho_{\text{reactor}}} = \left( 1 + \frac{\gamma-1}{2} M^2 \right)^{-1/(\gamma-1)} \quad (5.10)$$

$$v = M \sqrt{\frac{\gamma R T_{\text{reactor}}}{W}} \left( 1 + \frac{\gamma-1}{2} M^2 \right)^{-1/2} \quad (5.11)$$

The supersonic free jet continues to expand until it reaches the Mach disk, shown in Figure 5-7. Behind the Mach disk is the so-called “Zone of Silence”, and it is from within this region that the gas must be sampled. The location of the Mach disk,  $x_M$ , is given by an empirical formula:

$$\frac{x_M}{d} = \frac{2}{3} \sqrt{\frac{P_{\text{reactor}}}{P_{\text{orifice}}}} \quad (5.12)$$

In order to determine the location of the Mach disk, we need to estimate the pressure in the low-vacuum region surrounding the reactor tube. This pressure is related to the pumping speed at the plate and the temperature and pressure inside the reactor:

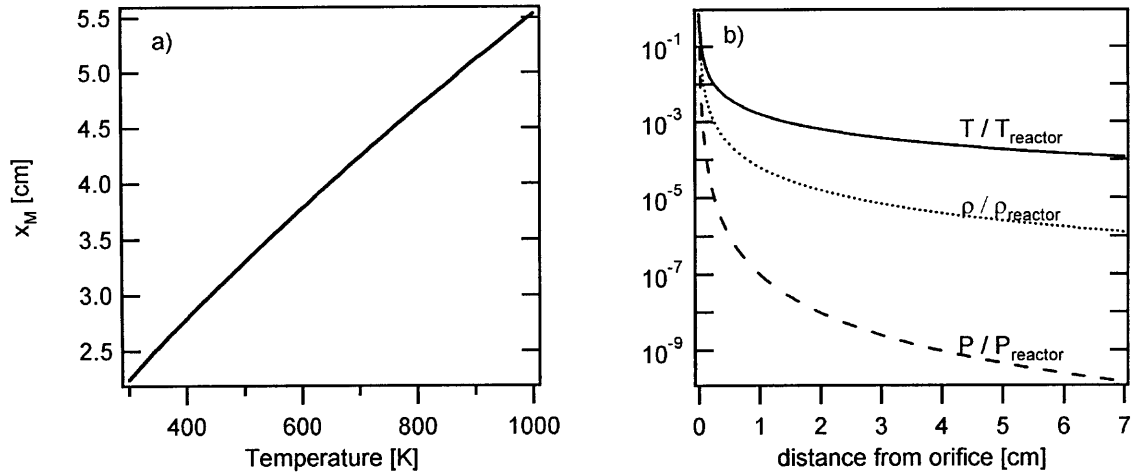
$$P_{\text{orifice}} = \frac{C}{S_{\text{orifice}}} \frac{T_{\text{low-vacuum}}}{T_{\text{reactor}}} \sqrt{\frac{300}{T_{\text{reactor}}}} P_{\text{reactor}} d^2 \quad (5.13)$$

where  $C$  is a constant, with units of  $[\text{L cm}^{-2} \text{s}^{-1}]$ , which depends upon the gas composition, and is tabulated for various gases in reference [70]. For the calculations I assumed that the temperature in the low-vacuum region is room temperature. To estimate the pumping speed at the orifice, I assumed a conductance loss of  $\sim 700 \text{ L/s}$ , based upon the geometry of the low-vacuum region, and a pumping speed of  $\sim 2000 \text{ L/s}$  for the large turbo pump. The resulting pumping speed at the orifice should be  $\sim 500 \text{ L/s}$ .

$$\frac{1}{S_{\text{orifice}}} = \frac{1}{S_{\text{pump}}} + \frac{1}{S_{\text{conductance}}} \quad (5.14)$$

Combining Equations (5.6) through (5.14), we can now compute the flow properties of the gas at any point in the expansion. Figure 5-8a plots the location of the Mach disk as a function of reactor temperature. The location of the Mach disk, and hence the zone of silence, increases with temperature. Thus, in order for the room temperature experiments to work, the gas must be sampled from within 2 cm of the orifice. If the skimmer cannot be placed within 2 cm, then the room temperature experiments will result in sampling from the nonisentropic region, and the kinetic measurements will not be valid. Figure 5-8b plots the free jet properties as a function of distance from the orifice. In both plots, the gas is assumed to be pure Helium, since it represents the worst case scenario. The temperature of the gas is reduced by a factor of 10 within a millimeter of leaving the orifice. Similar, the terminal velocity is reached within 1 mm of the orifice. These plots do not take into consideration the location of the Mach disk, which obviously introduce a discontinuity into the plot. Instead, these plots assume that the skimmer is placed within the zone of silence, thereby preserving the isentropic expansion.

Another important consideration is the number of collisions a molecule experiences between leaving the photolysis region and arriving at the detector. I have divided the total number of collision into two regimes: (i) collisions within the reactor (i.e. collisions



**Figure 5-8** – Gas properties along the centerline. (a) Location of the Mach Disk, (b) The normalized temperature, pressure, and density as a function of distance from the orifice.

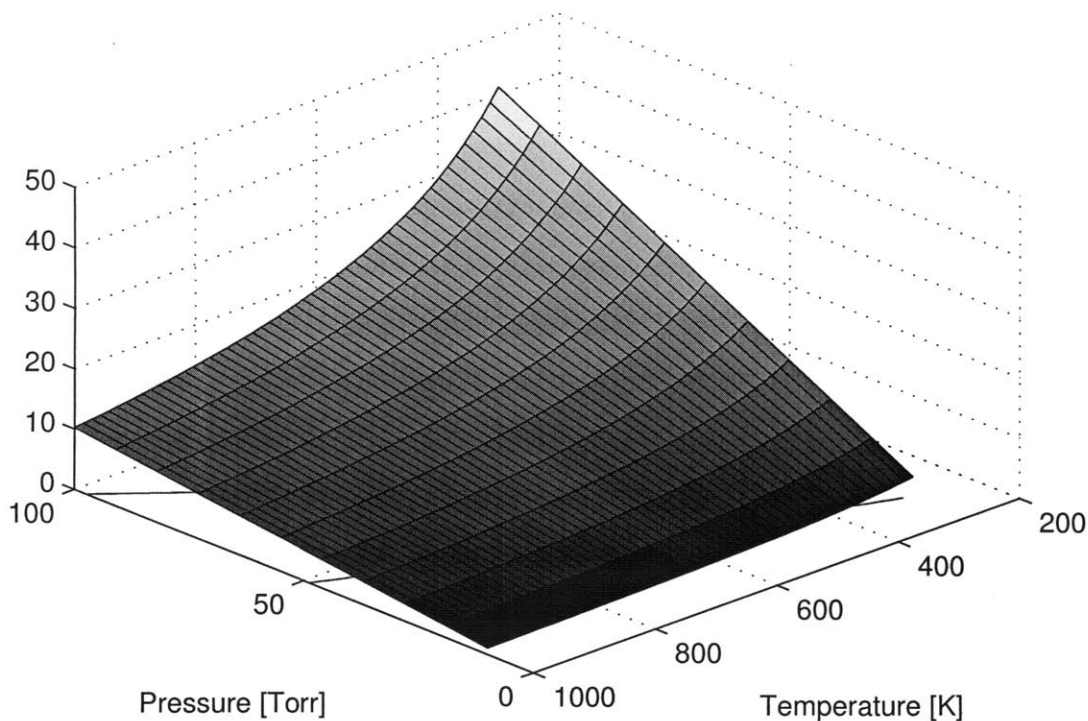
experienced between leaving the photolysis region and entering the orifice, assuming that the orifice does not penetrate the photolysis region), and (ii) collision within the free jet expansion (i.e. collisions experienced between the orifice and the detector). In both cases I estimated the number of collisions as the integral of the collision frequency divided by the velocity:

$$N_{\text{collisions, total}} = N_{\text{collisions, reactor}} + N_{\text{collisions, fje}}$$

$$N_{\text{collisions, reactor}} = \int_{x_{\text{photolysis}}}^{x_{\text{orifice}}} \frac{\omega(T, P; \text{gas})}{v(T, x; \text{gas})} dx \quad (5.15)$$

$$N_{\text{collisions, fje}} = \int_{x_{\text{orifice}}}^{x_{\text{detector}}} \frac{\omega(T, P; \text{gas})}{v(T, x; \text{gas})} dx \quad (5.16)$$

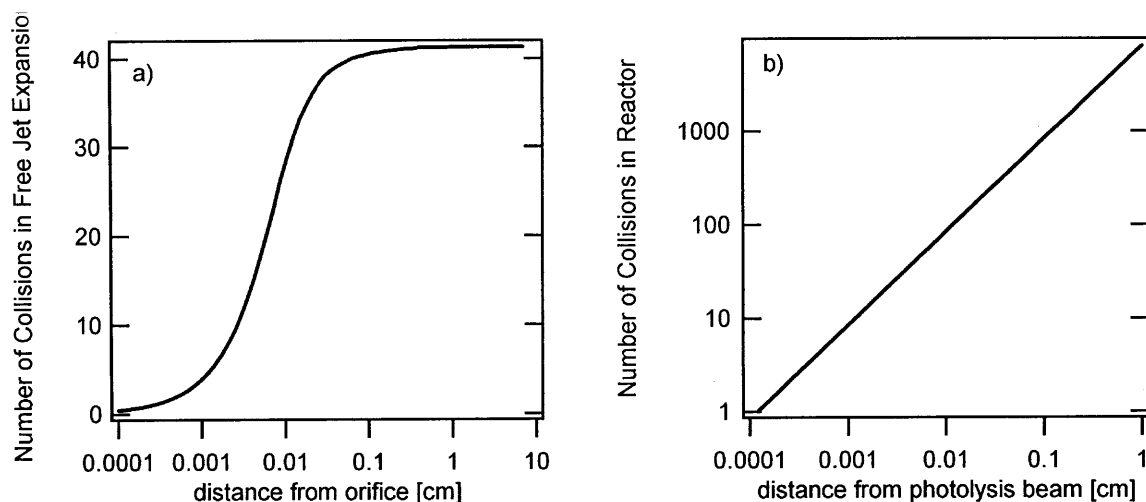
where  $\omega(T, P; \text{gas})$  is the collision frequency of the gas, which is calculated using a Lennard-Jones model, and  $v(T, x; \text{gas})$  is the velocity. I will begin with the collisions in the free jet expansion, Equation (5.16). I used the velocity profile Equation (5.11) in the denominator of the integrand. This equation was solved for  $300 < T < 1000$  K and  $10 < P < 100$  Torr, assuming a distance to detector of 6.1 cm. The results are shown in Figure 5-9. The maximum number of collisions is experienced at low temperatures and high pressures, which



**Figure 5-9** – Total number of collisions in free jet expansion as a function of temperature and pressure

makes sense, since the hard-sphere collision frequency scales as  $\omega \propto P/\sqrt{T}$ . Figure 5-10a illustrates how the number of collisions increase with the distance from the orifice. From this plot, it is clear that the most (e.g. 95%) of the collisions occur within 1 mm of the orifice, and that the terminal number of collisions has been reached within 1 cm of the orifice. Since all of the experiments are performed under dilute conditions using a Helium bath gas, and since Helium is an inefficient collider, a total of number of collisions on the order of 50 in the free jet expansion is acceptable. Therefore, based upon these calculations, the reactive gas should be sufficiently quenched once it exits the reactor tube.

The number of collisions within the reactor tube, however, is significantly larger. Here again we assume a Lennard-Jones collision frequency. For the gas within the tube, we do not have a direct formula for the velocity profile of the gas as it leaves the photolysis beam and enters the orifice. Since the bulk gas flow is normal to the orifice, there should be no bulk flow in the radial direction. However, the solution is undefined if the initial velocity is zero, so I have assumed an initial velocity equal to the average velocity of the Maxwell-Boltzmann distribution. I have assumed a velocity of the speed of sound at the



**Figure 5-10** – Total number of collisions as a function distance at 300 K and 100 Torr. (a) distance from the orifice to the detector, (b) distance from the photolysis beam to the orifice.

orifice exit, which is consistent with the assumption at the beginning of this section. The acceleration of gas particles from the average velocity to the speed of sound is not known, so for simplicity I have assumed a linear acceleration. The results of this calculations for 300 K and 100 T are shown in Figure 5-10b. This figure clearly illustrates the importance of getting the sampling nozzle as close to the photolysis beam as possible. If the nozzle can be maintained with 100  $\mu\text{m}$  of the photolysis beam, then there will be fewer than 100 collisions, which should be acceptable. On the other hand, if the nozzle is off by 1 cm, then there will be 10,000 collisions. Under those conditions, the gas composition in the detector will be completely different from the gas composition in the photolysis beam. The resulting data would not be worthless, since it would still provide a detailed analysis of the stable species; however, its usefulness for kinetic studies would be greatly diminished.

### 5.2.7 Collimation of the Molecular Beam

In the previous three sections, we established that the new design would (i) sample gas from within the photolysis region without disturbing the probe beam, (ii) quench the gas by the formation of a supersonic free jet expansion, and (iii) maintain a suitably low number of collisions. Additionally, in order to sample from within the isentropic region, the detector must be within 2 cm of the plate; to err on the safe side, it is preferable to have the

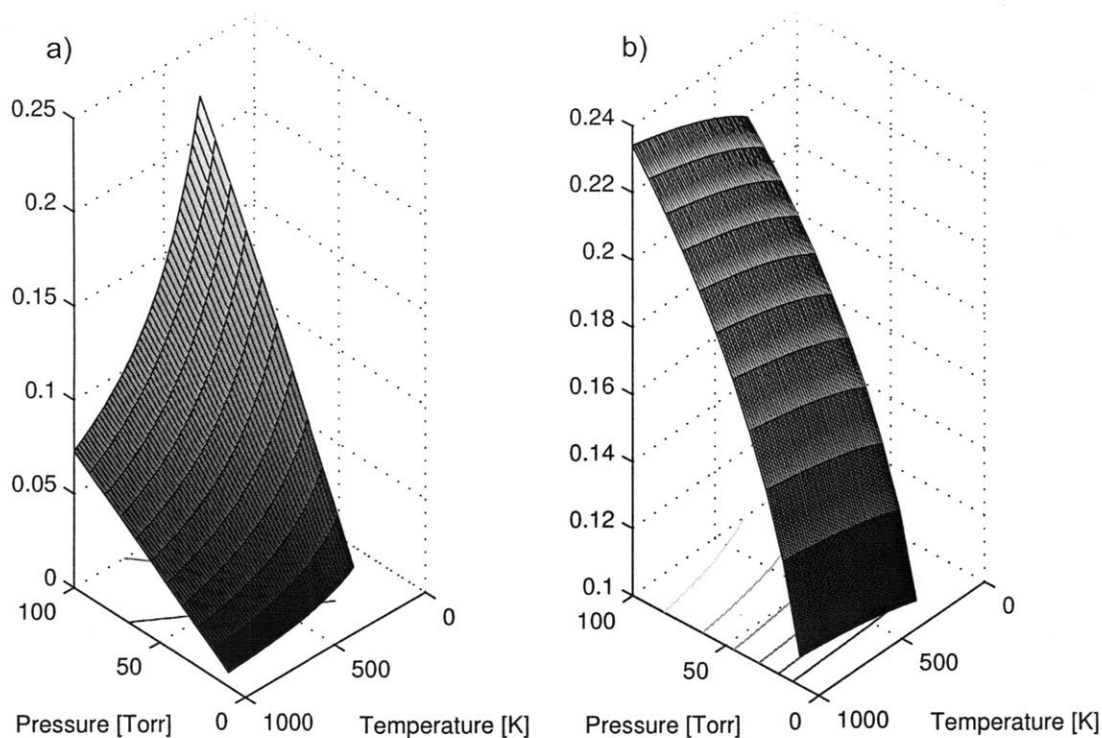
detector within 1 cm. This presents a few challenges. First, it is quite likely that the metal frame which holds the grounding mesh for the ion propulsion would cause some boundary layer interference, possibly increasing the number of collisions. Second, if the reactor is at 100 Torr, then the local pressure at the ionization source could exceed  $10^{-4}$  Torr. If the pressure in the ionization chamber exceeds  $10^{-4}$  Torr and contains any oxygen, then the egun filament would burn out. In order to avoid this, we would have to either (i) never perform oxidation experiments above 10 Torr, or (ii) replace the 2000 L/s turbo pump with an even larger diffusion pump. In order to avoid these two complications, we decided to use a nickel skimmer to collimate the free jet expansion into a molecular beam. This skimmer can be placed well inside the zone of silence. The result is a molecular beam that is pointed directly to the ionization chamber. Using the skimmer has three advantages. First, the diameter of the beam is smaller than metal frame that supports the grounding mesh, so there should be no boundary layer interference. Second, it pushes the egun filament out of the danger zone. Third, it allows us to use differential pumping between the low-vacuum and high-vacuum regions, which reduces the pumping requirements on the first-stage turbo pump.

In theory, there are design equations that can be used to determine the optimum placement for the skimmer tip. In practice, however, these equations are of limited use. The two equations are:

$$x_{\text{optimum},1}^{\text{skimmer}} = x_M \left( \frac{1}{1 + \frac{\epsilon \lambda_M}{x_M}} \right) \quad (5.17)$$

$$x_{\text{optimum},2}^{\text{skimmer}} = \frac{d}{8} \left[ \left( \frac{d}{\lambda_0} \right) \left( \frac{P_{\text{reactor}}}{P_{\text{orifice}}} \right) \right]^{1/3} \quad (5.18)$$

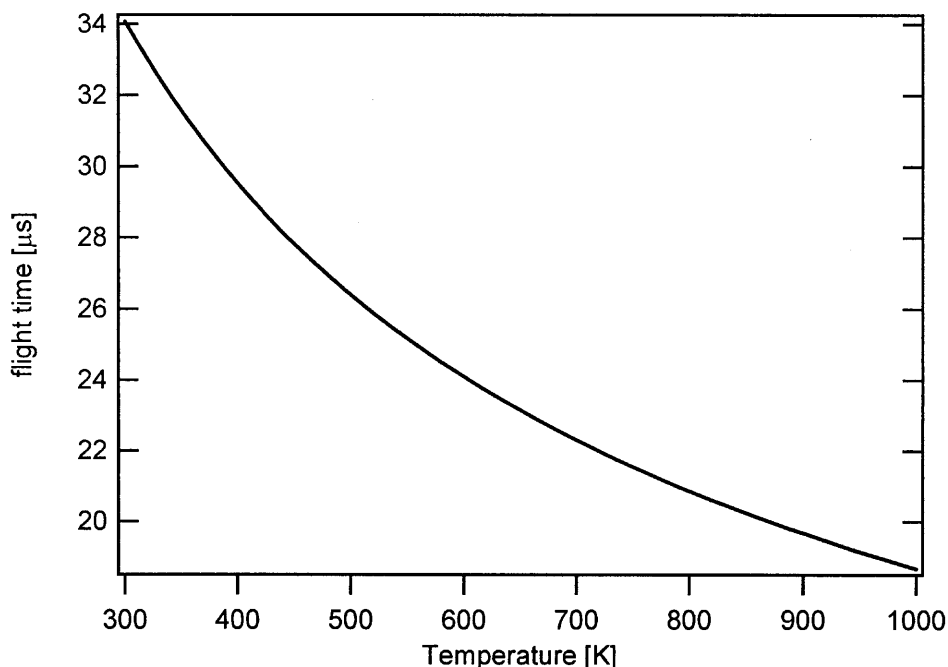
The reason for the limited applicability is (i) the two methods don't always agree for a given temperature, pressure, gas composition, and (ii) the range of values that each method returns is too broad. To illustrate these two points, consider two surface plots in Figure 5-11. The two plots predict similar ranges for the optimum skimmer placement: 0.007



**Figure 5-11** – Optimum skimmer placement for Helium, as predicted by (a) Equation (5.17), and (b) Equation (5.18)

$< x_{\text{optimum}}^{\text{skimmer}} < 0.23$  cm, but they show markedly different temperature dependencies. Furthermore, the values predicted can change by a factor of two or more for different gas compositions. Once the skimmer is in place, it will be extremely difficult to move it. The only way to move the position of the skimmer tip is to (i) use spacers at the base, or (ii) use a different skimmer with a different height (which forces a different skimmer diameter). Thus, rather than rely too much on the design equations for the skimmer placement, we opted to place the skimmer within  $\sim 1$  mm of the orifice. We purchased three different skimmers – with orifice diameters of 0.5 mm, 1 mm, and 2 mm, respectively – which will dictate the exact distance between the nozzle orifice and the skimmer orifice. We will then see which skimmer gives the best signal.

Once it was decided that we use a differential pumping / molecular beam assembly, the final task was to minimize the distance between the photolysis region and the opening to the detector (aka, the snout). This task is critical, since the density of the gas drops as the square of the distance from the origin. Given the design constraints detailed above, and



**Figure 5-12** – Flight time from nozzle orifice to detector snout as a function of temperature

given what is mechanically feasible from the machinists, we were able to achieve a total distance of 5.6 cm from the tip of the sample orifice to the ionization region, or 6.1 cm from the tip of the sample orifice to the inlet on the time-of-flight flight tube. The total flight time,  $\tau_{\text{flight time}}$ , from the nozzle orifice to the snout is calculated by integrating the inverse of the velocity with respect to position:

$$\tau_{\text{flight time}} = \int_{\text{orifice}}^{\text{snout}} \frac{1}{v(x, T)} dx \quad (5.19)$$

The average flight time is on the order of  $\sim 25$  microseconds, as seen in Figure 5-12. According to the calculations from Equation (5.10) the number density at this distance should be on the order of  $\sim 10^{13}$  molecules/cm<sup>3</sup> at 300 K and 100 Torr.

## 5.2.8 Estimation of Sensitivity

Josh Middaugh and I visited Prof. Lisa Pfefferle’s lab at Yale University. A staff scientist in her lab, Dr. Charles McEnally, gave us a detailed description of the photoionization mass



spectrometer they use to study concentration profiles in a stable flame. Their apparatus should provide a reasonable estimate on the measurement sensitivity we should expect with the new apparatus. Their reactor pressures are similar to ours. Their lab uses the exact same photoionization source that we will use, and their orifice-to-snout distance is also 6 cm. They routinely measure species in the 0.1 ppm detection level. Other things being equal, we should also be able to detect species with concentrations in the 0.1 ppm level using photoionization. For the vinyl radical chemistry performed by Dr. Ismail, the initial concentration of vinyl was typically on the order of 10 ppm. Consequently, if we can minimize the distance between the photolysis beam and the sample orifice so as to minimize the total number of collisions, and if we can indeed measure the rate of decay from 10 ppm to 0.1 ppm, then we should be able to perform kinetic studies for other radicals species that were not previously accessible with the pre-existing laser absorption cell.

### **5.3 Conclusion**

We have designed a new reactor for measuring reaction rates under combustion relevant conditions. This new reactor combines multi-pass laser absorption spectroscopy with time-of-flight mass spectrometry. The reactor tube has a novel sampling nozzle built into the side. This tube is surrounded by a low-vacuum region, which creates a supersonic free jet expansion. The low-vacuum region is connected to a high-vacuum region via a nickel skimmer, which collimates the free jet expansion into a molecular beam. This molecular beam is ionized in the high-vacuum region – either via electron impact or photoionization – before continuing to the detector.

Based upon the calculations presented in this chapter, the differential pumping system should allow us to (i) sample gas from the photolysis beam without disturbing the probe laser, (ii) rapidly quench the gas so that the chemical composition is frozen, and (iii) transport it to the ionization region and thence the detector with a minimum number of collisions. The photoionization detection limit should be on the order of 0.1 ppm, which should provide us with excellent of signal for kinetics experiments.



# Chapter 6

## Recommendations for Future Work

In this chapter I present some summaries and recommendations for future work.

### 6.1 Vinyl Plus Alkenes

The agreement between the measured rate coefficients of Dr. Ismail and the computed rate coefficients is so good that there is little point in trying to improve their accuracy. Instead, I would suggest three future projects to build on this work. First, it would be interesting to see how substitution to the vinyl radical would influence the kinetics. Presumably these vinylic radicals would still be very reactive, but slightly less electrophilic. This could be confirmed re-optimizing all the transition states in the alkene system, but using 1-methyl-vinyl, 2-methyl-vinyl, 1,2-dimethyl-vinyl (cis and trans), 2,2-dimethyl-vinyl, and 1,2,2-trimethyl-vinyl instead of vinyl. These transition state calculations would be relatively easy, since the geometry of the transition state isn't expected to change substantially from its early nature. These results could then be used to create more general rate rule for all vinylic radicals plus generic alkenes.

The second project would be to measure the product concentrations. Indeed, my colleague Joshua Middaugh has begun work on this project. He proposes to look at the reaction  $\text{vinyl} + \text{propene} \rightarrow \text{ethene} + \text{allyl}$  and measure the total concentration of allyl. The rate he would measure would be the sum of the H-abstraction and the addition-isomerization-decomposition rates. By changing the pressure at each temperature, he would change the

addition-isomerization-decomposition rate (the H-abstraction rate should remain constant). These experiments would be an excellent test of the Master Equation predictions.

The third project would expand the scope of the original project to include oxygenated species. Bio-fuels are a hot topic in combustion research, and these fuels have significantly more fuel-bound oxygen than fossil fuels. These oxygenated species – such as alcohols, ethers, and esters – lead to increased concentrations of aldehydes and ketones in flames. The experimental data on carbonyl groups is more limited than alkanes. In part, this limitation is due to the strong UV absorption properties of the C=O double bond, which fatally compromises the use of laser-flash photolysis for kinetic studies. I would propose using transition state theory to compute the rate coefficients for carbon-centered radical addition to formaldehyde, acetaldehyde, and acetone. I would focus on methyl, vinyl, and ethyl radicals. For my work on allyloxy decomposition, I computed the rate coefficients for vinyl + formaldehyde. This work remains unpublished. In vinyl + ethene, the dominant bimolecular product channel was 1,3-butadiene + H. Similarly for vinyl + formaldehyde, the dominant addition-isomerization-decomposition product channel is acrolein + H. In contrast vinyl + alkenes, the H-abstraction reaction to form ethene + HCO is faster than the addition reaction. Nonetheless, chemically activated product formation should be accounted for. Eventually I would expand the scope to include formyl and methoxy radicals. Although the forward rate coefficients (written in the exothermic direction) are not expected to be too significant, the reverse rates – i.e. the  $\beta$ -scission reaction for many ether- and ester-derived radicals – would be very important in the fuel decomposition pathway. Accurate calculation of these equilibrium coefficients would be essential in modeling bio-fuel decomposition.

## 6.2 Allyl + HO<sub>2</sub>

The conclusion of the allyl + HO<sub>2</sub> chapter is that there is considerable uncertainty in the rate allyl + HO<sub>2</sub> → propene + oxygen. This rate constant would be incredibly difficult to measure, since it would require some knowledge of the initial concentrations of both allyl and HO<sub>2</sub>. Such measurements would not be impossible, however. If, for example,

allyl-iodine were used as the photolytic precursor, then one could measure the initial concentration of allyl by measuring the initial concentration of I atoms, exactly as Huzeifa did in his thesis. Similarly, one could measure HO<sub>2</sub> using continuous wavelength infrared frequency modulation spectroscopy. These experiments would be challenging, and the resulting measurements would be for a complex system of reactions, so measurement of the H-abstraction reaction would remain indirect.

In general, the allyl + HO<sub>2</sub> chapter suggestions that more R + HO<sub>2</sub> reactions should be considered, in addition to the methyl and allyl reactions detailed thus far. Since these reactions convert the relatively unreactive HO<sub>2</sub> to the comparatively highly reactive OH radical, they play an important, under-investigated class of reactions. Since the HO<sub>2</sub> radical is intimately linked to the negative temperature coefficient in ignition studies, it is suggested that more reactions of this type be considered. Since these reactions are second-order with respect to radical concentration, only radicals with relatively high concentrations should be considered at first. Therefore, I should suggest ethyl as the next logical step.

### 6.3 Frequency Estimation

Although the group-additivity frequency method works well, it is far from perfect. Indeed, it does not work well for cyclic species. The biggest single improvement to frequency estimation for RMG would be to include 3D structures. Greg Magoon, a member of our group, is currently working on this project. 3D structures would allow for better estimates of the frequencies. It would also give access to rotational constants and reduced moments of inertia. All of these parameters would significantly improve the accuracy of the micro-canonical rates in RMG. In the shorter term, I would recommend creating a spectroscopic database. This database would contain the rotational constants, vibrational frequencies, reduced moments of inertia, and rotational barrier Fourier series. I have already calculated these parameters for the species in the thermo database. Since these  $\sim 200$  species are involved in many pressure-dependent channels, including their parameters would improve the resulting models.

A separate but related project would be a detailed examination of the eigenvalue solu-

tion method for the master equation. Specifically, a fascinating project would be to analyze the eigenvectors as the various isomers equilibrate at higher temperatures. In principle, it should be possible to predict when two wells have equilibrated. Once this is done, it would be quite simple to add their density of states, reduce the number of wells by one, and continue with the modified potential energy surface. This would allow us to use the eigenvalue method instead of the steady-state approximation method currently implemented.

Replacing the Inverse Laplace Transform method with more rigorous RRKM calculations would be fantastic, but this is nowhere near feasible in the short term, since the automation of transition state searches is far from robust.

## 6.4 Thermo Library

As detailed at the end of Chapter 4, the new thermo library is ripe for data mining. In the short term, I would recommend modifying RMG to use the NASA polynomials internally. In the intermediate term, I would recommend modifying RMG to include a spectroscopic library, for reasons detailed above. Again, it would be trivially simple to pull these parameters from the new library. The longer term project would be to data-mine this library and develop new group-additivity rules for heat capacity. The new group-additivity scheme would not be limited to temperatures below 1500 K. Instead, a larger and broader range of temperatures could be specified. By creating a larger and broader range of temperatures, RMG could fit the NASA polynomial directly to these values, rather than using the Wilhoit polynomial as an intermediate. This should substantially improve the accuracy of the NASA polynomials.

Ideally, I will continue to expand the database. As a practical matter, it would be difficult to expand the database beyond C4 chemistry for two reasons. First, the number of species increases exponentially. Second, the computational resources required for the RQCISD(T)/cc-pVQZ are too demanding for more than six or seven heavy atoms, at least on the current cluster. My proposal, then would be to develop the library to include all the species necessary for butanol oxidation. I have already included  $\sim 80\%$  of the species in Michael Harper's comprehensive butanol mechanism (including all the butanol isomers).

Some of the species in his mechanism are aromatic. As detailed in Section 4.3.1, the RQ-CISD(T) method is less accurate for the highly delocalized aromatic rings; something like LQCISD(T) would be more appropriate, if the chemical accuracy of  $\pm 1$  kcal/mol is to be preserved.

## 6.5 RMG in General

As represented in Venn diagram in the Introduction, RMG is a blend of computer science, numerical methods, and physical chemistry. The evolution of the project has necessitated that the software engineering be given precedence. However, thanks to the enormous work from the RMG development team, the software functions beautifully. It is my opinion, therefore, that more effort be given to the kinetics database. I would recommend two general strategies for improving the kinetics database. First, I would make it easier for a non-RMG developer to input a rate coefficient into the database. Dr. Richard West is restructuring the database to make this easier. Presently, when I calculate a rate coefficient, I put it in a personal Primary Reaction Library. RMG can use this rate coefficient for this particular rate, but it cannot learn from it. If it were easier to put the same rate parameters into the database, RMG would improve its estimates for all similar reactions. In practice, however, this process is time consuming; consequently, it is not done nearly enough. The result, then, is a collection of fractured primary reaction libraries and an under-developed kinetic database.

The second general strategy would be to look at the rate coefficients for any given mechanism and see which rate constants required the most averaging. By slowly and steadily filling in the biggest gaps in the kinetics database, RMG will require fewer averages per rate coefficient, and the resulting mechanisms will rapidly improve in accuracy.

With these improvements, RMG will be an indispensable tool for kineticists. Once the kinetic predictions are consistently more accurate, I can easily imagine that it will be adopted by the large kinetics community. An ideal application for RMG in the immediate future is to use RMG to help model a particular reaction system. For example, detailed transition state theory calculations can be done for the dozen-or-so most important reac-

tions, and RMG can be used to fill in the rest. My collaboration with Argonne and Sandia National Laboratories on propane oxidation, and Dr. Richard West's work on modeling shock tube decomposition of methyl-formate suggest that this strategy works very well.



# Bibliography

- [1] K. Andersson, P. A. Malmqvist, and B. O. Roos. 2nd-order perturbation-theory with a complete active space self-consistent field reference function. *Journal of Chemical Physics*, 96(2):1218–1226, Jan 1992.
- [2] D.C. Astholz, J. Troe, and W. Wieters. Unimolecular processes in vibrationally highly excited cycloheptatrienes. I. thermal isomerization in shock waves. *Journal of Physical Chemistry*, 70(11):5107–5166, 1979.
- [3] John R. Barker, Nicholas F. Ortiz, Jack M. Preses, Lawrence L. Lohr, Andrea Maranzana, and Philip J. Stimac. Multiwell-2008.3 software, 2008. <http://aoss.engin.umich.edu/multiwell/>.
- [4] James T. Bartis and B. Widom. Stochastic models of the interconversion of three or more chemical species. *J. Chem. Phys.*, 60:3474–3482, 1974.
- [5] D. L. Baulch, C. T. Bowman, C. J. Cobos, R. A. Cox, T. Just, J. A. Kerr, M. J. Pilling, D. Stocker, J. Troe, W. Tsang, R. W. Walker, and J. Warnatz. Evaluated kinetic data for combustion modeling: Supplement II. *Journal of Physical and Chemical Reference Data*, 34(3):757–1397, 2005.
- [6] Sidney W. Benson. *Thermochemical Kinetics: Methods for the Estimation of Thermochemical Data and Rate Parameters*. John Wiley and Sons, New York, first edition, 1976.
- [7] T. Beyer and D.F. Swinehart. Number of multiply-restricted partitions. *Communications of the ACM*, 16(6):379–379, 1973.

- [8] M. A. Blitz, D. E. Heard, and M. J. Pilling. OH formation from CH<sub>3</sub>CO + O<sub>2</sub>: A convenient experimental marker for the acetyl radical. *Chem. Phys. Lett.*, 365:374–379, 2002.
- [9] John Burkardt. DQED FORTRAN90. [http://people.sc.fsu.edu/~burkardt/f\\_src/dqed/dqed.html](http://people.sc.fsu.edu/~burkardt/f_src/dqed/dqed.html).
- [10] A.Y. Chang, J.W. Bozzelli, and A.M. Dean. Kinetic analysis of complex chemical activation and unimolecular dissociation reactions using QRRK theory and the modified strong collision approximation. *Zeitschrift fur Physicalische Chemie*, 214(Part 11):1533–1568, 2000.
- [11] Larry A. Curtiss, Krishnan Raghavachari, Paul C. Redfern, Vitaly Rassolov, and John A. Pople. Gaussian-3 (G3) theory for molecules containing first and second-row atoms. *Journal of Chemical Physics*, 109(18):7764–7776, 1998.
- [12] M. E. Earle, R. Mills, and J. M. Roscoe. The photolysis of methyl vinyl ketone at 308 nm. *Journal of Photochemistry and Photobiology a-Chemistry*, 206(1):71–79, 2009.
- [13] Askar Fahr and S. E. Stein. Reactions of vinyl and phenyl radicals with ethyne, ethene and benzene. *Proc. Comb. Inst.*, 22:1023–1029, 1989.
- [14] D. Feller and D. A. Dixon. Extended benchmark studies of coupled cluster theory through triple excitations. *Journal of Chemical Physics*, 115(8):3484–3496, Aug 2001.
- [15] H. Fischer and L. Radom. Factors controlling the addition of carbon-centered radicals to alkenes-an experimental and theoretical perspective. *Angewandte Chemie-International Edition*, 40(8):1340–1371, 2001.
- [16] Wendell Forst. *Unimolecular Reactions: A Concise Introduction*. Cambridge University Press, Cambridge, England, first edition, 2003.

- [17] M. J. Frisch, G. W. Trucks, H. B. Schlegel, G. E. Scuseria, M. A. Robb, J. R. Cheeseman, J. A. Montgomery J., T. Vreven, K. N. Kudin, J. C. Burant, J. M. Millam, S. S. Iyengar, J. Tomasi, V. Barone, B. Mennucci, G. Cossi M.; Scalmani, N. Rega, G. A. Petersson, H. Nakatsuji, M. Hada, M. Ehara, K. Toyota, R. Fukuda, J. Hasegawa, M. Ishida, T. Nakajima, Y. Honda, O. Kitao, H. Nakai, M. Klene, X. Li, J. E. Knox, H. P. Hratchian, J. B. Cross, V. Bakken, C. Adamo, J. Jaramillo, R. Gomperts, R. E. Stratmann, O. Yazyev, A. J. Austin, R. Cammi, C. Pomelli, J. W. Ochterski, P. Y. Ayala, K. Morokuma, G. A. Voth, P. Salvador, J. J. Dannenberg, V. G. Zakrzewski, S. Dapprich, A. D. Daniels, M. C. Strain, O. Farkas, D. K. Malick, A. D. Rabuck, K. Raghavachari, J. B. Foresman, J. V. Ortiz, Q. Cui, A. G. Baboul, S. Clifford, J. Cioslowski, B. B. Stefanov, G. Liu, A. Liashenko, P. Piskorz, I. Komaromi, R. L. Martin, D. J. Fox, T. Keith, M. A. Al-Laham, C. Y. Peng, A. Nanayakkara, M. Challacombe, P. M. W. Gill, B. Johnson, W. Chen, M. W. Wong, C. Gonzalez, and J. A. Pople, 2004.
- [18] Y. Georgievskii and S. J. Klippenstein. Transition state theory for multichannel addition reactions: Multifaceted dividing surfaces. *Journal of Physical Chemistry A*, 107(46):9776–9781, Nov 2003.
- [19] Y. Georgievskii, S. J. Klippenstein, and L. B. Harding. VaReCoF, 2006.
- [20] Y. Georgievskii, J. A. Miller, and S. J. Klippenstein. Association rate constants for reactions between resonance-stabilized radicals:  $C_3H_3+C_3H_3$ ,  $C_3H_3+C_3H_5$ , and  $C_3H_5+C_3H_5$ . *Physical Chemistry Chemical Physics*, 9(31):4259–4268, Aug 2007.
- [21] Robert G. Gilbert and Sean C. Smith. *Theory of Unimolecular and Recombination Reactions*. Blackwell Scientific, Oxford, England, first edition, 1990.
- [22] D. M. Golden. Pressure dependent reactions for atmospheric and combustion models. *Chemical Society Reviews*, 37(4):717–731, 2008.
- [23] C. F. Goldsmith, H. Ismail, and W. H. Green. Pressure and temperature dependence of the reaction of vinyl radical with alkenes III: Measured rates and predicted product

- distributions for vinyl plus butene. *Journal of Physical Chemistry A*, 113(47):13357–13371, Nov 2009.
- [24] C. Franklin Goldsmith, Huzeifa Ismail, Paul R. Abel, and William H. Green. Pressure and temperature dependence of the reaction of vinyl radical with alkenes II: Measured rates and predicted product distributions for vinyl plus propene. *Proceedings of the Combustion Institute*, 32:139–148, 2009.
- [25] N. J. B. Green and Z. A. Bhatti. Steady-state master equation methods. *Phys. Chem. Chem. Phys.*, 9:4275–4290, 2007.
- [26] Richard Hanson and Fred Krogh. Dqed. <http://www.netlib.org/opt/dqed.f>.
- [27] Larry B. Harding, Yuri Georgievskii, and Stephen J. Klippenstein. Roaming radical kinetics in the decomposition of acetaldehyde. *Journal of Physical Chemistry A*, in press, 2009.
- [28] Michael E. Harding, Juana Vazquez, Branko Ruscic, and Angela K. Wilson. High-accuracy extrapolated ab initio thermochemistry. III. additional improvements and overview. *Journal of Chemical Physics*, 128(11411):11411–1 11411–15, 2008.
- [29] D. J. Henry, M. L. Coote, R. Gomez-Balderas, and L. Radom. Comparison of the kinetics and thermodynamics for methyl radical addition to C=C, C=O, and C=S double bonds. *Journal of the American Chemical Society*, 126(6):1732–1740, Feb 2004.
- [30] B. Heyberger, F. Battin-Leclerc, V. Warth, R. Fournet, G. M. Come, and G. Scacchi. Comprehensive mechanism for the gas-phase oxidation of propene. *Combustion and Flame*, 126(4):1780–1802, Sep 2001.
- [31] J. G. Hill, J. A. Platts, and H. J. Werner. Calculation of intermolecular interactions in the benzene dimer using coupled-cluster and local electron correlation methods. *Physical Chemistry Chemical Physics*, 8(35):4072–4078, 2006. ISI Document Delivery No.: 078NA Times Cited: 85 Cited Reference Count: 54 Hill, J. Grant Platts, James A. Werner, Hans-Joachim ROYAL SOC CHEMISTRY CAMBRIDGE.

- [32] H. Hippler, J. Troe, and H. J. Wendelken. Collisional deactivation of vibrationally highly excited polyatomic-molecules .2. direct observations for excited toluene. *Journal of Chemical Physics*, 78(11):6709–6717, 1983.
- [33] H. Hou, A. Li, H. Y. Hu, Y. Li, H. Li, and B. S. Wang. Mechanistic and kinetic study of the  $\text{CH}_3\text{CO} + \text{O}_2$  reaction. *J. Chem. Phys.*, 122:224304–224314, 2005.
- [34] H. E. Hunziker, H. Knepp, A. D. McLean, P. Siegbahn, and H. R. Wendt. Visible electronic absorption spectrum of vinyl radical. *Canadian Journal of Chemistry*, 61(5):993–5, 1983.
- [35] Huzeifa Ismail. Addition and recombination reactions of unsaturated radicals using a novel laser kinetics spectrometer. Master’s thesis, Massachusetts Institute of Technology, 2008.
- [36] Huzeifa Ismail, Paul R. Abel, William H. Green, Askar Fahr, Leonard E. Jusinski, Adam M. Knepp, Judit Zdor, Giovanni Meloni, Talitha M. Selby, David L. Osborn, and Craig A. Taatjes. Temperature-dependent kinetics of the vinyl radical ( $\text{C}_2\text{H}_3$ ) self-reaction. *Journal of Physical Chemistry A*, 113(7):1278–1286, 2009.
- [37] Huzeifa Ismail, C. Franklin Goldsmith, Paul R. Abel, Pui-Teng Howe, Askar Fahr, Joshua B. Halpern, Leonard E. Jusinski, Yuri Georgievskii, Craig A. Taatjes, and William H. Green. Pressure and temperature dependence of the reaction of vinyl radical with ethylene. *Journal of Physical Chemistry A*, 111(29):6843–6851, 2007.
- [38] A. W. Jasper, S. J. Klippenstein, and L. B. Harding. Theoretical rate coefficients for the reaction of methyl radical with hydroperoxyl radical and for methylhydroperoxide decomposition. *Proceedings of the Combustion Institute*, 32:279–286, 2009.
- [39] K.G Joback. Master’s thesis, Massachusetts Institute of Technology, 1984.
- [40] H. S. Johnston and J. Heicklen. Tunnelling corrections for unsymmetrical eckart potential energy barriers. *Journal of Physical Chemistry*, 66(3):532–533, 1962.

- [41] Harold S. Johnston and Julian Heicklen. Tunnelling corrections for unsymmetrical eckart potential energy barriers. *Journal of Physical Chemistry*, 66:532–533, 1962.
- [42] L. S. Kassel. Studies in homogeneous gas reactions II: Introduction of quantum theory. *J. Phys. Chem.*, 32:1065–1079, 1928.
- [43] James A. Kerr and Aric M.J. Parsonage. Evaluated kinetic data on gas phase hydrogen transfer reactions of methyl radicals. *Journal of Molecular Structure*, 38:286–287, 1976.
- [44] S. J. Klippenstein. Variational optimizations in the rice-ramsberger-kassel-marcus theory calculations for unimolecular dissociations with no reverse barrier. *Journal of Chemical Physics*, 96(1):367–371, Jan 1992.
- [45] S. J. Klippenstein, Y. Georgievskii, and L. B. Harding. Predictive theory for the combination kinetics of two alkyl radicals. *Physical Chemistry Chemical Physics*, 8(10):1133–1147, Mar 2006.
- [46] S. J. Klippenstein and L. B. Harding. Kinetics of the H plus NCO reaction. *Proceedings of the Combustion Institute*, 32:149–155, 2009.
- [47] Stephen J. Klippenstein, A.F. Wagner, R.C. Dunbar, David M. Wardlaw, and Jim A. Miller. Variflex, 2002.
- [48] W. Klopper, B. Ruscic, D. P. Tew, F. A. Bischoff, and S. Wolfsegger. Atomization energies from coupled-cluster calculations augmented with explicitly-correlated perturbation theory. *Chemical Physics*, 356:14–24, 2009.
- [49] Vadim D. Knyazev, Ilia A. Dubinsky, Irene R. Slagle, and David Gutman. Unimolecular decomposition of t-C<sub>4</sub>H<sub>9</sub> radical. *Journal of Physical Chemistry*, 98(20):5279–5289, 1994.
- [50] Vadim D. Knyazev and Irene R. Slagle. Experimental and theoretical study of the C<sub>2</sub>H<sub>3</sub> reversible arrow H + C<sub>2</sub>H<sub>2</sub> reaction. tunneling and the shape of falloff curves. *Journal of Physical Chemistry*, 100(27):16899–16911, 1996.

- [51] G. Kovács, J. Zádor, E. Farkas, R. Nádasdi, I. Szilágyi, S. Dóbé, T. Bérces, F. Márta, and G. Lendvay. Kinetics and mechanism of the reactions of CH<sub>3</sub>CO and CH<sub>3</sub>C(O)CH<sub>2</sub> radicals with O<sub>2</sub>. low-pressure discharge flow experiments and quantum chemical computations. *Phys. Chem. Chem. Phys.*, 9:4142–4154, 2007.
- [52] K. C. Lau, Y. Liu, and L. J. Butler. Probing the barrier for CH<sub>2</sub>CHCO → CH<sub>2</sub>CH+CO by the velocity map imaging method. *Journal of Chemical Physics*, 123(5):9, Aug 2005.
- [53] J. Lee, C. J. Chen, and J. W. Bozzelli. Thermochemical and kinetic analysis of the acetyl radical (CH<sub>3</sub>C.O) + O<sub>2</sub> reaction system. *J. Phys. Chem. A*, 106:7155–7170, 2002.
- [54] T. J. Lee, A. P. Rendell, and P. R. Taylor. Comparison of the quadratic configuration-interaction and coupled-cluster approaches to electron correlation including the effect of triple excitations. *International Conf in Honor of Professor John a Pople : Forty Years of Quantum Chemistry*, 94:5463–5468, Oct 15-19 1989.
- [55] R. Lesclaux, P. Rouse1, B. Veyret, and C. Pouchant. Gas-phase reactivity of the HCO radical with unsaturated hydrocarbons: An experimental and theoretical study. *J. Am. Chem. Soc.*, 108:3872–3879, 1986.
- [56] S.G. Lias, J.E. Bartmess, J.F. Liebman, J.L. Holmes, R.D. Levin, and W.G. Mallard. "Ion Energetics Data", volume 69. National Institute of Standards and Technology, 2009.
- [57] W. Liu, C. K. Law, and T. F. Lu. Multiple criticality and staged ignition of methane in the counterflow. *International Journal of Chemical Kinetics*, 41(12):764–776, Dec 2009.
- [58] Z. H. Lodhi and R. W. Walker. Decomposition of 4,4-dimethylpent-1-ene in the presence of oxygen between 400-degrees-c and 500-degrees-c - oxidation chemistry of allyl radicals. *Journal of the Chemical Society-Faraday Transactions*, 87(5):681–689, Mar 1991.

- [59] Z. H. Lodhi and R. W. Walker. Oxidation of allyl radicals - kinetic-parameters for the reactions of allyl radicals with HO<sub>2</sub> and O<sub>2</sub> between 400 and 480-degrees-c. *Journal of the Chemical Society-Faraday Transactions*, 87(15):2361–2365, Aug 1991.
- [60] J. G. Lopez, C. L. Rasmussen, M. U. Alzueta, Y. Gao, P. Marshall, and P. Glarborg. Experimental and kinetic modeling study of C<sub>2</sub>H<sub>4</sub> oxidation at high pressure. *Proceedings of the Combustion Institute*, 32:367–375, 2009.
- [61] K Sabbe Maarten. Personal communication with author, 2009.
- [62] A. Maranzana, J. R. Barker, and G. Tonachini. Master equation simulations of competing unimolecular and bimolecular reactions: Application to OH production in the reaction of acetyl radical with O<sub>2</sub>. *Phys. Chem. Chem. Phys.*, 9:4129–4141, 2007.
- [63] R. A. Marcus and O. K. Rice. The kinetics of the recombination of methyl radical and iodine atoms. *J. Phys. Coll. Chem.*, 55:894–908, 1951.
- [64] J. M. L. Martin. Ab initio total atomization energies of small molecules - towards the basis set limit. *Chemical Physics Letters*, 259(5-6):669–678, Sep 1996.
- [65] D. M. Matheu. *Integrated Pressure-Dependence in Automated Mechanism Generation: A New Tool for Building Gas-Phase Kinetic Models*. PhD thesis, Massachusetts Institute of Technology, 2004.
- [66] P. M. Mayer, C. J. Parkinson, D. M. Smith, and L. Radom. An assessment of theoretical procedures for the calculation of reliable free radical thermochemistry: A recommended new procedure. *Journal of Chemical Physics*, 108(2):604–615, Jan 1998.
- [67] A. M. Mebel, E. W. G. Diau, M. C. Lin, and K. Morokuma. Ab initio and RRKM calculations for multichannel rate constants of the C<sub>2</sub>H<sub>3</sub>+O<sub>2</sub> reaction. *Journal of the American Chemical Society*, 118(40):9759–9771, Oct 1996.
- [68] R. Mereau, M. T. Rayez, J. C. Rayez, F. Caralp, and R. Lesclaux. Theoretical study on the atmospheric fate of carbonyl radicals: kinetics of decomposition reactions. *Physical Chemistry Chemical Physics*, 3(21):4712–4717, 2001.



- [69] J. V. Michael, D. G. Keil, and R. B. Klemm. Rate constants for the reaction of hydroxyl radicals with acetaldehyde from 244-528 k. *J. Chem. Phys.*, 83:1630–1636, 1985.
- [70] David R. Miller. *Atomic and Molecular Beam Methods*, volume 1, chapter 2. Oxford University Press, 1988.
- [71] J. A. Miller and S. J. Klippenstein. The recombination of propargyl radicals: Solving the master equation. *Journal Of Physical Chemistry A*, 105(30):7254–7266, Aug 2 2001.
- [72] James A. Miller and Stephen J. Klippenstein. From the multiple-well master equation to phenomenological rate coefficients: Reactions on a C<sub>3</sub>H<sub>4</sub> potential energy surface. *Journal of Physical Chemistry A*, 107(15):2680–2692, 2003.
- [73] James A. Miller, Stephen J. Klippenstein, and Christophe Raffy. Solution of some one- and two-dimensional master equation models for thermal dissociation: The dissociation of methane in the low-pressure limit. *Journal of Physical Chemistry A*, 106(19):4904–4913, 2002.
- [74] Johanna L. Miller. Theoretical study of the straight-chain C<sub>4</sub>H<sub>7</sub> radical isomers and their dissociation and isomerization transition states. *Journal of Physical Chemistry A*, 108(12):2268–2277, 2004.
- [75] J. A. Montgomery, M. J. Frisch, J. W. Ochterski, and G. A. Petersson. A complete basis set model chemistry. VI. use of density functional geometries and frequencies. *Journal of Chemical Physics*, 110(6):2822–2827, Feb 1999.
- [76] John H. Moore, Christopher C. Davis, and Michael A. Coplan. *Building Scientific Apparatus*. Cambridge University Press, Cambridge, England, fourth edition, 2009.
- [77] Michael D. Morse. *Methods of Experimental Physics: Atomic, Molecular, and Optical Physics*, volume 2, chapter 2. Academic Press, Inc., 1996.

- [78] C. D. Pibel, A. McIlroy, C. A. Taatjes, S. Alfred, K. Patrick, and J. B. Halpern. The vinyl radical,  $(\tilde{A})^{\prime\prime}-(\tilde{X})^{\prime}$  spectrum between 530 and 415 nm measured by cavity ring-down spectroscopy. *Journal of Chemical Physics*, 110(4):1841–1843, Jan 1999.
- [79] K. S. Pitzer. Energy levels and thermodynamic functions for molecules with internal rotation. II unsymmetrical tops attached to a rigid frame. *Journal of Chemical Physics*, 14(4):239–243, April 1946.
- [80] K. S. Pitzer and W. D. Gwinn. Energy levels and thermodynamic functions for molecules with internal rotation. I rigid frame with attached tops. *Journal of Chemical Physics*, 10(7):428–440, Jul 1942.
- [81] K. S. Pitzer and J.E. Kilpatrick. Energy levels and thermodynamic functions for molecules with internal rotation. III. compound rotation. *Journal of Chemical Physics*, 17(1):1064–1074, Nov 1949.
- [82] C. L. Rasmussen, J. Hansen, P. Marshall, and P. Glarborg. Experimental measurements and kinetic modeling of CO/H<sub>2</sub>/O<sub>2</sub>/NO, conversion at high pressure. *International Journal of Chemical Kinetics*, 40(8):454–480, 2008.
- [83] C. L. Rasmussen, J. G. Jakobsen, and P. Glarborg. Experimental measurements and kinetic modeling of CH<sub>4</sub>/O<sub>2</sub> and CH<sub>4</sub>/C<sub>2</sub>H<sub>6</sub>/O<sub>2</sub> conversion at high pressure. *International Journal of Chemical Kinetics*, 40(12):778–807, 2008.
- [84] A. Rauk, R. J. Boyd, S. L. Boyd, D. J. Henry, and L. Radom. Alkoxy radicals in the gaseous phase: beta-scission reactions and formation by radical addition to carbonyl compounds. *Canadian Journal of Chemistry-Revue Canadienne De Chimie*, 81(6):431–442, Jun 2003.
- [85] O. K. Rice and H. C. Ramsperger. Theories of unimolecular gas reactions at low pressures. *J. Am. Chem. Soc.*, 49:1617–1629, 1927.

- [86] H. Richter and J. B. Howard. Formation of polycyclic aromatic hydrocarbons and their growth to soot - a review of chemical reaction pathways. *Progress in Energy and Combustion Science*, 26(4-6):565–608, 2000.
- [87] M. K. Sabbe, M. F. Reyniers, V. Van Speybroeck, M. Waroquier, and G. B. Marin. Carbon-centered radical addition and beta-scission reactions: Modeling of activation energies and pre-exponential factors. *Chemphyschem*, 9(1):124–140, Jan 11 2008.
- [88] J. H. Seinfeld and S. N. Pandis. *Atmospheric Chemistry and Physics - From Air Pollution to Climate Change*. John Wiley and Sons, second edition, 2006.
- [89] Milena Shahu, Chun-Hui Yang, Charles D. Pibel, Andrew McIlroy, Craig A. Taatjes, and Joshua B. Halpern. Vinyl radical visible spectroscopy and excited state dynamics. *Journal of Chemical Physics*, 116(19):8343–8352, 2002.
- [90] Sandeep Sharma, Michael R. Harper, and William H. Green. CanTherm. <http://github.com/GreenGroup/CanTherm>.
- [91] Sandeep Sharma, Sumathy Raman, and William H Green. *Journal of Physical Chemistry A*, (submitted).
- [92] Alexander A. Shestov, Konstantin V. Popov, Irene R. Slagle, and Vadim D. Knyazev. Kinetics of the reaction between vinyl radical and ethylene. *Chemical Physics Letters*, 408(4-6):339–343, 2005.
- [93] Jing Song. Building robust chemical reaction mechanisms: Next generation of automatic model construction software. ph.d dissertation. Master’s thesis, Massachusetts Institute of Technology, 2004.
- [94] N. D. Stothard and R. W. Walker. Determination of the arrhenius parameters for the initiation reaction  $C_3H_6 + O_2 \rightarrow CH_2CHCH_2 + HO_2$ . *Journal of the Chemical Society-Faraday Transactions*, 87(2):241–247, Jan 1991.
- [95] D. E. Szpunar, J. L. Miller, L. J. Butler, and F. Qi. 193-nm photodissociation of acryloyl chloride to probe the unimolecular dissociation of  $CH_2CHCO$  radicals and  $CH_2CCO$ . *Journal of Chemical Physics*, 120(9):4223–4230, Mar 2004.

- [96] R. K. Talkudar, M. E. Davis, L. Zhu, and A. R. Ravishankara. *19th International Symposium on Gas Kinetics*, 2006.
- [97] W. Tsang. Chemical kinetic data-base for hydrocarbon pyrolysis. *Industrial & Engineering Chemistry Research*, 31(1):3–8, Jan 1992.
- [98] W. Tsang and R. F. Hampson. Chemical kinetic database for combustion chemistry .1. methane and related-compounds. *Journal of Physical and Chemical Reference Data*, 15(3):1087–1279, 1986.
- [99] Wing Tsang. Chemical kinetic data base for combustion chemistry. part V. propene. *Journal of Physical and Chemical Reference Data*, 20(2):221–73, 1991.
- [100] G. S. Tyndall, J. J. Orlando, T. J. Wallington, and M. D. Hurley. Pressure dependence of the rate coefficients and product yields for the reaction of CH<sub>3</sub>CO radicals with O<sub>2</sub>. *Int. J. Chem. Kin.*, 29:655–663, 1997.
- [101] H.-J. Werner, P. J. Knowles, R. Lindh, F. R. Manby, M. Schuetz, , et al. Molpro, version 2006.1, a package of ab initio programs, 2006.
- [102] B. Widom. Molecular transitions and chemical reaction rates. *Science*, 148:1555–1560, 1955.
- [103] B. Widom. Reaction kinetics in stochastic models. *J. Chem. Phys.*, 35:44–52, 1971.
- [104] B. Widom. Reaction kinetics in stochastic models. *J. Chem. Phys.*, 61:672–680, 1974.
- [105] H. B. Xie, Y. H. Ding, and C. C. Sun. Theoretical study on the reaction mechanism of vinyl radical with formaldehyde. *Journal of Physical Chemistry A*, 109(37):8419–8423, Sep 2005.
- [106] Xueliang L. Yang, C. Franklin Goldsmith, and Robert S. Tranter. Decomposition and vibrational relaxation in CH<sub>3</sub>I and self-reaction of CH<sub>3</sub> radicals. *Journal of Physical Chemistry A*, 113(29):8307–8317, 2009.

- [107] Y. Zhao and D. G. Truhlar. The M06 suite of density functionals for main group thermochemistry, thermochemical kinetics, noncovalent interactions, excited states, and transition elements: two new functionals and systematic testing of four M06-class functionals and 12 other functionals. *Meeting on Practicing Chemistry with Theoretical Tools*, 120:215–241, Jan 15-18 2007.
- [108] P. Zou, K. E. Strecker, J. Ramirez-Serrano, L. E. Jusinski, C. A. Taatjes, and D. L. Osborn. Ultraviolet photodissociation of vinyl iodide: understanding the halogen dependence of photodissociation mechanisms in vinyl halides. *Physical Chemistry Chemical Physics*, 10(5):713–728, 2008.